REPORT DOCUMENTATION PAGE

Form Approved
OMB No. 0704-0188

PLEASE DO NOT RETURN YOUR FORM TO THE ABOVE ORGANIZATION.

1. REPORT DATE *(DD-MM-YYYY)*	2. REPORT TYPE	3. DATES COVERED *(From - To)*
12-16-2014	Final	08/01/2011-07/31/2014

4. TITLE AND SUBTITLE
Self-Assembly of Large Scale Shape Controlled DNA Nano- Structures

5a. CONTRACT NUMBER

5b. GRANT NUMBER
N00014-11-1-0914

5c. PROGRAM ELEMENT NUMBER

6. AUTHOR(S)
Peng Yin, Ph.D.

5d. PROJECT NUMBER

5e. TASK NUMBER

5f. WORK UNIT NUMBER

7. PERFORMING ORGANIZATION NAME(S) AND ADDRESS(ES)
President and Fellows of Harvard College
Office of Sponsored Programs
Smith Center, Suite 600
Cambridge, MA 02138

8. PERFORMING ORGANIZATION REPORT NUMBER
167821

9. SPONSORING/MONITORING AGENCY NAME(S) AND ADDRESS(ES)
ONR REG BOSTON N62879
495 SUMMER STREET ROOM 627
BOSTON, MA 02210-2109

10. SPONSOR/MONITOR'S ACRONYM(S)
ONR

11. SPONSOR/MONITOR'S REPORT NUMBER(S)
N62879

12. DISTRIBUTION/AVAILABILITY STATEMENT
Approved for Public Release; distribution is Unlimited

13. SUPPLEMENTARY NOTES

14. ABSTRACT
We proposed to develop a methodology by using short synthetic DNA strands to build complex DNA nano-structures. In such a methodology, each short synthetic DNA strand, called DNA brick, is designed as a modular building block to assemble large structure with nanometer scale geometry control. We are using the methodology to build a variety of complex nano-structures, including 1D, 2D, 3D discrete structures and extended crystals. We are also developing a number of real world applications based on these novel structures. The successful development of this modular nanostruction methodology and the associated real world applications will have transformative impact.

15. SUBJECT TERMS
DNA nanotechnology, nucleic acid structures, patterning, barcoding

16. SECURITY CLASSIFICATION OF:			17. LIMITATION OF ABSTRACT	18. NUMBER OF PAGES	19a. NAME OF RESPONSIBLE PERSON
a. REPORT	b. ABSTRACT	c. THIS PAGE			Peng Yin
U	U	U	UU		19b. TELEPHONE NUMBER *(Include area code)* 617-432-7731

20141219266

Technical Report for N000141110914

Self-Assembly of Large-Scale Shape-Controlled DNA Nano-Structures

Principle Investigator: Peng Yin, Harvard University

Contents

1 Heading 3

2 Scientific and technical objectives 3

3 Approach 3

4 Concise accomplishment 3

5 Expanded accomplishments 4

5.0.1 DNA brick nano-structures . . . 4
5.0.2 Three-Dimensional Structures Self-Assembled from DNA Bricks . . . 5
5.0.3 Extended DNA crystals . . . 5
5.0.4 Diverse motifs for complex 2D shapes . . . 5
5.0.5 Assembly conditions of 2D shapes . . . 6
5.0.6 DNA cages . . . 6
5.0.7 Assembly across scales: DNA-directed hydrogel assembly . . . 6
5.1 Structural DNA nanotechnology application . . . 7
5.1.1 Structural DNA nanotechnology application: Geometrically encoded fluorescent barcodes . . . 7
5.1.2 Structural DNA nanotechnology application: Metallized DNA as etching mask for graphene . . . 7
5.1.3 Structural DNA nanotechnology application: Patterning inorganic oxides using DNA templates . . . 7
5.1.4 Structural DNA nanotechnology application: DNA Foundries for Shape-controlled inorganic material synthesis . . . 8

6 Major problems/issues (if any) 8

7 Technology transfer 8

8 Foreign collaborations and supported foreign nationals 8

9 Productivity **9**
9.1 Refereed journal article 9
9.2 Non-refereed journal article 10
9.3 Workshops and conferences 10
9.4 Awards/Honors 12

10 Award participants **12**

11 Appendix: Paper preprints and reprints **13**
11.1 DNA brick nano-structures 13
11.1.1 Two-Dimensional Structures Self-Assembled from DNA tiles 13
11.1.2 Three-Dimensional Structures Self-Assembled from DNA Bricks 14
11.1.3 Extended DNA crystals 15
11.1.4 Diverse motifs for complex 2D shapes 16
11.1.5 Assembly conditions of 2D shapes 17
11.2 DNA hydrogels 18
11.3 DNA cages 19
11.4 Assembly across scales: DNA-directed hydrogel assembly 20
11.5 Structural DNA nanotechnology application 21
11.5.1 Structural DNA nanotechnology application: Geometrically encoded fluorescent barcodes 21
11.5.2 Structural DNA nanotechnology application: Metallized DNA as etching mask for graphene 22
11.5.3 Structural DNA nanotechnology application: Patterning inorganic oxides using DNA templates 23
11.5.4 Structural DNA nanotechnology application: DNA Foundries for Shape-controlled inorganic material synthesis 24

1 Heading

- PI: Peng Yin
- Organization: Harvard University
- ONR Award Number: N000141110914
- Award Title: Self-Assembly of Large-Scale Shape-Controlled DNA Nano-Structures

2 Scientific and technical objectives

We proposed to develop a methodology by using short synthetic DNA strands to build complex DNA nano-structures. In such a methodology, each short synthetic DNA strand, called DNA brick, is designed as a modular building block to assemble large structure with nanometer scale geometry control. We are using the methodology to build a variety of complex nano-structures, including depth-defined 2D crystals and discrete 3D structures. We are also exploring the design space of these DNA brick structures to determine how motif changes effect the overall structure, and developing larger DNA bricks that assemble modularly to polyhedral cages by treating an origami structure as a brick. We are also developing a number of real world applications based on these novel structures. The successful development of this modular nano construction methodology and the associated real world applications will have transformative impact.

3 Approach

We report herein on the following approaches:

1. Development of fundamental molecular mechanisms that enable the assembly of complex DNA nano structures. See *Mechanisms* in next section.
2. Development of transformative real world applications based on such shape-controlled, uniquely addressable nano structures. See *Applications* in next section.

4 Concise accomplishment

- *Two-Dimensional Structures Self-Assembled from DNA tiles.* We describe a simple and robust method to construct complex two-dimensional (2D) structures by using short synthetic DNA strands that we call DNA tiles.
- *Three-Dimensional Structures Self-Assembled from DNA Bricks.* We describe a simple and robust method to construct complex three-dimensional (3D) structures by using short synthetic DNA strands that we call DNA bricks.
- *Complex Crystals with Prescribed Depth.* We describe here a novel molecular self-assembly framework that solves a key challenge in nano-fabrication, the construction of complex crystals with precisely controlled depth and prescribed intricate three-dimensional features.

- *Diverse motifs for complex 2D shapes.* We describe here the exploration of the design space for complex 2D DNA structures using single-stranded tile motif variations.
- *Assembly conditions of 2D shapes.* We explore the effect on formation conditions with different designs of the 2D DNA nano structures and develop a method for assembling structures under biocompatible conditions.
- *Polyhedra Self-Assembled from DNA tripods.* We describe here the assembly of large 20-60 MegaDalton synthetic molecular structure (12 times larger than DNA origami).
- *Assembly across scales: DNA-directed hydrogel assembly.* We describe here the DNA directed self-assembly of shape-controlled hydrogels.
- *Structural DNA nanotechnology application: Geometrically encoded fluorescent barcodes.* We describe here the construction of 216 submicrometre geometrically encoded fluorescent barcodes self-assembled from DNA.
- *Structural DNA nanotechnology application: Metallized DNA as etching mask for graphene.* Here we develop a metallized DNA nanolithography that allows transfer of spatial information to pattern two-dimensional nanomaterials capable of plasma etching.
- *Structural DNA nanotechnology application: Patterning inorganic oxides using DNA templates.* Here we develop a metallized DNA nanolithography that allows transfer of spatial information to pattern two-dimensional nanomaterials capable of plasma etching.
- *Structural DNA nanotechnology application: Casting shape-controlled inorganic materials.* We report a general strategy for designing and synthesizing inorganic nanostructures with arbitrarily prescribed three-dimensional shapes.

5 Expanded accomplishments

5.0.1 DNA brick nano-structures

Design space for complex DNA structures

Nucleic acids have emerged as effective materials for assembling complex nanoscale structures. To tailor the structures to function optimally for particular applications, a broad structural design space is desired. Despite the many discrete and extended structures demonstrated in the past few decades, the design space remains to be fully explored. In particular, the complex finite-sized structures produced to date have been typically based on a small number of structural motifs. Here, we perform a comprehensive study of the design space for complex DNA structures, using more than 30 distinct motifs derived from single-stranded tiles. These motifs self assemble to form structures with diverse strand weaving patterns and specific geometric properties, such as curvature and twist. We performed a systematic study to control and characterize the curvature of the structures, and constructed a flat structure with a corrugated strand pattern. The work here reveals the broadness of the design space for complex DNA nanostructures.

Please refer to Appendix 11.1.4 for more details.

5.0.2 Three-Dimensional Structures Self-Assembled from DNA Bricks

Three-Dimensional Structures Self-Assembled from DNA Bricks

We describe a simple and robust method to construct complex three-dimensional (3D) structures by using short synthetic DNA strands that we call "DNA bricks." In one-step annealing reactions, bricks with hundreds of distinct sequences self-assemble into prescribed 3D shapes. Each 32-nucleotide brick is a modular component; it binds to four local neighbors and can be removed or added independently. Each 8-base pair interaction between bricks defines a voxel with dimensions of 2.5 by 2.5 by 2.7 nanometers, and a master brick collection defines a "molecular canvas" with dimensions of 10 by 10 by 10 voxels. By selecting subsets of bricks from this canvas, we constructed a panel of 102 distinct shapes exhibiting sophisticated surface features, as well as intricate interior cavities and tunnels.

Please refer to Appendix 11.1.2 for more details.

5.0.3 Extended DNA crystals

Complex Crystals with Prescribed Depth

We describe here a novel molecular self-assembly framework that solves a key challenge in nanofabrication, the construction of complex crystals with precisely controlled depth and prescribed intricate three-dimensional features. Our approach uses single-stranded DNA components called DNA bricks.We demonstrate, for the first time, the construction of two-dimensional crystals with prescribed depths and intricate three-dimensional features with nanometer precision. These crystals can grow to micron size with prescribed depth up to 80 nm. They can be designed to display continuous or discontinuous cavities and channels, and to pack DNA helices at parallel and perpendicular angles relative to the plane of the crystals.

Please refer to Appendix 11.1.3 for more details.

5.0.4 Diverse motifs for complex 2D shapes

Design space for complex DNA structures

Nucleic acids have emerged as effective materials for assembling complex nanoscale structures. To tailor the structures to function optimally for particular applications, a broad structural design space is desired. Despite the many discrete and extended structures demonstrated in the past few decades, the design space remains to be fully explored. In particular, the complex finite-sized structures produced to date have been typically based on a small number of structural motifs. Here, we perform a comprehensive study of the design space for complex DNA structures, using more than 30 distinct motifs derived from single-stranded tiles. These motifs self-assemble to form structures with diverse strand weaving patterns and specific geometric properties, such as curvature and twist. We performed a systematic study to control and characterize the curvature of the structures, and constructed a flat structure with a corrugated strand pattern. The work here reveals the broadness of the design space for complex DNA nanostructures.

Please refer to Appendix 11.1.3 for more details.

5.0.5 Assembly conditions of 2D shapes

Isothermal self-assembly of complex DNA structures under diverse and biocompatible conditions

Nucleic acid nanotechnology has enabled researchers to construct a wide range of multidimensional structures in vitro. Until recently, most DNA-based structures were assembled by thermal annealing using high magnesium concentrations and nonphysiological environments. Here, we describe a DNA self-assembly system that can be tuned to form a complex target structure isothermally at any prescribed temperature or homogeneous condition within a wide range. We were able to achieve isothermal assembly between 15 and 69 °CC in a predictable fashion by altering the strength of strandÐstrand interactions in several different ways, for example, domain length, GC content, and linker regions between domains. We also observed the assembly of certain structures under biocompatible conditions, that is, at physiological pH, temperature, and salinity in the presence of the molecular crowding agent polyethylene glycol (PEG) mimicking the cellular environment. This represents an important step toward the self-assembly of geometrically precise DNA or RNA structures in vivo.

Please refer to Appendix 11.1.3 for more details.

5.0.6 DNA cages

Polyhedra self-assembled from DNA tripods and characterized with 3D DNA-PAINT

DNA self-assembly has produced diverse synthetic three-dimensional polyhedra. These structures typically have a molecular weight no greater than 5 megadaltons. We report a simple, general strategy for one-step self-assembly of wireframe DNA polyhedra that are more massive than most previous structures. A stiff three-arm-junction DNA origami tile motif with precisely controlled angles and arm lengths was used for hierarchical assembly of polyhedra. We experimentally constructed a tetrahedron (20 megadaltons), a triangular prism (30 megadaltons), a cube (40 megadaltons), a pentagonal prism (50 megadaltons), and a hexagonal prism (60 megadaltons) with edge widths of 100 nanometers. The structures were visualized by means of transmission electron microscopy and three-dimensional DNA-PAINT super-resolution fluorescent microscopy of single molecules in solution.

Please refer to Appendix 11.3 for more details.

5.0.7 Assembly across scales: DNA-directed hydrogel assembly

DNA directed self-assembly of shape-controlled hydrogels

Using DNA as programmable, sequence specific "glues", shape-controlled hydrogel units were self-assembled into prescribed structures. Aggregates were produced using hydrogel cubes with edge length ranging from 30 micrometers to 1 millimeter, demonstrating assembly across scales. In a simple one-pot agitation reaction, 25 dimers were constructed in parallel from 50 distinct hydrogel cube species, demonstrating highly multiplexed assembly. Using hydrogel cuboids displaying face-specific DNA glues, diverse structures were achieved in aqueous and in interfacial agitation systems. These include dimers, extended chains, and open network structures in an aqueous system; and dimers, chains of fixed length, T-junction, and square shapes in the interfacial system, demonstrating the versatility of the assembly system.

Please refer to Appendix 11.2 for more details.

5.1 Structural DNA nanotechnology application

5.1.1 Structural DNA nanotechnology application: Geometrically encoded fluorescent barcodes

Submicrometre intensity-encoded fluorescent barcodes self-assembled from DNA

The identification and differentiation of a large number of distinct molecular species with high temporal and spatial resolution is a major challenge in biomedical science. Fluorescence microscopy is a powerful tool, but its multiplexing ability is limited by the number of spectrally distinguishable fluorophores. Here, we used (deoxy)ribonucleic acid (DNA)- origami technology to construct submicrometre nanorods that act as fluorescent barcodes. We demonstrate that spatial control over the positioning of fluorophores on the surface of a stiff DNA nanorod can produce 216 distinct barcodes that can be decoded unambiguously using epifluorescence or total internal reflection fluorescence microscopy. Barcodes with higher spatial information density were demonstrated via the construction of super-resolution barcodes with features spaced by 40 nm. One species of the barcodes was used to tag yeast surface receptors, which suggests their potential applications as in situ imaging probes for diverse biomolecular and cellular entities in their native environments.

Please refer to Appendix 11.5.1 for more details.

5.1.2 Structural DNA nanotechnology application: Metallized DNA as etching mask for graphene

Metallized DNA nanolithography for encoding and transferring spatial information for graphene patterning

We report a general strategy for designing and synthesizing inorganic nanostructures with arbitrarily prescribed three-dimensional shapes. Computationally designed DNA strands self-assemble into a stiff "nano-mold" that contains a user-specified three-dimensional cavity and encloses a nucleating gold "seed". Under mild conditions, this seed grows into a larger cast structure that fills and thus replicates the cavity. We synthesized a variety of nanoparticles with three nanometer resolution: three distinct silver cuboids with three independently tunable dimensions, silver and gold nanoparticles with diverse cross sections, and composite structures with homo-/heterogeneous components. The designer equilateral silver triangular and spherical nanoparticles exhibited plasmonic properties consistent with electromagnetism-based simulations. Our framework is generalizable to more complex geometries and diverse inorganic materials, offering a range of applications in biosensing, photonics, and nanoelectronics.

Please refer to Appendix 11.5.4 for more details.

5.1.3 Structural DNA nanotechnology application: Patterning inorganic oxides using DNA templates

Nanoscale Growth and Patterning of Inorganic Oxides Using DNA Nanostructure Templates

We describe a method to form custom-shaped inorganic oxide nanostructures by using DNA nanostructure templates. We show that a DNA nanostructure can modulate the rate of chemical vapor deposition of SiO2 and TiO2 with nanometer-scale spatial resolution. The resulting oxide nanostructure inherits its shape from the DNA template. This method generates both positive-tone and negative-tone patterns on a wide range of substrates and is compatible with conventional silicon nanofabrication processes. Our result opens the door to the use of DNA nanostructures as general-purpose templates for high-resolution nanofabrication.

Please refer to Appendix 11.5.4 for more details.

5.1.4 Structural DNA nanotechnology application: DNA Foundries for Shape-controlled inorganic material synthesis

Casting Metal Structures within Programmable DNA Molds

We report a general strategy for designing and synthesizing inorganic nanostructures with arbitrarily prescribed three-dimensional shapes. Computationally designed DNA strands self-assemble into a stiff "nano-mold" that contains a user-specified three-dimensional cavity and encloses a nucleating gold "seed". Under mild conditions, this seed grows into a larger cast structure that fills and thus replicates the cavity. We synthesized a variety of nanoparticles with three nanometer resolution: three distinct silver cuboids with three independently tunable dimensions, silver and gold nanoparticles with diverse cross sections, and composite structures with homo-/heterogeneous components. The designer equilateral silver triangular and spherical nanoparticles exhibited plasmonic properties consistent with electromagnetism-based simulations. Our framework is generalizable to more complex geometries and diverse inorganic materials, offering a range of applications in biosensing, photonics, and nanoelectronics.

Please refer to Appendix 11.5.4 for more details.

6 Major problems/issues (if any)

None.

7 Technology transfer

See "Patents".

8 Foreign collaborations and supported foreign nationals

Peng Yin, Maier Avendano Amado, Alexander Green, Nikhil Gopalkrishnan, Dongran Han, Ralf Jungmann, Yonggang Ke, Jie Shen, Wei Sun, Michelle Vhudzijena, Wei Li Wang, Diming Wei, Sungwook Woo

9 Productivity

9.1 Refereed journal article

1. W. Sun, E. Boulais, Y. Hakobyan, W. Wang, A. Guan, M. Bathe, and P. Yin, *DNA 'Genome' for Programming 3D Inorganic Shapes. Science*, submitted.

2. Y. Ke, L. L. Ong, W. Sun, J. Song, M. Dong, W.M. Shih, and P. Yin, *Complex Crystals with Prescribed Depths. Nature Chemistry*, accepted in principle.

3. R. Iinuma†, Y. Ke†, R. Jungmann†, T. Schlichthaerle, J.B. Woehrstein, and P. Yin*, *Polyhedra Self-Assembled from DNA Tripods and Characterized by 3D DNA-PAINT.* **Science**, 344:65-69, 2014

    - This paper describes a general strategy for the self-assembly of wire-frame polyhedra using stiff, tunable DNA-tripods. The structures were characterized using 3D DNA-PAINT super-resolution microscopy.

4. B. Wei, M. Dai, C. Myhrvold, Y. Ke, R. Jungmann and P. Yin. *Design space for complex DNA structures.* Submitted, 2013.

5. J.P. Sadowski, C.R. Calvert, D.Y. Zhang, N.A. Pierce and P. Yin. *Developmental self-assembly of a DNA tetrahedron.* Submitted, 2013.

6. Y. Ke, L. L. Ong, W. Sun, J. Song, M. Dong, W. M. Shih and P. Yin. *Complex crystals with prescribed depth.* Submitted, 2013.

7. W. Sun, A.X. Guan, P. Yin, *Casting metal structures within programmable DNA molds.* Submitted, 2013.

8. R. Jungmann, M.S. Avendano, J.B. Woehrstein, M. Dai, W.M. Shih and P. Yin. *Multiplexed cellular 3D super-resolution imaging with DNA-PAINT.* Submitted, 2013

9. H. Qi, M. Ghodousi, Y. Du, C. Grun, H. Bae, P. Yin*, and A. Khademhosseini*. *DNA Directed Self-Assembly of Shape-Controlled Hydrogels.* In press. **Nature Communications**, 2013

10. C. Myhrvold, M. Dai, P.A. Silver and P. Yin. *Isothermal self-assembly of DNA structures under diverse and biocompatible conditions.* In press. **Nano Letters**. 2013

11. S.P. Surwade, F. Zhou, B. Wei, W. Sun, P. Yin*, and H. Liu*. *Nanoscale Growth and Patterning of Inorganic Oxides using DNA Nanostructure Templates.* **J. Am. Chem. Soc.**, 135:6778-81, 2013.

12. Z. Jin, W. Sun, Y. Ke, C. Shih, G.L.C. Paulus, Q. Wang, B. Mu, P. Yin*, and M. Strano*, *Metalized DNA nanolithography for encoding and transferring spatial information for graphene patterning.* **Nature Communications**, 4:1663, 2013.

13. Y. Ke, L. Ong, W. Shih, and P. Yin*, *Three-Dimensional Structures Self-Assembled from DNA Bricks.* **Science**, 338:1177-1183, 2012. Note: cover story

14. C. Lin, R. Jungmann, A.M. Leifer, C. Li, D. Levner, W. Shih*, and P. Yin*, *Sub-micrometer Geometrically Encoded Fluorescent Barcodes Self-Assembled from DNA*. **Nature Chemistry**, 4:832-839, 2012.

9.2 Non-refereed journal article

None.

9.3 Workshops and conferences

1. Twenty Ninth Chinese Chemical Society Annual Conference, Beijing, China, Aug. 5th, 2014.
2. EITA-New Media and Bio, Cambridge, MA, July 31st, 2014.
3. Second Annual workshop on Micro- and Nanotechnologies in Medicine, Cambridge, MA, July 31st, 2014.
4. SEED2014 (Synthetic Biology, Engineering, Evolution and Design), Manhattan Beach, CA, July 14th, 2014. [Young Investigator Award Lecture].
5. Blavatnik Science Symposium, New York City, NY, July 8th, 2014.
6. Seventh world congress on biomechanics (DNA mechanics and assembly session), Boston, MA, July 6th, 2014.
7. Seventh world congress on biomechanics (Nucleic acid nanostructures session), Boston, MA, July 6th, 2014.
8. BIO International Convention, San Diego, CA, June 25th, 2014.
9. International Workshop on DNA-Based Nanotechnology: Digital Chemistry (DNATEC14), Dresden, Germany, May 5th, 2014.
10. Oncology Research Seminars, Koch Institute for Integrative Cancer Research, MIT, Cambridge, MA, Apr. 28th, 2014.
11. Foundation of Nanosciences (FNANO2014), Snowbird, Apr. 16th, 2014.
12. Biological Imaging Meeting, Northwestern University, Evanston, March 28th, 2014.
13. National Academy of Sciences Frontiers of Engineering and Sciences Program, Rio de Janerio, Brazil, March 17th, 2014.
14. Biophysics seminar, MIT, Cambridge, MA, Feb. 12th, 2014.
15. NSF Nanoscale Science and Engineering Grantees Conference: Current and Future Trends in Nanotechnology and Environment and Nanomanufacturing, Arlington, VA, Dec. 6th, 2013.
16. The Nano Area of Advance at Chalmers University of Technology, Goteborg, Sweden, Nov. 28th, 2013.

17. Fourth International Congress on Biotechnology and Genomics, Monterrey, Mexico, Nov. 21st, 2013.

18. NIH Common Fund High-Risk High-Reward Symposium, Bethesda, MD, Nov. 18th, 2013.

19. Department of Chemistry and Biotechnology, Tokyo University, Tokyo, Japan, Oct. 30th, 2013.

20. Annual Meeting of Chem-Bio Informatics Society, Tokyo, Japan, Oct. 30th, 2013.

21. Department of Chemistry, Kyoto University, Kyoto, Japan, Oct. 29th, 2013.

22. Annual Meeting of the Biophysical Society of Japan, Kyoto, Japan, Oct. 29th, 2013.

23. U.S. Army Research Office Workshop: Challenges and Opportunities in Nanomanufacturing, Raleigh, NC, Oct. 1st, 2013.

24. International Conference on DNA Computing and Molecular Programming, Tempe, Sep. 27th, 2013.

25. Symposium on Advanced Nano/Biosystems: Design, Fabrication, and Characterization, University of Illinois at Urbana-Champaign, Urbana, IL, Sep. 25th, 2013.

26. The Ninth International Fab Lab Conference, Yokohama, Japan, Aug. 21st, 2013.

27. NSF Workshop on BioMEMS and Tissue Engineering, Cambridge, July 30th, 2013.

28. NSF Workshop: Advanced Biomanufacturing, Arlington, VA. July 14, 2013.

29. The Sixth International Meeting on Synthetic Biology (SB 6.0), London, England, July 10th, 2013

30. Sino-US Synthetic Biology Workshop, Tianjin, China, June 21st, 2013

31. Fourth International Wyss Symposium: Nanotherapeutics and Diagnostics, Boston, June 6th, 2013

32. The Nanoscience Nexus - the 1st International Conference of Kavli Nanoscience Institutes, Puerto Rico, May 30th, 2013

33. Department of Chemistry, University of Arizona, Tempe, Apr. 12th, 2013

34. University of Michigan, Ann Arbor, March 13th, 2013

35. The Science of Digital Fabrication Workshop, MIT, Cambridge, March 8th, 2013

36. Frontiers of Information Science and Technology (FIST), Shanghai, China, Dec. 10th, 2012.

37. Micro and Nanoengineering in Medicine Conference, Maui, Hawaii. Best Junior Faculty Talk Award, Dec. 4th, 2012.

38. Department of Chemistry, University of Pittsburgh, Pittsburgh, Nov. 1st, 2012.

39. School of Engineering and Applied Sciences, Bioengineering seminar series, Harvard University, Cambridge, Sep. 25th, 2012.

40. Eighteenth International Meeting on DNA Computing and Molecular Prgoramming (DNA18), Plenary talk, Aarhus, Denmark, Aug. 14th, 2012.

41. Sino-US Synthetic Biology Workshop, Tianjin, China, Aug. 2nd, 2012.

42. Learning through research workshop, Paris, July 14th, 2012.

43. College of Engineering, Peking University, Beijing, June 12th, 2012.

44. Ninth Conference on Foundations of Nanoscience: Self-Assembled Architectures and Devices (FNANO12), Snowbird, Utah, Apr. 17th, 2012.

45. School of Engineering and Applied Sciences, Harvard University, Cambridge, Apr. 10th, 2012.

46. Department of Chemistry, Tsinghua University, Beijing, Mar. 6th, 2012.

47. NSF Molecular Programming Project Workshop, Friday Harbor, June 18th, 2011.

48. Weizmann Institute, Israel, March 14th, 2011.

9.4 Awards/Honors

- Peng Yin, World Economic Forum Young Scientist Award, 2014
- Peng Yin, ACS Synthetic Biology Young Scientist Award, 2014
- Peng Yin, Blavatnik National Awards for Young Scientists, Finalist, 2014
- Peng Yin, NSF Expedition in Computing Award, 2013
- Peng Yin, NIH Transformative Research Award, 2013
- Stewart Trust Pilot Program Award, 2011
- DARPA Young Faculty Award (YFA), 2011
- ONR Young Investigator Program (YIP) Award, 2011

10 Award participants

Military Personnel: N/A

Salary Support: Peng Yin, Maier Avendano Amado, Robert Barish, Jeffrey Yutien Chen, Wesley Chen, Alexander Green, Nikhil Gopalkrishnan, Dongran Han, Alexander Jaffe, Ralf Jungmann, Yonggang Ke, Luvena Ong, Joanna Robaszewski, Jie Shen, Wei Sun, Michelle Vhudzijena, Wei Li Wang, Diming Wei, Sungwook Woo

11 Appendix: Paper preprints and reprints

11.1 DNA brick nano-structures

11.1.1 Two-Dimensional Structures Self-Assembled from DNA tiles

LETTER

doi:10.1038/nature11075

Complex shapes self-assembled from single-stranded DNA tiles

Bryan Wei[1,2], Mingjie Dai[2,3] & Peng Yin[1,2]

Programmed self-assembly of strands of nucleic acid has proved highly effective for creating a wide range of structures with desired shapes[1–25]. A particularly successful implementation is DNA origami, in which a long scaffold strand is folded by hundreds of short auxiliary strands into a complex shape[9,14–16,18–21,25]. Modular strategies are in principle simpler and more versatile and have been used to assemble DNA[2–5,8,10–13,17,23] or RNA[7,22] tiles into periodic[3,4,7,22] and algorithmic[5] two-dimensional lattices, extended ribbons[10,12] and tubes[4,12,13], three-dimensional crystals[17], polyhedra[11] and simple finite two-dimensional shapes[7,8]. But creating finite yet complex shapes from a large number of uniquely addressable tiles remains challenging. Here we solve this problem with the simplest tile form, a 'single-stranded tile' (SST) that consists of a 42-base strand of DNA composed entirely of concatenated sticky ends and that binds to four local neighbours during self-assembly[12]. Although ribbons and tubes with controlled circumferences[12] have been created using the SST approach, we extend it to assemble complex two-dimensional shapes and tubes from hundreds (in some cases more than one thousand) distinct tiles. Our main design feature is a self-assembled rectangle that serves as a molecular canvas, with each of its constituent SST strands—folded into a 3 nm-by-7 nm tile and attached to four neighbouring tiles—acting as a pixel. A desired shape, drawn on the canvas, is then produced by one-pot annealing of all those strands that correspond to pixels covered by the target shape; the remaining strands are excluded. We implement the strategy with a master strand collection that corresponds to a 310-pixel canvas, and then use appropriate strand subsets to construct 107 distinct and complex two-dimensional shapes, thereby establishing SST assembly as a simple, modular and robust framework for constructing nanostructures with prescribed shapes from short synthetic DNA strands.

Our 42-base SST motif[12] consists of four domains (Fig. 1a), grouped into two pairs (domains 1 and 2 and domains 3 and 4) that each consists of 21 nucleotides in total. We design the intermolecular binding interactions of these domains such that a collection of distinct SST tiles will arrange into a DNA lattice composed of parallel helices connected by single-stranded linkages (Fig. 1b, left and middle), forming a 'brick-wall' pattern (Fig. 1b, right). The linkages between two adjacent helices are expected to be the phosphates that connect domains 2 and 3 of the SSTs, and are thus shown artificially stretched in the diagrams. They are spaced two helical turns (that is, 21 base pairs) apart and are all located in the same tangent plane between the two helices. The rectangular lattice sketched in Fig. 1b contains six parallel helices, each measuring about eight helical turns; we refer to this as a 6 helix × 8 helical turn (6H × 8T) rectangle. This basic strategy can be adapted to design rectangles with different dimensions, and arbitrary shapes approximated with an SST brick-wall pattern (Fig. 1c). By concatenating pairs of half-tiles on its top and bottom boundaries into full tiles, we can transform the rectangle in Fig. 1b into a tube with a prescribed circumference and length (Fig. 1d).

A pre-designed rectangular SST lattice (Fig. 1e, top right) can also be viewed as a 'molecular canvas', where each SST serves as a 3 nm × 7 nm 'molecular pixel'. Designing a shape amounts to selecting its constituent pixels on the canvas, as illustrated by the two examples in Fig. 1e.

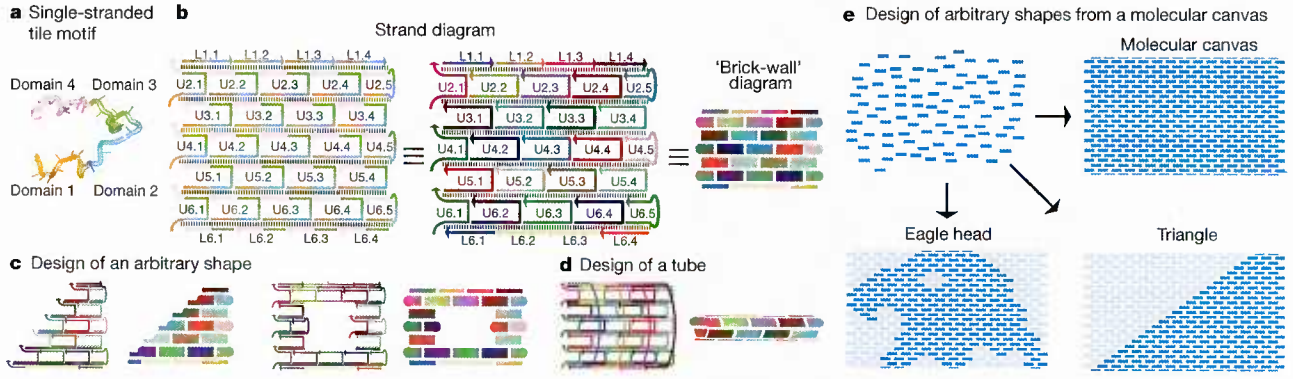

Figure 1 | Self-assembly of molecular shapes using single-stranded tiles. **a**, The canonical SST motif, adapted from ref. 12. **b**, Design of an SST rectangle structure. Left and middle: two different views of the same secondary structure diagram. Each standard (full) tile has 42 bases (labelled U), and each top and bottom boundary (half) tile has 21 bases (labelled L). Right: a simplified 'brick-wall' diagram. Standard tiles are depicted as thick rectangles, boundary tiles are depicted as thin rectangles and the unstructured single-stranded portions of the boundary tiles are depicted as rounded corners. Each strand has a unique sequence. Colours distinguish domains in the left panel and distinguish strands in the middle and right panels. **c**, Selecting an appropriate subset of SST species from the common pool in **b** makes it possible to design a desired target shape, for example a triangle (left) or a rectangular ring (right). **d**, Design of a tube with prescribed width and length. **e**, Arbitrary shapes can be designed by selecting an appropriate set of monomers from a pre-synthesized pool that corresponds to a molecular canvas (top right). To make a shape, the SST strands corresponding to its constituent pixels (dark blue) will be included in the strand mixture and the remainder (light blue) will be excluded.

[1]Department of Systems Biology, Harvard Medical School, Boston, Massachusetts 02115, USA. [2]Wyss Institute for Biologically Inspired Engineering, Harvard University, Boston, Massachusetts 02115, USA. [3]Program in Biophysics, Harvard University, Boston, Massachusetts 02115, USA.

These shapes, and more than 100 others, were designed and experimentally constructed, demonstrating the self-assembly of complex molecular shapes from modular components (Supplementary Fig. 1).

Following the design in Fig. 1b, we assembled a 24H × 28T rectangle (Fig. 2a) from 362 distinct SST species (310 internal, standard full-length SSTs, 24 full-length SSTs on vertical boundaries whose exposed single-stranded domains are replaced by poly(T) (multiple thymine bases), and 28 half-length SSTs on horizontal boundaries). The rectangle, which has a molecular weight comparable to a DNA origami structure made with an M13 phage scaffold[9], was made using unpurified DNA strands that had their sequences designed to minimize sequence symmetry[26] (Methods) and were then mixed without careful adjustment of stoichiometry. After single-step (one-pot) annealing that involved cooling from 90 to 25 °C over 17 h in 25 mM Mg^{2+} buffer (see Supplementary Information, section 2.3, for the effects of buffer ion strength and annealing time on the assembly yield), the solution was subjected to 2% native agarose gel electrophoresis and produced one dominant band (Fig. 2b, lane U). This band was extracted and purified by centrifugation, with the purified product migrating as a single band on the gel (Fig. 2b, lane P) and appearing in atomic force microscopy (AFM) images with the expected rectangular morphology (Fig. 2c) with approximately the expected dimensions (64 ± 2 nm × 103 ± 2 nm, $N = 30$). Successful streptavidin attachment at selected internal and boundary positions, corresponding to tiles displaying biotin-modified strands, further verified the formation of the full rectangle and also demonstrated the unique addressability of the constituent tiles (Supplementary Information, section 2.4).

Native gel electrophoresis of samples stained with SYBR Safe gave a 17% assembly yield (referred to as 'gel yield'), calculated from the ratio of the fluorescent intensity of the product band to that of the entire lane (after background correction). We note that the structure- and sequence-dependent variation in the staining efficiency of SYBR Safe (Supplementary Fig. 3) suggests that this ratio is a bounded (<50%) overestimate (Supplementary Information, section 2.2.1) and that the actual yield is probably 12–17%. In the remainder of the paper, we report the unadjusted yield measurement, which should be considered as an approximate estimate (within 50% accuracy).

The fraction of purified product appearing as 'well-formed' rectangles (defined as those showing no defects more than 15 nm in diameter in the expected outline or more than 10 nm in diameter in the interior) was determined as a percentage of all identifiable shapes in an AFM field, giving an 'AFM yield' of 55% ($N = 163$; Supplementary Fig. 6). This number is probably an underestimate of the actual fraction of well-formed structures within the purified product owing to the relative fragility of SST rectangles, which can result in significant post-purification damage caused by sample deposition or imaging (Supplementary Information, section 2.2.2). Such fragility may be mitigated by introducing more covalent bonds into the assembled structures, for example through either ligation[27] of two ends of an SST or crosslinking[28] of neighbouring SSTs.

Following the design strategy sketched in Fig. 1d, 24H × 28T rectangles were transformed into 24H × 28T tubes with a gel yield of 14% (Fig. 2d, e). Transmission electronic microscopy (TEM) images of the purified product revealed tube-like structures with approximately the expected lengths of 98 ± 2 nm and diameters of 24 ± 1 nm (Fig. 2f), and gave a TEM yield of 82% ($N = 89$). The TEM yield is the percentage of identifiable tubes whose lengths are within 5 nm of the expected full length of 98 nm, estimated by assuming a length of 3.5 nm (see below) per helical turn.

The successful construction of seven different rectangles (Fig. 2g) and five different tubes (Fig. 2i) with distinct dimensions and molecular weights (Fig. 2h) illustrates the benefits of the modular nature of SST assembly (see Supplementary Information, section 3, for design and characterization details). These structures include a 12H × 177T tube made of more than 1,000 distinct SST species, which represents a 60-fold increase in the number of distinct tile species contained in a finite and uniquely addressable shape[7,8]. These rectangle and tube series allow us also to plot their measured lengths and widths against the designed number of constituent helices and the number of helical turns within a helix, which gives a linear relationship (Pearson correlation, $R^2 > 0.99$) with an average helix width and average helical turn length of 2.6 nm and 3.5 nm, respectively (Supplementary Information, section 3.5). High-resolution AFM imaging of an assembled structure yielded a helical width of 2.6 nm (Supplementary Fig. 38), consistent with the above value.

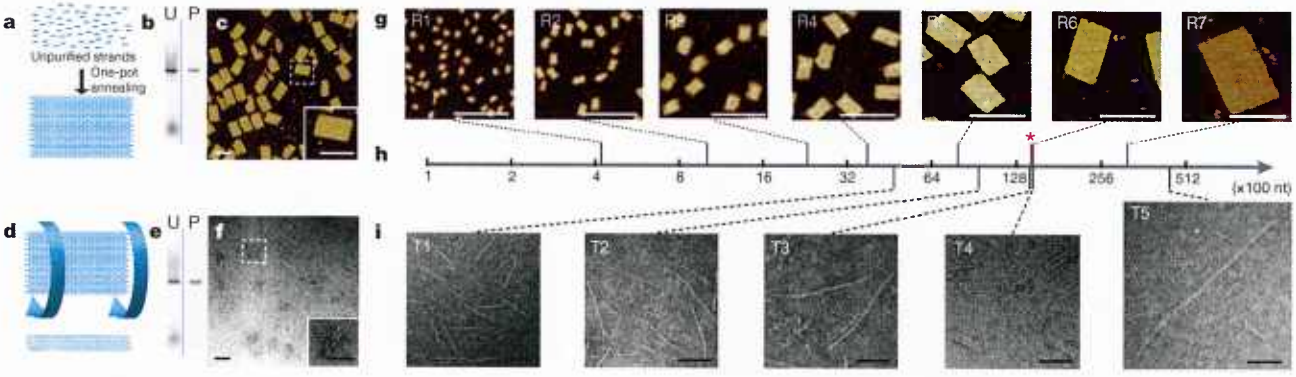

Figure 2 | Self-assembly of SST rectangles and tubes. **a**–**c**, 24H × 28T SST rectangle. **a**, Schematic of rectangle formation. For a more detailed depiction, see Supplementary Fig. 2. Supplementary Information, section 6, contains strand diagrams for this and all other SST rectangles and tubes, and sections 7 and 8 contain sequences for all the structures constructed in this paper. **b**, 2% native agarose gel electrophoresis. U, unpurified; P, purified (by gel extraction from lane U). **c**, AFM image. Inset shows a magnified view of the outlined structure. See Supplementary Fig. 2 for a larger AFM image. **d**–**f**, 24H × 28T SST tube. **d**, Schematic of tube design. **e**, 2% native agarose gel electrophoresis. **f**, TEM image. Inset shows a magnified view of the outlined structure. See Supplementary Information, section 2.5, for a larger image. **g**–**i**, Rectangles and tubes across scales. **g**, AFM images of SST rectangles. The designed dimensions are 4H × 4T (R1), 6H × 7T (R2), 10H × 10T (R3), 12H × 14T (R4), 18H × 20T (R5), 24H × 28T (R6) and 36H × 41T (R7). **h**, Logarithmic molecular weight. The pink asterisk indicates the weight of a typical M13 DNA origami[9] as a reference point. nt, nucleotide. **i**, TEM images of SST tubes. The designed dimensions are 8H × 28T (T1), 8H × 55T (T2), 8H × 84T (T3), 24H × 28T (T4) and 12H × 117T (T5). All scale bars, 100 nm. See Supplementary Information, section 3.1, for the schematics of the rectangles and tubes and for a depiction of the molecular weights of all 118 distinct structures we constructed. See Supplementary Information, section 3.2, for the number of distinct constituent SST species (ranging from 12 to 1,068), the number of nucleotides (420 to 44,856), the measured widths (11 to 91 nm) and lengths (16 to 621 nm), the measured gel yield (0.4% to 32%), and the measured AFM yield (25% to 61%) of the 12 rectangles and tubes shown here. See Supplementary Information, sections 3.3 (rectangles) and 3.4 (tubes), for gel results, larger AFM and TEM images, and gel- and imaging-based yield analyses. The formation of full-length 8H × 84T tubes and full-length 12H × 177T tubes was also confirmed by streptavidin labelling of the tube ends (Supplementary Information, section 3.4.4).

We next sought to construct arbitrary shapes using the idea of a molecular canvas (Fig. 1e), with the 24H × 28T rectangle as the canvas and its 310 internal SSTs as the molecular pixels. Attempts to assemble a triangle by simply annealing the SST species that correspond to the triangle pixels resulted in severe aggregation and no detectable product band on an agarose gel (data not shown). The aggregation was attributed to non-specific interactions between exposed single-stranded domains of the SST on the hypotenuse boundary of the triangles. Two designs were tested to eliminate aggregation: one in which we replaced each exposed domain with a poly(T) segment of the same length, and one in which we covered each with an 'edge protector' that has a segment complementary to the exposed domain followed by a 10- or 11-nucleotide poly(T) segment. Both designs eliminated aggregation and produced the desired triangles with comparable yields (Supplementary Information, section 4.2), and can thus be used to construct a pool of SST strands and auxiliary strands representing the full molecular canvas. We chose the edge protector design because it involves a smaller (×4 instead of ×15) number of auxiliary species (Supplementary Fig. 43) and synthesized 1,344 edge protectors (each 21 nucleotides in length) supplementing the existing 362 SST strands (Supplementary Information, section 4.2). With this modification, a prescribed shape can be created by selecting appropriate SST strands and the auxiliary strands that correspond to the shape's boundary. We used this method to construct the triangle and the three other shapes shown in Fig. 3.

To explore the generality and robustness of the molecular canvas method, we designed a total of 110 distinct shapes (including the shapes described above) (Supplementary Information, section 4.3). Of the targeted designs, 103 produced discernible product bands on the gel and the expected shapes under AFM in the first assembly trial; this corresponds to a 94% success rate. The seven failed designs were challenging shapes resembling 0, 3, ~, @, a hollow H and two Chinese characters (Supplementary Fig. 57). The first four (0, 3, ~, @) were slightly redesigned to eliminate potential weak points (for example narrow connections) and then assembled successfully. We did not attempt to redesign the remaining three failed shapes, given their geometrical complexity. Combining these assembly trials gives 107 successful designs out of a total of 114 (a 94% success rate), with gel yields of targeted shapes ranging from 6% to 40%. Figure 4 shows AFM images of 100 distinct shapes. See Supplementary Information, sections 4.3 and 4.6, for schematics of the canvas design and AFM images, and section 4.5 for detailed gel yields.

We wrote a computer program to automate picking and mixing strands from a master library (Supplementary Fig. 58). This program provides the user with a graphical interface to draw (or load a picture of) a target shape, and then outputs instructions for a robotic liquid handler to pick and mix the required strands for subsequent annealing. Each robot batch produces 48 shapes in roughly 48 h, reducing several man-hours of labour to one machine-hour per shape and also avoiding potential human mistakes. The robot was used to construct 44 of the shapes described above.

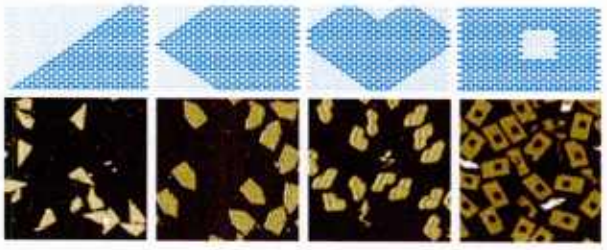

Figure 3 | Simple shapes designed using a molecular canvas. Top, schematics; bottom, 500 nm × 500 nm AFM images. The structures were constructed using the edge protector strategy, with respective gel yields of 16%, 19%, 22% and 16% (left to right; Supplementary Information, section 4.5), and AFM yields of 37%, 37%, 51% and 36% (left to right; Supplementary Information, section 4.7).

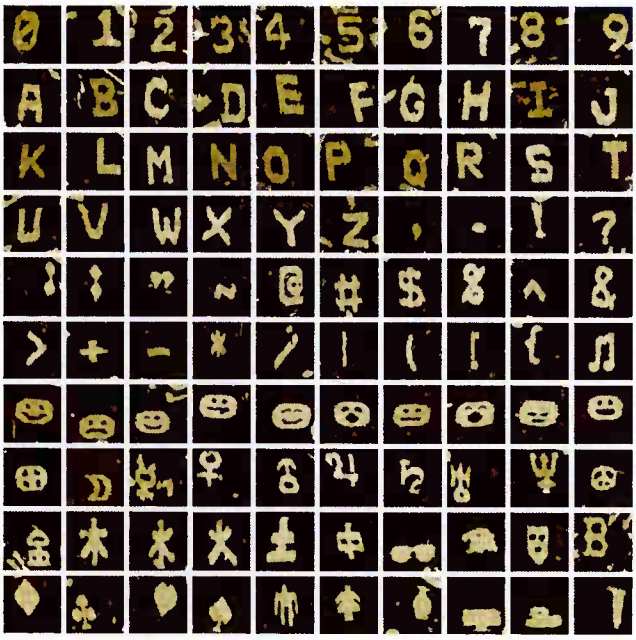

Figure 4 | Complex shapes designed using a molecular canvas. AFM images of 100 distinct shapes, including the 26 capital letters of the Latin alphabet, 10 Arabic numerals, 23 punctuation marks and other standard keyboard symbols, 10 emoticons, 9 astrological symbols, 6 Chinese characters and various miscellaneous symbols. Each image is 150 nm × 150 nm in size.

Different shapes were assembled and purified separately and then mixed together for efficient AFM imaging (for example, Supplementary Fig. 72 shows a mixture of the 26 letters of the Latin alphabet). The shapes were all derived from the same canvas, but coexisted stably after assembly: there was no sign of shapes merging or deforming each other. The structures almost always appeared under the AFM with the desired orientation, facing up towards the viewer (for example, in Supplementary Fig. 84 this is true of 96% of the structures, $N = 49$). Such biased landing on the mica surface used for AFM imaging is consistent with free SST structures in solution being rolled up as a result of their intrinsic curvature[12], and unrolling and becoming flattened when adsorbed onto the mica surface. This feature is useful for controlling landing orientation, but the expected curvature and accumulation of twist[16,21] in SST structures pose considerable challenges to straightforward scaling up of SST assemblies to large sizes. Flat SST structures free of curvature and twist could be constructed by shifting relative positions between linkage points[12,18], by deleting bases[16,21] or by using a corrugated design[4,19]. Such modifications might in principle give access to larger structures and even facilitate further scaling up using hierarchal assembly strategies[19–21], but may interfere with the standardized modular form of the present SST motif.

DNA origami[9,14–16,18–21,25] typically produces hybrid structures half composed of biological components (the M13 scaffold) and half composed of synthetic components with sequences derived from the biological part (the staple strands). By contrast, our SST structures are made entirely of *de novo* designed and synthesized short DNA strands, and we thus have greater sequence as well as material choice. For example, we constructed a 24H × 28T rectangle (Supplementary Information, section 5.1) from SST motifs with completely random sequences (that is, no sequence symmetry requirement was imposed; Methods) and a nuclease-resistant 4H × 4T rectangle (Supplementary Fig. 87) made of L-DNA, the mirror image of natural D-DNA. In

addition to L-DNA, SSTs could also be made from other informational polymers such as DNA with chemically modified backbones or artificial bases, or RNA.

Like DNA origami[9,14–16,18–21,25], the SST method works robustly with unpurified strands without the need for careful adjustment of their stoichiometry, and with sequences that are not optimally designed (for example completely random sequences). But whereas the central design feature of DNA origami is a long scaffold, which is considered to give rise to this method's success and robustness[9,25], SST assembly uses only short synthetic strands that enable it to emulate the programmable modularity characteristic of DNA or RNA tiling[2–5,7,8,10–13,17,22,23]. Yet unlike a multistranded tile[2–5,7,8,10,11,13,17,22,23] with a well-defined and structurally rigid core, an SST monomer[12] is a floppy DNA strand that is composed entirely of concatenated sticky ends and only folds into a rectangular shape because of its interaction with neighbouring SSTs during assembly. That the SST method is nevertheless successful and robust calls for a systematic investigation of the assembly mechanism and kinetics. It is conceivable that sparse and slow nucleation followed by fast growth allows complete assembly, with the required rate separation between nucleation and growth arising from structural reconfiguration or assembly-induced folding of SSTs that can increase the configurational entropy penalty[12] and thus raise the assembly nucleation barrier.

DNA origami[9,14–16,18–21,25] folds a long scaffold strand with many short staple strands into a prescribed shape without the strand getting tangled up; our SST method shows that a large number of small monomers can self-assemble into a desired structure that is not compromised by ill-formed by-products. These features illustrate the complementarity of the two approaches, which may represent the extremes of a rich spectrum of strategies for creating complex shapes and structures through the cooperative self-assembly of diverse components. Thus, the SST method[12] and DNA origami[9,14–16,18–21,25], and approaches that use multistranded DNA and RNA tiles[2–5,7,8,10,11,13,17,22,23], logic gates[29] and kinetic hairpins[30], suggest the presence of a vast design space that remains to be explored for the creation of nucleic acid nanostructures, and more generally for information-directed molecular self-assembly.

METHODS SUMMARY

DNA sequences were generated by minimizing sequence symmetry[24] (for most structures) or by populating the SST motifs with completely random sequences (for the structure in Supplementary Fig. 86). Without careful adjustment of stoichiometry, unpurified strands were mixed manually or using a liquid-handling robot and supplemented with 12.5 or 25 mM Mg^{2+}. After one-pot annealing from 90 to 25 °C over x hours ($17 \leq x \leq 58$; for most structures, $x = 17$), the solution was subjected to native agarose gel electrophoresis. The desired product band was extracted, purified by centrifugation and imaged with AFM or TEM.

Full Methods and any associated references are available in the online version of the paper at www.nature.com/nature.

Received 20 November 2011; accepted 22 March 2012.

1. Seeman, N. C. Nucleic acid junctions and lattices. *J. Theor. Biol.* **99,** 237–247 (1982).
2. Fu, T. J. & Seeman, N. C. DNA double-crossover molecules. *Biochemistry* **32,** 3211–3220 (1993).
3. Winfree, E., Liu, F., Wenzler, L. A. & Seeman, N. C. Design and self-assembly of two-dimensional DNA crystals. *Nature* **394,** 539–544 (1998).
4. Yan, H., Park, S. H., Finkelstein, G., Reif, J. H. & LaBean, T. H. DNA-templated self-assembly of protein arrays and highly conductive nanowires. *Science* **301,** 1882–1884 (2003).
5. Rothemund, P. W. K., Papadakis, N. & Winfree, E. Algorithmic self-assembly of DNA Sierpinski triangles. *PLoS Biol.* **2,** e424 (2004).
6. Shih, W., Quispe, J. & Joyce, G. A 1.7-kilobase single-stranded DNA that folds into a nanoscale octahedron. *Nature* **427,** 618–621 (2004).
7. Chworos, A. *et al.* Building programmable jigsaw puzzles with RNA. *Science* **306,** 2068–2072 (2004).
8. Park, S. H. *et al.* Finite-size, fully-addressable DNA tile lattices formed by hierarchical assembly procedures. *Angew. Chem. Int. Ed.* **45,** 735–739 (2006).
9. Rothemund, P. W. K. Folding DNA to create nanoscale shapes and patterns. *Nature* **440,** 297–302 (2006).
10. Schulman, R. & Winfree, E. Synthesis of crystals with a programmable kinetic barrier to nucleation. *Proc. Natl Acad. Sci. USA* **104,** 15236–15241 (2007).
11. He, Y. *et al.* Hierarchical self-assembly of DNA into symmetric supramolecular polyhedra. *Nature* **452,** 198–201 (2008).
12. Yin, P. *et al.* Programming DNA tube circumferences. *Science* **321,** 824–826 (2008).
13. Sharma, J. *et al.* Control of self-assembly of DNA tubules through integration of gold nanoparticles. *Science* **323,** 112–116 (2009).
14. Douglas, S. M. *et al.* Self-assembly of DNA into nanoscale three-dimensional shapes. *Nature* **459,** 414–418 (2009).
15. Andersen, E. S. *et al.* Self-assembly of a nanoscale DNA box with a controllable lid. *Nature* **459,** 73–76 (2009).
16. Dietz, H., Douglas, S. M. & Shih, W. M. Folding DNA into twisted and curved nanoscale shapes. *Science* **325,** 725–730 (2009).
17. Zheng, J. P. *et al.* From molecular to macroscopic via the rational design of self-assembled 3D DNA crystal. *Nature* **461,** 74–77 (2009).
18. Han, D. *et al.* DNA origami with complex curvatures in three-dimensional space. *Science* **332,** 342–346 (2011).
19. Liu, W., Zhong, H., Wang, R. & Seeman, N. Crystalline two dimensional DNA origami arrays. *Angew. Chem. Int. Ed.* **50,** 264–267 (2011).
20. Zhao, Z., Liu, Y. & Yan, H. Organizing DNA origami tiles into larger structures using preformed scaffold frames. *Nano Lett.* **11,** 2997–3002 (2011).
21. Woo, S. & Rothemund, P. Programmable molecular recognition based on the geometry of DNA nanostructures. *Nat. Chem.* **3,** 620–627 (2011).
22. Delebecque, C. J., Lindner, A. B., Silver, P. A. & Aldaye, F. A. Organization of intracellular reactions with rationally designed RNA assemblies. *Science* **333,** 470–474 (2011).
23. Lin, C., Liu, Y., Rinker, S. & Yan, H. DNA tile based self-assembly: building complex nanoarchitectures. *ChemPhysChem* **7,** 1641–1647 (2006).
24. Seeman, N. Nanomaterials based on DNA. *Annu. Rev. Biochem.* **79,** 65–87 (2010).
25. Tørring, T., Voigt, N. V., Nangreave, J., Yan, H. & Gothelf, K. V. DNA origami: a quantum leap for self-assembly of complex structures. *Chem. Soc. Rev.* **40,** 5636–5646 (2011).
26. Seeman, N. De novo design of sequences for nucleic acid structural engineering. *J. Biomol. Struct. Dyn.* **8,** 573–581 (1990).
27. O'Neill, P., Rothemund, P. W. K., Kumar, A. & Fygenson, D. Sturdier DNA nanotubes via ligation. *Nano Lett.* **6,** 1379–1383 (2006).
28. Rajendran, A., Endo, M., Katsuda, Y., Hidaka, K. & Sugiyama, H. Photo-crosslinking-assisted thermal stability of DNA origami structures and its application for higher-temperature self-assembly. *J. Am. Chem. Soc.* **133,** 14488–14491 (2011).
29. Seelig, G., Soloveichik, D., Zhang, D. Y. & Winfree, E. Enzyme-free nucleic acid logic circuits. *Science* **314,** 1585–1588 (2006).
30. Yin, P., Choi, H. M. T., Calvert, C. R. & Pierce, N. A. Programming biomolecular self-assembly pathways. *Nature* **451,** 318–322 (2008).

Supplementary Information is linked to the online version of the paper at www.nature.com/nature.

Acknowledgements We thank S. Chandarasekaran, X. Lim, W. Sun and R. Conturie for technical assistance; A. Marblestone, R. Barish, W. Shih, Y. Ke, E. Winfree, S. Woo, P. Rothemund and D. Woods for discussions; and J. Aliperti for help with preparation of the draft. This work was funded by Office of Naval Research Young Investigator Program Award N000141110914, Office of Naval Research Grant N000141010827, NSF CAREER Award CCF1054898, NIH Director's New Innovator Award 1DP20D007292 and a Wyss Institute for Biologically Inspired Engineering Faculty Startup Fund (to P.Y.).

Author Contributions B.W. designed the system, conducted the experiments, analysed the data and wrote the paper. M.D. conducted the experiments, analysed the data and wrote the paper. P.Y. conceived and guided the study, analysed the data and wrote the paper.

Author Information Reprints and permissions information is available at www.nature.com/reprints. The authors declare competing financial interests: details accompany the full-text HTML version of the paper at www.nature.com/nature. Readers are welcome to comment on the online version of this article at www.nature.com/nature. Correspondence and requests for materials should be addressed to P.Y. (py@hms.harvard.edu).

METHODS

DNA sequence design. DNA sequences were designed with the UNIQUIMER software[31] by minimizing the sequence symmetry[24] (for most of the structures) or by populating the SST motifs with completely random sequences (for the random sequence set in Supplementary Fig. 86). For design based on sequence minimization, there are several criteria for sequence generation. (1) Nucleotides (that is, A, C, G and T) are randomly generated one by one. (2) Nucleotides complementary to those generated are matched following the base-pairing rule: A to T and vice versa; C to G and vice versa. (3) No repeating segment beyond a certain length (eight or nine nucleotides) is permitted. When such repeating segments emerge during design, the most recently generated nucleotides will be mutated until the repeating-segment requirement is satisfied. (4) No four consecutive A, C, G or T bases are allowed. (5) Pre-specified nucleotides at the single-stranded linkage points (for example T and G as the twenty-first and twenty-second nucleotides, respectively, for most of the strands) are used to avoid sliding bases around the linkage points. In the design using completely random sequences (Supplementary Fig. 86), restrictions (3) to (5) were not applied.

Manual design and/or optimization was used for the design of handle segment sequences (for example the handle segment to accommodate a 3′ biotin strand for streptavidin labelling and concatenation of poly(T) domains). Additionally, in some cases segments from different SST structures were manually combined to transform an existing structure into a new structure. For example, additional rows of SSTs were introduced to convert a rectangle design into a tube design (for example in converting the 24H × 28T rectangle design to the 24H × 28T tube design, and converting the 24H × 28T rectangle design to the 8H × 84T tube design). Similarly, we also manually converted a tube design into a rectangle design (for example in converting the 12H × 177T tube into the 36H × 41T rectangle).

Sample preparation. DNA strands were synthesized by Integrated DNA Technology, Inc. (http://www.idtdna.com) or the Bioneer Corporation (http://us.bioneer.com). To assemble the structures, DNA strands were mixed to a roughly equal molar final concentration of 100 nM per strand species for most of the structures (except for different shapes based on the 24H × 28T rectangle, which were prepared at 200 nM) in ×0.5 TE buffer (5 mM Tris, pH 7.9, 1 mM EDTA) supplemented with 12.5 or 25 mM $MgCl_2$. We note that the DNA concentrations were based on the manufacturer's specifications and that no additional in-house calibration was performed. Thus, the stoichiometry for the strands was not tightly controlled. The mixture was then annealed in a PCR thermal cycler by cooling from 90 to 25 °C over a period of 17–58 h with different cooling programmes. The annealed samples were then subjected to 1.5% or 2% agarose gel electrophoresis (gel prepared in ×0.5 TBE buffer supplemented with 10 mM $MgCl_2$ and pre-stained with SYBR Safe) in an ice-water bath. Then the target gel bands were excised and put into a Freeze 'N Squeeze column (Bio-Rad). The gel pieces were finely crushed using a microtube pestle in the column and the column was then directly subjected to centrifugation at 438*g* for 3 min. Samples centrifuged through the column were collected for concentration estimation by the measurement of ultraviolet absorption at 260 nm. Such estimation is useful for estimating the dilution factor before AFM or TEM imaging.

Streptavidin labelling. Streptavidin labelling was done in two different ways.

(1) Labelling the top and bottom rows or internal loci of the 24H × 28T rectangle. Each tile of the top and bottom rows (or internal loci) of the 24H × 28T rectangle was modified to have a 3′ 17-nucleotide handle (TT as spacer and GGAAGGGATGGAGGA to be complementary to the 3′ biotin-modified strand whose sequence is TCCTCCATCCCTTCC-biotin). Special tiles of the top and bottom rows (or internal loci), and the rest of the component tiles of the rectangular lattice, were mixed with such handle-complementary 3′ biotin-modified strands at ×1 to ×2 concentration in ×0.5 TE buffer (25 mM $MgCl_2$). (When the concentration of special and common component tiles was 100 nM and there were 14 different special tile species, a ×1 concentration of the 3′ biotin-modified strands was 100 × 14 = 1400 nM.) They were then annealed over 17 h and purified after agarose gel electrophoresis. The purified sample was then subjected to AFM imaging. After the first round of imaging, streptavidin (1 μl at 10 mg ml^{-1} in ×0.5 TE buffer, 10 mM $MgCl_2$) was added to the imaging sample (~40 μl) for an incubation period of 2 min before re-imaging.

(2) Labelling the poly(T) ends of tube structures. After tube purification, 3′ biotin-modified poly(A) strands (×5 to ×10 concentration relative to the poly(T) counterparts) were mixed with the sample at room temperature (~25 °C) overnight. The sample was then subjected to AFM imaging. After the first round of imaging, streptavidin (1 μl at 10 mg ml^{-1} in ×0.5 TE buffer, 10 mM $MgCl_2$) was added to the imaging sample on mica for an incubation period of 2 min before re-imaging.

Robot automation for sample preparation. A custom MATLAB program was designed to aid the design of complex shapes and to automate strand mixing using a liquid-handling robot (Bravo, Agilent). For each shape, 5 μl of each SST resuspended in water at 10 μM was picked and mixed into a final volume of less than 2 ml (the exact volume was determined by the number of constituent strands for the target shape), and was then vacuum evaporated to 200 μl of 250 nM solution. This mixture was then supplemented with 50 μl of 62.5 mM Mg^{2+} buffer to reach a 250-μl final mixture ready for annealing. This pre-annealing solution had the following final concentrations: 200 nM DNA strand per SST species and 12.5 mM Mg^{2+}. Each run accommodated 48 shapes and took around 2 d to finish.

AFM imaging. AFM images were obtained using a Multimode SPM with a Digital Instruments Nanoscope V controller (Vecco). A 5-μl drop (2–5 nM) of annealed and purified sample and then a 40-μl drop of ×0.5 TE buffer (10 mM $MgCl_2$) were applied to a freshly cleaved mica surface and left for approximately 2 min. Sometimes additional dilution of the sample was performed to achieve the desired sample density. On a few occasions, supplementary 10 mM $NiCl_2$ was added to increase the strength of DNA–mica binding[32]. Samples were imaged using the liquid tapping mode. The AFM tips used were C-type triangular tips (resonant frequency, f_0 = 40–75 kHz; spring constant, k = 0.24 N m^{-1}) from the SNL-10 silicon nitride cantilever chip (Vecco Probes).

TEM imaging. For imaging, a 3.5-μl sample (1–5 nM) was adsorbed onto glow-discharged carbon-coated TEM grids for 4 min and then stained for 1 min using a 2% aqueous uranyl formate solution containing 25 mM NaOH. Imaging was performed using a JEOL JEM-1400 operated at 80 kV.

Yield quantification with SYBR Safe. Yield was first estimated by analysis using native agarose gel electrophoresis. The ratio between the fluorescence intensity of the target band and that of the entire lane was adopted to represent the gross yield of structural formation. For the 24H × 28T rectangle, as an independent, alternative quantification procedure the intensity of the target band was compared with a standard sample (1,500-base-pair band from a 1-kb DNA ladder mixture). The mass value of the target band was deduced from the intensity–mass curve based on the standard sample, and was used to calculate the yield of the desired structure. See Supplementary Information, section 2.2.1, for more details.

Measurement and statistics. AFM measurements were obtained using NANOSCOPE ANALYSIS (version 1.20; Vecco). The 'cross-section' function was used to measure distances (lengths and widths of the rectangles of different sizes). 'Well-formed' structures were chosen for the measurements. TEM images of the tubes were analysed using IMAGEJ (version 1.43u; NIH). The 'straight line' function was used to measure tube width. The 'segmented line' function was used to highlight and measure tube contour length. Thirty sample points were collected for each distance measurement (for example that of the width of a 24H × 28T rectangle) and the statistics (for example the mean and the standard deviation) were based on the 30 data points. See Supplementary Information, section 3.5, for measurement details.

31. Wei, B., Wang, Z. & Mi, Y. Uniquimer: software of de novo DNA sequence generation for DNA self-assembly: an introduction and the related applications in DNA self-assembly. *J. Comput. Theor. Nanosci.* **4**, 133–141 (2007).
32. Hansma, H. G. & Laney, D. E. DNA binding to mica correlates with cationic radius: assay by atomic force microscopy. *Biophys. J.* **70**, 1933–1939 (1996).

11.1.2 Three-Dimensional Structures Self-Assembled from DNA Bricks

Three-Dimensional Structures Self-Assembled from DNA Bricks

Yonggang Ke *et al.*

Science **338**, 1177 (2012);
DOI: 10.1126/science.1227268

Three-Dimensional Structures Self-Assembled from DNA Bricks

Yonggang Ke,[1,2,3] Luvena L. Ong,[1,4] William M. Shih,[1,2,3] Peng Yin[1,5]*

We describe a simple and robust method to construct complex three-dimensional (3D) structures by using short synthetic DNA strands that we call "DNA bricks." In one-step annealing reactions, bricks with hundreds of distinct sequences self-assemble into prescribed 3D shapes. Each 32-nucleotide brick is a modular component; it binds to four local neighbors and can be removed or added independently. Each 8–base pair interaction between bricks defines a voxel with dimensions of 2.5 by 2.5 by 2.7 nanometers, and a master brick collection defines a "molecular canvas" with dimensions of 10 by 10 by 10 voxels. By selecting subsets of bricks from this canvas, we constructed a panel of 102 distinct shapes exhibiting sophisticated surface features, as well as intricate interior cavities and tunnels.

Self-assembly of nucleic acids (DNA and RNA) provides a powerful approach for constructing sophisticated synthetic molecular structures and devices (*1*–*31*). Structures have been designed by encoding sequence complementarity in DNA strands in such a manner that by pairing up complementary segments, the strands self-organize into a prescribed target structure under appropriate physical conditions (*1*). From this basic principle, researchers have created diverse synthetic nucleic acid structures (*27*–*30*) such as lattices (*4*, *6*, *8*–*10*, *25*), ribbons (*15*), tubes (*6*, *15*, *25*, *26*), finite two-dimensional (2D) and 3D objects with defined shapes (*2*, *9*–*11*, *13*, *16*–*19*, *22*, *23*, *26*), and macroscopic crystals (*20*). In addition to static structures, various dynamic systems have been constructed (*31*), including switches (*5*), walkers (*7*, *14*, *21*), circuits (*12*, *14*, *24*), and triggered assembly systems (*14*). Additionally, because DNA and RNA can be interfaced with other functional molecules in a technologically relevant fashion, synthetic nucleic acid structures promise diverse applications; researchers are using nucleic acid structures and devices to direct spatial arrangement of functional molecules (*6*, *25*, *32*–*34*), facilitate protein structure determination (*35*), develop bioimaging probes (*33*, *34*), study single-molecule biophysics (*36*), and modulate biosynthetic and cell-signaling pathways (*25*, *37*).

An effective method for assembling megadalton nanoscale 2D (*11*) and 3D shapes (*16*–*19*, *23*) is DNA origami (*29*), in which a long "scaffold" strand (often a viral genomic DNA) is folded to a predesigned shape via interactions with hundreds of short "staple" strands. However, each distinct shape typically requires a new scaffold routing design and the synthesis of a different set of staple strands. In contrast, construction from standardized small components (such as DNA tiles) that each can be included, excluded, or replaced without altering the rest of the structure—modular assembly—offers a simpler approach to constructing shapes. In addition, if all components are short strands that can be chemically synthesized, the resulting structures would have greater chemical diversity than DNA origami, which typically contains half biological material (the scaffold) in mass and half synthetic material (the staples). A variety of structures have been assembled by using DNA (*3*, *4*, *6*, *8*, *10*, *13*, *15*, *20*) and RNA (*9*, *22*, *25*) tiles, including periodic (*4*, *6*, *25*) and algorithmic (*8*) 2D lattices, extended ribbons (*15*) and tubes (*6*, *15*, *25*), 3D crystals (*20*), polyhedra (*13*, *22*), and finite 2D shapes (*9*, *10*). However, modular self-assembly of finite-sized, discrete DNA structures has generally lacked the complexity that DNA origami can offer.

Only recently have researchers demonstrated finite complex 2D shapes (*26*) self-assembled from hundreds of distinct single-stranded tiles (SSTs) (*15*). Unlike a traditional multistranded tile (*3*, *4*, *6*, *8*–*10*, *13*, *20*, *25*), which is a well-folded, compact structure displaying several sticky ends, an SST is a floppy single-strand DNA composed entirely of concatenated sticky ends. In one-pot reactions, hundreds of SSTs self-assemble into desired target structures mediated by inter-tile binding interactions; no scaffold strand is required. The simplicity and modularity of this approach allowed the authors to build more than 100 distinct shapes by selecting subsets of tiles from a common 2D "molecular canvas." This latest success has challenged previous thinking that modular components, such as DNA tiles, are not suitable for assembling complex, singularly addressable shapes (*38*). This presumption was largely based on a supposed technically challenging requirement for perfect strand stoichiometry (the relative ratio of the strands). Deviations from equality were expected to result in predominating partial structure formation (*38*). The surprising success of SST assembly may have bypassed this challenge via putative slow and sparse nucleation followed by fast growth (*26*), so that a large number of particles complete their formation well before depletion of the component strand pool.

Here, we generalize the concept of single-stranded "tiles" to "bricks" and thus extend our modular-assembly method from 2D to 3D. A canonical DNA brick is a 32-nucleotide (nt) single strand with four 8-nt binding domains (sticky ends). In simple one-step annealing reactions, prescribed target 3D structures self-assemble robustly from hundreds of unpurified brick strands that are mixed together with no tight control of stoichiometry. The modularity of our method enabled the construction of 102 distinct structures by simply selecting subsets of bricks from a common 3D cuboid molecular canvas consisting of 1000 voxels (fig. S1) (*39*); each voxel fits 8 base pairs (bp) and measures approximately 2.5 by 2.5 by 2.7 nm. These structures include solid shapes, with sophisticated geometries and surface patterns and hollow shapes, with intricate tunnels and enclosed cavities. Additionally, we have constructed structures with alternative packing geometries or using noncanonical brick motifs, demonstrating the method's versatility. The work here thus establishes DNA bricks as a simple, robust, modular, and versatile framework for constructing complex 3D nanostructures by using only short synthetic DNA strands. More generally, it demonstrates how complex 3D molecular structures can be assembled from small, modular components mediated strictly by local binding interactions.

Design of DNA-Brick Structures and a 3D Molecular Canvas

In our design, a DNA brick is a 32-nt strand that we conceptualize as four consecutive 8-nt domains (Fig. 1A). Each DNA brick bears a distinct nucleotide sequence. All DNA bricks adopt an identical shape when incorporated into the target structure: two 16-nt antiparallel helices joined by a single phosphate linkage. The two domains adjacent to the linkage are designated as "head" domains, and the other two are designated as "tail" domains. A DNA brick with a tail domain bearing sequence "a" can interact productively with a neighboring brick with a complementary "a*" head domain in a stereospecific fashion. Each pairing between bricks defines three parallel helices packed to produce a 90° dihedral angle (Fig. 1B, top); this angle derives from the approximate 3/4 right-handed helical twist of 8 bp of DNA.

We introduce a LEGO-like model to depict the design in a simple manner (Fig. 1B, bottom). The model intentionally overlooks the detailed helical

[1]Wyss Institute for Biologically Inspired Engineering, Harvard University, Boston, MA 02115, USA. [2]Department of Cancer Biology, Dana-Farber Cancer Institute, Harvard Medical School, Harvard University, Boston, MA 02115, USA. [3]Department of Biological Chemistry and Molecular Pharmacology, Harvard Medical School, Harvard University, Boston, MA 02115, USA. [4]Harvard–Massachusetts Institute of Technology (MIT) Division of Health Sciences and Technology, MIT, Cambridge, MA 02139, USA. [5]Department of Systems Biology, Harvard Medical School, Harvard University, Boston, MA 02115, USA.

*To whom correspondence should be addressed. E-mail: py@hms.harvard.edu

structure and strand polarity but preserves the aspect ratios and some of the orientational constraints on interactions between DNA bricks: The two protruding round plugs, pointing in the same direction as the helical axes, represent the two tail domains; the two connected cubes with recessed round holes represent the two head domains. A brick must adopt one of two classes of orientation, horizontal or vertical (Fig. 1B). The two bricks connect to form a 90° angle via hybridization, represented as the insertion of a plug into a hole. An insertion is only allowed between a plug and a hole that carry complementary sequences with matching polarity (which is not graphically depicted in the current model for expositional simplicity). In fig. S2, we present a more detailed LEGO-like model that explicitly tracks the polarity of the DNA bricks and their stereospecific interaction pattern.

Structural periodicities of the design are illustrated in a 6H (helix) by 6H (helix) by 48B (bp) cuboid structure (Fig. 1, C and D). Bricks can be grouped into 8-bp layers that contain their head domains. Bricks follow a 90° counterclockwise rotation along successive 8-bp layers, resulting in a repeating unit with consistent brick orientation and arrangement every four layers. For example, the first and fifth 8-bp layers in Fig. 1D share the same arrangement of bricks. Within an 8-bp layer, all bricks share the same orientation and form a staggered arrangement to tile the layer. On the boundary of each layer, some DNA bricks are bisected to half-bricks, representing a single helix with two domains. The cuboid is self-assembled from DNA bricks in a one-step reaction. Each brick carries a particular sequence that directs it to fit only to its predesigned position. Because of its modular architecture, a predesigned DNA brick structure can be used for construction of smaller custom shapes assembled from subsets of DNA bricks (Fig. 1E). Detailed strand diagrams for the DNA brick structures are provided in figs. S3 and S4.

3D molecular canvas. The LEGO-like model can be further abstracted to a 3D model that contains only positional information of each 8-bp duplex. A 10H by 10H by 80B cuboid is conceptualized as a 3D molecular canvas that contains 10 by 10 by 10 voxels. Each voxel fits an 8-bp duplex and measures 2.5 by 2.5 by 2.7 nm (Fig. 1F). Based on the 3D canvas, a computer program first generates a full set of DNA bricks, including full-bricks and half-bricks that can be used to build a prescribed custom shape. Using 3D modeling software, a designer then needs only to define the target shapes by removing unwanted voxels from the 3D canvas—a process resembling 3D sculpting. Subsequently, the computer program analyzes the shape and automatically selects the correct subset of bricks for self-assembly of the shape.

Self-Assembly of DNA-Brick Cuboid Structures

Using the above design strategy, we constructed a wide range of DNA brick structures (*39*). We

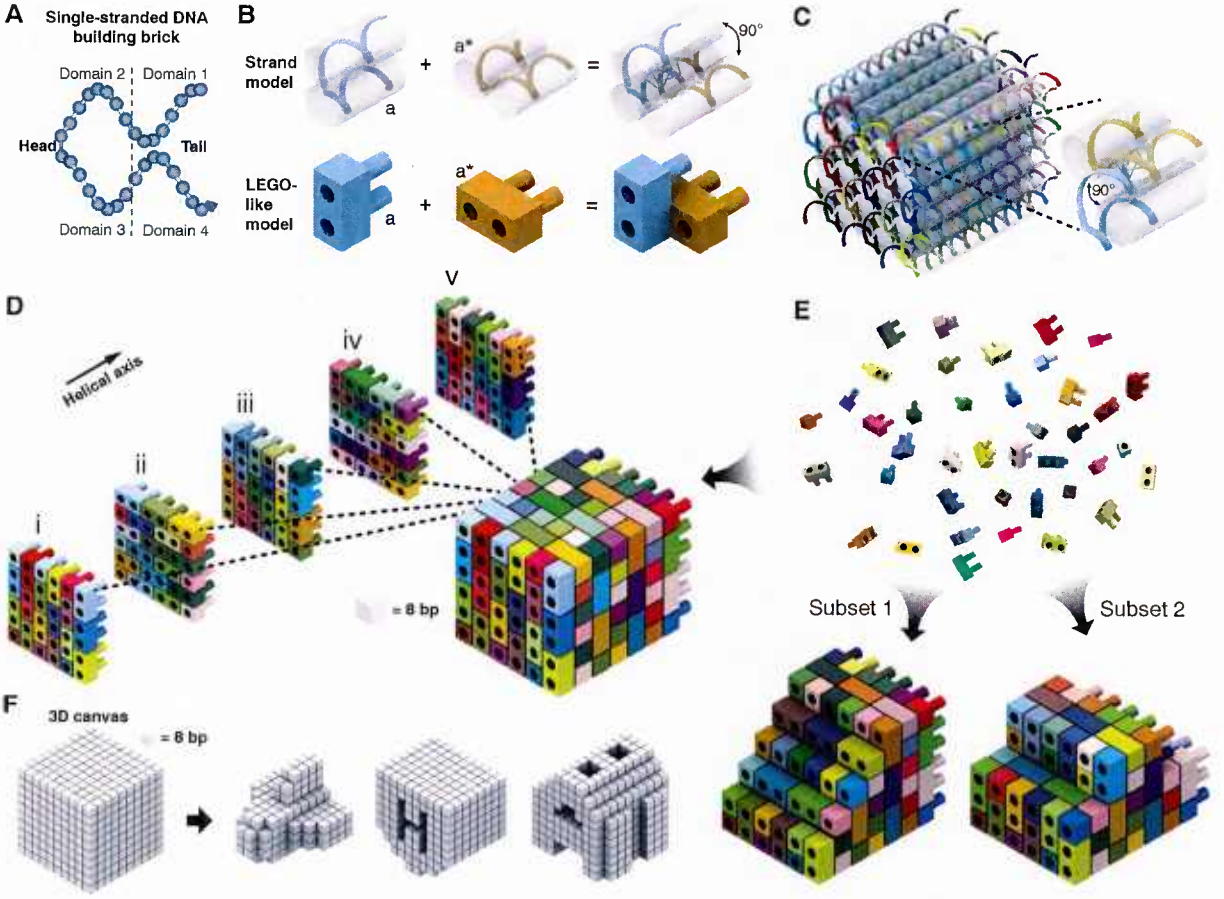

Fig. 1. Design of DNA brick structures analogous to structures built of LEGO® bricks. (**A**) A 32-nt four-domain single-stranded DNA brick. Each domain is 8 nt in length. The connected domains 2 and 3 are "head" domains; domains 1 and 4 are "tail" domains. (**B**) Each two-brick assembly forms a 90° dihedral angle via hybridization of two complementary 8-nt domains "a" and "a*". (**C**) A molecular model that shows the helical structure of a 6H by 6H by 48B cuboid 3D DNA structure. Each strand has a particular sequence, as indicated by a distinct color. The inset shows a pair of bricks. (**D**) A LEGO-like model of the 6H by 6H by 48B cuboid. Each brick has a particular sequence. The color use is consistent with (B). Half bricks are present on the boundary of each layer. (**E**) The 6H by 6H by 48B cuboid is self-assembled from DNA bricks. The bricks are not interchangeable during self-assembly because of the distinct sequence of each brick. Using the 6H by 6H by 48B as a 3D molecular canvas, a smaller shape can be designed by using a subset of the bricks. (**F**) 3D shapes designed from a 10 by 10 by 10–voxel 3D canvas; each voxel fits 8 bp (2.5 nm by 2.5 nm by 2.7 nm).

first constructed 3D cuboid structures of a variety of sizes and aspect ratios (Fig. 2).

Random sequence design. The sequences of DNA bricks were designed by random assignments of base pairs (A-T, C-G) to 3D structures. We first tested two versions of a 6H by 6H by 64B cuboid, with either random sequences or specially designed sequences (designed by smoothing binding energy, minimizing undesired secondary structure, and reducing sequence symmetry) and observed comparable self-assembly yields (fig. S5). We also tested three sets of random sequences using a 4H by 12H by 120B cuboid and again observed similar assembly yields (figs. S6 and S7; more discussion on domain similarity of random sequence design is provided in fig. S8). Thus, random sequences were applied to all subsequent designs.

Protector bricks. Including unpaired single strands at the ends of DNA duplexes has proven to be effective for mitigating unwanted aggregation that results from blunt-end stacking (*11*). An 8-nt single-stranded domain protruded out from every 5′ or 3′ end of all DNA duplexes in our 3D structure designs (Fig. 1C). The sequences of these 8-nt domains were replaced with eight continuous thymidines to further prevent undesired nonspecific binding interactions between exposed single-stranded domains. DNA bricks with modified head or tail poly-T domains are named "head protectors" or "tail protectors," respectively.

Boundary bricks. A 16-nt half brick could be merged with a preceding 32-nt full brick along the direction of its helix to form a 48-nt strand (figs. S9 to S11). We observed a 1.4-fold improvement in assembly yield for a 6H by 6H by 64B cuboid when this 48-nt boundary-strand design was implemented, possibly reflecting accelerated nucleation of target structure formation. Hence, this merge strategy was applied to all of our 3D structures.

Assembly and characterization of 6H by 10H by 128B cuboid. For a detailed characterization study, we constructed a 6H by 10H by 128B cuboid (Fig. 2A). It consists of 459 strands (7680 bp, with a molecular weight comparable with that of an M13-based DNA origami; design details are provided in figs. S12 and S13). Unpurified DNA strands were mixed together at nominally equal ratios without careful adjustment of stoichiometry (*39*). To determine the optimal assembly conditions, we tested two annealing ramps (24-hour annealing and 72-hour annealing), two strand concentrations (100 and 200 nM per strand), and eight $MgCl_2$ concentrations (10, 20, 30, 40, 50, 60, 70, and 80 mM). Equal amounts of each sample (2 pmol per strand) were then subjected to EtBr-stained 2% agarose gel electrophoresis (fig. S14). The best gel yield (~4% as calculated by yield = measured mass of product/mass of all strands) was achieved at the following conditions: 200 nM per strand, 72-hour annealing, 40 mM $MgCl_2$ (fig. S15). The above gel yield reflects only an approximate estimate for the incorporation ratio of the monomer strands (*26*).

For comparison, 4 to 14% gel yield was reported for 3D DNA origami with similar size and aspect ratios [such as the 10H by 6H by 98B and other origami cuboids in (*40*)]. The origami gel yield was estimated as yield = (scaffold strands incorporated into product/total scaffold strands); the loss of excessive staple strands (normally 5- to 10-fold more than the scaffold strand) was not taken into account. For DNA bricks, the optimal 40 mM $MgCl_2$ was higher than the optimal $MgCl_2$ concentration for 3D origami folding, which typically is below 30 mM (*18*). Column-purified DNA bricks product (~50% recovery efficiency) (Fig. 2B) migrated as a single band on agarose gel and appeared under transmission electron microscopy (TEM) with expected morphology (Fig. 2C) and measured dimensions of 0.34 nm (± 0.01 nm SD) per base pair and 2.5 nm (± 0.2 nm SD) per helix width. For the gel-purified product, "the percentage of intact structures" was estimated at 55% by counting the ratio of intact particles over all the particles in TEM images (fig. S16). This percentage of intact structures is comparable with the previously reported percentages of 3D square-lattice DNA origami (27% for a 6H by 12H by 80B cuboid, 59% for an 8H by 8H by 96B cuboid) (*41*).

Special designs can be applied to increase the assembly yield of the 6H by 10H by 128B cuboid. "Head protectors" and "tail protectors" appeared especially unstable because half of their 8-nt domains are unpaired. By merging "head protectors" of the 6H by 10H by 128B cuboid with their neighboring strands (figs. S17 and S18), a modified version 6H by 10H by 128B-M cuboid was obtained and showed 190% improvement in gel assembly yield and 17% improvement in the percentage of intact structures under TEM over the standard 6H by 10H by 128B cuboid (fig. S19). Thus, 3D structures can be further stabilized by using special design rules, such as this merging strategy. However, this modification requires deletions of crossovers between helices, which may potentially create global or local deformations, and was not used for constructions in the remainder of the paper.

Structures of different sizes. Eighteen distinct cuboid structures that contain 9, 16, 36, 60, 96, and 144 helices were designed, annealed using the optimal conditions previously identified for the 6H by 10H by 128B cuboid self-assembly, and characterized through gel and TEM (Fig. 2D and

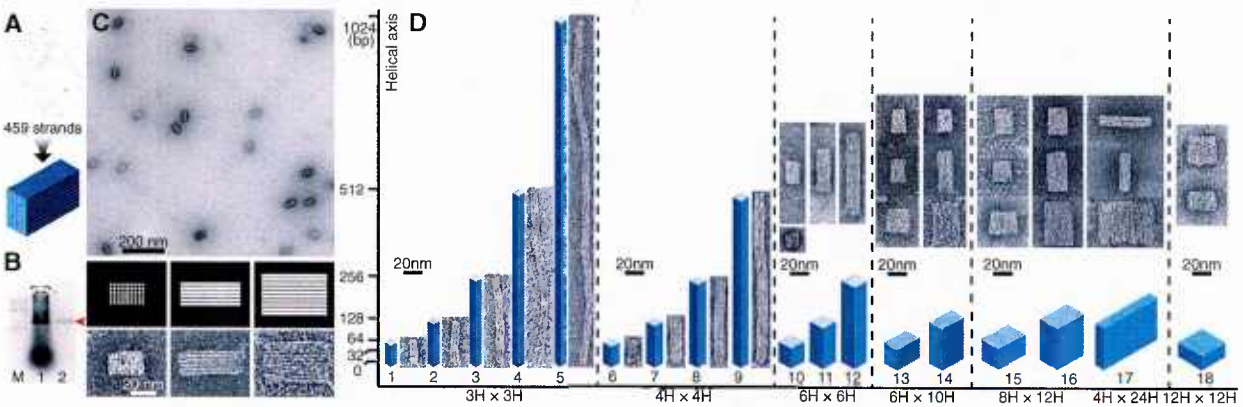

Fig. 2. Cuboid structures self-assembled from DNA bricks. **(A)** DNA bricks self-assembled into a 6H by 10H by 128B cuboid in a one-step thermal annealing process. **(B)** Agarose gel electrophoresis showing 50% purification recovery efficiency of the 6H by 10H by 128B cuboid. Lane M contains the 1-kb ladder. Lanes 1 and 2 contain unpurified and purified 6H by 10H by 128B cuboid structures, respectively. The red arrow points to the cuboid product band. **(C)** TEM images of gel-purified 6H by 10H by 128B cuboid. Zoomed-in images (bottom) and corresponding computer-generated graphics (middle) show three different projection views. **(D)** Designs and TEM images of 18 cuboids of a variety of dimensions. Horizontal axis is labeled with the cross-section dimensions of the cuboids; vertical axis is labeled with the lengths of the constituent helices. The lengths are 48B (shape 18), 64B (shapes 1, 6, 10, 13, and 15), 120B (shapes 16 and 17), 128B (shapes 2, 7, 11, and 14), 256B (shapes 3, 8, and 12), 512B (shapes 4 and 9), and 1024B (shape 5). Each 3D cylinder model is drawn proportionally to the relative dimensions of the cuboid; corresponding TEM images are shown to the right or above each model.

fig. S20). Additional TEM images are shown in figs. S21 to S27. Measured dimensions of intact particles for each structure agree with the designs (fig. S28). Gel yields varied from <1 to ~80% (figs. S20C and S28). For structures with the same number of helices, smaller cuboids exhibited higher assembly yields. The highest yield (80%) was observed for the smallest object, the 3H by 3H by 64B cuboid; the lowest yields (<1%) were observed for the 8H by 12H by 120B, 4H by 24H by 120B, and 12H by 12H by 48B cuboids. The biggest DNA objects constructed in this paper are an 8H by 12H by 120B cuboid (formed by 728 strands) and a 4H by 24H by 120B cuboid (formed by 710 strands), which are identical in molecular weight (24,576 nt, 8 MD, and 60% more massive than an M13-based DNA origami). Increasing the concentration for the brick strands helped to increase the yield for a small cuboid, 4H by 4H by 128B (fig. S29). In some cases, higher molecular weight bands can be detected above the product band; these bands are likely multimers caused by nonspecific interactions between assembled products. For example, for the 6H by 10H by 64B structure, TEM revealed that an upper band contained dimers of the cuboids (fig. S30). Cuboids with 32-bp (32B) helices were also tested but failed to assemble (fig. S20). This is likely due to the fact that these cuboids contained only one crossover between each pair of neighboring helices and hence were less stable.

Complex Shapes Made from a 10 by 10 by 10–Voxel 3D Canvas

Using the 10 by 10 by 10–voxel 3D canvas (Figs. 1F and 3A and fig. S31), we next constructed 102 distinct shapes (Fig. 3), demonstrating the modularity of the DNA brick strategy.

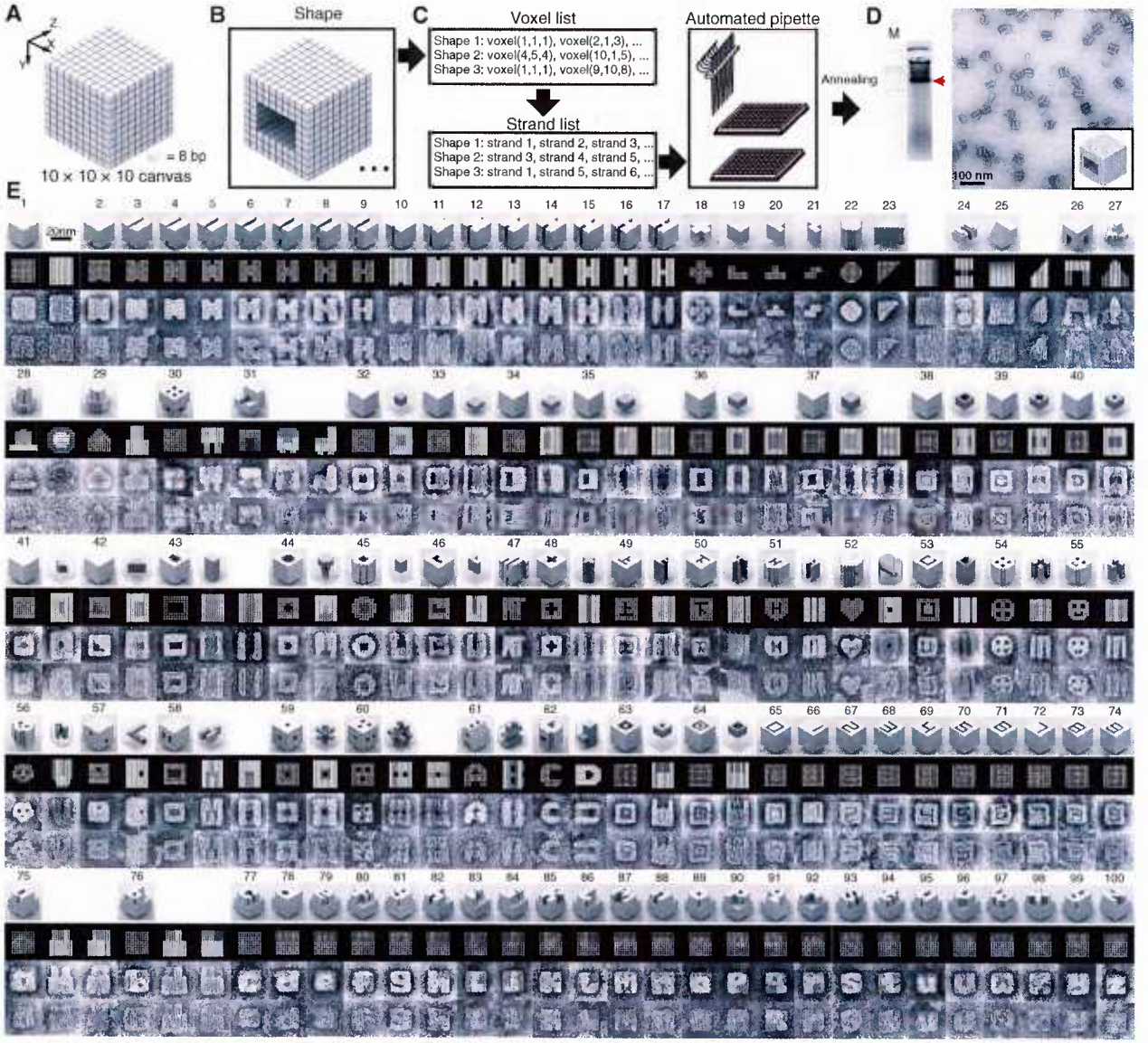

Fig. 3. Shapes made from a 3D molecular canvas. (**A**) A 10 by 10 by 10–voxel 3D canvas. *z* axis is the helical axis. Each voxel (8 bp) measures 2.5 by 2.5 by 2.7 nm. (**B**) Shapes are designed by editing voxels by using 3D modeling software. (**C**) A computer program recognizes the voxel composition of each shape and generates a list of strands to form this shape. The list then is used to direct an automated liquid-handling robot to mix the strands. (**D**) After annealing, the shapes are characterized by means of agarose gel electrophoresis and TEM imaging. Lane M contains the 1-kb ladder. The product band is indicated by the red arrow. (**E**) Computer-generated models and TEM images of shapes. The top row for each shape depicts a 3D model, followed by a computer-generated projection view, an image averaged from six different particles visualized by using TEM, and a representative raw TEM image. More raw images are shown in figs. S38 to S54. In a number of cases, multiple projections are presented. Some shapes with cavities or tunnels are depicted with additional transparent 3D views that highlight the deleted voxels (colored dark gray). For example, the top right model of shape 32 shows the enclosed cuboid cavity.

DNA bricks and derivatives. Any brick in the 3D canvas can become either a boundary half brick (exposed at the edges of a layer and bisected) (Fig. 1D), a protector brick (located in the first or last layer along *z* axis), or even both at same time, in a custom shape design. Thus, modified versions of each brick were generated with all combinations of domain-deletion (bisect to a half-brick), polythymidine-sequence-substitution (change to protector bricks), and boundary-brick-merger (change to 48-nt boundary bricks) to accommodate the possibilities (two types of strands with low occurring frequency and four types of strands with only one binding domain were excluded in our implementation) (fig. S32). Overall, a master collection of 4455 strands (with a total of 138,240 nt) were generated by a computer program to guarantee that a designed shape could be assembled with head/tail protector bricks and 48-nt boundary bricks. Custom shapes were assembled via selecting subsets of the master collection without synthesizing new strands.

Automated design process. By rendering the 3D canvas using 3D modeling software, we can edit voxels and visualize a shape using a graphical user interface (Fig. 3B). Then, the voxel information of multiple shapes is interpreted by a custom program to generate a list of strands involved in the formation of each shape. This list is subsequently processed to direct an automated liquid-handling robot to select DNA strands from source plates and pipette them to the wells of a product plate, mixing strands for many shapes in a high-throughput manner (Fig. 3C). The strands will be subsequently annealed in separate test tubes to produce the desired structures (Fig. 3D). The complete design workflow is shown in figs. S33 and S34. To use existing computational tools previously developed by other researchers, we can also convert shapes to caDNAno files (*40*). Each shape's conformation then can be simulated using CanDo (*42*), a software tool for computing 3D structures of DNA origami (fig. S35).

Using the 3D canvas and following the automated design process, we successfully constructed 102 distinct shapes (gels in figs. S36 and S37; TEM images of shapes 1 to 100 in Fig. 3E; and raw TEM images for all the shapes in figs. S38 to S54).

Shapes 1 to 17. The basic design constraints were studied by using a group of shapes containing two 4H by 10H by 80B blocks connected by a middle "connecting block" (shapes 2 to 17). The connecting blocks were two-voxel wide along *x* axis and systematically designed to possess decreasing numbers of voxels along *y* axis (shapes 2 to 9) or *z* axis (shapes 10 to 17). Eliminating voxels along the *x* axis should have the same effect as eliminating voxels along the *y* axis because of the shape symmetry. Agarose gel electrophoresis revealed that in both systems, as the connector became overly thin, the gel yields for the intact structures decreased, and partial structures (putative unconnected 4H by 10H by 80B blocks) became more prominent (for example, in lanes for shapes 8, 9, and 15 to 17 in fig. S36). However, reducing the number of voxels along the *z* axis appeared to decrease the yield more significantly than along the *y* axis. Shape 9, which contained only a 2-voxel connection along the *y* axis, gave 6% gel yield. In contrast, the yield for shape 17 (2-voxel along the *z* axis) dropped to 1%. Overall, these observations suggest safe design criteria of at least two continuous voxels along the *x* axis or *y* axis (2 helices) and three *z* axis voxels (24 bp) for stable features. However, as demonstrated in following experiments, smaller features (for example, two *z* axis voxels, shapes 33 to 37; one *x* axis or *y* axis voxel, shapes 64 to 74) can still stably exist in certain shapes in which these features are presumably reinforced by other voxels in close proximity.

Solid shapes 18 to 31. A number of solid shapes were designed including *z* direction extrusions of simple geometric shapes (shapes 18 to 23) and more intricate objects (shapes 24 to 31; also, shape 102 in fig. S54). Gel yields and TEM images of these objects provided more knowledge of the design space of our methodology. For example, shapes 26 and 27, which both contained 3-helix-thick appendages anchored only on one edge, were occasionally found without these protrusions or with them but containing defects. Thus, such thin features, although obeying our design criteria, appeared to be less stable than were the better-supported or thicker features.

Closed-cavity shapes 32 to 42. Previously, a few examples of 3D DNA origami with closed cavities were demonstrated, including a box (*16*), a tetrahedron (*17*), a sphere, and an ellipsoid (*23*). We created a series of "empty boxes" with different sizes of cuboid cavities (shapes 32 to 37) as well as more intricate cavity shapes (such as a square ring, cross, and triangle; shapes 38 to 42).

Open-cavity shapes 43 to 62. We constructed shapes with a single open cavity (tunnel) of varying width, depth, and geometry (shapes 43 to 53) and multiple-parallel cavities (shapes 54 to 56). Shapes with noncrossing perpendicular tunnels (shape 57), turning and branching tunnels (shape 58), and crossing tunnels (shapes 59, 60; also, shape 101 in fig. S54) were also demonstrated. Furthermore, we constructed tunnel-containing cuboids with modified outer surfaces in order to create varying external views from different angles, as demonstrated by shapes 60 to 62.

Features-on-solid-base shapes 63 to 100. Sophisticated features were designed on a solid base, including a full set of 10 Arabic numerals (shapes 65 to 74) and 26 lowercase letters for the English alphabet (shapes 75 to 100). Two concentric ring structures (shapes 63 and 64) and the numerals (shapes 65 to 74) contained features as thin as one voxel (2.5 nm), suggesting that the design criteria (for example, thin structures tend to fail) are contingent on the surrounding environment of a particular feature. These shapes also highlight the capacity of creating extruded features that would otherwise be unattainable via 2D assembly (*26*).

For most shapes, assembly yields were between a few percent and 30% [figs. S36 and S37; in comparison, yields of five 3D DNA origami structures were reported as 7 to 44% (*18*)]. Only five shapes had assembly yields higher than 30%; three shapes had assembly yields lower than 1%.

In spite of our success in making a variety of intricate 3D shapes, some shapes exhibited undesired properties. For example, shapes 60 to 62 only showed <1% of intact particles in TEM images; some fine features of a shape (such as the two wings of shape 27) could be damaged or even completely missing if the shape was extracted from an agarose gel band. We also observed four failed designs that did not produce clear product bands on agarose gels (fig. S55A). Two features-on-solid-base designs showed strong bands on agarose gels (fig. S55B), and were of the expected size in TEM images. However, their features were not clearly resolved under TEM, suggesting that the shapes may have formed, but the features were too subtle to be visualized.

Generality of DNA Brick Self-Assembly

To explore the generality of the DNA brick assembly framework, we constructed structures with brick motifs other than the 32-nt canonical brick motif. These structures include those with alternative lattice geometries that have been previously demonstrated by DNA origami (*11*, *18*, *43*).

Single-layer (2D) structures. Conceptually, a single-layer structure can be constructed by "extraction" of a layer from a 3D brick structure [Fig. 4A and fig. S56, comparison with a 2D single-stranded tile rectangle design (*26*)]. A 30H by 1H by 126B rectangle was intentionally modified to be 10.5 bp per turn instead of 10.67 bp per turn (for 3D design) in order to get a relatively flat structure (fig. S57). Gel yield was estimated to be 18% (fig. S58), which is comparable with 2D single-stranded tile structures (*26*). TEM (Fig. 4B) and atomic force microscopy (AFM) (Fig. 4C) revealed expected rectangle structures. On the basis of AFM images, the dimensions were measured as 0.31 nm (± 0.01 nm SD) per base pair and 2.6 nm (± 0.3 nm SD) per helix width.

3D honeycomb-lattice structures. We then created 10.8-bp per turn (33.3° twist per base pair) honeycomb-lattice (HC) and hexagonal-lattice (HL) DNA structures. Four types of four-domain DNA strands were designed for HC structures (Fig. 4, D and E). A 6H by 6H by 84B-HC structure was successfully constructed and characterized (Fig. 4F and fig. S59). Particles in TEM images were measured to be 13 nm (± 0.9 nm SD) by 22 nm (± 1.0 nm SD) by 29 nm (± 1.2 nm SD). Assembly yield was estimated to be 30% (fig. S60).

3D hexagonal-lattice DNA structures. Two types of strands are used to build a HL structure: a linear strand with multiple 9-nt domains and an 18-nt strand with two 9-nt domains that are connected by a crossover (Fig. 4, G and H).

A 6H by 7H by 108B-HL structure was constructed and characterized (Fig. 4I and fig. S61). Particles in TEM images were measured to be 13 nm (± 0.8 nm SD) by 18 nm (± 1.1 nm SD) by 35 nm (± 2.2 nm SD). Assembly yield was estimated to be 26% (fig. S62).

Other brick motifs. We also constructed a 6H by 10H by 64B cuboid that arranges brick strands in an alternating fashion between layers (figs. S63 and S64) and two 6H by 6H by 64B cuboids that implement two other brick motif designs (figs. S65 and S66). One design is based on "chopping" the scaffold of a DNA origami to short strands (fig. S65A). The other adopts standardized motifs that are each 32 nt long and have two crossovers (fig. S65B). These designs further demonstrate the versatility of DNA brick self-assembly.

Discussion

DNA bricks provide a simple, modular, and robust framework for assembling complex structures from short strands. Simplicity: A canonical brick is a standardized 32-nt single strand composed of four 8-nt binding domains; bricks interact via simple local binding rules. Modularity: With no scaffold present, an assembly of bricks has a modular architecture; each brick can be added or removed independently. Robustness: The assembly process is robust to variations in sequence composition (random sequences are used), strand synthesis (unpurified strands suffice), and stoichiometry (no tight control is required). Together, the simple and standardized motif, modular architecture, and robust performance permit straightforward automation of the design and construction process. A software tool takes as input a 3D shape specification and directs a liquid-handling robot to select and mix presynthesized brick strands to form the shape. Using a 1000-voxel canvas, 102 diverse shapes were rapidly prototyped. These shapes demonstrate a new level of geometrical sophistication, as exemplified by the intricate tunnel and cavity features.

The DNA brick framework is not restricted to the canonical 32-nt motif and can be generalized to include various other motifs (Fig. 4), enabling the construction of 3D structure with diverse lattice-packing geometries. In addition, previously demonstrated single-stranded tiles (*15*, *26*) can be viewed as a special case of bricks in which each pair of neighboring bricks form a 180° angle. For comparison, in hexagonal-, square-, and honeycomb-lattice structures, neighboring bricks form 60°, 90°, and 120° angles, respectively. These different angles are achieved by changing the domain lengths of bricks. Furthermore, neighboring bricks may be merged into a longer strand, which may facilitate nucleation or strengthen structurally weak positions. The DNA brick (and single-stranded tile) method differs from previous multistranded tiles in that each brick monomer is a floppy single strand and only folds into a bricklike shape when incorporated into the assembly. It also differs from DNA origami by not using a scaffold strand. However, DNA origami can also be related to the brick framework, in which half of the bricks are concatenated into a long scaffold (fig. S65A). The successes of constructions that use only short strands (as in bricks) and those that include a long scaffold (as in origami) together suggest a full spectrum of motif possibilities with strands of diverse lengths: Longer strands may provide better structural support, and shorter ones may provide finer modularity and features; the eclectic use of both may lead to the most rapid progression toward greater complexity.

The DNA brick structures constructed here are still far below the size limit allowed by sequence uniqueness. Making the conservative assumption (by neglecting the contribution of cooperativity) that every domain must display a different sequence, a structure using canonical 32-nt, four-domain bricks could potentially reach a size of 8 nt by 4^8 (524,288 nucleotides). In our experiments, the assembly process appeared to tolerate (sparse) identical domains (fig. S8), further expanding the potential obtainable size. Further exponential increase in size could potentially be achieved by using bricks with longer domains or by encoding algorithmic growth patterns (*8*) in

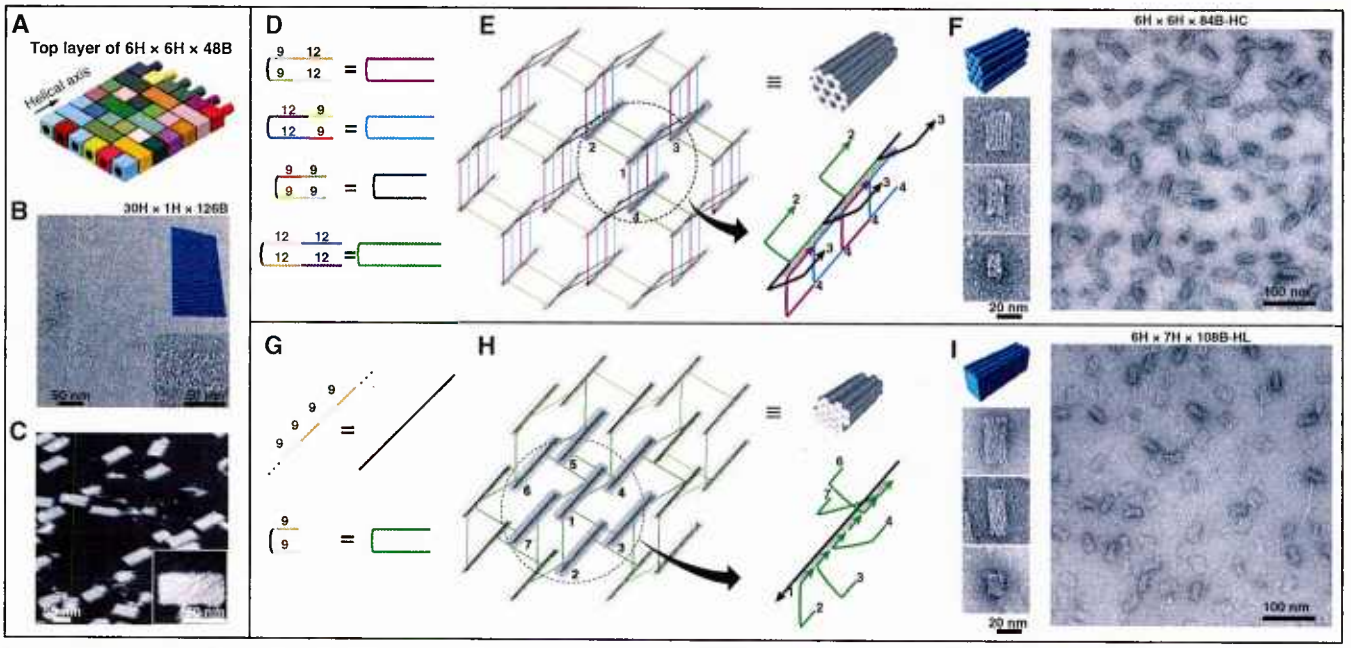

Fig. 4. Generality of DNA brick self-assembly. (**A** to **C**) The design and construction of a single-layer brick structure. (A) DNA bricks of the top layer of the 6H by 6H by 48B cuboid in Fig. 1D, with the crossovers to the layer below removed. (B) TEM images of a 30H by 1H by 126B rectangle. Top right inset shows the model of the design. Bottom right inset contains a zoomed-in image of the structure. (C) AFM images of the 30H by 1H by 126B rectangle. Inset contains a zoomed-in image of the structure. (**D** to **I**) The designs and constructions of 3D honeycomb-lattice [(D) to (F)] and hexagonal-lattice [(G) to (I)] brick structures. [(D) and (G)] The strands used for (D) honeycomb-lattice and (G) hexagonal-lattice self-assembly. The number of nucleotides in each domain is indicated in the left panel. [(E) and (H)] Strand diagrams of (E) an 84-bp honeycomb-lattice structure and (H) a 54-bp hexagonal-lattice structure. The right bottom image depicts an enlarged image of the circled helix bundle. Strand colors match those described on the right side of (D) or (G). Numbers indicate DNA helices. [(F) and (I)] TEM images of (F) a 6H by 6H by 84B-HC hexagonal-lattice structure and (I) a 6H by 7H by 108B-HL 3D hexagonal-lattice structure. 3D model and zoomed-in images of different projection views are shown to left.

the assembly. However, in practice, low yields were already observed for larger designs (up to 24,576 nucleotides attempted thus far). Solving this challenge may require improvements in structure and sequence design, enzymatic synthesis for higher-quality strands, optimized thermal or isothermal (*44*) annealing conditions, and a detailed understanding and perhaps explicit engineering of the kinetic assembly pathways (*8*, *14*, *44*) of DNA brick structures.

The DNA brick structure, with its modular architecture, sophisticated geometry control, and synthetic nature, will further expand the range of applications and challenges that nucleic acid nanotechnology has already started to address—for example, to arrange technologically relevant guest molecules into functional devices (*6*, *25*, *32*–*34*), to serve as programmable molecular probes and instruments for biological studies (*33*, *34*, *36*), to render spatial control for biosynthesis of useful products (*25*), to function as smart drug delivery particles (*37*), and to enable high-throughput nanofabrication of complex inorganic materials for electronics or photonics applications (*6*, *32*). The modularity of the brick structure may facilitate rapid prototyping of diverse functional nanodevices. Its sophisticated and refined geometrical control may enable applications that require high-precision arrangements of guest molecules. Because the brick structure is composed entirely of short synthetic strands (no biologically derived scaffold), it is conceivable to make bricks by using synthetic informational polymers other than the natural form of DNA. Such polymers may include L-DNA (*26*), DNA with chemically modified backbones or artificial bases, or chemically synthesized or in vitro (or even in vivo) transcribed RNA. This material diversity may potentially produce nanostructures with not only prescribed shapes but also designer chemical (or biochemical) properties (such as nuclease resistance or reduced immunogenicity) that would be useful for diverse applications requiring the structure to function robustly in complex environments, such as in living cells or organisms.

References and Notes

1. N. C. Seeman, *J. Theor. Biol.* **99**, 237 (1982).
2. J. H. Chen, N. C. Seeman, *Nature* **350**, 631 (1991).
3. T. J. Fu, N. C. Seeman, *Biochemistry* **32**, 3211 (1993).
4. E. Winfree, F. Liu, L. A. Wenzler, N. C. Seeman, *Nature* **394**, 539 (1998).
5. B. Yurke, A. J. Turberfield, A. P. Mills Jr., F. C. Simmel, J. L. Neumann, *Nature* **406**, 605 (2000).
6. H. Yan, S. H. Park, G. Finkelstein, J. H. Reif, T. H. LaBean, *Science* **301**, 1882 (2003).
7. W. B. Sherman, N. C. Seeman, *Nano Lett.* **4**, 1203 (2004).
8. P. W. K. Rothemund, N. Papadakis, E. Winfree, *PLoS Biol.* **2**, e424 (2004).
9. A. Chworos *et al.*, *Science* **306**, 2068 (2004).
10. S. H. Park *et al.*, *Angew. Chem. Int. Ed.* **45**, 735 (2006).
11. P. W. K. Rothemund, *Nature* **440**, 297 (2006).
12. G. Seelig, D. Soloveichik, D. Y. Zhang, E. Winfree, *Science* **314**, 1585 (2006).
13. Y. He *et al.*, *Nature* **452**, 198 (2008).
14. P. Yin, H. M. T. Choi, C. R. Calvert, N. A. Pierce, *Nature* **451**, 318 (2008).
15. P. Yin *et al.*, *Science* **321**, 824 (2008).
16. E. S. Andersen *et al.*, *Nature* **459**, 73 (2009).
17. Y. Ke *et al.*, *Nano Lett.* **9**, 2445 (2009).
18. S. M. Douglas *et al.*, *Nature* **459**, 414 (2009).
19. H. Dietz, S. M. Douglas, W. M. Shih, *Science* **325**, 725 (2009).
20. J. Zheng *et al.*, *Nature* **461**, 74 (2009).
21. T. Omabegho, R. Sha, N. C. Seeman, *Science* **324**, 67 (2009).
22. I. Severcan *et al.*, *Nat. Chem.* **2**, 772 (2010).
23. D. Han *et al.*, *Science* **332**, 342 (2011).
24. L. Qian, E. Winfree, *Science* **332**, 1196 (2011).
25. C. J. Delebecque, A. B. Lindner, P. A. Silver, F. A. Aldaye, *Science* **333**, 470 (2011).
26. B. Wei, M. Dai, P. Yin, *Nature* **485**, 623 (2012).
27. C. Lin, Y. Liu, S. Rinker, H. Yan, *ChemPhysChem* **7**, 1641 (2006).
28. N. B. Leontis, A. Lescoute, E. Westhof, *Curr. Opin. Struct. Biol.* **16**, 279 (2006).
29. W. M. Shih, C. Lin, *Curr. Opin. Struct. Biol.* **20**, 276 (2010).
30. N. C. Seeman, *Annu. Rev. Biochem.* **79**, 65 (2010).
31. D. Y. Zhang, G. Seelig, *Nat. Chem.* **3**, 103 (2011).
32. A. Kuzyk *et al.*, *Nature* **483**, 311 (2012).
33. H. M. T. Choi *et al.*, *Nat. Biotechnol.* **28**, 1208 (2010).
34. C. Lin *et al.*, *Nat. Chem.* **4**, 832 (2012).
35. M. J. Berardi, W. M. Shih, S. C. Harrison, J. J. Chou, *Nature* **476**, 109 (2011).
36. N. D. Derr *et al.*, *Science* **338**, 662 (2012).
37. S. M. Douglas, I. Bachelet, G. M. Church, *Science* **335**, 831 (2012).
38. P. W. K. Rothemund, E. S. Andersen, *Nature* **485**, 584 (2012).
39. Materials and methods, supplementary figures and texts, and DNA sequences are available as supplementary materials on *Science* Online.
40. S. M. Douglas *et al.*, *Nucleic Acids Res.* **37**, 5001 (2009).
41. Y. Ke *et al.*, *J. Am. Chem. Soc.* **131**, 15903 (2009).
42. C. E. Castro *et al.*, *Nat. Methods* **8**, 221 (2011).
43. Y. Ke, N. V. Voigt, K. V. Gothelf, W. M. Shih, *J. Am. Chem. Soc.* **134**, 1770 (2012).
44. R. Schulman, B. Yurke, E. Winfree, *Proc. Natl. Acad. Sci. U.S.A.* **109**, 6405 (2012).

Acknowledgments: The authors thank M. Dai for technical assistance; E. Winfree, B. Wei, and S. Woo for discussions; and D. Pastuszak for assistance in draft preparation. This work is supported by an Office of Naval Research (ONR) Young Investigator Program award N000141110914, an ONR grant N000141010827, an Army Research Office grant W911NF1210238, an NSF CAREER award CCF1054898, an NIH Director's New Innovator award 1DP2OD007292, and a Wyss Institute Faculty Startup Fund to P.Y., and by a Wyss Institute Faculty Grant, ONR grants N000014091118 and N000141010241, and an NIH Director's New Innovator award 1DP2OD004641 to W.M.S.. L.L.O. is supported by an NSF graduate research fellowship. Y.K. conceived the project, designed and performed the experiments, analyzed the data, and wrote the paper; L.L.O. designed and performed the experiments, analyzed the data, and wrote the paper; W.M.S. conceived the project, discussed the results, and wrote the paper; P.Y. conceived, designed, and supervised the study, interpreted the data, and wrote the paper. The DNA sequences for the nanostructures can be found in the supplementary materials. A provisional patent has been filed based on this work.

Supplementary Materials

www.sciencemag.org/cgi/content/full/338/6111/1177/DC1
Materials and Methods
Supplementary Text
Figs. S1 to S66
Tables S1 to S20

11 July 2012; accepted 16 October 2012
10.1126/science.1227268

A Reconciled Estimate of Ice-Sheet Mass Balance

Andrew Shepherd,[1]* Erik R. Ivins,[2]* Geruo A,[3] Valentina R. Barletta,[4] Mike J. Bentley,[5] Srinivas Bettadpur,[6] Kate H. Briggs,[1] David H. Bromwich,[7] René Forsberg,[4] Natalia Galin,[8] Martin Horwath,[9] Stan Jacobs,[10] Ian Joughin,[11] Matt A. King,[12,27] Jan T. M. Lenaerts,[13] Jilu Li,[14] Stefan R. M. Ligtenberg,[13] Adrian Luckman,[15] Scott B. Luthcke,[16] Malcolm McMillan,[1] Rakia Meister,[8] Glenn Milne,[17] Jeremie Mouginot,[18] Alan Muir,[8] Julien P. Nicolas,[7] John Paden,[14] Antony J. Payne,[19] Hamish Pritchard,[20] Eric Rignot,[18,2] Helmut Rott,[21] Louise Sandberg Sørensen,[4] Ted A. Scambos,[22] Bernd Scheuchl,[18] Ernst J. O. Schrama,[23] Ben Smith,[11] Aud V. Sundal,[1] Jan H. van Angelen,[13] Willem J. van de Berg,[13] Michiel R. van den Broeke,[13] David G. Vaughan,[20] Isabella Velicogna,[18,2] John Wahr,[3] Pippa L. Whitehouse,[5] Duncan J. Wingham,[8] Donghui Yi,[24] Duncan Young,[25] H. Jay Zwally[26]

We combined an ensemble of satellite altimetry, interferometry, and gravimetry data sets using common geographical regions, time intervals, and models of surface mass balance and glacial isostatic adjustment to estimate the mass balance of Earth's polar ice sheets. We find that there is good agreement between different satellite methods—especially in Greenland and West Antarctica—and that combining satellite data sets leads to greater certainty. Between 1992 and 2011, the ice sheets of Greenland, East Antarctica, West Antarctica, and the Antarctic Peninsula changed in mass by −142 ± 49, +14 ± 43, −65 ± 26, and −20 ± 14 gigatonnes year^{-1}, respectively. Since 1992, the polar ice sheets have contributed, on average, 0.59 ± 0.20 millimeter year^{-1} to the rate of global sea-level rise.

Fluctuations in the mass of the polar ice sheets are of considerable societal importance, because they affect global sea levels (*1*, *2*) and oceanic conditions. They occur as a consequence of their internal dynamics and changes in atmospheric and oceanic conditions (*3*–*5*). Analysis of the geological record suggests that past climatic changes have precipitated

11.1.3 Extended DNA crystals

nature chemistry

ARTICLES

PUBLISHED ONLINE: 19 OCTOBER 2014 | DOI: 10.1038/NCHEM.2083

DNA brick crystals with prescribed depths

Yonggang Ke[1,2,3*†‡], Luvena L. Ong[1,4‡], Wei Sun[1,5‡], Jie Song[6], Mingdong Dong[6], William M. Shih[1,2,3] and Peng Yin[1,5*]

The ability to assemble functional materials with precise spatial arrangements is important for applications ranging from protein crystallography to photovoltaics. Here, we describe a general framework for constructing two-dimensional crystals with prescribed depths and sophisticated three-dimensional features. The crystals are self-assembled from single-stranded DNA components called DNA bricks. We demonstrate the experimental construction of DNA brick crystals that can grow to micrometre size in their lateral dimensions with precisely controlled depths up to 80 nm. They can be designed to pack DNA helices at angles parallel or perpendicular to the plane of the crystal and to display user-specified sophisticated three-dimensional nanoscale features, such as continuous or discontinuous cavities and channels.

The production of two-dimensional materials, particularly crystals with prescribed depths and intricate three-dimensional features, provides an enabling platform for nanofabrication. For example, these two-dimensional crystals could be integrated with inorganic nanomaterials to develop complex nanoelectronics[1] and photonics systems[2,3]. Although thin film structures have been created using either electron/ion beam lithography[3] or self-assembly of block copolymers[4,5], fabricating two-dimensional materials that simultaneously achieve precisely tunable thickness as well as prescribed complex surface and internal features (for example, channels or pores) with sub-5 nm resolution remains challenging[3,6–8].

A promising route to address this challenge is structural DNA nanotechnology[9]. DNA has been used to create complex discrete shapes[9–25] and extended periodic crystals[26–38], including ribbons[33], tubes[27,32,33,35], two-dimensional crystals[18,26–32,36–38] and three-dimensional crystals[34]. DNA structures can serve as scaffolds for precise patterning of functional moieties (for example, gold nanoparticles) for electronics and photonics applications[35,39,40]. However, in contrast to current organic polymeric films[41], the two-dimensional DNA crystals are typically restricted to a single layer of DNA helices with ~2 nm depth. A three-dimensional crystal has been reported previously, but it grows in all three dimensions with no control in depth and uses a small triangular repeating unit[34]. One major categorical gap in constructing atomically precise DNA structures—and, more generally, synthetic molecular structures—is the lack of a general framework for making complex two-dimensional crystals with precisely controlled depths and sophisticated three-dimensional features. Successful construction of such structures could enable a wide range of applications ranging from nanoelectronics and plasmonics to biophysics and molecular diagnosis.

Using single-stranded DNA bricks[21,22,33], we describe here a simple, robust and general approach to engineer complex micrometre-sized two-dimensional crystals with prescribed depths and complex three-dimensional features with nanometre resolution. In previous reports[26–32,34–38], DNA crystals have typically been formed via a two-stage hierarchical process, in which individual strands first assemble into a discrete building block (often known as a DNA tile), and individual tiles then assemble into crystals. In contrast, DNA brick crystals grow non-hierarchically, and the growth of DNA crystals from short, floppy, single-stranded DNA bricks does not involve the assembly of preformed discrete multi-stranded building blocks with well-defined shapes. During the brick crystal growth, assembly and disassembly occur via relatively weak intermolecular interactions involving the addition or subtraction of a single short strand at a time.

We constructed a total of 32 DNA brick crystals. These crystals can grow up to several micrometres in their lateral dimensions with a prescribed depth of up to 80 nm, and display sophisticated user-specified nanometre-scale three-dimensional features, including intricate cavities, channels and tunnels (Supplementary Fig. 1). Additionally, the non-hierarchical nature of the assembly permits isothermal formation of the crystals. We illustrated the scaffolding utility of these crystals by functionalizing them with parallel arrays and layers of tightly packed (1–2 nm spaced) gold nanoparticles.

Design and assembly of DNA brick crystals

The crystal design was based on previous discrete three-dimensional DNA brick structures[22]. A DNA brick is a 32-nucleotide (nt) strand with four 8-nt binding domains, and can be modelled as a Lego-like brick (Fig. 1a). In a one-step annealing reaction, DNA bricks—each with a distinct sequence—assemble into a prescribed structure by binding to their designated neighbours. Implementing 'connecting' bricks between discrete structures yields DNA brick crystals. The design strategy is illustrated using a 6H (helix) × 6H (helix) × 24B (base pair) cuboid structure that can be programmed to grow along three orthogonal axes (Fig. 1b). To achieve growth along the z axis (parallel to the helical axes), the domains in the first layer are modified to be complementary to the domains in the last layer. Growth along the x axis or y axis is achieved by including bricks that each have two domains bound to one face of the cuboid and the other two domains bound to the opposing face (see Supplementary Fig. 2 for detailed strand connection patterns). The crystals are designed to form via non-hierarchical growth, with

[1]Wyss Institute for Biologically Inspired Engineering, Harvard University, Boston, Massachusetts 02115, USA, [2]Department of Cancer Biology, Dana-Farber Cancer Institute, Harvard Medical School, Boston, Massachusetts 02115, USA, [3]Department of Biological Chemistry and Molecular Pharmacology, Harvard Medical School, Boston, Massachusetts 02115, USA, [4]Harvard-MIT Division of Health Sciences and Technology, Massachusetts Institute of Technology, Cambridge, Massachusetts 02139, USA, [5]Department of Systems Biology, Harvard Medical School, Boston, Massachusetts 02115, USA, [6]Center for DNA Nanotechnology at the Interdisciplinary Nanoscience Center (iNANO), Aarhus University, 8000 Aarhus C, Denmark; †Present address: Wallace H. Coulter Department of Biomedical Engineering, Georgia Institute of Technology and Emory University, Atlanta, Georgia 30322, USA; ‡These authors contributed equally to this work. *e-mail. py@hms.harvard.edu; yonggang.ke@emory.edu

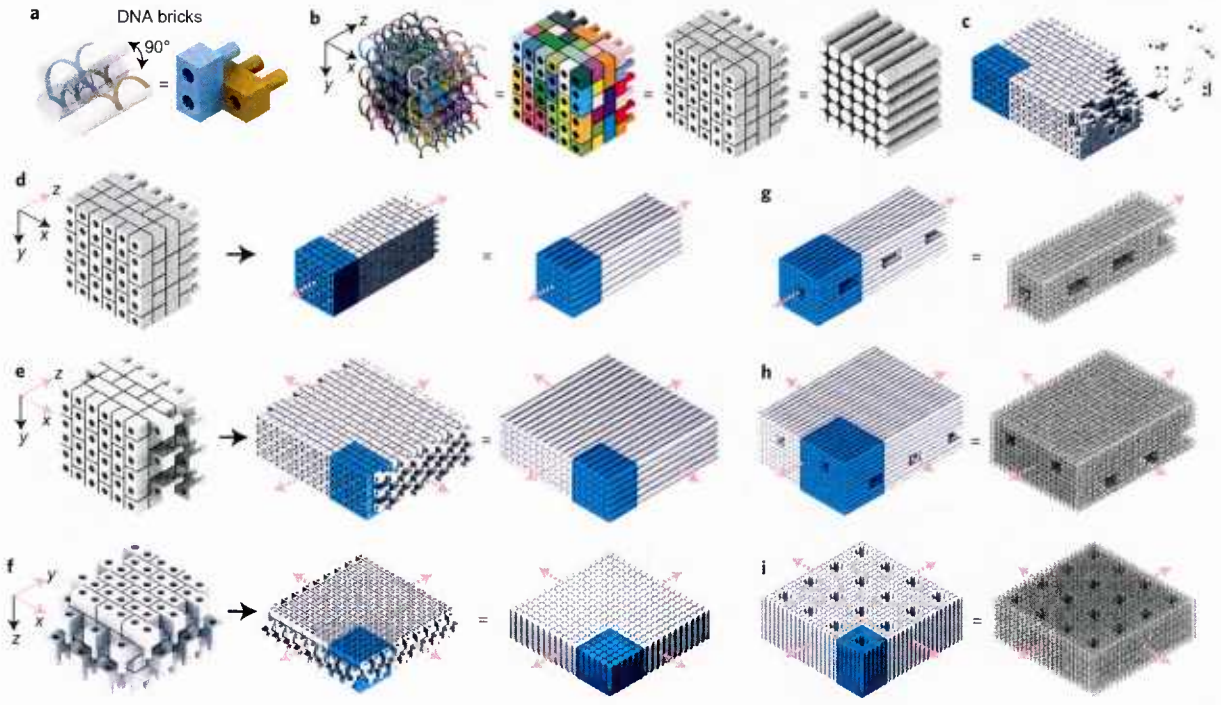

Figure 1 | Design of DNA brick crystals. **a**, Strand (left) and brick (right) models showing two 32-nt DNA bricks that form a 90° angle. **b**, Models of a 6H (helix) × 6H (helix) × 24B (base pair) cuboid with increasing levels of abstraction: (left to right) a strand model, a brick model (in which colours distinguish brick species), a brick model with all bricks coloured grey, and a model where cylinders represent DNA double helices. **c**, Individual DNA strands, rather than pre-assembled multi-brick blocks, are directly incorporated into the growing crystal. **d**–**f**, Brick and cylinder models of a one-dimensional Z-crystal (**d**), a two-dimensional ZX-crystal (**e**) and a two-dimensional XY-crystal (**f**) designed from the 6H × 6H × 24B cuboid. **g**–**i**, Cylinder and DNA-helix models of crystals with pores and tunnels: Z-crystal with a tunnel and periodic pores (**g**); ZX-crystal with two groups of parallel tunnels (**h**); XY-crystal with periodic pores (**i**). Repeating units of the crystals are denoted by blue boxes. Pink arrows indicate the directions of crystal growth.

individual bricks (rather than preformed multi-brick blocks) directly incorporated into the crystal (Fig. 1c).

We constructed four groups of crystals: (1) Z-crystals: one-dimensional 'DNA-bundle' crystals extending along the z axis (Fig. 1d); (2) X-crystals: one-dimensional crystals extending along the x axis; (3) ZX-crystals: two-dimensional 'multilayer' crystals extending along the z axis and the x axis (Fig. 1e); (4) XY-crystals: two-dimensional 'DNA-forest' crystals extending along the x axis and y axis (Fig. 1f). Using different designs of repeating units, DNA crystals with prescribed depths and features (for example, pores, channels and tunnels) can be made (Fig. 1g–i). Here, we define a 'channel' as a surface-exposed cavity extending across multiple repeating units, a 'pore' as a hole across a single repeating unit, and a 'tunnel' as a series of concatenated pores. A crystal is named as '[the growth direction(s)]–[the dimensions of the repeating unit]–[the shape of the unit]'. For instance, an 'XY-6H × 6H × 24B-cuboid' crystal is a two-dimensional XY-crystal with a cuboid-shaped 6H × 6H × 24B repeating unit. Like discrete DNA brick structures[22], the sequences for DNA-brick crystals were randomly generated. All crystals used a 10.67 base pair (bp)/turn reciprocal twist density, which is slightly underwound compared to the 10.5 bp/turn of natural B-form DNA.

Each crystal was assembled by mixing unpurified DNA brick strands in a roughly equimolar ratio in the presence of 40 mM $MgCl_2$, without careful adjustment of strand stoichiometry. After 72 h or 168 h one-pot annealing, assembled crystals were imaged using transmission electron microscopy (TEM), cryo-electron microscopy (cryo-EM) or atomic force microscopy (AFM), without further purification. See Methods for details.

One-dimensional DNA-bundle crystals (Z-crystals)

Both solid Z-crystals (Fig. 2a–f) and Z-crystals with tunnels (Fig. 2g–i) were constructed successfully.

Solid Z-crystals with different cross-sectional shapes. We first constructed three solid Z-crystals with distinct square-shaped cross-sections (6H × 6H × 32B, 8H × 8H × 32B and 10H × 10H × 32B; Fig. 2a–c). We then demonstrated crystals with more complex cross-sections: a Z-8H × 8H × 128B-spiral crystal with a surface helical channel along the z axis (Fig. 2d), a Z-43H × 32B-triangle crystal (Fig. 2e) and a Z-44H × 32B-hexagon crystal (Fig. 2f). The spiral channel was clearly visible in the TEM image of the Z-8H × 8H × 128B-spiral crystal. However, many broken structures were also observed for this spiral crystal (Supplementary Fig. 6).

Z-crystals with tunnels. Three Z-crystals with tunnels were tested (Fig. 2g–i). The cross-section of the Z-56H × 32B-tunnel is an 8H × 8H square with a 2H × 4H rectangle removed from the centre (Fig. 2g). The Z-108H × 32B-tunnel has a 12H × 12H square cross-section with a 6H × 6H hole (Fig. 2h). The Z-60H × 64B-tunnel crystal contains a 2H × 2H tunnel along the z axis and 8H × 2H × 24B pores that intersect the 2H × 2H tunnel every 64 bp along the z axis (Fig. 2i). TEM images of the Z-60H × 64B-tunnel showed many splintered structures containing only half of the designed DNA helices, probably reflecting the weakening effect of the periodic 8H × 2H × 24B pores on the connections between the top and bottom halves of the structures along the y axis.

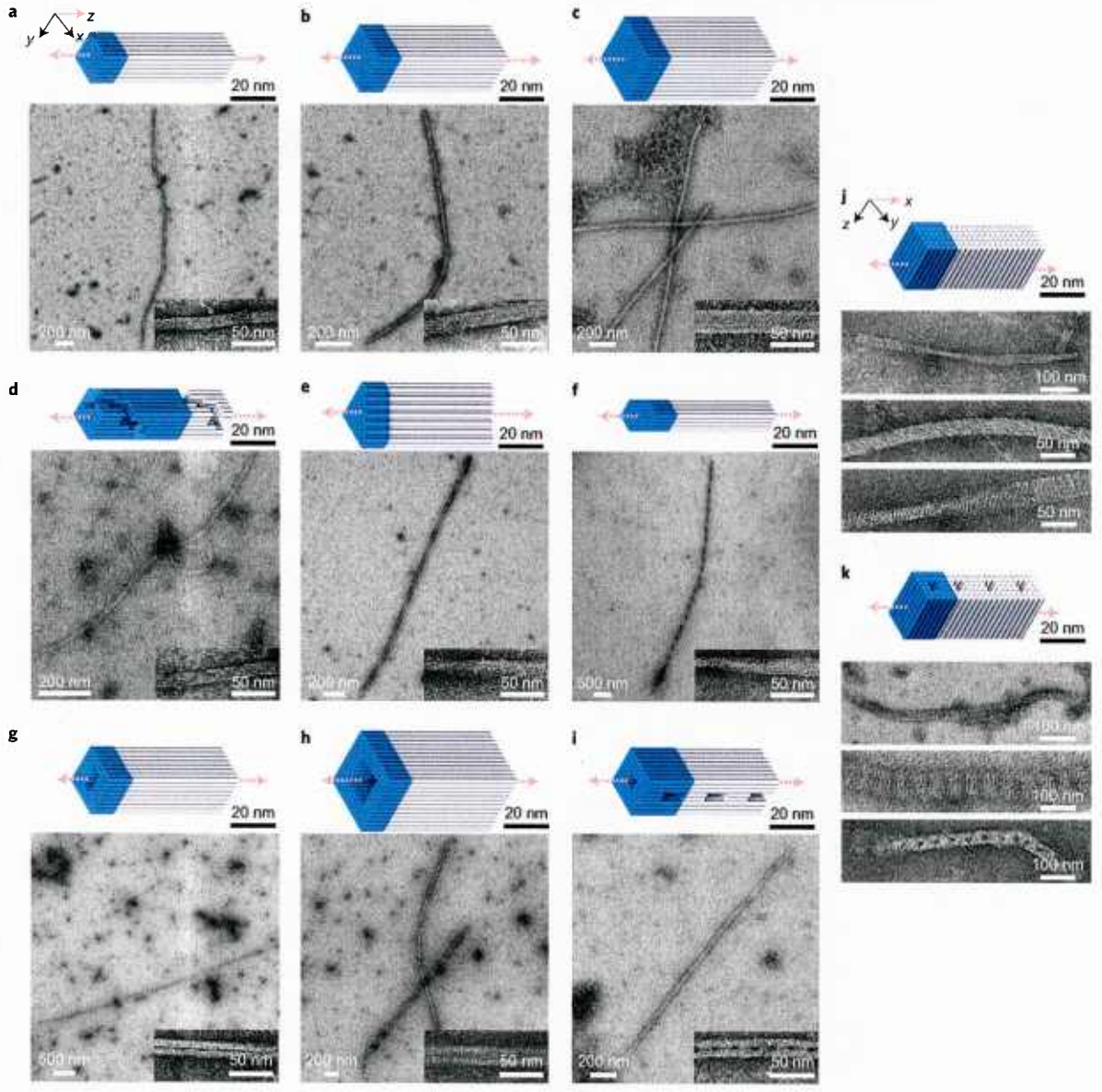

Figure 2 | One-dimensional DNA crystals. a–i, Z-crystals: cylinder models and TEM images. **a–c**, Z-crystals with solid cross-sections: 6H × 6H (**a**), 8H × 8H (**b**), 10H × 10H (**c**). **d–f**, Z-crystals with different cross-sectional shapes: 8H × 8H Z-crystal with right-handed spiral channel (**d**); 43H Z-crystal with triangle-shaped cross-section (**e**); 44H Z-crystal with hexagon-shaped cross-section (**f**). **g–i**, Z-crystals with porous cross-sections: 8H × 8H Z-crystal with a 2H × 4H tunnel (**g**); 12H × 12H Z-crystal with a 6H × 6H tunnel (**h**); 8H × 8H Z-crystal with a 2H × 2H tunnel and perpendicular 8H × 2H × 24B pores (**i**). **j,k**, Cylinder models (top) and TEM images (bottom) of X-crystals: X-6H × 6H × 64B-cuboid crystal (**j**); 6H × 6H X-crystal with 2H × 2H pores (**k**). Unit cells of crystals are denoted by blue boxes. See Supplementary Figs 3–12 for more TEM images.

All Z-crystals displayed a global right-handed twist, which probably resulted from the stress generated by the underwound design[17,42]. Zoomed-out TEM images of Z-crystals are provided in Supplementary Figs 3–11.

One-dimensional X-crystals

We constructed two one-dimensional crystals that extended along the *x* axis: an X-6H × 6H × 64B-cuboid crystal (Fig. 2j) and an X-32H × 64B-pore crystal (Fig. 2k). Both appeared well-formed and were observed to have grown up to a few hundred nanometres in length in TEM images. See Supplementary Fig. 12 for larger images.

Two-dimensional DNA multilayer crystals (ZX-crystals)

Solid ZX-crystals (Fig. 3a–d), ZX-crystals with channels, pores and tunnels (Fig. 3e–h) and an offset ZX-crystal (Fig. 3i) were successfully constructed.

Solid ZX-crystals. Four solid ZX-crystals were designed from 4H × 32B units that contained 4, 6, 10 and 20 layers of helices, respectively (Fig. 3a–d). The thickness of each ZX-crystal was directly measured at the crease where the crystal folded over onto itself in TEM images. The thicknesses of the 4-, 6-, 10- and 20-layer ZX-crystals were measured to be ~10, 15, 25 and 50 nm, respectively, proving all layers of the crystals were completely

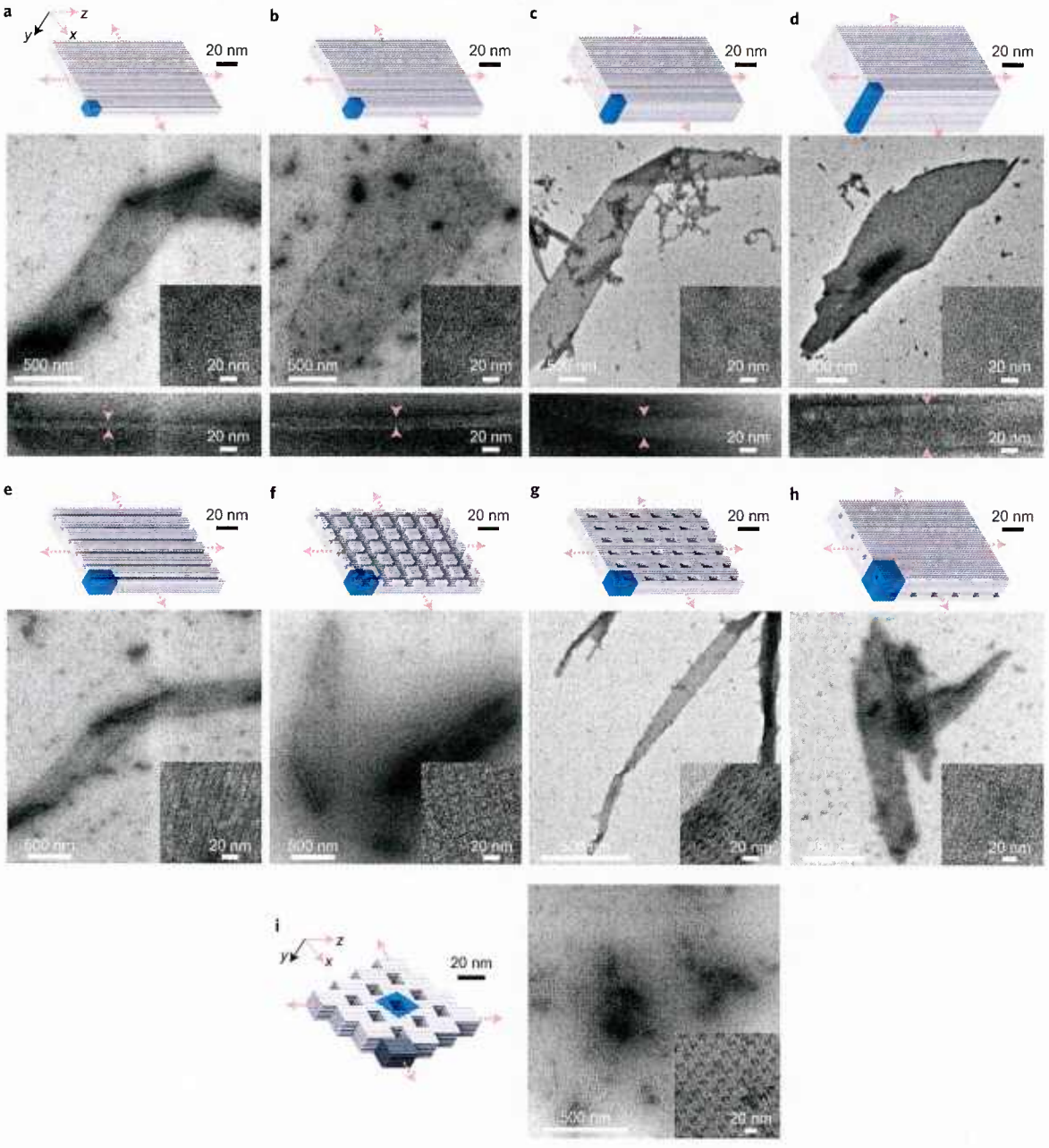

Figure 3 | Two-dimensional multilayer ZX-crystals. Cylinder models (top) and TEM images (bottom) for each crystal. **a–d**, Solid ZX-crystals: 4-layer (**a**), 6-layer (**b**), 10-layer (**c**), 20-layer (**d**) solid ZX-crystals. Arrows indicate positions for thickness measurements of the crystals. **e–h**, ZX-crystals with channels, pores and tunnels: 6-layer crystal with 2H × 2H parallel channels (**e**); 6-layer crystal with two groups of crossing channels (2H × 2H channels that run parallel to the DNA helical axis and 2H × 32B channels that run perpendicular to the DNA helical axis) (**f**); 6-layer crystal with 2H × 6H × 32B pores (**g**); 10-layer crystal with two groups of non-contacting tunnels (2H × 2H tunnels parallel to the DNA helical axis and 2H × 24B tunnels perpendicular to DNA helical axis) (**h**). In **h**, the two groups of tunnels are separated by two layers of DNA helices. **i**, Offset-ZX-6H × 6H × 64B-cuboid ZX-crystal. The dark grey part represents a 6H × 6H × 64B-cuboid repeating unit. Unit cells of crystals are denoted by blue boxes. See Supplementary Figs 13–21 for more TEM images.

formed and that the width of each DNA helix was ~2.5 nm in diameter.

ZX-crystals with channels, pores and tunnels. We first designed three ZX-crystals from a 6H × 6H × 32B cuboid unit (Fig. 3e–g). Four helices were removed from the cuboid to generate ZX-32H × 64B-channel (Fig. 3e). The second design, ZX-32H × 64B-cross-channel, was obtained by further removing a perpendicular 2H × 32B channel from ZX-32H × 64B-channel (Fig. 3f). The third design, ZX-6H × 6H × 64B-pore, contained a 2H × 4H × 32B vertical pore along the *y* axis in each cuboid unit (Fig. 3g). This design yielded narrow and long crystals. The most complex ZX-crystal design is the ZX-96H × 64B-cross-tunnel crystal (Fig. 3h). Its repeating unit can be considered as a

10H × 10H × 64B-cuboid with a 2H × 2H × 64B-pore along the *z* axis and with a 10H × 2H × 24B-pore along the *x* axis. In this structure, the design contains two types of parallel tunnel separated by two layers of DNA. These tunnels appear perpendicular when viewed from the ZX projection.

Offset two-dimensional ZX-crystal. We constructed a ZX-crystal that extended 6H × 6H × 64B-cuboid repeating units along the *z* axis and *x* axis using an 'offset-register' scheme: the crystal's *z* axis extension was shifted 4H along the *x* axis, and the crystal's *x* axis extension was shifted 32B along the *z* axis (Fig. 3i).

All ZX-crystals showed a small amount of right-handed twist, which also probably arose from the 10.67 bp/turn underwound design. As a result, we observed that the crystals sometimes appeared twisted and folded on top of themselves in TEM images. We also observed that all ZX-crystals grew faster along the *z* axis than the *x* axis, consistent with observations from previous crystal growth studies[26]. See Supplementary Figs 13–21 for more TEM images.

Two-dimensional DNA forest crystals (XY-crystals)

We constructed solid XY-crystals (Fig. 4a–d), XY-crystals with pores and surface channels (Fig. 4e–i) and XY-crystals that form a tube structure (Fig. 4j).

Solid XY-crystals. Solid XY-crystals of variable depths were constructed (Fig. 4a–d). Using a 4H × 4H-cuboid unit of various heights, we constructed four XY-crystals with 64B (21 nm), 128B (42 nm), 192B (63 nm) and 256B (84 nm) designed depths.

XY-crystals with pores and channels. XY-32H × 64B-pore and XY-32H × 128B-pore crystals were constructed (Fig. 4e,f). Both designs contained periodic 2H × 2H pores separated by 4H in each dimension. The two crystals resemble 21 nm and 42 nm porous membranes, respectively. Cryo-EM imaging was applied to these two crystals (Supplementary Fig. 22). Based on three-dimensional reconstruction data, their depths were measured to be 26 ± 2 nm (32H × 64B-pore) and 45 ± 3 nm (32H × 128B-pore), respectively (Fig. 4g,h), in good agreement with the theoretical values (21 nm and 42 nm). The slight discrepancy is likely to be a result of theoretical estimations not accounting for the single-stranded poly-T at the ends of the duplex. The depths of these two crystals were also measured by AFM to be ~16 nm and 36 nm, respectively (Supplementary Fig. 23). The smaller depths obtained from AFM probably reflect compression of the crystal by the cantilever.

An XY-4H × 8H × 96B-channel crystal was constructed (Fig. 4i). It contained a solid 64B (42 nm) base and parallel channels. The channels were 4H (10 nm) in width and 32B (21 nm) in height and were separated by four layers of helices.

A tube-shaped XY-crystal. An XY-4H × 4H × 32B-tube crystal (Fig. 4j) was designed using the same strategy as for the other XY-crystals. However, when assembled in 40 mM $MgCl_2$, this thin 32B (10.6 nm) XY-crystal formed a tube (Supplementary Figs 24 and 25) instead of a flat two-dimensional crystal, probably due to the uneven distribution of connections between helices (Supplementary Fig. 24).

Annealing the XY-4H × 4H × 32B-tube at higher $MgCl_2$ concentration produced tubes with larger diameters, presumably due to a greater reduction in repulsion between negatively charged DNA helices. At 60 mM $MgCl_2$ we observed many tubes with diameters between 140 and 300 nm (Supplementary Fig. 26). To further test our hypothesis that the tube formation is caused by the asymmetric distribution of crossovers, we designed an XY-4H × 4H × 32B-cuboid crystal in which the DNA bricks were arranged in an alternating fashion between layers[22]. Connections between helices in this design were symmetrically distributed along both the *x* axis and the *y* axis (Supplementary Fig. 65). This alternating design produced only flat crystal structures (Supplementary Fig. 27). Additionally, the thicker 64, 128, 192 and 256B XY-crystals with non-alternating designs had 2, 4, 6 and 8 connections between each pair of neighbouring helices, respectively. No visible curvature was observed for these designs in TEM images (Supplementary Figs 28–31).

General observations. Unlike the ZX-crystals, the XY-crystals did not show a global right-handed twist. The lack of global twist can be explained by the following analysis. For simplicity, assume an XY-crystal forms a perfect cylinder containing *n* helices. The overall twist (in radians) of the cylinder is $\theta = TL/JG$, where T is the applied torque resulting from the underwound design, L is the helix length, G is the modulus rigidity of a helix, and J is the torsion constant. The first three parameters can be considered as constants. The torsion constant J for a cylinder as a function of cross-sectional (x–y plane) radius can be approximated as $\pi r^4/2$ (r^4 is proportional to n^2), where r is the circular cross-sectional radius. Thus, θ is inversely proportional to n^2. As an XY-crystal grows to include a large number of helices, its global twist θ rapidly becomes negligible.

As both growth directions (*x* axis and *y* axis) for an XY-crystal are perpendicular to the DNA helical axis, the XY-crystal grew in an isotropic fashion and did not exhibit any apparent directional preference. Because crystal growth along the *x* axis or *y* axis is slower than growth along the *z* axis (as discussed for ZX-crystals), the 72 h annealing often produces either no XY-crystals or XY-crystals smaller than 100 nm in their lateral dimensions. Accordingly, we used a 168 h annealing ramp for all XY-crystals.

XY-crystals provide a particularly attractive platform for DNA-directed guest molecule assembly. The surface of an XY-crystal can be considered as a 'breadboard'[13] on which guest molecules can be conveniently attached to the ends of DNA helices at 2.5 nm resolution in the lateral plane.

See Supplementary Figs 25–34 for more TEM images of XY-crystals.

Crystal growth mechanism

The non-hierarchical growth mechanism of DNA brick crystals was verified by the following experiments: (1) analysis of the boundaries of DNA brick crystals based on high-resolution TEM images revealed that these crystals lack well-defined, complete structural repeating units on their boundaries; (2) the annealing profile of the formation of the crystals revealed a single transition temperature (rather than two or more transition temperatures characteristic of hierarchically formed DNA crystals[32,36]); (3) time-lapse analysis of the TEM images and gel electrophoresis of the assembly process revealed the absence of repeating units of designed size.

Boundary analysis. We studied the edge of the XY-32H × 64B-pore crystal by counting the number of units that match that of the designed repeating unit (Supplementary Fig. 35). In hierarchically assembled crystals, the designed repeating units are first formed before they are assembled into a crystal. As a result, the edges of the crystal often consist of the shape of the designed repeating unit (for example, >90% of the edges of a previously reported hierarchically assembled crystal[36]; Supplementary Fig. 36). In contrast, only 2% of the edges of the XY-32H × 64B-pore brick crystal match that of the designed shape (Supplementary Fig. 37), consistent with a non-hierarchical assembly mechanism. See Supplementary Section 6.1 for more details.

Annealing curve. To study the annealing profile of the brick crystals we assembled the ZX-4H × 20H × 32B and XY-32H × 64B-pore crystals in the presence of SYBR Green I (Supplementary Figs 38 and 39).

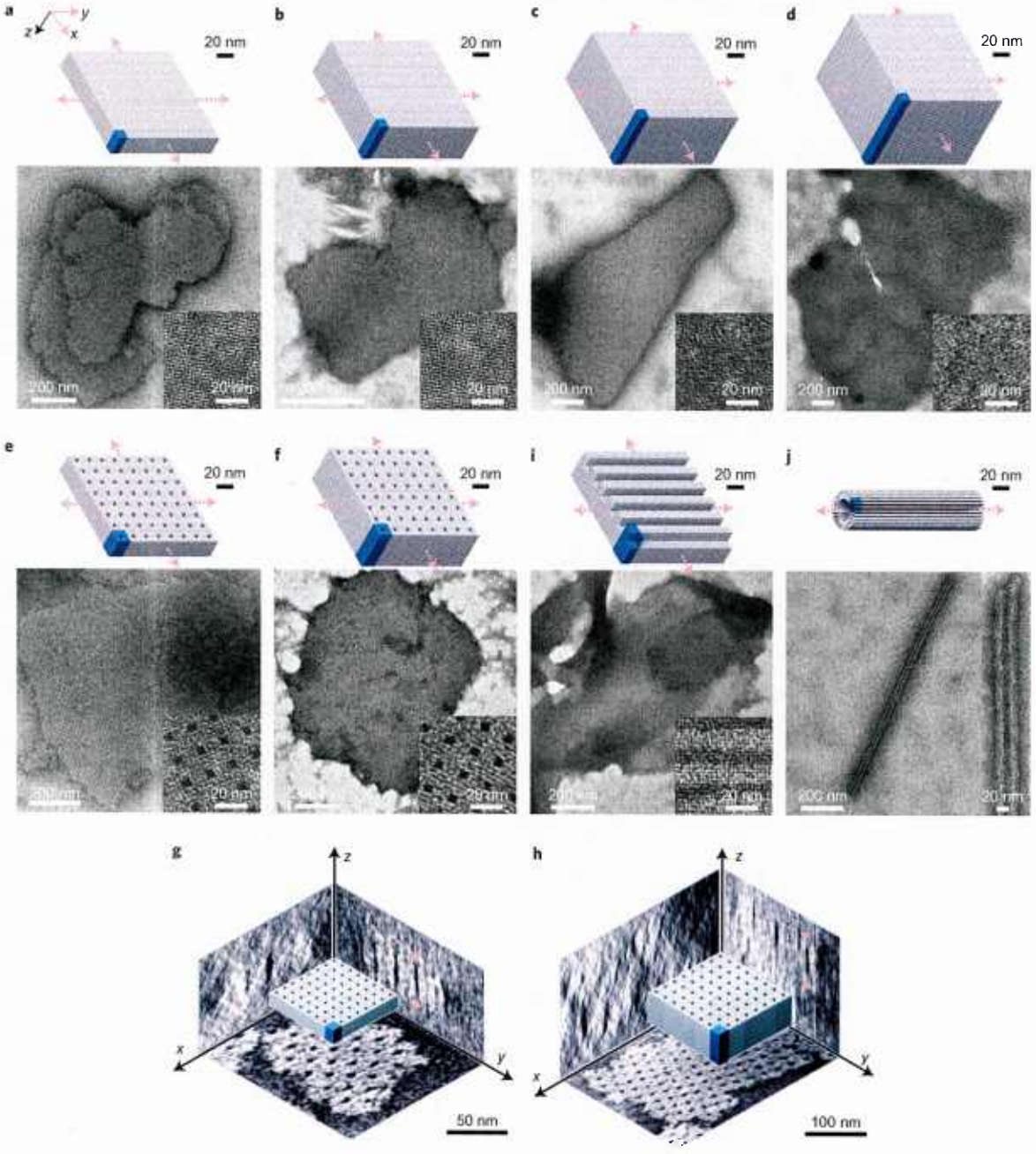

Figure 4 | Two-dimensional DNA forest XY-crystals. Cylinder models (top) and TEM images (bottom) for each crystal. **a**–**d**, Solid XY-crystals: 64B (**a**), 128B (**b**), 192B (**c**), 256B (**d**) solid XY-crystals designed from a 4H × 4H cuboid. **e**,**f**, XY-crystals with pores: 32 × 64B-pore XY-crystal with 2H × 2H × 64B parallel pores (**e**); 32H × 128B-pore XY-crystal with 2H × 2H × 128B parallel pores (**f**). **g**,**h**, Cryo-EM three-dimensional reconstruction images showing the three projections of the XY-32H × 64B-pore crystal (**g**) and the XY-32H × 128B-pore crystal (**h**). Arrows indicate positions of thickness measurements. **i**, A 96B XY-crystal with 4H × 32B parallel channels. **j**, A tube crystal formed by 32B helices with helical axis perpendicular to the tube axis. Unit cells of crystals are denoted by blue boxes. See Supplementary Figs 25–34 for more TEM images.

Annealing curves for both brick crystals depict a single, sharp transition peak, which occurred at ~40 °C for the ZX-crystal (Supplementary Fig. 38b,c) and 30 °C for the XY-crystal (Supplementary Fig. 39b,c), consistent with a non-hierarchical assembly process where individual component strands are directly incorporated into the lattices. See Supplementary Section 6.2 for more details.

Time-lapse analysis with gel electrophoresis and TEM. Time points before, at and after the transition temperature were sampled for both the above two ZX- and XY-crystals to confirm the lack of well-formed, discrete repeating units. Gel electrophoresis showed no intermediate band between the well and monomers (Supplementary Figs 38d and 39d), as expected. Although TEM imaging revealed some small, randomly sized and

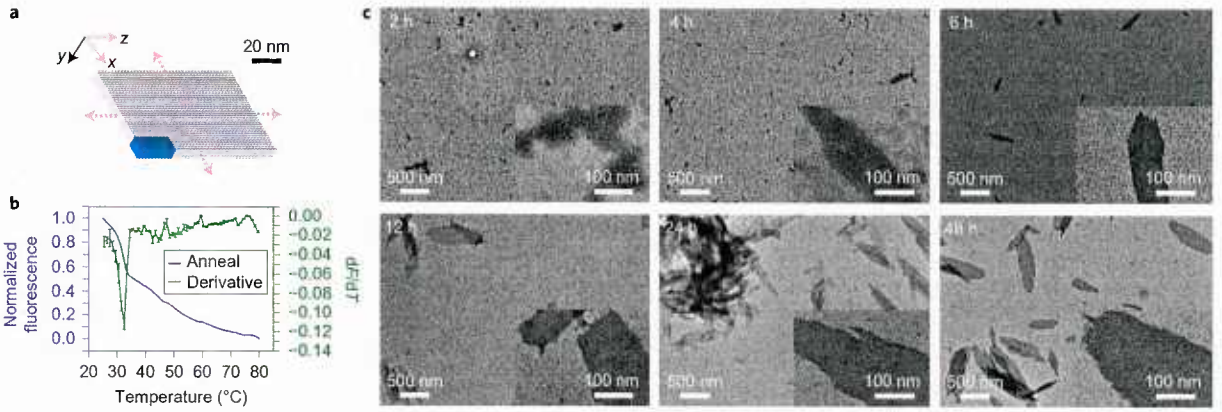

Figure 5 | Isothermal assembly of brick crystals. a, Cylinder model of a ZX-6H × 4H × 96B crystal. **b**, Annealing curve (blue) with the derivative of the fluorescence with respect to temperature (green) of the ZX-6H × 4H × 96B crystal. Annealing curves were obtained in the presence of 0.3 × SYBR Green I at 500 nM of each strand. Error bars represent standard error from the mean acquired from three measurements. **c**, TEM images of the ZX-6H × 4H × 96B crystal incubated at 33 °C for various durations. Samples were diluted four times before deposition on the TEM grids.

shaped clusters of strands, no uniformly sized and shape-defined structures were observed, supporting the designed non-hierarchical assembly mechanism (Supplementary Figs 38e and 39e). See Supplementary Section 6.2 for more details.

Isothermal assembly

The single transition temperature of the DNA brick crystallization suggests that these crystals should be able to assemble isothermally. We therefore assembled a ZX-6H × 4H × 96B-cuboid crystal isothermally at the observed annealing transition temperature of 33 °C (Fig. 5a, Supplementary Fig. 40c). Gel electrophoresis showed no discrete monomer band during annealing (Supplementary Fig. 40d). Time-lapse TEM images further supported the non-hierarchical assembly mechanism: structures around 100 nm in size appeared after 2 h and rapidly grew to micrometre-sized structures by 48 h (Fig. 5c). See Supplementary Section 6.3 for more details.

Yield and defect analysis

We used crystal deposition density and the strand depletion ratio to estimate the approximate yield of brick crystals. After four-times dilution, an isothermally assembled ZX-6H × 4H × 96B sample produced 0.23 structures per μm^2 on a TEM grid (Supplementary Fig. 41), while Förster resonance energy transfer analysis of dye-labelled ZX-6H × 6H × 64B sample suggested an 80% strand depletion ratio (Supplementary Fig. 42). Analysis of the pore morphology of XY-32H × 64B-pore TEM images indicated a 9% defect rate (Supplementary Fig. 43). See Supplementary Section 7 for more details.

Patterning gold nanoparticles

Gold nanoparticles have previously been arranged into discrete patterns[39,40,43] and single-layer periodic patterns[35] using DNA structures as templates. However, it remains challenging to form close-packed periodic patterns, especially multilayer patterns, of gold nanoparticles. This challenge is addressed here using DNA crystals. We constructed two close-packed gold-nanoparticle superstructures on DNA brick crystals: (1) parallel lines of gold particles arranged on a ZX-4H × 6H × 96B-channel crystal (Supplementary Fig. 44) spaced on average 2 nm apart (Fig. 6a,b), and (2) parallel gold-nanoparticle monolayers, with each particle spaced on average 1–2 nm apart, on an XY-4H × 4H × 64-cuboid (Fig. 6c–e). Aligning gold nanoparticles into micrometre-scale ordered arrays is required in diverse plasmonic applications. In particular, nanoparticle arrays with sub-2 nm face-to-face spacing are expected to exhibit strong plasmonic coupling[44]. See Supplementary Section 8 for more experimental details.

Discussion

Crystallization of increasingly large macromolecular complexes can be challenging. Traditionally, the process is hierarchical; that is, the complexes incorporate into the crystal as preformed monomeric units[26–32,34–38]. However, the homogeneity of complex monomers

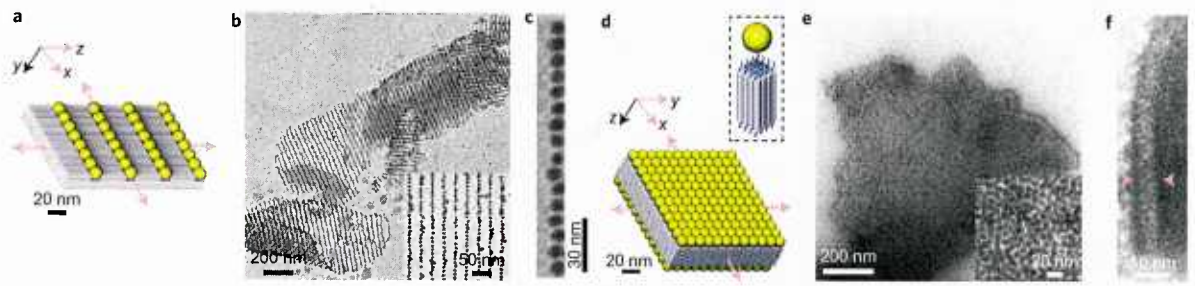

Figure 6 | Gold nanoparticles patterned using DNA brick crystals. a–c, Model (**a**) and TEM images (**b**,**c**) of parallel lines of 10 nm gold nanoparticles closely packed on a ZX-4H × 6H × 96-channel crystal. **c**, Zoomed-in TEM image of a single chain of gold nanoparticles. **d–f**, Model (**d**) and TEM images (**e**,**f**) of close-packed gold-nanoparticle monolayers formed on the top and bottom surfaces of an XY-4H × 4H × 64B-cuboid crystal. Inset of **d**: single-stranded poly-T extensions on each end of the helix and a 10 nm gold nanoparticle occupying a 4H × 4H surface. A crystal displays curvatures on the edge (**f**). Pink arrows indicate the curved positions where the two gold-nanoparticle monolayers can be seen.

is often difficult to ensure and the addition of a defective monomer can compromise the growth of a well-ordered crystal. Furthermore, the kinetics of joining large monomers can be slow because of their size, especially in the case when they repel each other due to like charges. Finally, effective crystallization is thought to require error correction that involves near-equilibrium incorporation and dissociation of monomers to erase defects on the path to the lowest energy state. Therefore, if the strength of the interaction between monomers is too strong, which is more likely for large structures, irreversible rather than reversible self-assembly may dominate, resulting in defective crystals.

In contrast, our DNA brick framework explores a non-hierarchical route to crystallization that achieves reversible assembly of rapidly diffusing subcomponents without sacrificing the complexity of the larger repeating unit in the final crystals. Using a modular strategy that utilizes standardized components—such as our DNA bricks—a repeating unit can contain thousands of base pairs, enabling the implementation of designs bearing intricate features. Although we define a repeating unit for ease of design, there is no difference between bricks within each repeating unit and those that connect the repeating units, so bricks can be added to or subtracted from the growing crystal one at a time. A corollary is that the boundary where one repeating unit begins and the next one ends is arbitrary.

Microscale two-dimensional DNA brick crystals with prescribed depths and three-dimensional nanoscale features provide a new platform for developing diverse applications. In biophysics, host–guest two-dimensional DNA crystals could facilitate cryo-EM imaging and three-dimensional reconstruction of protein structures[45]. Thicker two-dimensional crystals are more rigid and resistant to dynamic thermal fluctuations, providing better translational alignment of proteins; their three-dimensional cavities could potentially hold the guest molecule in a specific conformation, providing better orientational alignment within each unit cell. In photovoltaics, bottom-up self-assembly of nanomaterials, such as nanowires[46], provides a promising route to producing high-efficiency photovoltaic devices. DNA brick crystals may prove useful for self-assembling three-dimensional nanomaterials with nanometre precision, thus achieving enhanced cooperation effects and energy conversion efficiency for photovoltaic devices. In nanofabrication, these two-dimensional DNA crystals may serve as etching masks for fabricating diverse inorganic-materials-based devices and circuits, providing better shape programmability than current block-copolymer-based masks[5].

Methods

Design diagrams. DNA strand diagrams are provided in Supplementary Section 9 (Supplementary Figs 45–76).

Sample preparation. DNA strands were synthesized by Integrated DNA Technology (www.idtdna.com). To assemble the structures, unpurified DNA strands were mixed in an equimolar stoichiometric ratio from a 100 μM stock in 0.5 × Tris/EDTA buffer (5 mM Tris, pH 7.9, 1 mM EDTA) supplemented with 40 mM $MgCl_2$. For Z-crystals and ZX-crystals, the final concentration of each strand was adjusted to roughly 200 nM. For X-crystals and XY-crystals, the highest possible concentration (no addition of extra water) was used for annealing.

Annealing ramps and isothermal assembly. The strand mixture was annealed in a PCR thermo cycler using a fast linear cooling step from 80 °C to 60 °C over 1 h, then a 72 h or 168 h linear cooling ramp from 60 °C to 25 °C. The annealing ramps were named according to the length of the second cooling step (as 72 h annealing or 168 h annealing). Most ZX-crystals were folded using 72 h annealing, except the ZX-96H × 64B-cross-tunnels, which used 168 h annealing. All XY-crystals were folded with 168 h annealing. For isothermal assembly of DNA crystals, the sample solution was incubated at 33 °C for up to 48 h.

DNA modification of 10 nm gold nanoparticles. Conjugation of thiolated DNA onto 10 nm gold nanoparticles was achieved following a previously reported protocol[47]. In a typical experiment, 20 μl 2.5 μM phosphine-coated 10 nm gold nanoparticles were mixed with 0.5 μl 2 M $NaNO_3$ and 0.65 μl 100 μM thiolated DNA in 0.25 × Tris/borate/EDTA (TBE) buffer. The reaction solution was incubated at room temperature for 36 h in the dark. After that, the reaction solution was loaded into 1% agarose gel containing 0.5 × TBE buffer. The electrophoresis was running at 95 V for 1 h in a gel box on an ice-water bath. The purple band was recovered by pestle crushing, followed by centrifugation for 3 min at 10,000 r.p.m. at room temperature using 'Freeze' N Squeeze' DNA Gel Extraction spin columns (Bio-Rad). Recovered DNA-modified gold nanoparticles were stored at 4 °C in the dark for further use. The sequence for the thiolated DNA was 5′-AAAAAAAAAA-/3ThioMC3-D/.

Gold-nanoparticle decoration of DNA crystals. To 15 μl 400 mM NaCl solution, 0.8 μl (ZX-4H × 6H × 96B-channel crystal) or 0.6 μl (XY-4H × 4H × 64B-cuboid crystal) DNA samples were added. Then, 0.2 μl 95 nM 10 nm gold nanoparticles were introduced. After pipetting 50 times, the reaction mixture was left at room temperature for 3 h in the dark.

TEM imaging. For imaging, 2.5 μl annealed sample was adsorbed for 2 min onto glow-discharged, carbon-coated TEM grids. The grids were then stained for 10 s using a 2% aqueous uranyl formate solution containing 25 mM NaOH. Imaging was performed using a JEOL JEM-1400 TEM operating at 80 kV.

Cryo-EM imaging. A 5 μl droplet of the crystal sample was added onto the positively charged carbon grids, blotted for 5.5 s, and plunge-frozen in liquid ethane using a Vitrobot (FEI). Grids were then loaded into a Titan Krios TEM (FEI), which was operated at 300 kV with nominal −3 μm defocus using a dose of 1.5 e $Å^{-2}$. The specimen was tilted in <2° increments over a total angular range of ±60°. All images were obtained using automated data-acquisition software. Three-dimensional reconstructions from the above tilt series were carried out with the weighted back-projection method, and further analysis of tomograms was done using IMOD software[48].

Annealing and melting curves. Strands (500 nM) were folded (following the annealing ramp protocol described above) in the presence of 0.3 × SYBR Green I using the Eppendorf Mastercycler realplex 4 PCR. Samples were read once during the first cooling step and four times during the second cooling step. Following annealing, the same samples were melted at a rate of 0.2 °C min^{-1}. Samples (9 μl) were removed during annealing or melting for TEM and gel electrophoresis analysis.

Agarose gel electrophoresis. Annealed samples were subjected to 1.5% or 2% native agarose gel electrophoresis for 2 h (gel prepared in 0.5 × TBE buffer supplemented with 10 mM $MgCl_2$ and 0.005% (vol/vol) EtBr) or 1 × SYBR Safe in an ice-water bath.

AFM imaging. AFM images were obtained using a MultiMode VIII SPM (Bruker) equipped with a liquid cell. A 2 μl volume of sample was placed onto the surface of highly ordered pyrolytic graphite, which was pretreated with ultraviolet-ozone for 30 s. The 50 μl of Tris/acetate/EDTA buffer (12.5 mM Mg^{2+}, 5 mM Ni^{+}) was added into the liquid cell, and images were collected using silicon nitride cantilevers (Olympus).

Received 26 May 2014; accepted 9 September 2014; published online 19 October 2014

References

1. Melosh, N. A. *et al.* Ultrahigh-density nanowire lattices and circuits. *Science* **300,** 112–115 (2003).
2. Qi, M. *et al.* A three-dimensional optical photonic crystal with designed point defects. *Nature* **429,** 538–542 (2004).
3. Liu, N., Hentschel, M., Weiss, T., Alivisatos, A. P. & Giessen, H. Three-dimensional plasmon rulers. *Science* **332,** 1407–1410 (2011).
4. Tang, C. B., Lennon, E. M., Fredrickson, G. H., Kramer, E. J. & Hawker, C. J. Evolution of block copolymer lithography to highly ordered square arrays. *Science* **322,** 429–432 (2008).
5. Tavakkoli, K. G. A. *et al.* Templating three-dimensional self-assembled structures in bilayer block copolymer films. *Science* **336,** 1294–1298 (2012).
6. Liu, N. *et al.* Three-dimensional photonic metamaterials at optical frequencies. *Nature Mater.* **7,** 31–37 (2008).
7. Edward, E. W., Montague, M. F., Solak, H. H., Hawker, C. J. & Nealey, P. F. Precise control over molecular dimensions of block-copolymer domains using the interfacial energy of chemically nanopatterned substrates. *Adv. Mater.* **16,** 1315–1319 (2004).
8. Kim, S. O. *et al.* Novel complex nanostructure from directed assembly of block copolymers on incommensurate surface patterns. *Adv. Mater.* **19,** 3271–3275 (2007).
9. Seeman, N. C. Nucleic acid junctions and lattices. *J. Theor. Biol.* **99,** 237–247 (1982).
10. Chen, J. & Seeman, N. C. The synthesis from DNA of a molecule with the connectivity of a cube. *Nature* **350,** 631–633 (1991).
11. Fu, T. J. & Seeman, N. C. DNA double-crossover molecules. *Biochemistry* **32,** 3211–3220 (1993).
12. Shih, W. M., Quispe, J. D. & Joyce, G. F. A 1.7-kilobase single-stranded DNA that folds into a nanoscale octahedron. *Nature* **427,** 618–621 (2004).
13. Rothemund, P. W. K. Folding DNA to create nanoscale shapes and patterns. *Nature* **440,** 297–302 (2006).

14. He, Y. *et al.* Hierarchical self-assembly of DNA into symmetric supramolecular polyhedra. *Nature* **452,** 198–201 (2008).
15. Andersen, E. S. *et al.* Self-assembly of a nanoscale DNA box with a controllable lid. *Nature* **459,** 73–76 (2009).
16. Douglas, S. M. *et al.* Self-assembly of DNA into nanoscale three-dimensional shapes. *Nature* **459,** 414–418 (2009).
17. Dietz, H., Douglas, S. M. & Shih, W. M. Folding DNA into twisted and curved nanoscale shapes. *Science* **325,** 725–730 (2009).
18. Woo, S. & Rothemund, P. W. K. Programmable molecular recognition based on the geometry of DNA nanostructures. *Nature Chem.* **3,** 620–627 (2011).
19. Han, D. *et al.* DNA origami with complex curvatures in three-dimensional space. *Science* **332,** 342–346 (2011).
20. Sobczak, J-P. J., Martin, T. G., Gerling, T. & Dietz, H. Rapid folding of DNA into nanoscale shapes at constant temperature. *Science* **338,** 1458–1461 (2012).
21. Wei, B., Dai, M. & Yin, P. Complex shapes self-assembled from single-stranded DNA tiles. *Nature* **485,** 623–626 (2012).
22. Ke, Y., Ong, L. L., Shih, W. M. & Yin, P. Three-dimensional structures self-assembled from DNA bricks. *Science* **338,** 1177–1183 (2012).
23. Han, D. *et al.* DNA gridiron nanostructures based on four-arm junctions. *Science* **339,** 1412–1415 (2013).
24. Wei, B. *et al.* Design space for complex DNA structures. *J. Am. Chem. Soc.* **135,** 18080–18088 (2013).
25. Iinuma, R. *et al.* Polyhedra self-assembled from DNA tripods and characterized with 3D DNA-PAINT. *Science* **344,** 65–69 (2014).
26. Winfree, E., Liu, F., Wenzler, L. A. & Seeman, N. C. Design and self-assembly of two-dimensional DNA crystals. *Nature* **394,** 539–544 (1998).
27. Yan, H., Park, S. H., Finkelstein, G., Reif, J. H. & LaBean, T. H. DNA-templated self-assembly of protein arrays and highly conductive nanowires. *Science* **301,** 1882–1884 (2003).
28. Liu, D., Wang, M., Deng, Z., Walulu, R. & Mao, C. Tensegrity: construction of rigid DNA triangles with flexible four-arm DNA junctions. *J. Am. Chem. Soc.* **126,** 2324–2325 (2004).
29. Rothemund, P. W. K., Papadakis, N. & Winfree, E. Algorithmic self-assembly of DNA Sierpinski triangles. *PLoS Biol.* **2,** 2041–2053 (2004).
30. He, Y., Chen, Y., Liu, H., Ribbe, A. E. & Mao, C. Self-assembly of hexagonal DNA two-dimensional (2D) arrays. *J. Am. Chem. Soc.* **127,** 12202–12203 (2005).
31. Malo, J. *et al.* Engineering a 2D protein–DNA crystal. *Angew. Chem. Int. Ed.* **44,** 3057–3061 (2005).
32. Ke, Y., Liu, Y., Zhang, J. P. & Yan, H. A study of DNA tube formation mechanisms using 4-, 8-, and 12-helix DNA nanostructures. *J. Am. Chem. Soc.* **128,** 4414–4421 (2006).
33. Yin, P. *et al.* Programming DNA tube circumferences. *Science* **321,** 824–826 (2008).
34. Zheng, J. P. *et al.* From molecular to macroscopic via the rational design of a self-assembled 3D DNA crystal. *Nature* **461,** 74–77 (2009).
35. Sharma, J. *et al.* Control of self-assembly of DNA tubules through integration of gold nanoparticles. *Science* **323,** 112–116 (2009).
36. Liu, W., Zhong, H. & Seeman, N. C. Crystalline two dimensional DNA origami arrays. *Angew. Chem. Int. Ed.* **50,** 264–267 (2011).
37. Majumder, U., Rangnekar, A., Gothelf, K. V., Reif, J. H. & LaBean, T. H. Design and construction of double-decker tile as a route to three-dimensional periodic assembly of DNA. *J. Am. Chem. Soc.* **133,** 3843–3845 (2011).
38. Wang, T., Schiffels, D., Cuesta, S. M., Fygenson, D. K. & Seeman, N. C. Design and characterization of 1D nanotubes and 2D periodic arrays self-assembled from DNA multi-helix bundles. *J. Am. Chem. Soc.* **134,** 1606–1616 (2012).
39. Kuzyk, A. *et al.* DNA-based self-assembly of chiral plasmonic nanostructures with tailored optical response. *Nature* **483,** 311–314 (2012).
40. Acuna, G. P. *et al.* Fluorescence enhancement at docking sites of DNA-directed self-assembled nanoantennas. *Science* **338,** 506–510 (2012).
41. Park, S. *et al.* Macroscopic 10-terabit per square-inch arrays from block copolymers with lateral order. *Science* **323,** 1030–1033 (2009).
42. Ke, Y. *et al.* Multilayer DNA origami packed on a square lattice. *J. Am. Chem. Soc.* **131,** 15903–15908 (2009).
43. Aldaye, F. A. & Sleiman, H. F. Sequential self-assembly of a DNA hexagon as a template for the organization of gold nanoparticles. *Angew. Chem. Int. Ed.* **45,** 2204–2209 (2006).
44. Tan, S. F. *et al.* Quantum plasmon resonances controlled by molecular tunnel junctions. *Science* **343,** 1496–1499 (2014).
45. Selmi, D. N. *et al.* DNA-templated protein arrays for single-molecule imaging. *Nano Lett.* **11,** 657–660 (2011).
46. Dang, X. N. *et al.* Virus-templated self-assembled single-walled carbon nanotubes for highly efficient electron collection in photovoltaic devices. *Nature Nanotech.* **6,** 377–384 (2011).
47. Sharma, J. *et al.* Toward reliable gold nanoparticle patterning on self-assembled DNA nanoscaffold. *J. Am. Chem. Soc.* **130,** 7820–7821 (2008).
48. Kremer, J. R., Mastronarde, D. N. & McIntosh, J. R. Computer visualization of three dimensional image data using IMOD. *J. Struct. Biol.* **116,** 71–76 (1996).

Acknowledgements

This work is supported by ONR Young Investigator Program Award N000141110914, ONR Grants N000141010827, N000141410610 and N000141310593, ARO Grant W911NF1210238, NSF CAREER Award CCF1054898, NSF Expedition in Computing Award CCF1317291, NSF Grants CCF1162459, CMMI1333215, CMMI1334109 and CMMI1344915, NIH Director's New Innovator Award 1DP2OD007292 and a Wyss Institute Faculty Startup Fund to P.Y., and by a Wyss Institute Faculty Grant, ARO MURI grant W911NF1210420, ONR Grants N000014091118 and N000141010241 and NIH Director's New Innovator Award 1DP2OD004641 to W.M.S. L.L.O. is supported by an NSF Graduate Research Fellowship. J.S. acknowledges AUFF funding from Aarhus University and the Niels Bohr Foundation from The Royal Danish Academy of Science. M.D. acknowledges financial support from the Danish National Research Foundation and the Villum Foundation.

Author contributions

Y.K., L.L.O. and W.S. made equal contributions to this work. Y.K. conceived the project, designed and performed the experiments, analysed the data and wrote the paper. L.L.O. and W.S. designed and performed the experiments, analysed the data and wrote the paper. J.S. and M.D. performed the cryo-EM and AFM experiments, analysed the data and wrote the paper. W.M.S discussed the results and wrote the paper. P.Y. conceived, designed and supervised the study, interpreted the data and wrote the paper.

Additional information

Supplementary information is available in the online version of the paper. Reprints and permissions information is available online at www.nature.com/reprints. Correspondence and requests for materials should be addressed to P.Y. and Y.K.

Competing financial interests

A provisional US patent application based on the work described in this manuscript has been filed.

11.1.4 Diverse motifs for complex 2D shapes

JACS
JOURNAL OF THE AMERICAN CHEMICAL SOCIETY

Article

pubs.acs.org/JACS

Design Space for Complex DNA Structures

Bryan Wei,[†,‡] Mingjie Dai,[†,§] Cameron Myhrvold,[†,‡] Yonggang Ke,[†,⊥] Ralf Jungmann,[†,‡] and Peng Yin*[,†,‡]

[†]Wyss Institute for Biologically Inspired Engineering, Harvard Medical School, Boston, Massachusetts 02115, United States

[‡]Department of Systems Biology, Harvard University, Boston, Massachusetts 02115, United States

[§]Program in Biophysics, Harvard University, Boston, Massachusetts 02115, United States

[⊥]Dana Farber Cancer Institute, Boston, Massachusetts 02115, United States

Supporting Information

ABSTRACT: Nucleic acids have emerged as effective materials for assembling complex nanoscale structures. To tailor the structures to function optimally for particular applications, a broad structural design space is desired. Despite the many discrete and extended structures demonstrated in the past few decades, the design space remains to be fully explored. In particular, the complex finite-sized structures produced to date have been typically based on a small number of structural motifs. Here, we perform a comprehensive study of the design space for complex DNA structures, using more than 30 distinct motifs derived from single-stranded tiles. These motifs self-assemble to form structures with diverse strand weaving patterns and specific geometric properties, such as curvature and twist. We performed a systematic study to control and characterize the curvature of the structures, and constructed a flat structure with a corrugated strand pattern. The work here reveals the broadness of the design space for complex DNA nanostructures.

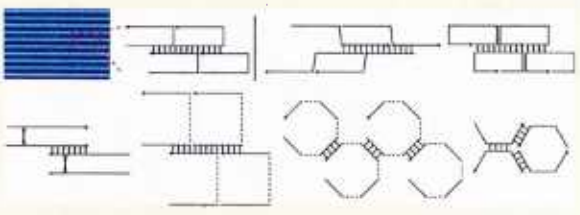

INTRODUCTION

Self-assembly of nucleic acids (DNA and RNA) provides a powerful approach for constructing sophisticated synthetic molecular structures and devices. By encoding sequence complementarity into component DNA strands, prescribed structures can be assembled under the appropriate formation conditions.[1] After three decades of development, the complexity of synthetic DNA structures has grown from simple branched junctions[1] formed from just a few strands to complex 2D and 3D objects composed of hundreds or even thousands of distinct strands.[2−22] Moreover, researchers have demonstrated the construction of dynamic systems, including switches,[23] walkers,[24−26] circuits,[25,27,28] and triggered assembly systems.[25] Additionally, as diverse functional molecules can be modified onto specific sites of DNA structures,[19,29−32] DNA nanotechnology has enabled applications such as nanofabrication,[33] protein structure determination,[34] fluorescent bioimaging,[31,32] single molecule biophysics,[35] biosynthetic and cell-signaling pathways modulation.[19,36]

Two methods that are particularly effective for assembling discrete mega-Dalton structures with arbitrarily prescribed shapes are DNA origami,[10,14−18,22] and single-stranded tiles (SSTs)[20] and bricks.[21] In DNA origami, hundreds of short, synthetic DNA strands fold a long scaffold (typically the M13 viral genome) into a desired structure.[10,16−18,22] More recently, researchers have demonstrated finite complex 2D and 3D shapes self-assembled from hundreds to thousands of distinct single-stranded tiles and bricks.[20,21]

Unlike DNA origami, no scaffold strand is required for SST structure, which are composed entirely of short synthetic DNA strands. The elimination of the scaffold strand makes SSTs effective tools for systematic and rapid study of the geometry, sequence, and structural design space for complex DNA structures. First, as SST-based structures have a modular architecture—each strand can be included, removed, or replaced independently—SSTs enable rapid prototyping of the shape space (more than 100 distinct, sophisticated 2D[20] and 3D[21] shapes were experimentally demonstrated). Second, as the strand sequences are no longer restricted to be derived from the biogenic scaffold sequence, SSTs enable rapid probing of the sequence space (structures were formed from both specifically designed and randomly generated sequences[20,21]). Lastly and importantly, by removing the restriction of scaffold routing through the shape and using diverse structural motifs derived from the canonical SST motif,[20] we will demonstrate here a systematic study of the structural design space for forming complex DNA nanostructures.

To tailor the structures to function optimally for particular applications, a broad design space for DNA nanostructures is desired. Despite the many discrete and extended structures demonstrated in the past few decades, the structural design space has yet to be fully explored. In particular, complex, finite-sized structures formed by origami and SST are primarily based on double- or single-stranded versions of the basic DAE (antiparallel double-crossover molecules with an even number of half-helical turns) motif[3] and their derivatives. Beyond origami and SST, however, a richer motif space has been

Received: June 20, 2013

   dx.doi.org/10.1021/ja4062294 | J. Am. Chem. Soc. XXXX, XXX, XXX−XXX

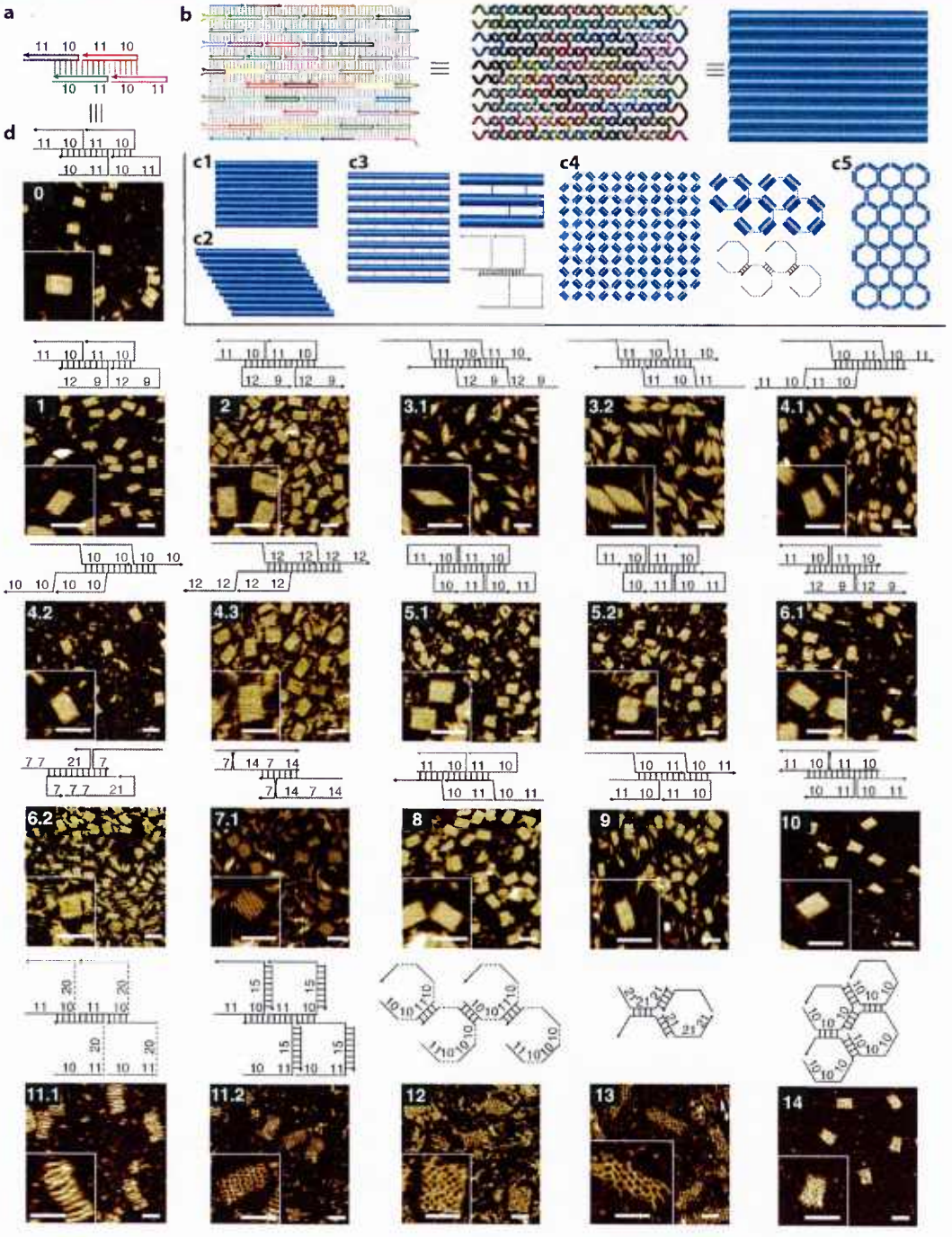

Figure 1. Motif designs and AFM imaging. A representative subset of the motifs studied is shown here; see SI, section SI1.3 for the full repertoire. (a) A 2×2 unit (containing four SSTs) of the canonical motif (motif 0). Colors distinguish sequences. (b) Strand diagram (left), helix diagram (middle), and cylinder diagram (right) of a 10 helix × 11 turn (10H×11T) structure formed from motif 0. (c) Cylinder diagrams for structures formed from different motifs; a cylinder depicts a DNA duplex and a line depicts a single-strand DNA segment: (c1) structures from motifs 0–2 and 4–10 have a rectangle shape containing parallel-arranged double-helices; (c2) structures from motifs 3.1 and 3.2 have a parallelogram shape containing parallel-arranged double-helices; (c3) structures from motif 11 have a rectangle shape containing parallel-arranged double-helices connected by single-stranded linkers; (c4) structures from motif 12 have a rectangle shape with a "fishnet" pattern (composed of short duplex segments connected by single-stranded linkers); (c5) structures from motifs 13 and 14 have a rectangle shape with a honeycomb pattern composed of short DNA duplex segments. (d) Strand diagrams and the corresponding AFM images for structures formed from different motifs. Top panel: a 2×2 repeating unit. Numbers indicate domain or linker lengths in nucleotide. Bottom panel: AFM image. Inset shows a magnified view. Scale bars, 50 nm. See SI, section SI1.5 for the measured dimensions and measured gel yields (5–44%).

dx.doi.org/10.1021/ja4062294 | J. Am. Chem. Soc. XXXX, XXX, XXX–XXX

explored for forming relatively simple discrete and extended structures. This has been achieved using various structural motifs, such as diverse double-crossover motifs,[3,4] PX-based structures,[7,37] structures with flexible linker joints,[11,14,15,29,38] wire-frame structures,[1,2,7,8,11,38−41] and metal−DNA junctions.[42]

The next challenge is to develop a versatile method for creating complex, discrete-sized DNA nanostructures with diverse structural motifs, strand weaving patterns, and desired structural properties. Building on the richness of the previous structural motifs for building DNA nanostructures, and taking advantage of the designability and flexibility of SST-based assembly, we performed a comprehensive study of the design space for constructing complex, finite-sized DNA structures. We tested more than 30 distinct motifs derived from SSTs.[20] Most motifs self-assembled to form structures with diverse strand-weaving patterns and specific geometric properties, such as curvature and twist. Moreover, we performed a systematic study to control and characterize the curvature of the structures, and constructed a flat structure with a corrugated strand pattern. Our success in assembling a myriad of different motifs demonstrates the robustness and versatility of the SST approach. More generally, it reveals the broadness of the design space for constructing complex DNA nanostructures.

■ RESULTS AND DISCUSSIONS

Motif Design Parameters. We began our study for the structural design space with the canonical U-shaped SST motif (motif 0, Figure 1a,b) reported in our previous work.[12,20] This 42-base SST motif has four consecutive domains (each measuring 10 or 11 nt).[12,20] By pairing up complementary domains, individual tiles self-assemble into DNA lattices composed of parallel-arranged double-helices connected by periodic single-stranded crossover linkages. Note that the linkage is merely a phosphate in the DNA backbone. In the diagrams in Figure 1, the linkage is artificially stretched to more clearly show the strand-weaving pattern. Starting with this simple U-shaped motif, we systematically explored important parameters for motif design. Below, we first give an overview of some important parameters and their putative effects on the geometrical, mechanical, and thermodynamic properties of the structures. In the next section, we describe the motif design and its implementation, in detail.

Domain Length. Motif 0 contains 10 and 11 nt domains. For most of the motifs explored in our study (including motif 0), we tested several different domain lengths. Changing domain length could affect (1) the geometrical properties of the assembled structure, such as curvature[17,18] and twist;[17,43,44] (2) thermodynamic properties, such as formation and melting temperature; and (3) mechanical properties, such as structural rigidity and internal strain.[17,45] Domain length is thus a basic design variable that we explored extensively in our study. Changing domain length also directly affects the crossover patterns described below.

Crossover Type. Structures formed from motif 0 possess single-stranded, antiparallel crossovers. In our study, we explored four combinations of single-[12,46] vs double-stranded crossovers, with parallel vs antiparallel orientations.[3] Here we use "parallel" (or "antiparallel") to describe crossovers in which the orientation of the strand forming the crossover is the same (or opposite) on both sides of the crossover.[3] The crossover type directly affects the weaving patterns of the strands and the geometrical properties of the structure, which may in turn affect their mechanical and thermodynamic properties. For example, geometrically, the parallel or antiparallel crossovers result in structures composed of double-helices that are connected in a parallel or antiparallel fashion, referred to as *parallel-connected double-helices* or *antiparallel-connected double-helices*. Note that we also use the term *parallel-arranged double-helices* to refer to the double-helices connected by either parallel or antiparallel crossovers. In the antiparallel crossover-based structure, all the crossovers display the major grooves on the same side of the structure[47] and as a result, induce an accumulated curvature for the structure. In contrast, the parallel crossover-based structure avoids such asymmetry and curvature. In the antiparallel crossover-based structure, the major groove of one double-helix faces the minor groove of an adjacent double-helix;[3] in contrast, the parallel crossover-based structure has major−major and minor−minor groove pairings. Hence, the former should have less strain and more thermal stability.[3] Compared with double-stranded crossover, single-stranded crossover-based structures may be structurally less rigid, mechanically less strained, and in turn, thermodynamically more stable.

Crossover Pattern. Motif 0 has a 21 nt crossover spacing for crossovers between the two adjacent double-helices; along one particular double-helix, a crossover appears every 10 or 11 nt. We systematically changed crossover patterns. Crossover patterns could also lead to a combination of geometric, thermodynamic, and mechanical effects. Geometrically, the curvature of the overall structure (as determined by the dihedral angle formed between three adjacent double-helices) can be tuned by translating all crossover points along the direction parallel to the helical axis while preserving the spacing;[17,18] twist, on the other hand, depends on the crossover spacing.[17,43,44] Mechanically, strain could accumulate in twisted and/or curved structures.[17,43,44] Such mechanical stress in turn could affect the thermodynamic properties of the structure.

Symmetry. By adjusting domain length, crossover type, and crossover patterns, we can design structures with more symmetric strand weaving patterns, such as corrugated patterns.[29] Such symmetry can help to eliminate curvature in the structure.

Linkers. Structures formed from motif 0 are composed of compact parallel-arranged double-helices connected by periodic single-stranded crossovers (composed of a single phosphate in the DNA backbone). In our study, we included single-stranded linkers of varying lengths between helices and between binding domains. This results in structures that are geometrically and structurally more flexible. Inclusion of linkers should also help to relieve the electrostatic repulsion between adjacent double-helices, hence stabilizing the structure.

Structures Formed from Diverse Motifs. *Overview.* By systematically exploring the above as well as some other design parameters, we tested a total of 36 different motifs, 32 of which formed desired structures (an 89% success rate). A representative subset of all successful motif designs is shown in Figure 1 (see SI, section SI1.3 for the full repertoire). Different morphologies were presented, including compact rectangle and parallelogram of packed DNA duplexes (Figure 1c1,c2), rectangles of spaced DNA duplexes (Figure 1c3), and rectangles of square and hexagonal lattices (Figure 1c4,c5).

Structure Assembly and Characterization. The DNA structures were assembled with unpurified DNA strands with randomly designed sequences, and were mixed at roughly equimolar without careful adjustment of stoichiometry. After single-step (one-pot) annealing from 90 to 25 °C over 17 h in

dx.doi.org/10.1021/ja4062294 | J. Am. Chem. Soc. XXXX, XXX, XXX−XXX

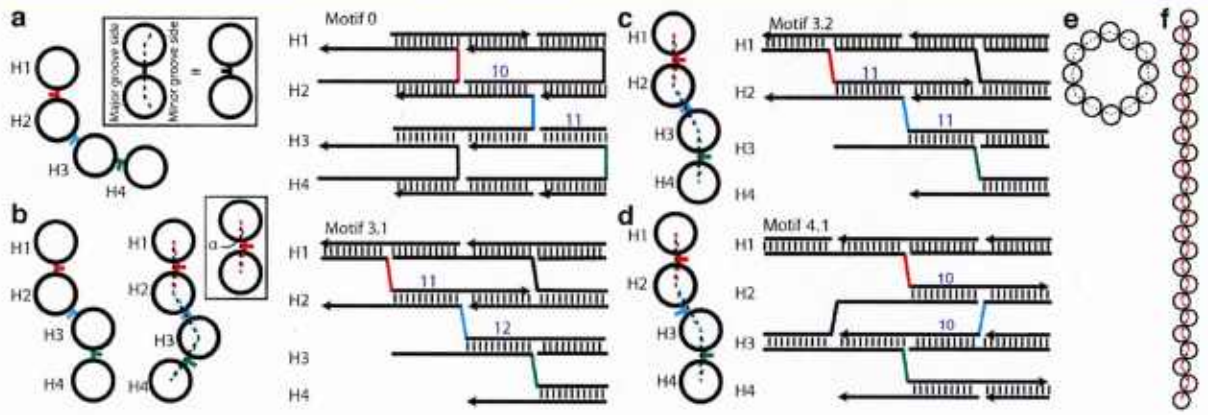

Figure 2. Curvature models. (a) Curvature model (left) and corresponding strand diagram (right) of motif 0. Inset depicts the major groove side vs minor groove side. (b) Curvature model of motif 3.1 without (left) and with (right) offset angle α. (c) Curvature model of motif 3.2 with offset angle α. (d) Curvature model of motif 4.1. In this corrugated design, the offset angle α is canceled out so the overall curvature is independent of α. (e,f) Predicted cross-sectional views of 24-helix structures formed from motifs 0 and 4.1, respectively. See SI, section SI2.1 and Figure SI39 for modeling and calculation details.

0.5×TE buffer supplemented with 15 mM Mg^{2+} (see SI, section SI1.2 for the effects of buffer ion strength and annealing time on the assembly yields), the solution was subjected to 2% native agarose gel electrophoresis and produced one dominant product band, the ratio between the fluorescence intensity of the product band and that of the entire lane was used to approximate the yield of structure formation, which was measured to range from 5% to 44% (Figure SI1).

Annealed samples were subjected to atomic force microscopy (AFM) imaging and showed the expected morphology and dimensions. For samples with relatively low yields (motifs 4.6, 7.2, and 10), structures were gel-purified from the product bands on a 2% agarose gel prior to AFM imaging. See SI, section SI1.3, for larger AFM images and section SI1.5 for measurements of the sizes of the structures.

Changing Domain Lengths: Motif 1. First, we adjusted the domain lengths of two adjacent domains within a double-helix from 10 or 11 nt to 9–12 nt (motif 1). This changes the distance between adjacent crossovers along the same double-helix, resulting in the relative change of the dihedral angle formed by the three adjacent double-helices by 34°. This motif was later used to build a larger structure for curvature study.

Bidirectional Motifs: Motif 2. Next, we flipped the orientation of the U-shaped motifs in every other row, resulting in a structure composed of U-shaped SSTs with alternating orientations along adjacent rows. Such a modification makes the overall structure more symmetric along the helical direction.

Z-Shaped Motifs: Motifs 3.1 and 3.2. Structures formed from U-shaped motifs have antiparallel crossovers. We then designed structures with two Z-shaped motifs and obtained structures containing parallel crossovers. Such parallel crossover weaving patterns are expected to cancel out the curvature resulting from the asymmetric arrangement of major and minor grooves at the crossovers (see Curvature section for details) and was used for curvature study.

Corrugated Structures: Motif 4.1. We further changed the orientation of every other row in the Z-shaped motif to form a symmetric structure with a corrugated[29] strand pattern. This corrugation should in principle eliminate any curvature and result in a perfectly flat structure. This structure was used in the curvature study below.

Twisted Structures: Motifs 4.2–4.6. Based on the corrugated structure from motif 4.1, we changed the crossover spacing from the canonical two full helical turns (i.e., 21 nt) to 20, 22, 24, 26, 18 nt using motifs 4.2–4.6, respectively. This introduced a significant internal twist to the structure.[17,43,44] The structures with 20 nt crossover spacing (motif 4.2) were used for the twist study and significant twist was observed (see below). The yield of the structure with the shortest spacing (motif 4.6) was relatively low (26%) compared to that of the rest of the group (33–42%).

Double-Stranded Crossovers: Motifs 5.x, 6.x, and 7.x. Structures formed from motifs 0–4 contain single-stranded, half crossovers between adjacent double-helices. We next tested structures with double-stranded, full crossovers. We first tried to shift the nicking points in the original U-shaped motif to be positioned away from the crossovers (motifs 5.1–5.3). Then we continued to design H-shaped motifs by increasing crossover spacing from two helical turns to four helical turns (motifs 6.1–6.3). We also designed X-shaped motifs that were derived Z-shaped motifs (motifs 7.1 and 7.2). Structures with full crossovers have nicks on the duplex (rather than at the crossovers), which could permit the use of enzymatic ligation to covalently join the two ends of an SST molecule to form a ring.

Hybrid Motifs: Motifs 8–10. We combined different motifs to form hybrid structures with both U-shaped and Z-shaped rows (motifs 8 and 9) or with H-shaped and X-shaped rows (motif 10).

Linkers at Crossovers: Motifs 11.1–11.4. At the crossovers, we placed single-stranded DNA linkers with varying lengths (20 nt, 10 nt, and 2 nt for motif 11.1, 11.3, and 11.4 respectively). We also tested to form structures with 15 bp double-stranded linkers (motif 11.2). In addition to the 10H×11T structure, we also used motif 11.1 to form a 24H×29T structure (Figure SI29), demonstrating the scalability of structures formed from linker motifs.

Linkers between Neighboring Domains: Motif 12. We formed structures from a motif with linkers between every pair of neighboring domains (motif 12). In the resulting structures, individual 10 or 11 bp double-stranded DNA duplexes were

dx.doi.org/10.1021/ja4062294 | J. Am. Chem. Soc. XXXX, XXX, XXX–XXX

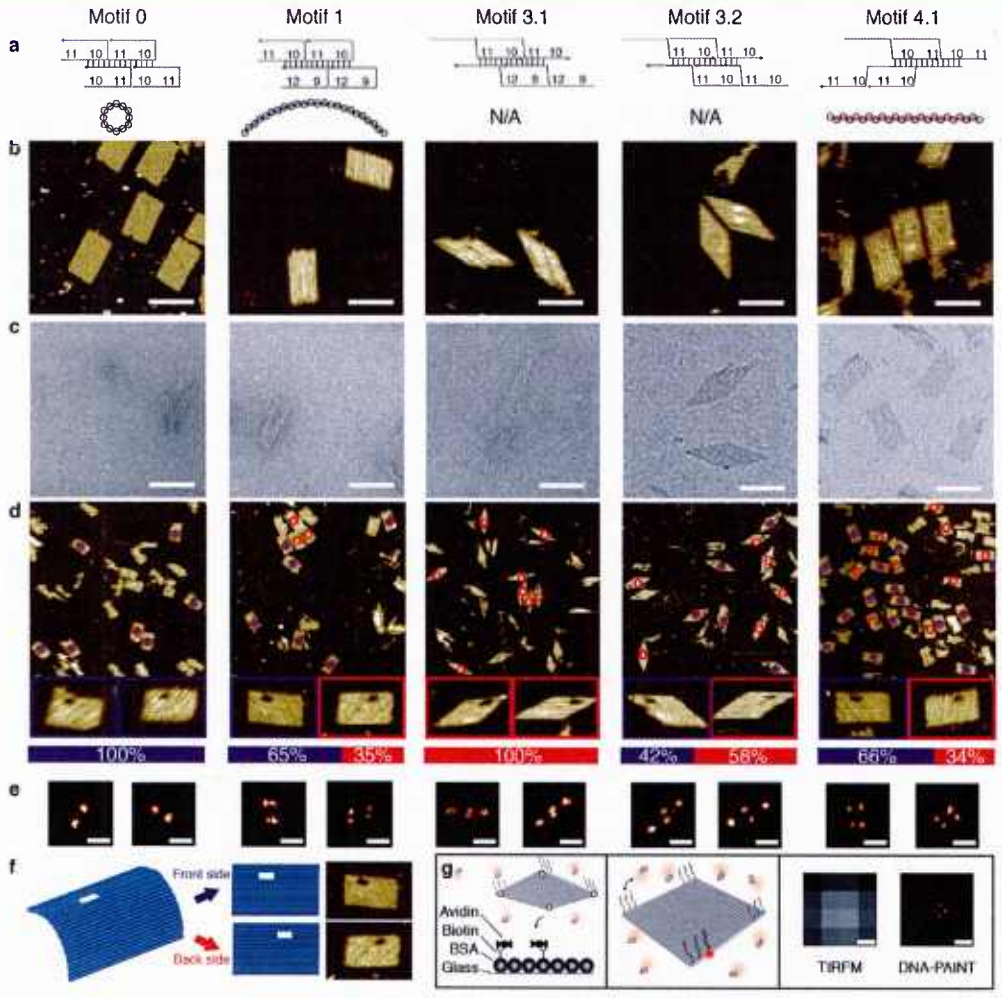

Figure 3. Curvature characterization. See SI, section SI2.1 for curvature calculation and modeling details. (a) Strand diagrams (top) and curvature models in cross section views (bottom). (b) AFM images. Scale bars, 100 nm. See SI, section SI2.3 for larger images. (c) TEM images. Scale bars, 100 nm. See SI, section SI2.4 for larger images. (d) AFM-based landing assay results. A structure that landed with its front side facing up is marked with a blue dot inside a red circle; the one with back side facing up is marked by a hollow red circle. Magnified views show the structures with orientational markers (front side structures in blue boxes and back side structures in red boxes). The ratio between two landing orientations is shown in the bar chart in the bottom panel (blue, front side; red, back side). See SI, section SI2.5 for larger images and more details. (e) Representative DNA-PAINT super-resolution images of different SST structures labeled at four corners (scale bars, 100 nm). Measured point distances for motifs 0, 1, 3.1, 3.2, and 4.1 were 73 nm, 27 and 73 nm (short and long axis), 31 and 154 nm (parallelogram short and long diagonal), 45 and 148 nm (parallelogram short and long diagonal), and 45 and 77 nm (short and long axis), respectively. (f) Schematics of AFM-based landing assay. (g) Schematics of DNA-PAINT super-resolution imaging. Left panel: an SST structure was labeled on the top surface with 9 nt single-stranded "docking" sites for DNA-PAINT imaging strands. It was also labeled on the bottom surface with biotinylated strands for surface attachment. Center panel: imager strands bind transiently to the docking sites in the four corners, producing apparent blinking. Right panel: diffraction-limited TIRFM image (left) and super-resolution image (right). Scale bars, 100 nm.

connected by flexible 10 nt, single-stranded poly-T linkers. The structure was thus likely loosely connected without well-defined morphology. AFM imaging was performed only after the addition of 10 nt poly-A strands, which were used to complement the poly-T linkers, and helped to result in a structure with better defined shape. After poly-A complementation, grid-like structures were observed.

Wire-frame Lattices: Motifs 13 and 14. We constructed hexagonal lattices with different mesh sizes: one formed from a motif with three 21-nt domains (motif 13) and another from a motif with six 10-nt domains (motif 14). The hexagon pattern is similar to previous work on hexagon lattice-based tubes.[41] In contrast to the typical structures composed of parallel-arranged double-helices linked by periodic (half) crossovers, these wire-frame structures[40,41] are composed of short duplex fragments connected with junction points. Interestingly, due to the electrostatic repulsions between adjacent DNA double-helices, a structure composed of parallel-arranged double-helices typically possesses a gap (e.g., 0.5−1.5 nm in DNA origami[10,14,16] and SST structures[12,20,21]) between the adjacent crossovers, and can be viewed as a wire-frame structure with a rectangular mesh pattern. In SI, section SI1.4, we discuss the transformation between parallel pattern and rectangular wire-frame pattern in more detail.

dx.doi.org/10.1021/ja4062294 | J. Am. Chem. Soc. XXXX, XXX, XXX−XXX

Curvature. *Modeling and Design.* The strand-weaving pattern of the strands can affect the curvature of the structure. Figure 2 summarizes our strategies to control structure curvature. SI, section SI2.1 gives modeling and analysis details.

Domain Length Adjustment. Working toward our goal of controlling curvature to design a flat structure, we first attempted to reduce curvature by adjusting the domain length of the canonical U-shaped SST motif. Assuming that the crossover points between adjacent double-helices are collinear with the centers of the adjacent double-helices, our model predicts an average curvature of 30° per double-helix for the motif 0, and 720° for the 24H×29T rectangle (see Figure 2a,e for cross-sectional view of zoomed-in structure and the overall structure; see SI, section SI2.1.1 for detailed calculation). This curvature was confirmed by our experimental data (Figure 3, column motif 0).

By adopting a domain length of 9/12 nt (motif 1) instead of the canonical 10/11 nt in motif 0, we were able to reduce the calculated average curvature per double-helix from 30° to −4°, and −96° for the 24H rectangle (see SI, section SI2.1.1 for detailed calculation). This reduced curvature was confirmed by experimental data (Figure 3, column motif 1).

However, a 2D structure (such as that formed by motif 0 or motif 1) designed with antiparallel crossovers will always possess a side that displays minor grooves at crossovers and another side that displays major grooves at crossovers.[47] As such, the curvature will not be perfectly counterbalanced for antiparallel crossover-based structures designed from U-shaped motifs (Figure 2a).

Parallel Crossover Design. Next, we hypothesize that the curvature induced by the asymmetric arrangement of major and minor grooves at the crossovers on the two sides of the structures would be negated in parallel crossover-based structures[3] formed from Z-shaped motifs: here, on either side of the structure, the crossovers display major and minor grooves in an alternating fashion. Like the U-shaped motif, we assume the crossover points of adjacent double-helices are collinear with the centers of the adjacent double-helices, and designed a Z-shaped motif (motif 3.1)-based structure that is expected to be perfectly flat (see Figures 2b, left panel; see SI, section SI2.1.2 for detailed calculation). However, our experimental data revealed significant curvature in the structure (Figure 3, column motif 3.1).

The discrepancy between our model and our experiments led us to revise the previous assumption that the crossover points of adjacent double-helices are collinear with the centers of the adjacent double-helices. Although our experimental results from U-shaped motifs (motifs 0 and 1) did not invalidate such an assumption, the results from Z-shaped motifs were clearly incompatible with this collinear assumption. To reconcile this discrepancy between the model and the experimental results, we introduced an offset angle α formed between a base at the crossover and the two center points of the adjacent double-helices (middle panels of Figures 2b and SI39b). In a structure formed from motif 3.1, this offset angle at the crossover always appears on the same side of the structure, resulting in an accumulative curvature for this otherwise flat structure.

Incidentally, another structure based on a Z-shaped motif with a different domain length (motif 3.2) appeared approximately flat in our experiments (Figure 3, column motif 3.2). Assuming this structure (motif 3.2) has 0° curvature, we back-calculated an approximate value for the offset angle α (8.5°, Figure 2c). Using this α value, the 24H×29T structure formed from motif 3.1 was expected to have significant curvature (see Figure 2b, middle panel; see SI, section SI2.1.2 for detailed calculation), consistent with experimental observation of a curved structure.

Corrugation Design. We next devised a corrugated design (motif 4.1) where the offset angle α appears alternately on the two sides of the structure, thus canceling out the curvature effect (independent of its value, Figure 2d,f; see SI, section SI2.1.3 for detailed calculation). The predicted flatness of the structure was experimentally verified (Figure 3, column motif 4.1).

Curvature: Experimental Characterization. We performed a case study below to test the curvature of 24H×29T rectangle structures of a number of motifs.

Characterization by AFM and TEM. To study the curvature of the structures, we constructed 24H×29T structures with each of the above five motifs. Sequence design and structure assembly were conducted in a similar fashion as their 10H×11T counterparts. Then the annealed samples were subjected to 2% native gel electrophoresis (see Figure SI41 for gel data), and the product band was extracted, purified by centrifugation, and imaged with AFM and TEM. Under AFM, all the structures appeared as flat, single-layer structures on mica surface (Figure 3b); no curvature information was revealed. However TEM images more effectively reflected the structure configurations in solution (Figure 3c): the structure generated from motif 0 (720° curvature expected) appeared as a dense, rolled-up rectangle; the structure from motif 1 (−96° expected) appeared as a wider rectangle; rolled-up and flat parallelograms were observed for the structure made from motifs 3.1 and 3.2, respectively; and a flat rectangle was observed for structure from motif 4.1 (0° curvature expected).

AFM-Based Landing Assay. The different curvature configurations of the structures were also confirmed by two innovative assays. The first was the AFM-based landing assay[20] in which a small hole was introduced to the top-left corners of the structure as an orientational marker (Figure 3f). If the marker was more likely to show up at the top left corner rather than its mirror image (top right corner), it indicated the structure landed on the mica with its front side facing up, suggesting the structure curved up instead of down (motif 0). On the contrary, if the mirror image (back side facing up) was more likely, the structures had the tendency to curve down (motif 3.1). If the marker showed no bias for either side, the structure would be flat. Our experimental results (Figure 3d) showed a perfect bias for the rolled-up structures in the predicted curving direction [motif 0, 100% front side facing up (N = 36); motif 3.1, 100% back side facing up (N = 57)]. However, possibly due to a limited sample size, the assay did not effectively differentiate between other less curved structures [motif 1, 65%, front side facing up (N = 74); motif 3.2, 42% front side facing up (N = 45); motif 4.1, 66% front side facing up (N = 203)]. Note that only well-formed structures (defined as those showing no defects >15 nm in diameter in the expected boundary, nor >10 nm in diameter in the interior of the structure) were counted in our statistics. See SI, section SI2.5 for details.

Super-Resolution Fluorescence Microscopy Assay. Super-resolution fluorescence microscopy was the second approach employed to assess the curvature of SST structures (Figure 3g). Here we used DNA-PAINT[48,32,35] to obtain sub-diffraction images of SST structures. DNA-PAINT exploits the repetitive, transient binding of short fluorescently labeled oligonucleotides

dx.doi.org/10.1021/ja4062294 | J. Am. Chem. Soc. XXXX, XXX, XXX−XXX

("imager" strands) to complementary strands ("docking" sites) on a structure or molecule of interest. Using total internal fluorescence microscopy (TIRFM), binding events of imager strands to docking sites were observed as single-molecule events and the fluorescence emission was fitted to a 2D Gaussian function, yielding sub-diffraction resolution images. SST structures were "labeled" with DNA-PAINT docking sites by extending the three outmost strands in each of the four corners by a 9 nt long sequence at their 3′-end (Figure 3g, center panel). The structures also carried four biotinylated strands pointing toward the opposite side of the docking strands for surface attachment (Figure 3g, left panel). Once bound to a functionalized glass slide, fluorescently labeled DNA-PAINT imager strands were introduced, which transiently bound to the docking strands. The right panel of Figure 3g includes a typical diffraction-limited TIRF image of a DNA nanostructure alongside the DNA-PAINT image after reconstruction. The increase in resolution is clearly visible.

The results of the DNA-PAINT study on the five different SST motifs are in good agreement with the TEM analysis as well as the AFM-based landing assay (Figure 3e). For motif 0, only two apparent points in a distance corresponding to the long side of the rectangular structure were visible, suggesting a "rolled-up" structure where the two corners were placed right next to each other, or only one of the two corners was available to bind the imager strand. In contrast, in the structure from motif 1 we observed four separate points, two of which were in close proximity, suggesting a slightly curved structure. Images for motifs 3.1 and 3.2 were consistent with an almost rolled-up structure (3.1) and a flat parallelogram structure (3.2), respectively. Finally, the image for motif 4.1 (with four visible corners) suggests a flat rectangular structure.

Twist. Besides assessing the curvature in different SST designs, we also studied the twist of the SST structures by creating homopolymers of motifs 4.1 and 4.2. We designed the leftmost column of the SST tiles to pair with the rightmost column of the rectangle. As a consequence, multiple units of rectangles align in tandem to form a long polymer with individual rectangles as monomer units (Figure SI58, top). Polymerization helps to identify the small degrees of twist that would be difficult if not impossible to visualize using only monomeric structures.[17,44] AFM images revealed that the homopolymers formed from motif 4.1 yielded ribbons with virtually no global twist (Figure SI58a, bottom). This was expected, as the design used 21 bases between adjacent crossover points, thus obeying 10.5 bp spacing per helical turn as in the natural form of B-DNA. In contrast, polymers formed from motif 4.2 showed a global left-handed twist (Figure SI58b, bottom). This is consistent with the fact that motif 4.2 used 20 bases between adjacent crossover points and was expected to produce a locally overwound double-helix. Our results agree with earlier studies of curvature and twist for DNA origami structures[17,43,44] and suggest that the twist of the SST structures can be modulated by changing crossover spacing distances.

■ CONCLUSION

In summary, we evaluated more than 30 SST motifs that form lattice structures with diverse strand weaving patterns. Most of the motifs self-assembled into the designed structures with reasonable yields. Using some of the motifs, a systematic study was conducted to reduce the curvature in the assembled structure. The difference in curvature was characterized by TEM, an AFM-based landing assay, and super-resolution microscopy. A corrugated weaving pattern was predicted and experimentally verified to produce a flat structure.

The simple and robust nature of SSTs has enabled us to survey the structural space for forming complex structures in a rapid and comprehensive fashion. An unprecedented collection of diverse weaving patterns was demonstrated. We were able to define simple-to-implement design rules that lead to structures with specific geometric properties such curvature and twist. More broadly, the diverse collection of motifs will allow us to modulate the geometrical, mechanical, and thermodynamic parameters. We demonstrated the tuning of curvature and twist with the new motifs. In a related work,[49] we demonstrated that by using the motifs reported here, we can form complex DNA nanostructures isothermally at any prescribed temperature between 15 and 69 °C, and under biocompatible conditions. The work here thus provides a new set of tools for modulating the structural properties of complex DNA structures, and reveals the broad design space for forming such structures.

■ METHODS

Finite DNA nanostructures were first designed with different motifs, and then random sequences were generated to fill in the specific structures and populate complementary domains. Without careful adjustment of stoichiometry, unpurified strands were mixed and supplemented with 0.5×TE and 15 mM Mg^{2+}. After one-pot annealing from 90 to 25 °C over 17 h, the solution was subjected to native agarose gel electrophoresis. The annealed samples, or the gel-purified samples from extraction of the desired band by centrifugation were imaged with AFM or TEM. The curvature and twist of certain structures were studied by AFM, TEM, and super-resolution fluorescent imaging.

DNA Sequence Design. Most DNA sequences were designed with the Uniquimer software by populating the motifs with random sequences[50] while maintaining the required complementarity relations. The following design rules were applied for sequence generation: (1) Nucleotides (i.e., A, C, G, T) are generated one by one randomly. (2) Complementary nucleotides to one generated are matched following the base-pairing rule: A to T, C to G and vice versa. (3) Specific segments (e.g., four consecutive A, C, G, T) are not allowed. When such segments emerge during design, the most recent generated nucleotide will be mutated until disallowance of specific segments is satisfied. Due to the difficulty of designing structures with wire-frame motifs, a separate script was developed following the same design principles. Manual design and/or optimization was used for the linker segment sequences (e.g.,motifs 11.1−11.4 and motif 12) and the handle segment sequences (e.g., handle segment sequences for structures of motifs 0, 1, 3.1, 3.2, and 4.1 in super-resolution study.

Sample Preparation. DNA strands were synthesized by Integrated DNA Technology, Inc. (http://www.idtdna.com). To assemble the structures, DNA strands were mixed to roughly equal molar concentration of 200 nM for smaller structures (all 10H×11T structures, structures with linkers and wire-frame structures) and 100 nM for larger structures (24H×29T and 24H×28T structures for the curvature study) in 0.5×TE buffer (5 mM Tris, pH 7.9, 1 mM EDTA) supplemented with 15 mM $MgCl_2$. The mixtures was then annealed in a PCR thermo cycler by cooling from 90 to 25 °C over a period of 17 h with a specific cooling program.[20] The annealed samples were then subjected to 2% agarose gel electrophoresis (gel prepared in 0.5×TBE buffer supplemented with 10 mM $MgCl_2$ and pre-stained with SYBR safe) in an ice water bath. If necessary, the target gel bands were excised out and put into a Freeze N′ Squeeze column (Bio-Rad). The gel pieces were crushed using a microtube pestle in the column and the column was then directly subjected to centrifuge at 438*g* for 3 min. Purified samples were collected in the eluate, and concentrations were determined by Nanodrop absorption at 260 nm prior to AFM or TEM imaging.

dx.doi.org/10.1021/ja4062294 | J. Am. Chem. Soc. XXXX, XXX, XXX−XXX

AFM Imaging. AFM images were obtained using an SPM Multimode with Digital Instruments Nanoscope V controller (Vecco). A 5 μL droplet (2−10 nM) of annealed (or purified) sample and then a 40 μL drop of 0.5×TE/10 mM $MgCl_2$ solution were applied to a freshly cleaved mica surface and left for approximately 2 min. Sometimes, additional dilution of the sample was performed to achieve the desired sample density. As for the cases of 10H×11T structures, 20 μL of supplemental 10 mM $NiCl_2$ was added to increase the strength of DNA−mica binding.[51] The images were taken under the liquid tapping mode, with C-type triangular tips (resonant frequency, f_0 = 40−75 kHz; spring constant, k = 0.24 N m^{-1}) from the SNL-10 silicon nitride cantilever chip (Bruker Corp.).

TEM Imaging. For TEM imaging, a 3.5 μL sample (1−5 nM) was adsorbed onto glow discharged carbon-coated TEM grids for 4 min and then stained for 1 min or a few seconds using a 2% aqueous uranyl formate solution containing 25 mM NaOH. Imaging was performed using a JEOL JEM-1400 TEM operated at 80 kV.

Super-Resolution Imaging. Super-resolution studies were performed with DNA PAINT.[48] The samples were diluted in DNA-PAINT imaging buffer (5 mM Tris-HCl (pH 8.0), 10 mM $MgCl_2$, 1 mM EDTA, 0.05% Tween-20) to 50 pM and immobilized to a coverslip in a flow chamber via biotin streptavidin binding interaction. To fix the samples, solutions containing 1 mg/mL BSA-biotin, 2 mg/mL streptavidin, and biotin-labeled DNA nanostructures were flushed into the flow chamber and incubated in the above order. The chamber was then washed with DNA-PAINT imaging buffer containing 20 nM ATTO655-labeled imager strands and sealed with 5 min epoxy before imaging. DNA-PAINT super-resolution images were acquired on an inverted Nikon Ti-E microscope (Nikon Instruments, Melville, NY) with the Perfect Focus System, applying an objective-type TIRF configuration using a Nikon TIRF illuminator with an oil-immersion objective (100× Plan Apo, NA 1.49, Oil, Nikon). A 647 nm laser (Agilent MLC400B, 80 mW at the objective) was used for TIRF excitation. The laser beam was filtered with a clean up filter (642/20 Chroma Technologies) and coupled into the microscope objective using a multiband beam splitter (zt405/488-491/561/638rpc, Chroma Technologies). Fluorescence was spectrally filtered with an emission filter (700/75 Chroma Technologies) and imaged on an EMCCD camera (Andor iXon 3, Andor Technologies, North Ireland). A total of 5000 frames were recorded at a frame rate of 10 Hz. Super-resolution images were reconstructed using spot-finding and 2D Gaussian fitting algorithms programed in LabVIEW (National Instruments) available for download at www.dna-paint.org.

Yield Quantification by Gel Electrophoresis. Yield was estimated by analysis using native agarose gel electrophoresis, pre-stained with SYBR Safe DNA stain. The ratio between the fluorescence intensity of the product band and that of the entire lane was taken as an estimate of the gross yield of structural formation.

Structure Size Measurement and Statistics. AFM measurements were obtained using Nanoscope Analysis (version 1.20; Vecco). The "cross-section" function was used to measure distances (lengths and widths of the structures of different sizes). Well-formed structures were chosen for the measurements. TEM images were analyzed using ImageJ (version 1.46r; NIH). The straight line function was used to measure widths of certain structures. Six or ten sample points were collected for each distance measurement and the statistics (e.g., the mean and the standard deviation) were based on those 6 or 10 data points.

■ ASSOCIATED CONTENT

Supporting Information

Experimental details, additional figures, and sequence data for each structure. This information is available free of charge via the Internet at http://pubs.acs.org.

■ AUTHOR INFORMATION

Corresponding Author

py@hms.harvard.edu

Notes

The authors declare the following competing financial interest(s): A provisional patent based on this work is pending.

■ ACKNOWLEDGMENTS

We thank Wei Sun and Hoang Lu for technical assistance and David Zhang, Erik Winfree, William Sherman, and Robert Barish for discussion. DNA-PAINT data were collected at the Nikon Imaging Center at Harvard Medical School. This work was funded by Office of Naval Research (ONR) Young Investigator Program award N000141110914, ONR grant N000141010827, National Science Foundation (NSF) Faculty Early Career Development Award 1054898, NSF grant 1162459, National Institutes of Health Director's New Innovator Award 1DP2OD007292, and a Wyss Institute Faculty Startup Fund to P.Y. M.D. acknowledges an international student research fellowship from the Howard Hughes Medical Institute. C.M. acknowledges a graduate research fellowship from the Fannie and John Hertz Foundation. R.J. acknowledges a postdoctoral fellowship from the Alexander von Humboldt Foundation.

■ REFERENCES

(1) Seeman, N. C. *J. Theor. Biol.* **1982**, *99*, 237−247.
(2) Chen, J.; Seeman, N. C. *Nature* **1991**, *350*, 631−633.
(3) Fu, T. J.; Seeman, N. C. *Biochemistry* **1993**, *32*, 3211−3220.
(4) Winfree, E.; Liu, F.; Wenzler, L. A.; Seeman, N. C. *Nature* **1998**, *394*, 539−544.
(5) Chworos, A.; Severcan, I.; Koyfman, A. Y.; Weinkam, P.; Oroudjev, E.; Hansma, H. G.; Jaeger, L. *Science* **2004**, *306*, 2068−2072.
(6) Rothemund, P. W. K.; Papadakis, N.; Winfree, E. *PLoS Biol.* **2004**, *2*, 2041−2053.
(7) Shih, W. M.; Quispe, J. D.; Joyce, G. F. *Nature* **2004**, *427*, 618−621.
(8) Goodman, R. P.; Schaap, I. A. T.; Tardin, C. F.; Erben, C. M.; Berry, R. M.; Schmidt, C. F.; Turberfield, A. J. *Science* **2005**, *310*, 1661−1665.
(9) Park, S. H.; Pistol, C.; Ahn, S. J.; Reif, J. H.; Lebeck, A. R.; Dwyer, C.; Labean, T. H. *Angew. Chem., Int. Ed.* **2006**, *45*, 735−739.
(10) Rothemund, P. W. K. *Nature* **2006**, *440*, 297−302.
(11) He, Y.; Ye, T.; Su, M.; Zhang, C.; Ribbe, A. E.; Jiang, W.; Mao, C. *Nature* **2008**, *452*, 198−201.
(12) Yin, P.; Hariadi, R.; Sahu, S.; Choi, H. M. T.; Park, S. H.; LaBean, T. H.; Reif, J. H. *Science* **2008**, *321*, 824−826.
(13) Zheng, J. P.; Birktoft, J.; Chen, Y.; Wang, T.; Sha, R. J.; Constantinou, P.; Ginell, S.; Mao, C.; Seeman, N. C. *Nature* **2009**, *461*, 74−77.
(14) Ke, Y.; Sharma, J.; Liu, M.; Jahn, K.; Liu, Y.; Yan, H. *Nano Lett.* **2009**, *9*, 2445−2447.
(15) Andersen, E. S.; Dong, M.; Nielsen, M. M.; Jahn, K.; Subramani, R.; Mamdouh, W.; Golas, M. M.; Sander, B.; Stark, H.; Oliveira, C. L. P.; Pedersen, J. S.; Birkedal, V.; Besenbacher, F.; Gothelf, K. V.; Kjems, J. *Nature* **2009**, *459*, 73−76.
(16) Douglas, S. M.; Dietz, H.; Liedl, T.; Högberg, B.; Graf, F.; Shih, W. M. *Nature* **2009**, *459*, 414−418.
(17) Dietz, H.; Douglas, S. M.; Shih, W. M. *Science* **2009**, *325*, 725−730.
(18) Han, D.; Pal, S.; Nangreave, J.; Deng, Z.; Liu, Y.; Yan, H. *Science* **2011**, *332*, 342−346.
(19) Delebecque, C. J.; Lindner, A. B.; Silver, P. A.; Aldaye, F. A. *Science* **2011**, *333*, 470−474.
(20) Wei, B.; Dai, M.; Yin, P. *Nature* **2012**, *485*, 623−626.
(21) Ke, Y.; Ong, L. L.; Shih, W. M.; Yin, P. *Science* **2012**, *338*, 1177−1183.
(22) Han, D.; Pal, S.; Yang, Y.; Jiang, S.; Nangreave, J.; Liu, Y.; Yan, H. *Science* **2013**, *339*, 1412−1415.

(23) Yurke, B.; Turberfield, A. J.; Mills, A. P.; Simmel, F. C.; Neumann, J. L. *Nature* **2000**, *406*, 605–608.
(24) Sherman, W. B.; Seeman, N. C. *Nano Lett.* **2004**, *4*, 1203–1207.
(25) Yin, P.; Choi, H. M. T.; Calvert, C. R.; Pierce, N. A. *Nature* **2008**, *451*, 318–322.
(26) Omabegho, T.; Sha, R.; Seeman, N. C. *Science* **2009**, *324*, 67–71.
(27) Seelig, G.; Soloveichik, D.; Zhang, D. Y.; Winfree, E. *Science* **2006**, *314*, 1585–1588.
(28) Qian, L.; Winfree, E. *Science* **2011**, *332*, 1196–1201.
(29) Yan, H.; Park, S. H.; Finkelstein, G.; Reif, J. H.; LaBean, T. H. *Science* **2003**, *301*, 1882–1884.
(30) Kuzyk, A.; Schreiber, R.; Fan, Z.; Pardatscher, G.; Roller, E.; Högele, A.; Simmel, F. C.; Govorov, A. O.; Liedl, T. *Nature* **2012**, *483*, 311–314.
(31) Choi, H. M. T.; Chang, J. Y.; Trinh, L. A.; Padilla, J. E.; Fraser, S. E.; Pierce, N. A. *Nat. Biotechnol.* **2010**, *28*, 1208–1212.
(32) Lin, C.; Jungmann, R.; Leifer, A. M.; Li, C.; Levner, D.; Church, G. M.; Shih, W. M.; Yin, P. *Nat. Chem.* **2012**, *4*, 832–839.
(33) Jin, Z.; Sun, W.; Ke, Y.; Shih, C.; Paulus, G. L. C.; Wang, Q. H.; Mu, B.; Yin, P.; Strano, M. S. *Nat. Commun.* **2013**, *4*, 1663.
(34) Berardi, M. J.; Shih, W. M.; Harrison, S. C.; Chou, J. J. *Nature* **2011**, *476*, 109–113.
(35) Derr, N. D.; Goodman, B. S.; Jungmann, R.; Leschziner, A. E.; Shih, W. M.; Reck-Peterson, S. L. *Science* **2012**, *338*, 662–665.
(36) Douglas, S. M.; Bachelet, I.; Church, G. M. *Science* **2012**, *335*, 831–834.
(37) Zhang, X.; Yan, H.; Shen, Z.; Seeman, N. C. *J. Am. Chem. Soc.* **2002**, *124*, 12940–12941.
(38) Zhang, C.; Su, M.; He, Y.; Zhao, X.; Fang, P. A.; Ribbe, A.; Jiang, W.; Mao, C. *Proc. Natl. Acad. Sci. U.S.A.* **2008**, *105*, 10665–10669.
(39) Mao, C.; Sun, W.; Seeman, N. C. *J. Am. Chem. Soc.* **1999**, *121*, 5437–5443.
(40) Malo, J.; Mitchell, J. C.; Venien-Bryan, C.; Harris, J. R.; Wille, H.; Sherratt, D. J.; Turberfield, A. J. *Angew. Chem., Int. Ed.* **2005**, *44*, 3057–3061.
(41) Wilner, O. I.; Orbach, R.; Henning, A.; Teller, C.; Yehezkeli, O.; Mertig, M.; Harries, D.; Willner, I. *Nat. Commun.* **2011**, *2*, 540.
(42) Yang, H.; Sleiman, H. *Angew. Chem., Int. Ed.* **2008**, *47*, 2443–2446.
(43) Ke, Y.; Douglas, S. M.; Liu, M.; Sharma, J.; Cheng, A.; Leung, A.; Liu, Y.; Shih, W. M.; Yan, H. *J. Am. Chem. Soc.* **2009**, *131*, 15903–15908.
(44) Jungmann, R.; Scheible, M.; Kuzyk, A.; Pardatscher, G.; Castro, C. E.; Simmel, F. C. *Nanotechnology* **2011**, *22*, 275301.
(45) Kim, D.; Kilchherr, F.; Dietz, H.; Bathe, M. *Nucleic Acids Res.* **2011**, *40*, 2862–2868.
(46) Liu, H.; Chen, Y.; He, Y.; Ribbe, A.; Mao, C. *Angew. Chem., Int. Ed.* **2006**, *45*, 1942–1945.
(47) Rothemund, P. W. K.; Ekani-Nkodo, A.; Papadakis, N.; Kumar, A.; Fygenson, D. K.; Winfree, E. *J. Am. Chem. Soc.* **2004**, *126*, 16344–16353.
(48) Jungmann, R.; Steinhauer, C.; Scheible, M.; Kuzyk, A.; Tinnefeld, P.; Simmel, F. C. *Nano Lett.* **2010**, *10*, 4756–4761.
(49) Myhrvold, C.; Dai, M.; Silver, P.; Yin, P. *Nano Lett.* **2013**, *13*, 4242–4248.
(50) Wei, B.; Wang, Z.; Mi, Y. *J. Comput. Theor. Nanosci.* **2007**, *4*, 133–141.
(51) Hansma, H. G.; Laney, D. E. *Biophys. J.* **1996**, *70*, 1933–1939.

dx.doi.org/10.1021/ja4062294 | *J. Am. Chem. Soc.* XXXX, XXX, XXX–XXX

11.1.5 Assembly conditions of 2D shapes

NANO LETTERS

Letter

pubs.acs.org/NanoLett

Isothermal Self-Assembly of Complex DNA Structures under Diverse and Biocompatible Conditions

Cameron Myhrvold,[†,‡] Mingjie Dai,[‡,§] Pamela A. Silver,[†,‡] and Peng Yin*[,†,‡]

[†]Department of Systems Biology, Harvard Medical School, Boston, Massachusetts 02115, United States

[‡]Wyss Institute for Biologically Inspired Engineering and [§]Program in Biophysics, Harvard University, Boston, Massachusetts 02115, United States

Supporting Information

ABSTRACT: Nucleic acid nanotechnology has enabled researchers to construct a wide range of multidimensional structures in vitro. Until recently, most DNA-based structures were assembled by thermal annealing using high magnesium concentrations and nonphysiological environments. Here, we describe a DNA self-assembly system that can be tuned to form a complex target structure isothermally at any prescribed temperature or homogeneous condition within a wide range. We were able to achieve isothermal assembly between 15 and 69 °C in a predictable fashion by altering the strength of strand−strand interactions in several different ways, for example, domain length, GC content, and linker regions between domains. We also observed the assembly of certain structures under biocompatible conditions, that is, at physiological pH, temperature, and salinity in the presence of the molecular crowding agent polyethylene glycol (PEG) mimicking the cellular environment. This represents an important step toward the self-assembly of geometrically precise DNA or RNA structures in vivo.

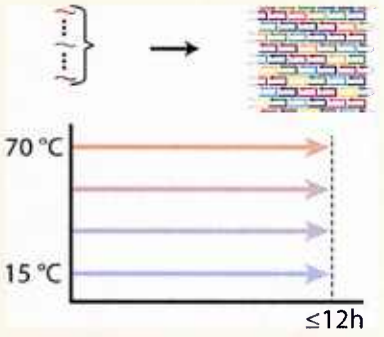

KEYWORDS: *DNA nanotechnology, isothermal assembly, single-stranded tiles, biocompatible assembly, molecular crowding*

Nucleic acid self-assembly has proven to be a powerful tool for constructing nanoscale structures due to the precise and predictable relationship between structure geometry and the encoded sequence. Over the past few decades, a wide range of DNA and RNA-based nanostructures have been demonstrated, including a variety of two-dimensional (2D) and three-dimensional (3D) geometries[1−14] and dynamic devices.[15−22] Additionally, such nanostructures can interface with and organize molecules, cells and other materials,[1,12,23−27] thereby enabling biophysical[24,28] and potential biomedical[23,29,30] applications. The self-assembly of individual strands into DNA nanostructures typically involves a thermal gradient in which the system temperature is first raised (e.g., to 80−90 °C) and then gradually lowered to room temperature. This thermal gradient can be replaced with a chemical gradient of a denaturing agent to isothermally assemble precisely controlled DNA origami structures.[31] In addition to gradient-based assembly, researchers have demonstrated the isothermal formation of extended crystals[12,32,33] using DNA and RNA tiles and discrete structures using DNA origami,[34] both under homogeneous conditions.

Isothermal assembly of DNA tiles and origami under homogeneous conditions represents important progress for the assembly of complex DNA nanostructures. Compared with thermal annealing, assembling structures in homogeneous conditions leads to rapid structure formation with higher yield and quality.[34] However, previous work on DNA tile crystals and origami still requires a highly optimized set of assembly conditions (temperature, salinity, etc.) that are structure-dependent and restricted to a narrow range, thereby limiting the scope of potential applications. In contrast, assembly across a wide range of conditions will increase the range of applications of DNA nanotechnology, especially when the assembly conditions are specified by the application, such as in vivo scaffolding[12] of metabolic enzymes (where the assembly is required to happen under intracellular conditions) or in situ imaging[35] (where the assembly is required to happen under harsh denaturing conditions). Thus, the next important challenge is to devise a general method in which, given a particular homogeneous condition and a target shape, the user can design a system that assembles under that particular condition into the desired shape, e.g. the isothermal assembly of a particular shape under any prescribed temperature over a wide temperature range. Such capability will greatly expand the application scope where an assembly system can be designed to operate under diverse homogeneous conditions specified by the desired application. Here we provide a general solution to this challenge.

The key innovation in our approach is that we exploit the tunable nature of single-stranded tile (SST) structures and demonstrate structural designs that can assemble isothermally at a wide range of temperature and salt concentrations,

Received: May 28, 2013
Revised: July 4, 2013
Published: August 26, 2013

including conditions mimicking intracellular environments. Compared with DNA origami, which typically uses a fixed scaffold sequence, single-stranded tiles (SSTs) give us the freedom to independently vary the sequence of any tile in the structure. We use this freedom to program the strength of strand–strand interactions, thereby shifting the optimal assembly temperature to a user-specified temperature. In other words, the assembly temperature of a structure is now an explicit design parameter. This will allow one to tune the design of a structure to fit a particular application.

We report the successful isothermal assembly of modified SST structures across a wide range of temperatures. Building upon our previous SST work,[5,13,14,36] we test 11 compact 2D SST structures (Figure 1a) and 17 flexible variants with single-stranded polyT linkers between the double-stranded domains (Figure 1b).[36] Instead of the traditional thermal annealing protocol (Figure 1c), all structures were assembled isothermally (Figure 1d). Our approach therefore represents a general method for isothermally assembling complex nanostructures across a wide range of specified temperatures. We generally find higher assembly temperatures for structures with longer domains, and lower temperatures for those with linkers. We also show that the assembly temperature can be modulated by changing the strand–strand binding energy in several ways, such as altering GC content of binding domains or disrupting continuity of complementary segments.

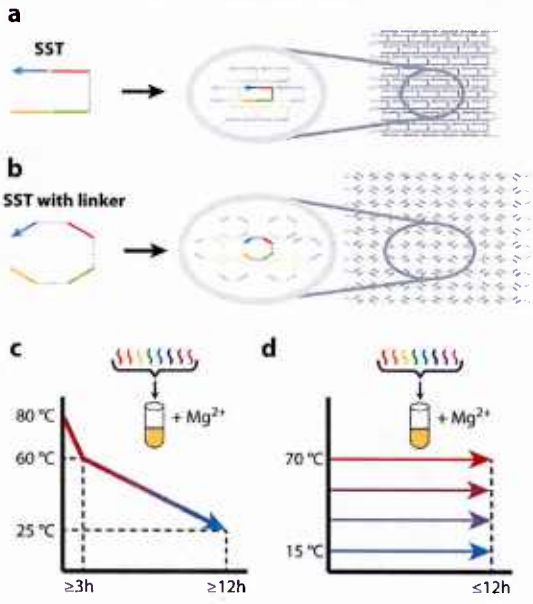

Figure 1. Self-assembly of DNA tiles under diverse and biocompatible conditions. (a,b) We use standard single-stranded tiles (SST; a) and SST tiles containing single-stranded linker regions between domains (b) to assemble 2D rectangular structures. A canonical SST has four domains that bind to four of its nearest neighbors. Each colored segment depicts an individual domain (unique in sequence and between 8 and 21 nt long in our study), a gray solid connection delineates the boundary between two domains, and a gray dotted line depicts a single-stranded linker region (between 1 and 16 nt in our study). Each complete structure (shown on the right) consists of 66 unique SSTs with edges protected by polyT segments to avoid aggregation (light gray segments). (c) A schematic depicting the traditional thermal annealing protocol for structure assembly, where temperature is generally ramped above 60 °C and slowly decreased over at least 12 h. (d) A schematic depicting our isothermal assembly protocol across a wide range of fixed temperatures and conditions for up to 12 h.

Finally, we report successful assembly of designed DNA nanostructures under biocompatible conditions, that is, at physiological temperature and pH, low salinity, and in the presence of molecular crowding agents. Flexible structures, which assemble at a wider range of conditions than their nonflexible counterparts, assemble well under biocompatible conditions. This represents a significant step toward the in vivo assembly of geometrically precise, nucleic acid nanostructures. More generally, this approach may enable additional biological applications of nanostructures in cases where in situ delivery of preassembled structures is not an option.

In our single-stranded tile (SST) system, each strand consists of four binding domains, with or without a single-stranded linker region between consecutive domains. In the presence of divalent cations, each strand is bound to its four neighbors via complementary domains, resulting in a self-assembled 2D SST structure.[13] Most of our structures are derived from motifs in our recent work[36] and consist of 66 SSTs that form a 2D rectangular shape. Two categories of motifs are used. The motifs without linkers form 2D rectangles composed of 10 parallel helices (with length ranging from 108 to 252 nt) connected by periodic single-stranded crossovers. Motifs with polyT linkers form flexible rectangular, fish-net patterns containing short segments of DNA helices connected by single-stranded linkers at all junctions. We varied domain length, linker length, and other design parameters. For an overview of the system, see Supporting Information Figure S1 and Text S1.

SST structures can isothermally assemble across a wide range of temperatures (Figure 2). We tested a set of U-shaped motifs[13,36] to form 2D rectangular structures. By altering the domain lengths of the SST motifs from 8 to 21 nt, we were able to achieve isothermal assembly across a 54 °C range (from 15 to 69 °C). Structure formation was assayed by gel electrophoresis and atomic force microscopy (AFM). A dominant product band was observed after isothermal assembly for 12 h at the indicated temperatures in the presence of 10 mM Mg^{2+}. The formation ranges indicated on the temperature line are a subset of the temperature ranges over which a dominant product band was observed on the gel (see Supporting Information Figure S2 for full range and raw gel data). In some cases, we observed the presence of high molecular weight bands or smears, presumably due to structure aggregation.

Imaging of the unpurified reaction or of the gel-purified product (indicated with an asterisk) revealed the formation of structures with the designed shapes. Structures with polyT linkers between domains were imaged after the addition of complementary polyA strands. They exhibited a wide range of conformations when imaged due to the flexibility inherent in the linker regions.

The assembly yield was quantified using native gel electrophoresis (Figure 3a). We assembled structures isothermally for 1 h (domain length <16 nt) or 12 h (domain length ≥16 nt) at a range of temperatures and then quantified the gel yield in each lane (which corresponds to a particular, fixed assembly temperature) using the TotalLab Quant gel quantification software (Figure 3b). Here, the yield is defined as the ratio of the intensity of the product band divided by the intensity of the entire lane after proper background correction.

dx.doi.org/10.1021/nl4019512 | Nano Lett. 2013, 13, 4242–4248

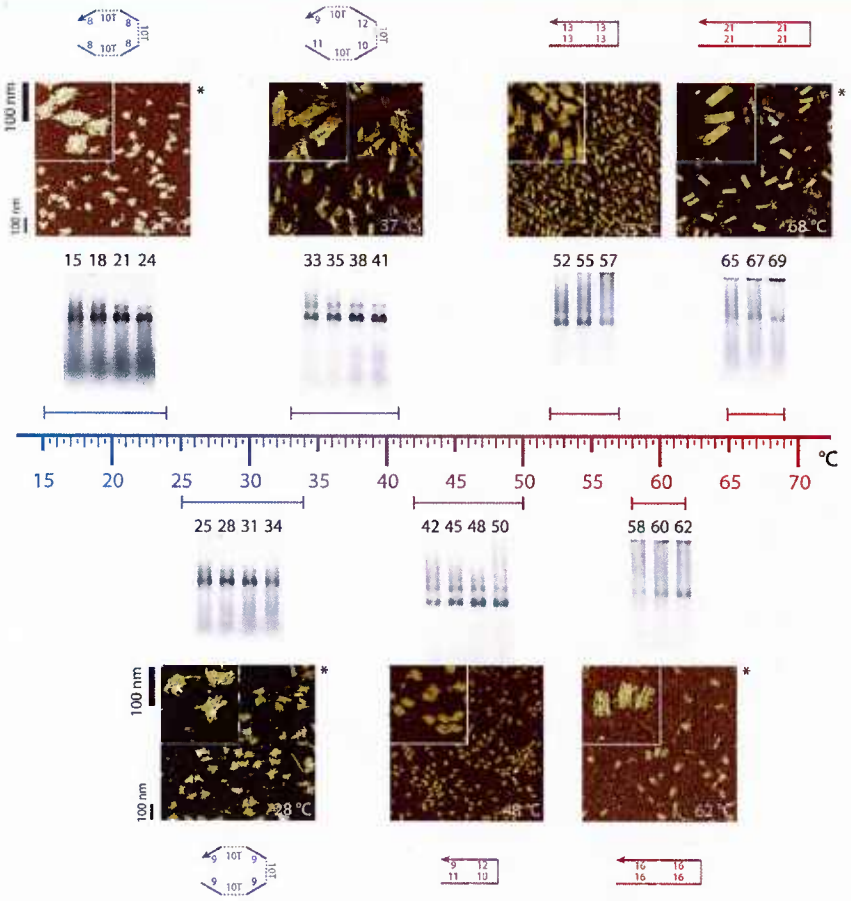

Figure 2. SST-based DNA nanostructures can assemble isothermally across a wide range of temperatures. Representative structures that assemble isothermally at different temperatures are shown and collectively cover the entire temperature range from 15 °C (blue) to 69 °C (red). Structures are ordered and displayed close to their optimal formation temperatures. For each structure, strand diagrams (outside), AFM images (middle), and gel electrophoresis results (inside) are shown. A tagged bar indicates part of the range of successful assembly temperatures shown by agarose gel electrophoresis (see Supporting Information Figure S2 for full gel images).The leftmost three structures contain 10T linkers between domains; the other structures do not, as shown in the strand diagrams. Numbers in strand diagrams indicate domain lengths (unit: nt). AFM images show the typical morphology at the indicated temperatures; images with an asterisk contain gel-purified structures. Structures were assembled isothermally for 12 h using 200 nM of each strand and 10 mM Mg^{2+}.

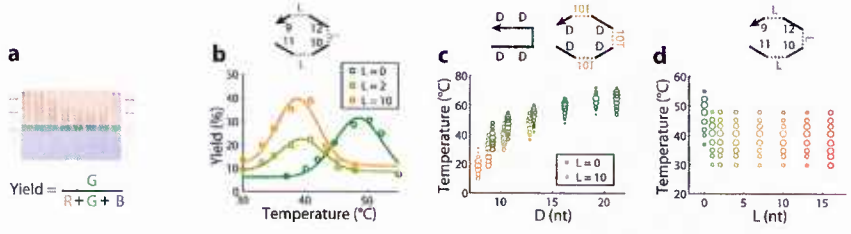

Figure 3. Quantification of optimal assembly temperature and effect of domain and linker lengths. Structures were assembled isothermally for 1 h across a temperature range using 200 nM of each strand and 10 mM Mg^{2+} and assayed using gel electrophoresis. (a) Gel images were quantified using TotalLab Quant software. Gel yield was defined as the integrated intensity of the formation band (green) divided by the total intensity of the lane (red + green + blue). (b) Gel yield of three representative structures (L = 0, 2, 10) and Gaussian fits (solid lines) are shown. (c,d) Formation yields as a function of temperature are shown for structures with varying domain lengths (D = 8–21; c) and linker lengths (L = 0–16; d). Each circle represents a single yield quantification, with its radius proportional to the measured yield; colors indicate linker length from no linker (L = 0; green) to 16T linker (L = 16; dark orange).

This is only an approximation of the true formation yield[13] but is useful for comparing relative yields for assembly under varying conditions. The yield curves were then fit to a Gaussian function with a constant background using custom MATLAB software (Figure 3b). The yield as a function of temperature is

dx.doi.org/10.1021/nl4019512 | Nano Lett. 2013, 13, 4242–4248

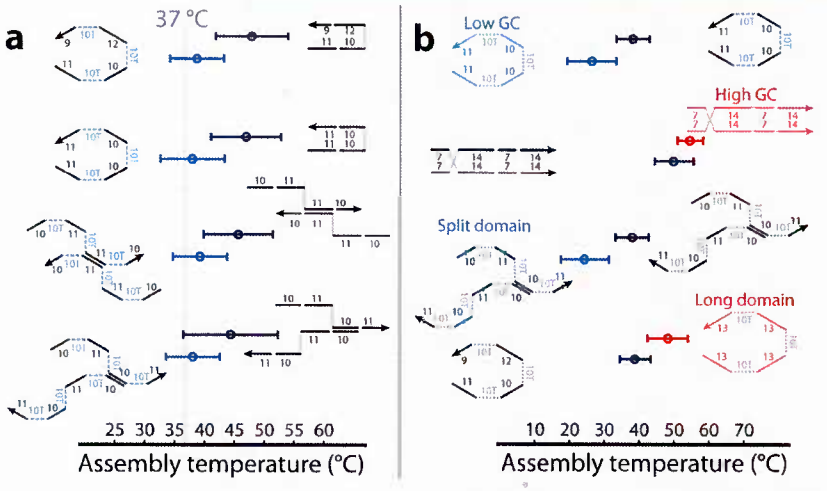

Figure 4. Optimal assembly temperatures can be rationally designed with linker domains and other methods. (a) Shifting to lower optimal assembly temperatures (blue) by addition of linkers (dashed line: physiological temperature). Strand diagrams of four representative designs with distinct strand geometry are shown. (b) Rational design of optimal assembly temperature (blue, lower; red, higher) with three other methods: altering the GC content of domains to 30% (low GC) or 70% (high GC), splitting domains in half and changing domain lengths. In the case of splitting domains, a single T nucleotide is inserted in the middle of each domain (blue dots) to split each strand into a 5-T-5-10T-6-T-5-10T-5-T-5-10T-5-T-6 sequence pattern. In both panels, numbers in strand diagrams indicate domain lengths (unit: nt), tagged bars delimit the full width at half-maximum (fwhm) of a Gaussian fit to the yield as a function of assembly temperature, and a circle denotes the optimal temperature (see Supporting Information Figure S4 for raw gel data).

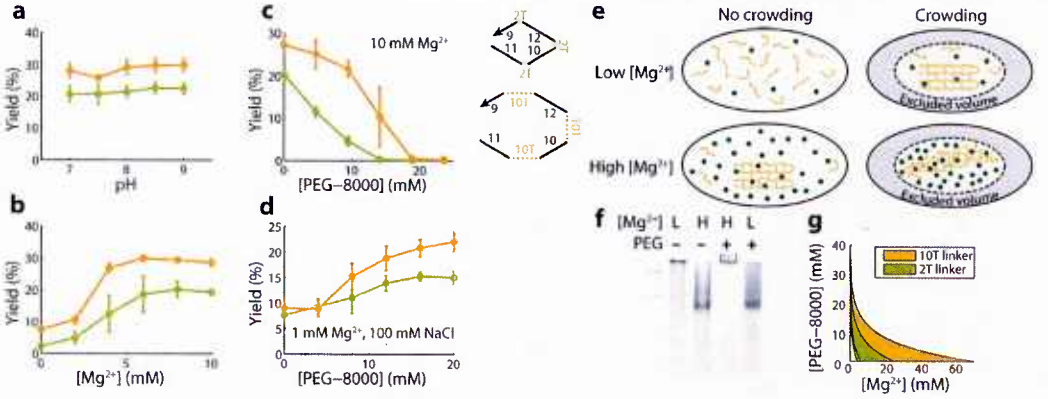

Figure 5. Assembly of structures under biocompatible conditions. (a–d) Effects of assembly conditions on formation yield of two representative structures (olive, 2T linker; orange, 10T linker; see strand diagrams). Structures were assembled for 1 h at 37 °C using 200 nM of each strand. Yields are calculated as in Figure 3a. Error bars indicate the standard deviation based on ≥3 replicate experiments. (a-c) Effects of pH, [Mg^{2+}], and [PEG-8000]on formation yield. Each parameter is varied alone while keeping the others at default values (0.5× TE buffer, pH 8, 10 mM Mg^{2+}, no PEG-8000). HEPES buffer was used for the pH 7 condition. (d) Combined effect of low salinity (1 mM Mg^{2+}, 100 mM NaCl) and [PEG-8000]. (e) A schematic of the crowding model: formation takes place at in vitro (no crowding, high salinity) or biocompatible (crowding, low salinity) conditions. Orange: component strands. Dark green: magnesium ions. (f) Gel result for the 10T linker structure at the four conditions shown in (e): with or without PEG-8000 (-, 0 mM; +, 20 mM), with low and high salinity (L, 1 mM Mg^{2+} 100 mM Na^{+}; H, 10 mM Mg^{2+}). (g) A simple mathematical model of crowding, based on effective concentrations (see Supporting Information Text S3 for details), predicts assembly under low [Mg^{2+}] and high [PEG-8000] conditions.

well-fit by a Gaussian function, indicating that our structures assemble optimally at a specific isothermal temperature.

We show dependence between the assembly temperature and the domain length (Figure 3c; see Supporting Information Figure S3a for raw gel data). The Gaussian fits obtained from curve fitting to the gel quantification data allowed us to obtain a mean and a full-width at half-maximum (fwhm) for each structure that define an optimal temperature and an optimal temperature range, respectively. The formation range is indicated by the extent of the scatterplot, and the relative yields at each temperature are indicated by the diameter of the marker. We examined two sets of structures, those with no linker between domains (green) and those with a 10T linker between domains (orange). In both cases, we observed that the formation range was a monotonically increasing function of the domain length with diminishing returns at higher temperatures. It should be noted that since all of our domains have a similar GC content (around 50%) that domain length is a proxy for the strength of strand–strand interactions in these experiments.

dx.doi.org/10.1021/nl4019512 | *Nano Lett.* 2013, 13, 4242–4248

Linkers between domains caused an ~10 °C downward shift in the assembly temperature (Figure 3d; see Supporting Information Figure S3b for raw gel data). Even a single T nucleotide between domains was sufficient to shift the assembly temperature; additional T nucleotides did not contribute to the temperature shift. As in Figure 3b, we show the formation range using a scatterplot, where the relative yield at each temperature is indicated by the diameter of the marker. The effect of the linkers did not depend on the polyT sequence; a linker consisting of 10 A nucleotides caused a similar downward shift in assembly temperature (see Supporting Information Figure S3c).

We redesigned many structures to assemble at the physiological temperature using polyT linkers (Figure 4a; see Supporting Information Figure S4a for raw gel data). As shown, the effect of polyT linkers was similar for several different strand geometries, causing a downward shift of the assembly temperature of 7–10 °C. In all cases, the redesigned structures formed well at the physiological temperature (37 °C), indicating the generality of this approach for programming the assembly temperature of DNA nanostructures. Furthermore, we demonstrated several additional strategies to shift the assembly temperature (Figure 4b; see Supporting Information Figure S4b for raw gel data): altering the strength of strand–strand interactions via the GC content, changing the length of the complementary domains within a structure, or splitting domains in half by inserting a single T nucleotide. Thus, there exists a wide variety of ways to program the assembly temperature of a DNA nanostructure. This should enable structures with varying geometries and morphologies that assemble at desired temperatures.

Flexible SST DNA structures assembled under biocompatible conditions. A number of structure designs assembled well at the physiological temperature (37 °C; Figures 2, 3, and 4). However, there exist other environmental variables, such as pH, salinity, and molecular crowding, which must be accounted for in order for structure assembly to be biocompatible. We tested two structure designs which assembled well at 37 °C in 1 h (Figure 3b), one with a 2T linker (olive) and one with a 10T linker (orange) by systematically varying other environmental variables in vitro (Figure 5; see Supporting Information Figure S5 for raw gel data). Yields are determined as in Figure 3a.

Physiological pH is compatible with structure assembly (Figure 5a). We varied the pH of the buffer in which the structures were assembled from 7 to 9, which encompassed the physiological pH range. Both structures assembled well across this pH range, indicating that the physiological pH should not prevent SST structures from self-assembling.

Low salinity hindered structure formation (Figure 5b). DNA nanostructures are typically assembled in vitro with a Mg^{2+} concentration in excess of 10 mM.[4,6,13,37] Recently, it was shown that sodium ions can also be interchanged for magnesium ions in some cases.[38] However, the free concentration of magnesium equivalents in the *E. coli* cytoplasm is approximately 2–4 mM (1–2 mM Mg^{2+}, 180–200 mM Na^+ or K^+ [39,40]). Our flexible SST designs assembled close to optimally at as low as 6 mM Mg^{2+} (2T linker, olive) or 4 mM Mg^{2+} (10T linker, orange), approaching but not quite reaching the biologically relevant salinity.

Crowded conditions decreased the assembly yield (Figure 5c). A crowded environment was simulated using polyethylene glycol with an average molecular weight of 8000 Da (PEG-8000). To test the effect of crowding on structure assembly, the PEG-8000 concentration was varied from 0 to 23.5 mM. A Mg^{2+} concentration of 10 mM was used in these experiments. We observed a decline in yield for both structure designs with increasing PEG-8000 concentrations, combined with the appearance of a high molecular weight band indicative of aggregation (see Supporting Information Figure S5c for raw gel data).These results indicate that a combination of crowding and high magnesium decreases assembly yield. Additionally, we have noted that the long linker design (orange) had a consistently higher yield than the short linker design (olive) under the conditions we tested (Figure 5a–d), perhaps due to increased flexibility enhancing the assembly process (e.g., by relieving the electrostatic repulsion between parallel DNA helices).

Molecular crowding compensated for low magnesium, thereby enhancing structure assembly (Figure 5d). When considered separately, both salinity and crowding pose challenges to biocompatible assembly of tile-based DNA nanostructures. However, when we tested the two conditions together by varying the PEG-8000 concentration from 0 to 20 mM with low salinity (1 mM Mg^{2+}, 100 mM Na^+) at pH 7.5, we observed that increased crowding actually improved the assembly yield. This effect was seen for both short (olive) and long linker designs (orange). Together, these results indicate that SST DNA nanostructures can be designed to assemble under biocompatible conditions.

We conjecture that molecular crowding enhances structure assembly by increasing the effective magnesium concentration (Figure 5e). In the absence of crowding, high salinity is required for assembly (top left), but in the presence of crowding high salinity inhibits assembly. This model is consistent with our experimental results; structure assembly (product band) is observed under high salinity with no crowding and low salinity with crowding but not under low salinity with no crowding or under high salinity with crowding (Figure 5f). We used this insight to construct a quantitative model of the effect of molecular crowding on structure assembly and predict a range of conditions under which assembly is likely to occur, indicated by the shaded regions (Figure 5g; see Supporting Information Text S3 and Figure S6 for details).

SST structures can be tuned to assemble isothermally across a range of temperatures from 15 to 69 °C. Additionally, we demonstrated four different ways to modulate the assembly temperature of a structure: changing domain length, altering domain GC content, adding a linker between domains, or splitting a domain in half. This has enabled us to design SST structures that can assemble well under biocompatible conditions. More generally, we now have the capability to design structures that can assemble under a diverse range of specified conditions. We noticed that structures tend to assemble with lower yield at extreme temperatures or conditions. However, the yield at a particular condition, or the range of assembly conditions, can be increased by extending the reaction time. Together, these results indicate that the isothermal SST assembly process is remarkably robust to the assembly temperature and conditions.

Our ability to assemble structures at room temperature can enable the study of structure assembly in real time using atomic force microscopy[22,32] or super-resolution microscopy techniques;[41] at the other end of the spectrum we can assemble structures at temperatures above the typical melting temperature of previous DNA nanostructures. More broadly, our

dx.doi.org/10.1021/nl4019512 | *Nano Lett.* 2013, 13, 4242–4248

unique ability to control the assembly temperature of DNA nanostructures allows structured to be tailored to in vivo or in situ applications where control of the ambient temperature may not be feasible. Our success in biocompatible assembly is particularly exciting because it is a key step toward in vivo assembly of geometrically precise nanostructures from many individual DNA or RNA components. Furthermore, biocompatible assembly takes us beyond the paradigm of annealing structures over many hours under precisely controlled reaction conditions. Our approach of rationally modulating the assembly conditions should be generalizable to other types of structures with a few potential constraints. One such constraint is that the component strands should not contain significant secondary structures that hinder their interactions with other strands. For example, the secondary structure of a typical M13 DNA origami scaffold strand may interfere with the designed structure formation at low temperatures. A scaffold with designed sequence could be used to overcome this constraint.

Beyond tunable SST structures, control over the assembly conditions could perhaps be further improved by exploiting toe-hold-mediated[42] strand displacement cascades,[17,43] for example, using the triggered isothermal assembly of reconfigurable hairpins.[18,35,44] Although the resulting hairpin-based structures (e.g., branched junctions,[18] polymers,[35,44,45] or dendrimers[18]) are not geometrically precise and typically involve very few component strands, they can be formed dynamically via the introduction of an initiator strand. Additionally, a simple two-component toe-hold exchange based system has been shown be robust to temperature, salinity, and concentration.[46] Thus, by integrating robustness of toe-hold based systems with the tunability and geometrical control of the SST systems described here, one may potentially design self-assembly systems that could allow for assembly across a wide range of temperatures and conditions without the need for condition-specific tuning.

A rational next step after biocompatible assembly is to assemble geometrically precise RNA nanostructures in vivo and to use them to organize metabolic enzymes or other functional biomolecules.[12] One could build upon the knowledge and experience from DNA SST assembly to design and rapidly prototype RNA structures that assemble under biocompatible conditions and act as scaffolds. With greater freedom in design geometry and positioning of protein-binding sites, one would be able to design and test interactions between multiple functional molecules across varying distances and geometrical patterns. One can thus survey a wider design space than has been achieved with previous protein[47,48] or RNA[12] scaffolds. DNA or RNA nanostructures could be delivered or expressed as individual strands and assembled directly at the site of interest. Taken together, our results present a new opportunity to assemble precise, programmable structures in biological and cellular environments, which could lead to exciting in vitro and in vivo applications.

■ ASSOCIATED CONTENT

Supporting Information

Supplementary methods, structure naming conventions, notes about experiments, modeling details, and six supplementary figures. This material is available free of charge via the Internet at http://pubs.acs.org.

■ AUTHOR INFORMATION

Notes

The authors declare no competing financial interest.

■ ACKNOWLEDGMENTS

We thank Bryan Wei, Dave Zhang, Erik Winfree, and Robert Barish for discussion. This work was funded by a DARPA Living Foundries grant HR0011-12-C-0061 to P.A.S. and P.Y., an Office of Naval Research (ONR) Young Investigator Program award N000141110914 to P.Y., an ONR grant N000141010827 to P.Y., an National Science Foundation (NSF) Faculty Early Career Development Award 1054898 and an NSF grant 1162459 to P.Y. C.M. acknowledges a graduate research fellowship from the Fannie and John Hertz Foundation. M.D. acknowledges an international student research fellowship from the Howard Hughes Medical Institute.

■ REFERENCES

(1) Yan, H.; Park, S. H.; Finkelstein, G.; Reif, J. H.; LaBean, T. H. *Science* **2003**, *301*, 1882–4.
(2) Chworos, A.; Severcan, I.; Koyfman, A. Y.; Weinkam, P.; Oroudjev, E.; Hansma, H. G.; Jaeger, L. *Science* **2004**, *306*, 2068–72.
(3) Rothemund, P. W. K.; Papadakis, N.; Winfree, E. *PLoS Biol.* **2004**, *2*, e424.
(4) Rothemund, P. W. K. *Nature* **2006**, *440*, 297–302.
(5) Yin, P.; Hariadi, R. F.; Sahu, S.; Choi, H. M. T.; Park, S. H.; Labean, T. H.; Reif, J. H. *Science* **2008**, *321*, 824–6.
(6) Douglas, S. M.; Dietz, H.; Liedl, T.; Högberg, B.; Graf, F.; Shih, W. M. *Nature* **2009**, *459*, 414–8.
(7) Dietz, H.; Douglas, S. M.; Shih, W. M. *Science* **2009**, *325*, 725–30.
(8) Zheng, J.; Birktoft, J. J.; Chen, Y.; Wang, T.; Sha, R.; Constantinou, P. E.; Ginell, S. L.; Mao, C.; Seeman, N. C. *Nature* **2009**, *461*, 74–7.
(9) Andersen, E. S.; Dong, M.; Nielsen, M. M.; Jahn, K.; Subramani, R.; Mamdouh, W.; Golas, M. M.; Sander, B.; Stark, H.; Oliveira, C. L. P.; Pedersen, J. S.; Birkedal, V.; Besenbacher, F.; Gothelf, K. V; Kjems, J. *Nature* **2009**, *459*, 73–6.
(10) Yang, H.; McLaughlin, C. K.; Aldaye, F. A.; Hamblin, G. D.; Rys, A. Z.; Rouiller, I.; Sleiman, H. F. *Nature Chem.* **2009**, *1*, 390–6.
(11) Han, D.; Pal, S.; Nangreave, J.; Deng, Z.; Liu, Y.; Yan, H. *Science* **2011**, *332*, 342–6.
(12) Delebecque, C. J.; Lindner, A. B.; Silver, P. A.; Aldaye, F. A. *Science* **2011**, *333*, 470–4.
(13) Wei, B.; Dai, M.; Yin, P. *Nature* **2012**, *485*, 623–6.
(14) Ke, Y.; Ong, L. L.; Shih, W. M.; Yin, P. *Science* **2012**, *338*, 1177–1183.
(15) Sherman, W. B.; Seeman, N. C. *Nano Lett.* **2004**, *4*, 1203–1207.
(16) Yin, P.; Yan, H.; Daniell, X. G.; Turberfield, A. J.; Reif, J. H. *Angew. Chem., Int. Ed.* **2004**, *43*, 4906–11.
(17) Zhang, D. Y.; Turberfield, A. J.; Yurke, B.; Winfree, E. *Science* **2007**, *318*, 1121–5.
(18) Yin, P.; Choi, H. M. T.; Calvert, C. R.; Pierce, N. a *Nature* **2008**, *451*, 318–22.
(19) Omabegho, T.; Sha, R.; Seeman, N. C. *Science* **2009**, *324*, 67–71.
(20) Lund, K.; Manzo, A. J.; Dabby, N.; Michelotti, N.; Johnson-Buck, A.; Nangreave, J.; Taylor, S.; Pei, R.; Stojanovic, M. N.; Walter, N. G.; Winfree, E.; Yan, H. *Nature* **2010**, *465*, 206–10.
(21) Qian, L.; Winfree, E. *Science* **2011**, *332*, 1196–201.
(22) Wickham, S. F. J.; Bath, J.; Katsuda, Y.; Endo, M.; Hidaka, K.; Sugiyama, H.; Turberfield, A. J. *Nat. Nanotechnol.* **2012**, *7*, 169–73.
(23) Douglas, S. M.; Bachelet, I.; Church, G. M. *Science* **2012**, *335*, 831–4.
(24) Derr, N. D.; Goodman, B. S.; Jungmann, R.; Leschziner, A. E.; Shih, W. M.; Reck-Peterson, S. L. *Science* **2012**, *338*, 662–5.

(25) Acuna, G. P.; Möller, F. M.; Holzmeister, P.; Beater, S.; Lalkens, B.; Tinnefeld, P. *Science* **2012**, *338*, 506−10.
(26) Lin, C.; Jungmann, R.; Leifer, A. M.; Li, C.; Levner, D.; Church, G. M.; Shih, W. M.; Yin, P. *Nature Chem.* **2012**, *4*, 832−9.
(27) Maune, H. T.; Han, S.-P.; Barish, R. D.; Bockrath, M.; Iii, W. A. G.; Rothemund, P. W. K.; Winfree, E. *Nat. Nanotechnol.* **2010**, *5*, 61−6.
(28) Douglas, S. M.; Chou, J. J.; Shih, W. M. *Proc. Natl. Acad. Sci. U.S.A.* **2007**, *104*, 6644−8.
(29) Lee, H.; Lytton-Jean, A. K. R.; Chen, Y.; Love, K. T.; Park, A. I.; Karagiannis, E. D.; Sehgal, A.; Querbes, W.; Zurenko, C. S.; Jayaraman, M.; Peng, C. G.; Charisse, K.; Borodovsky, A.; Manoharan, M.; Donahoe, J. S.; Truelove, J.; Nahrendorf, M.; Langer, R.; Anderson, D. G. *Nat. Nanotechnol.* **2012**, *7*, 389−93.
(30) Liu, X.; Xu, Y.; Yu, T.; Clifford, C.; Liu, Y.; Yan, H.; Chang, Y. *Nano Lett.* **2012**, *12*, 4254−9.
(31) Jungmann, R.; Liedl, T.; Sobey, T. L.; Shih, W.; Simmel, F. C. *J. Am. Chem. Soc.* **2008**, *130*, 10062−3.
(32) Evans, C. G.; Hariadi, R. F.; Winfree, E. *J. Am. Chem. Soc.* **2012**, *134*, 10485−92.
(33) Schulman, R.; Yurke, B.; Winfree, E. *Proc. Natl. Acad. Sci. U.S.A.* **2012**, *109*, 6405−10.
(34) Sobczak, J. J.; Martin, T. G.; Gerling, T.; Dietz, H. *Science* **2012**, *338*, 1458−61.
(35) Dirks, R. M.; Pierce, N. A. *Proc. Natl. Acad. Sci. U.S.A.* **2004**, *101*, 15275−8.
(36) Wei, B.; Dai, M.; Myhrvold, C.; Ke, Y.; Jungmann, R.; Yin, P. *J. Am. Chem. Soc.*, in press.
(37) Winfree, E.; Liu, F.; Wenzler, L. a; Seeman, N. C. *Nature* **1998**, *394*, 539−44.
(38) Martin, T. G.; Dietz, H. *Nat. Commun.* **2012**, *3*, 1103.
(39) Alatossava, T.; Jütte, H.; Kuhn, A.; Kellenberger, E. *J. Bacteriol.* **1985**, *162*, 413−9.
(40) Shabala, L.; Bowman, J.; Brown, J.; Ross, T.; McMeekin, T.; Shabala, S. *Environ. Microbiol.* **2009**, *11*, 137−48.
(41) Jungmann, R.; Steinhauer, C.; Scheible, M.; Kuzyk, A.; Tinnefeld, P.; Simmel, F. C. *Nano Lett.* **2010**, *10*, 4756−61.
(42) Yurke, B.; Turberfield, A. J.; Mills, A. P., Jr.; Simmel, F. C.; Neumann, J. L. *Nature* **2000**, *406*, 605−608.
(43) Seelig, G.; Soloveichik, D.; Zhang, D. Y.; Winfree, E. *Science (New York, N.Y.)* **2006**, *314*, 1585−8.
(44) Choi, H. M. T.; Chang, J. Y.; Trinh, L. A.; Padilla, J. E.; Fraser, S. E.; Pierce, N. A. *Nat. Biotechnol.* **2010**, *28*, 1208−12.
(45) Venkataraman, S.; Dirks, R. M.; Rothemund, P. W. K.; Winfree, E.; Pierce, N. A. *Nat. Nanotechnol.* **2007**, *2*, 490−4.
(46) Zhang, D. Y.; Chen, S. X.; Yin, P. *Nature Chem.* **2012**, *4*, 208−14.
(47) Dueber, J. E.; Wu, G. C.; Malmirchegini, G. R.; Moon, T. S.; Petzold, C. J.; Ullal, A. V; Prather, K. L. J.; Keasling, J. D. *Nat. Biotechnol.* **2009**, *27*, 753−9.
(48) Whitaker, W. R.; Davis, S. A; Arkin, A. P.; Dueber, J. E. *Proc. Natl. Acad. Sci. U.S.A.* **2012**, *109*, 18090−5.

11.2 DNA cages

Polyhedra Self-Assembled from DNA Tripods and Characterized with 3D DNA-PAINT

Ryosuke Iinuma *et al.*

Science **344**, 65 (2014);
DOI: 10.1126/science.1250944

Science (print ISSN 0036-8075; online ISSN 1095-9203) is published weekly, except the last week in December, by the American Association for the Advancement of Science, 1200 New York Avenue NW, Washington, DC 20005.

Polyhedra Self-Assembled from DNA Tripods and Characterized with 3D DNA-PAINT

Ryosuke Iinuma,[1]*† Yonggang Ke,[1,2,3]*‡ Ralf Jungmann,[1,4]* Thomas Schlichthaerle,[1] Johannes B. Woehrstein,[1,4] Peng Yin[1,4]§

DNA self-assembly has produced diverse synthetic three-dimensional polyhedra. These structures typically have a molecular weight no greater than 5 megadaltons. We report a simple, general strategy for one-step self-assembly of wireframe DNA polyhedra that are more massive than most previous structures. A stiff three-arm-junction DNA origami tile motif with precisely controlled angles and arm lengths was used for hierarchical assembly of polyhedra. We experimentally constructed a tetrahedron (20 megadaltons), a triangular prism (30 megadaltons), a cube (40 megadaltons), a pentagonal prism (50 megadaltons), and a hexagonal prism (60 megadaltons) with edge widths of 100 nanometers. The structures were visualized by means of transmission electron microscopy and three-dimensional DNA-PAINT super-resolution fluorescent microscopy of single molecules in solution.

DNA nanotechnology has produced a wide range of shape-controlled nanostructures (*1*–*10*). Hollow polyhedra (*1*, *5*, *11*–*26*) are particularly interesting because they resemble natural structures such as viral capsids and promise applications for scaffolding and encapsulating functional materials. Previous work has constructed diverse polyhedra, such as tetrahedra (*13*, *16*, *20*, *24*), cubes (*1*, *19*, *23*), bipyramids (*15*), truncated octahedra (*11*), octahedra (*12*), dodecahedra (*16*, *18*), icosahedra (*17*, *21*), nanoprisms (*14*, *22*, *25*, *26*), and buckyballs (*16*), with ≤80-nm sizes and ≤5-MD molecular weights (such as Fig. 1A, structures 1 to 8). Assembly strategies include step-wise synthesis (*1*, *11*, *21*, *22*), folding of a long scaffold (*12*, *19*, *20*, *24*, *25*), cooperative assembly of individual strands (*13*–*15*, *18*, *26*), and hierarchical assembly of branched DNA tiles (*16*, *17*, *23*).

A promising route to scaling up polyhedra is the hierarchical assembly of larger monomers. Previous work using small three-arm-junction (80 kD) (*16*, *23*) and five-arm-junction (130 kD) (*17*) tiles has produced several ≤5-MD polyhedra (such as Fig. 1A, structures 5 to 7). Additionally, a 15-MD icosahedron (Fig. 1A, structure 9) (*5*) was assembled from three double-triangle–shaped origami monomers. Perhaps because of the lack of precise geometric control of the flexible double-triangle monomers, this icosahedron has low yield (*5*), and this method has not been generalized to construct more complex polyhedra.

We developed a more general strategy for hierarchical self-assembly of polyhedra from megadalton monomers using a DNA "tripod," a 5-MD three-arm-junction origami tile [60 times more massive than previous three-arm tiles (*16*, *23*)]. The tripod motif features inter-arm angles controlled by supporting struts and strengthened by vertex helices. Self-assembly of tripods into wireframe polyhedra is further facilitated by a dynamic connector design. We constructed a tetrahedron (~20 MD), a triangular prism (~30 MD), a cube (~40 MD), a pentagonal prism (~50 MD), and a hexagonal prism (~60 MD) (Fig. 1A and fig. S1) (*27*). With 100-nm edges, these polyhedra have a size comparable with those of bacterial microcompartments such as carboxysomes.

To characterize the three-dimensional (3D) single-molecule morphology of these polyhedra, we used a DNA-based super-resolution fluorescence imaging method (resolution below the diffraction limit) called DNA-PAINT (a variation of point accumulation for imaging in nanoscale topography) (*28*–*30*). Unlike traditional transmission electron microscopy (TEM), which images the samples in a vacuum under dried and stained conditions, 3D DNA-PAINT introduces minimal distortion to the structures in a "native" hydrated imaging environment.

Design

In one-pot annealing, the scaffold and staple strands first assemble into a tripod origami monomer, and then the tripods (without intermediate purification) assemble into the polyhedron (Fig. 1A). Diverse polyhedra can be constructed by using tripods with different designed inter-arm angles. The tripod has three equal-length (~50 nm) stiff arms connected at the vertex (connection details are available in fig. S2) with controlled inter-arm angles (Fig. 1B). To ensure stiffness, each arm contains 16 parallel double-helices packed on a honeycomb lattice (*5*) with twofold rotational symmetry. A supporting "strut" consisting of two double-helices controls the angle between the

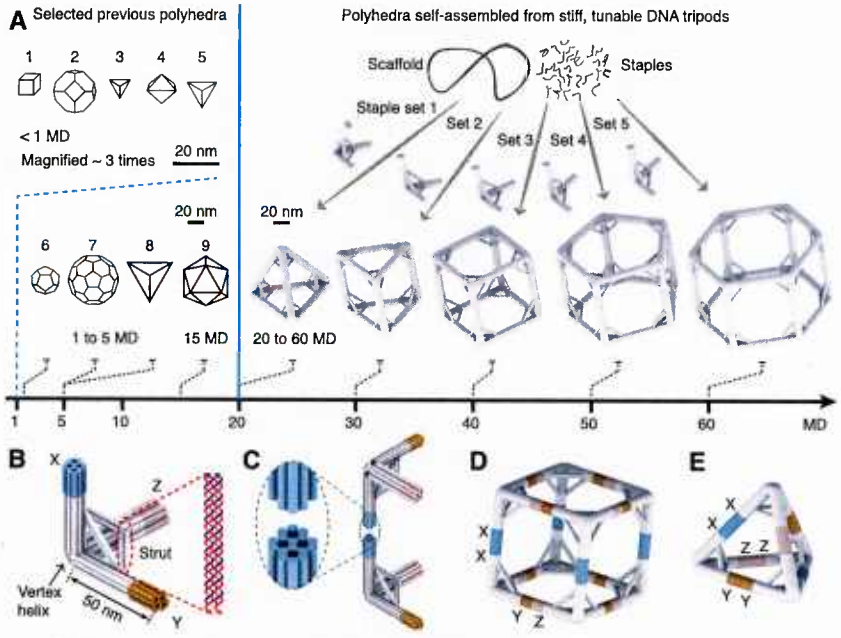

Fig. 1. DNA-origami polyhedra. (**A**) Polyhedra self-assembled from DNA tripods with tunable inter-arm angles, and comparison of their sizes and molecular weights with selected previous polyhedra (structures 1 to 9) (details are provided in fig. S1). (**B**) Design diagram of a tripod. Cylinders represent DNA double helices. Details of the arm connection at the vertex are provided in fig. S2. (**C**) Cylinder model illustrating the connection between two tripod monomers. (**D** and **E**) Connection schemes for assembling (E) the tetrahedron and (D) other polyhedra (represented here by the cube design).

[1]Wyss Institute for Biologically Inspired Engineering, Harvard University, Boston, MA 02115, USA. [2]Department of Cancer Biology, Dana-Farber Cancer Institute, Harvard Medical School, Boston, MA 02115, USA. [3]Department of Biological Chemistry and Molecular Pharmacology, Harvard Medical School, Boston, MA 02115, USA. [4]Department of Systems Biology, Harvard Medical School, Boston, MA 02115, USA.

*These authors contributed equally to this work.
†Present address: JSR Life Sciences Corporation, Ibaraki 305-0841, Japan.
‡Present address: Wallace H. Coulter Department of Biomedical Engineering, Georgia Institute of Technology and Emory University, Atlanta, GA 30322, USA.
§Corresponding author. E-mail: py@hms.harvard.edu

two arms. We name a tripod according to its three inter-arm angles (for example, the tetrahedron and the cube are respectively assembled from 60°-60°-60° and 90°-90°-90° tripods). To avoid potential unwanted aggregation resulting from blunt-end stacking of DNA helices (*4*), up to six short DNA double-helices (denoted "vertex helices") are included at the vertex so as to partially conceal its blunt duplex ends (Fig. 1B). The number of helices and their lengths vary for different polyhedra (fig. S2). Additionally, the vertex helices are expected to help maintain inter-arm angles by increasing rigidity of the vertices. Two connection strategies are used to assemble tripods into polyhedra. To facilitate exposition, the three arms are denoted as X-arm, Y-arm, and Z-arm (Fig. 1B). Connecting X-arm to X-arm (Fig. 1C) and Y-arm to Z-arm produces polyhedra (such as a cube) (Fig. 1D) other than the tetrahedron, which is assembled by connecting X to X, Y to Y, and Z to Z (Fig. 1E).

Results

Tripod Conformation Control with Struts

First, we verified that the inter-arm angle was controlled by the length of the supporting strut. Gel electrophoresis of 60°-60°-60° and 90°-90°-90° tripods revealed a dominant band for each tripod (Fig. 2A), confirming their correct formation. Consistent with its more compact designed conformation, the 60°-60°-60° tripod migrated slightly faster than did the 90°-90°-90° one. The two tripod bands each were purified, were imaged with TEM, and showed designed tripod-like morphologies (Fig. 2B). The measured inter-arm angles were slightly smaller than designed [53 ± 5° (SD, n = 60 tripods) for 60°-60°-60° tripods; 87 ± 4° (SD, n = 60 tripods) for 90°-90°-90° tripods], possibly reflecting a small degree of strut bending.

Connector Designs

The strands connecting the tripods are called "connectors." Connector designs affected the polyhedra assembly yields. Two designs were tested for the cube. In scheme i, each 30-base connector spanned two adjacent tripods, with a 28-base segment anchored on one tripod and another 2-base (sticky end) anchored on the other (Fig. 2C and fig. S3). Gel electrophoresis (shown in Fig. 2C and quantified in Fig. 2E) revealed that the assembly yield was affected by the number of connected helices (n): a product band was only observed for $4 \leq n \leq 12$; for $n < 4$, the dominant bands were monomers, likely reflecting overly

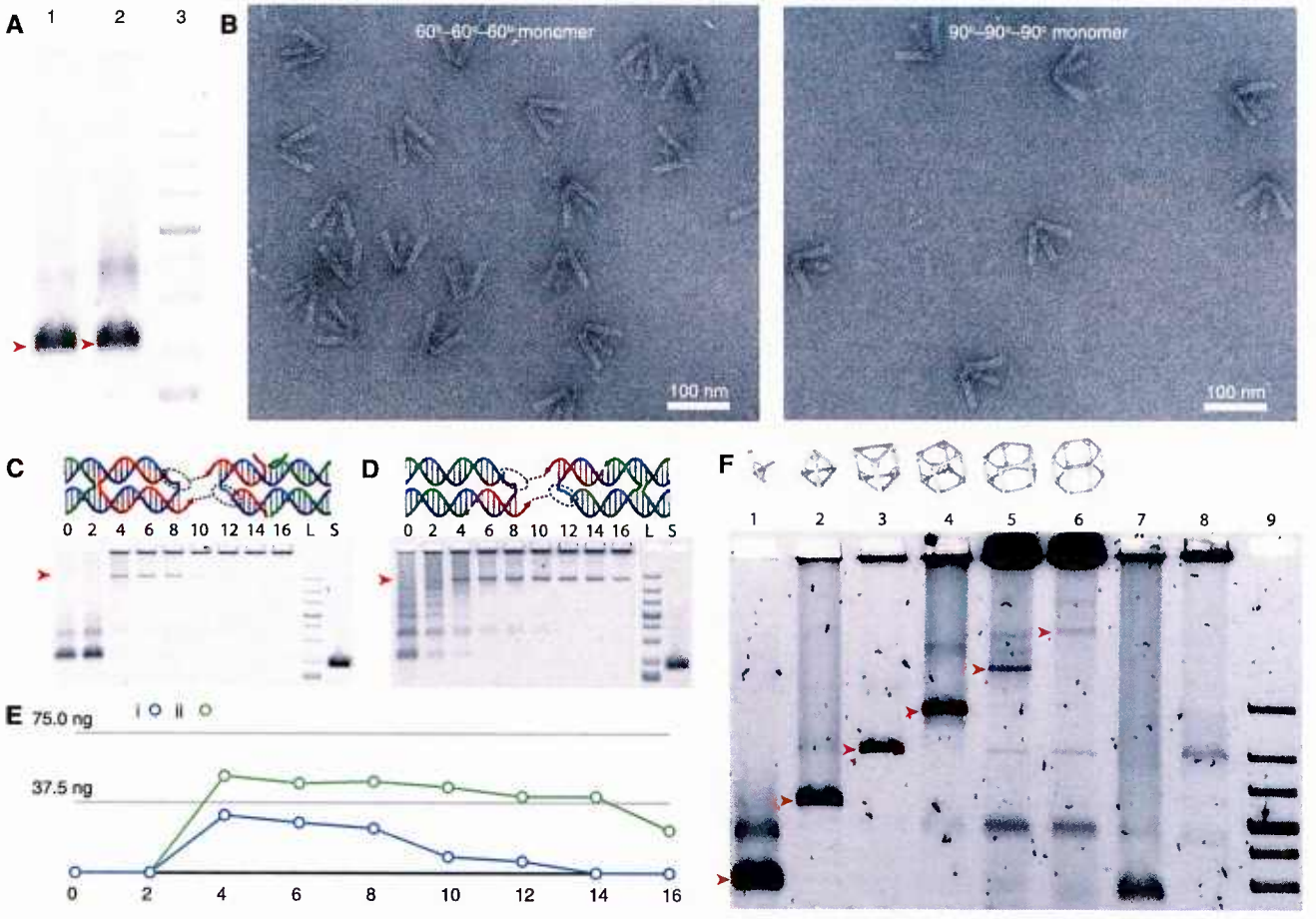

Fig. 2. Self-assembly of DNA tripods and polyhedra. (**A**) Gel electrophoresis and (**B**) TEM images of the 60°-60°-60° (lane 1 in the gel) and 90°-90°-90° (lane 2) tripods. Gel lane 3 is a 1-kb ladder. Gel electrophoresis involves 1.5% native agarose gel and ice water bath. (**C** and **D**) Two schemes of connector designs and corresponding gel electrophoresis results. For each scheme, the strand model depicts the connection between two pairs of DNA duplexes. The number above a gel lane denotes the number of connected helices between two adjacent arms. Lane L is a 1-kb ladder, and lane S is a scaffold. Arrowheads indicate the bands corresponding to assembled cubes. (**C**) Scheme i: long (30 nt) connector (red) including a 2-nt sticky end. The complete 30-nt connector is only shown on the left, with a 28-nt segment anchored on the left helices and a 2-nt exposed sticky end available for hybridization with the 90°-90°-90° right neighbor (dashed circle depicts hybridization site). (**D**) Scheme ii: short (11 nt) connector including a 2-nt sticky end. (**E**) Assembly yields of the cubes, calculated as intensity ratio between a cube band and the corresponding scaffold band. (**F**) Agarose gel electrophoresis of the polyhedra. Lane 1 is the 90°-90°-90° monomer. Lanes 2 to 6 are polyhedra. Lane 7 is the assembly reaction containing tripods without struts. Lane 8 is the assembly reaction containing 90°-90°-90° tripods without vertex helices. Lane 9 is a 1-kb ladder. Gel bands corresponding to desired products are marked with arrowheads. Gel electrophoresis involves 0.8% native agarose gel and ice water bath.

weak inter-monomer connections; for $n > 12$, aggregations dominated.

In scheme i, the connectors were stably anchored (forming 28 base pairs) on tripods before inter-monomer connection occurred. In scheme ii, the connector was shortened from 30 to 11 bases so that it should only be anchored to two adjacent tripods by 9- and 2-base segments in the assembled cube (Fig. 2D) and only dynamically binds to a monomeric tripod. Compared with the stably attached connector design, the dynamic connector design could potentially help correct inter-monomer mismatches that occurred during the assembly because such mismatches would be less likely frozen in a kinetic trap. Indeed, scheme ii showed substantially increased assembly yield (Fig. 2E). It was thus used for subsequent polyhedra designs, except for the tetrahedron, in which scheme i produced sufficient yield for this relatively simple structure. The assembly yields were estimated from the gel (Fig. 2F). The 90°-90°-90° monomer sample (Fig. 2F, lane 1) showed a strong monomer band and a putative dimer band (not studied with TEM, ~27% intensity as compared with the monomer). We define the assembly yield of a polyhedron as the ratio between its product band intensity and the combined intensity of the 90°-90°-90° monomer and dimer bands (lane 1) and obtained yields of 45, 24, 20, 4.2, and 0.11% for the tetrahedron, the triangular prism, the cube, the pentagonal prism, and the hexagonal prism, respectively (Fig. 2F).

Table 1. Strut designs of the polyhedra. All units are nanometers. Entries are the designed length of the strut connecting the (i) Y-arm and Z-arm, (ii) X-arm and Z-arm, or (iii) X-arm and Y-arm or the designed distance from the vertex to the strut attachment point on the (iv) X-, (v) Y-, or (vi) Z-arm.

	i	ii	iii	iv	v	vi
Tetrahedron	28	28	28	29	29	29
Triangular prism	18	26	26	18	18	18
Cube	30	30	30	21	21	21
Pentagonal prism	32	26	26	19	18	18
Hexagonal prism	37	28	28	20	20	20

Polyhedra Assembly

The lengths and the attachment points of the struts varied for each polyhedron (Table 1). The tetrahedron, the triangular prism, the cube, the pentagonal prism, and the hexagonal prism should

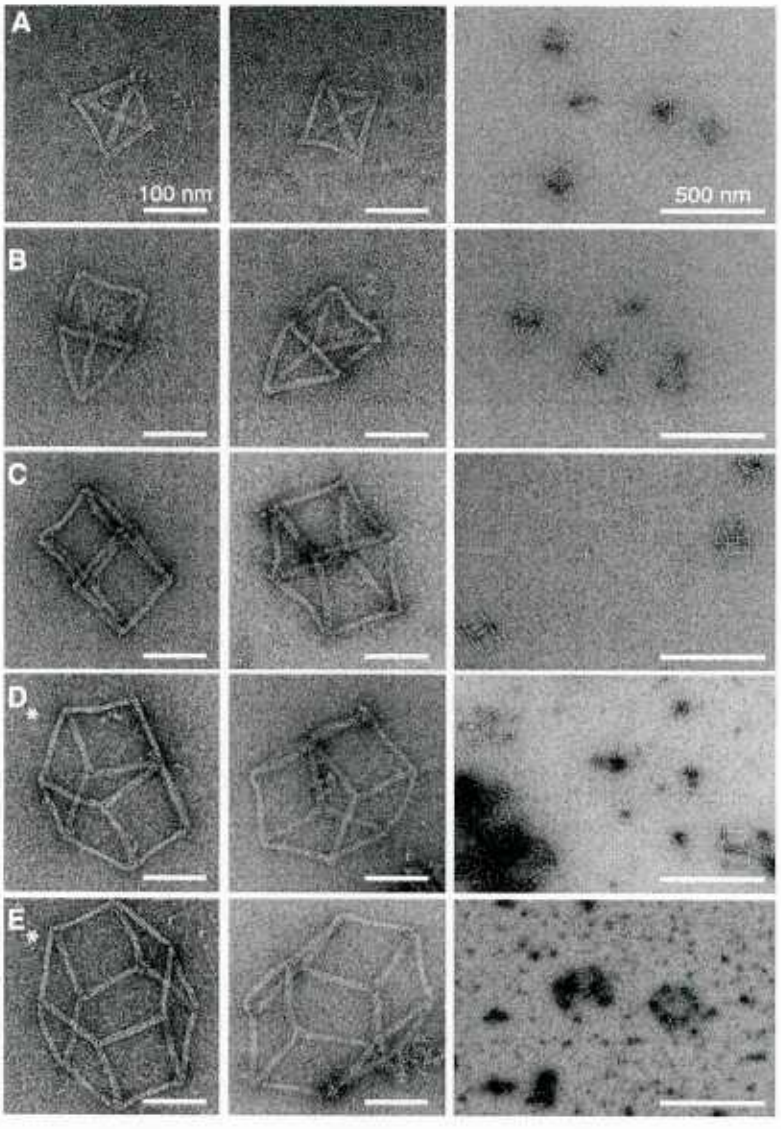

Fig. 3. TEM images of polyhedra. The zoomed-in (columns 1 and 2) and zoomed-out (column 3) images are shown for (**A**) the tetrahedron, (**B**) the triangular prism, (**C**) the cube, (**D**) the pentagonal prism, and (**E**) the hexagonal prism. Images of the tetrahedron, the triangular prism, and the cube were acquired from purified samples. Images of the pentagonal prism and the hexagonal prism were collected from crude samples (denoted with an asterisk). Scale bars are 100 nm in the zoomed-in TEM images and 500 nm in the zoomed-out images. Aggregates are clearly visible for unpurified samples [such as in (D), right].

be assembled from monomers with designed 60°-60°-60°, 90°-90°-60°, 90°-90°-90°, 90°-90°-108°, and 90°-90°-120° angles, respectively (Fig. 1A). The first three monomers indeed produced tetrahedra, triangular prisms, and cubes [verified with gel electrophoresis (Fig. 2F) and TEM imaging (Fig. 3, A to C)], suggesting accurate control for angles within 90°. However, the pentagonal prism was assembled from monomers with designed angles of 90°-90°-120° (instead of 90°-90°-108°), and the hexagonal prism from 90°-90°-140° (instead of 90°-90°-120°). Thus, the assembly of these two polyhedra requires monomers with designed Y-Z angles greater than those of the design criteria. This requirement likely reflects slight bending of the relevant struts, which could be compensated by using longer struts.

Effects of Struts and Vertex Helices

We next verified that both the struts and the vertex helices were required for the tripods to assemble into the designed polyhedron. Three samples were prepared for cube assembly by using tripods that contain (i) both the struts and the vertex helices (Fig. 2F, lane 4), (ii) the vertex helices but not the struts (lane 7), and (iii) the struts but not the vertex helices (lane 8); the latter samples were subjected to gel electrophoresis after annealing. The first sample showed a sharp strong band corresponding to the cube (verified with TEM) (Fig. 3C). The second failed to produce any clear product band. The third produced substantial aggregates and a clear but weak band with mobility comparable with that of the triangular prism. This band may correspond to a hexamer, but its molecular morphology was not investigated. On the basis of the above experiments, we included both the struts and the vertex helices in the tripods for subsequent polyhedra assembly.

TEM Characterization

Product bands were purified and imaged under TEM. For the tetrahedron, the triangular prism, and the cube, most structures appeared as intact polyhedra; a small fraction of broken structures (< 20%) were likely ruptured during the purification and imaging (Fig. 3, A to C). In contrast, few intact structures were observed for the purified pentagonal and hexagonal prisms. Thus, unpurified samples for these two were directly imaged, and the expected molecular morphologies were observed (Fig. 3, D and E). Additional images are provided in figs. S4 to S13. The struts are clearly visible in many images (a zoomed-in example is provided in fig. S14).

3D DNA-PAINT Super-Resolution Microscopy

Localization-based 3D super-resolution fluorescence microscopy (*31*–*33*) offers a minimally invasive way to obtain true single-molecule 3D images of DNA nanostructures in their "native" hydrated environment (distorted and broken tetrahedra, likely caused by the TEM imaging conditions, are shown in figs. S4 and S15). In stochastic reconstruction microscopy (*34*), most molecules are switched to a fluorescent dark (OFF) state, and only a few emit fluorescence (ON state). Each molecule is localized with nanometer precision by fitting its emission to a 2D Gaussian function. In DNA-PAINT, the "switching" between ON and OFF states is facilitated through the repetitive, transient binding of fluorescently labeled oligonucleotides

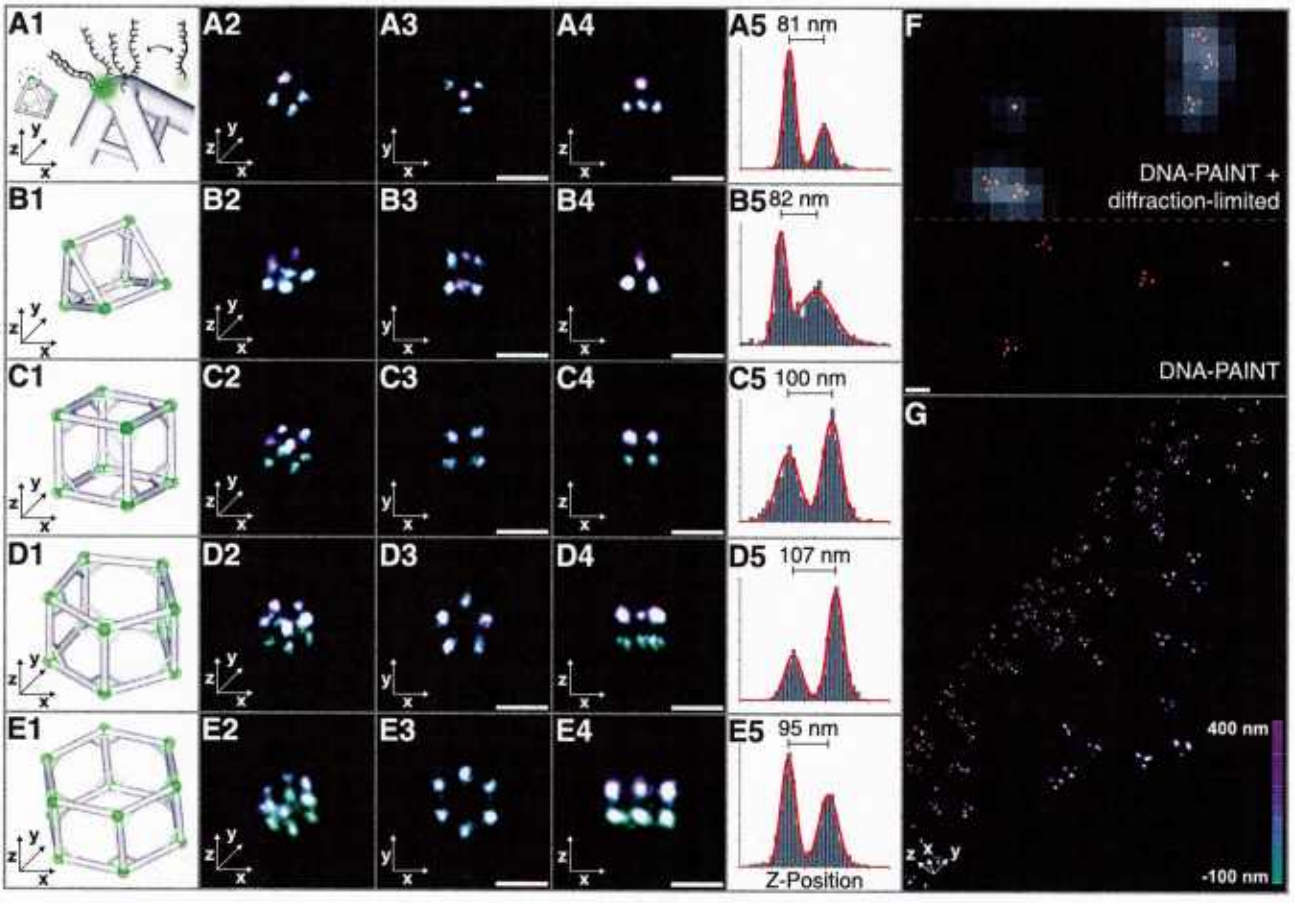

Fig. 4. 3D DNA-PAINT super-resolution fluorescence imaging of polyhedra. (**A1**) Staple strands at the vertices of each polyhedron were extended with single-stranded docking sequences for 3D DNA-PAINT super-resolution imaging. (**A1** to **E1**) Schematics of polyhedra, with DNA-PAINT sites highlighted in green. (**A2** to **E2**) 3D DNA-PAINT super-resolution reconstruction of typical polyhedra shown in the same perspective as depicted in A1 to E1. (**A3** to **E3**) 2D *x*-*y* projection. (**A4** to **E4**) 2D *x*-*z* projection. (**A5** to **E5**) Height measurements of the polyhedra obtained from the cross-sectional histograms in the *x*-*z* projections. (**F**) A larger 2D super-resolution *x*-*y* projection view of tetrahedra and drift markers (bright individual dots). The diffraction-limited image is superimposed on the super-resolution image in the upper half. (**G**) Tilted 3D view of a larger-field-of-view image of the tetrahedron. Drift markers appear as bright individual dots. Scale bars, 200 nm. Color indicates height in the *z* direction.

("imager" strands) to complementary "docking" strands (*24*, *28*, *29*, *35*).

We extended DNA-PAINT to 3D imaging (*29*) using optical astigmatism (*31*, *36*), in which a cylindrical lens used in the imaging path "converts" the spherical point spread function (PSF) of a molecule to an elliptical PSF when imaged out of focus. The degree and orientation of the elliptical PSF depends on the displacement and direction of the point source from the current focal imaging plane and is used to determine its z position (*31*, *36*). We applied 3D DNA-PAINT to obtain subdiffraction-resolution single-molecule images of the polyhedra. To ensure all the vertices of a polyhedron will be imaged, each vertex is modified with multiple (~18) 9-nucleotide (nt) docking strands (Fig. 4A1) in a symmetric arrangement (fig. S2). For surface immobilization, a subset of strands along the polyhedron edges were modified with 21-nt extensions, which were hybridized to biotinylated complementary strands attached to a streptavidin covered glass slide [(*27*), DNA sequences].

Using 3D DNA-PAINT microscopy, all five polyhedra showed designed 3D patterns of vertices (Fig. 4, columns 1 to 4) with expected heights (Fig. 4, A5 to E5), suggesting that the solution shape of the structures is maintained during surface immobilization and imaging. We quantified the tetrahedra formation and imaging yields (Fig. 4, F and G, and fig. S16). Out of 285 structures, 253 (89%) contained four spots in the expected tetrahedral geometry. Height measurement yielded 82 ± 15 nm, which is consistent with the designed value (82 nm). Single DNA-PAINT binding events were localized with an accuracy of 5.4 nm in x-y and 9.8 nm in z [(*27*) describes how localization accuracy was determined]. This z localization accuracy almost completely accounts for the 15-nm spread in the height measurement distribution. The calculated localization precisions translate to an obtainable resolution of ~13 nm in x and y, and ~24 nm in z. Movies S1 and S2 are 3D DNA-PAINT videos. Design is provided in figs. S17 to S22, and tables S1 to S7 have sequence details.

Discussion

Previous work demonstrated diverse DNA polyhedra self-assembled from small three-arm-junction tiles (~80 kD) (*16*, *23*), which consist of three double-helix arms connected by flexible single-stranded hinges. However, straightforward implementation of megadalton three-arm origami tiles by use of similar flexible inter-arm hinges (tripods with no struts or vertex helices) failed to produce well-formed polyhedra (Fig. 2F, lane 7). An origami tripod contains 50 times more distinct strands than do previous three-arm-junction tiles (formed from three distinct strands) and is 60 times more massive in molecular weight. Apart from the challenges associated with the more error-prone construction of the more complex monomers from individual strands, successful hierarchical assembly of such large monomers into polyhedra also needs to overcome much slower reaction kinetics, caused by the larger size and lower concentration of the tripod monomers. The stiff DNA tripods, with rationally designed inter-arm angles controlled by supporting struts and vertex helices, lead to successful construction of diverse polyhedra, suggesting that conformation control of branched megadalton monomers can facilitate their successful assembly into higher-order structures.

The design principles of DNA tripods may be extended to stiff megadalton n-arm ($n \geq 4$) branched motifs with controlled inter-arm angles. Self-assembly with such n-arm motifs could be used to construct more sophisticated polyhedra and potentially extended 2D and 3D lattices with ≤100-nm tunable cavities. Such structures could potentially be used to template guest molecules for diverse applications—for example, spatially arranging multiple enzymes into efficient reaction cascades (*37*) or nanoparticles to achieve useful photonic properties (*38*, *39*). Furthermore, the DNA polyhedra constructed here, with a size comparable with those of bacterial microcompartments, may potentially be used as skeletons for making compartments with precisely controlled dimensions and shapes by wrapping lipid membranes around their outer surfaces (*40*). Such membrane-enclosed microcompartments could potentially serve as bioreactors for synthesis of useful products or as delivery vehicles for therapeutic cargo (*25*).

For 3D characterization of DNA nanostructures, super-resolution fluorescence microscopy (such as 3D DNA-PAINT) provides complementary capabilities to present electron microscopy [such as cryogenic electron microscopy (cryo-EM) (*12*, *16*, *17*, *23*)]. Whereas cryo-EM offers higher spatial resolution imaging of unlabeled structures, DNA-PAINT is less technically involved to implement, obtains true single-molecule images of individual structures (rather than relying on class averaging), and preserves the multicolor capability of fluorescence microscopy (*29*). Additionally, DNA-PAINT in principle allows for observation of dynamic structural changes of nanostructures in their "native" hydrated environment, which is currently suitable for slow changes on the minutes time scale (such as the locomotion of synthetic DNA walkers) and potentially for faster motions with further development.

References and Notes

1. J. H. Chen, N. C. Seeman, *Nature* **350**, 631–633 (1991).
2. E. Winfree, F. Liu, L. A. Wenzler, N. C. Seeman, *Nature* **394**, 539–544 (1998).
3. P. W. Rothemund, N. Papadakis, E. Winfree, *PLOS Biol.* **2**, e424 (2004).
4. P. W. Rothemund, *Nature* **440**, 297–302 (2006).
5. S. M. Douglas *et al.*, *Nature* **459**, 414–418 (2009).
6. J. Zheng *et al.*, *Nature* **461**, 74–77 (2009).
7. B. Wei, M. Dai, P. Yin, *Nature* **485**, 623–626 (2012).
8. Y. Ke, L. L. Ong, W. M. Shih, P. Yin, *Science* **338**, 1177–1183 (2012).
9. D. Han *et al.*, *Science* **339**, 1412–1415 (2013).
10. V. Linko, H. Dietz, *Curr. Opin. Biotechnol.* **24**, 555–561 (2013).
11. Y. Zhang, N. C. Seeman, *J. Am. Chem. Soc.* **116**, 1661–1669 (1994).
12. W. M. Shih, J. D. Quispe, G. F. Joyce, *Nature* **427**, 618–621 (2004).
13. R. P. Goodman *et al.*, *Science* **310**, 1661–1665 (2005).
14. F. A. Aldaye, H. F. Sleiman, *J. Am. Chem. Soc.* **129**, 13376–13377 (2007).
15. C. M. Erben, R. P. Goodman, A. J. Turberfield, *J. Am. Chem. Soc.* **129**, 6992–6993 (2007).
16. Y. He *et al.*, *Nature* **452**, 198–201 (2008).
17. C. Zhang *et al.*, *Proc. Natl. Acad. Sci. U.S.A.* **105**, 10665–10669 (2008).
18. J. Zimmermann, M. P. Cebulla, S. Mönninghoff, G. von Kiedrowski, *Angew. Chem. Int. Ed. Engl.* **47**, 3626–3630 (2008).
19. E. S. Andersen *et al.*, *Nature* **459**, 73–76 (2009).
20. Y. Ke *et al.*, *Nano Lett.* **9**, 2445–2447 (2009).
21. D. Bhatia *et al.*, *Angew. Chem. Int. Ed. Engl.* **48**, 4134–4137 (2009).
22. H. Yang *et al.*, *Nat. Chem.* **1**, 390–396 (2009).
23. C. Zhang *et al.*, *J. Am. Chem. Soc.* **131**, 1413–1415 (2009).
24. D. M. Smith *et al.*, *J. Nucleic Acids* **2011**, 360954 (2011).
25. S. M. Douglas, I. Bachelet, G. M. Church, *Science* **335**, 831–834 (2012).
26. Z. Nie *et al.*, *Chem. Commun. (Camb.)* **49**, 2807–2809 (2013).
27. Materials and methods are available as supplementary materials on *Science* Online.
28. R. Jungmann *et al.*, *Nano Lett.* **10**, 4756–4761 (2010).
29. R. Jungmann *et al.*, *Nat. Methods* **11**, 313–318 (2014).
30. A. Sharonov, R. M. Hochstrasser, *Proc. Natl. Acad. Sci. U.S.A.* **103**, 18911–18916 (2006).
31. B. Huang, W. Wang, M. Bates, X. Zhuang, *Science* **319**, 810–813 (2008).
32. G. Shtengel *et al.*, *Proc. Natl. Acad. Sci. U.S.A.* **106**, 3125–3130 (2009).
33. J. J. Schmied *et al.*, *Nano Lett.* **13**, 781–785 (2013).
34. S. W. Hell, *Science* **316**, 1153–1158 (2007).
35. C. Lin *et al.*, *Nat. Chem.* **4**, 832–839 (2012).
36. H. P. Kao, A. S. Verkman, *Biophys. J.* **67**, 1291–1300 (1994).
37. J. Fu, M. Liu, Y. Liu, N. W. Woodbury, H. Yan, *J. Am. Chem. Soc.* **134**, 5516–5519 (2012).
38. G. P. Acuna *et al.*, *Science* **338**, 506–510 (2012).
39. A. Kuzyk *et al.*, *Nature* **483**, 311–314 (2012).
40. M. Langecker *et al.*, *Science* **338**, 932–936 (2012).

Acknowledgments: We thank S. Woo and W. Shih for discussions. This work is supported by an Office of Naval Research (ONR) Young Investigator Program Award (N000141110914), ONR grants (N000141010827 and N000141310593), an Army Research Office grant (W911NF1210238), a National Institutes of Health (NIH) Director's New Innovator Award (1DP2OD007292), a NIH Transformative Research Award (1R01EB018659), a NIH grant (5R21HD072481), a National Science Foundation (NSF) Faculty Early Career Development Award (CCF1054898), a NSF Expedition in Computing Award (CCF1317291), NSF grants (CCF1162459, CMMI1333215), a gift from JSR corporation, and a Wyss Institute for Biologically Inspired Engineering Faculty Startup Fund to P.Y. R.I. acknowledges support from JSR corporation. R.J. acknowledges support from the Alexander von Humboldt Foundation through a Feodor-Lynen Fellowship. R.I., Y.K., and R.J. contributed equally. R.I. and Y.K. designed the system, conducted the experiments, analyzed the data, and wrote the paper. R.J. designed and performed the super-resolution study, analyzed the data, and wrote the paper. T.S. and J.B.W. performed the super-resolution experiments and analyzed the data. P.Y. conceived, designed, and supervised the study; interpreted the data; and wrote the paper. All authors commented on and approved the manuscript.

Supplementary Materials

www.sciencemag.org/content/344/6179/65/suppl/DC1
Materials and Methods
Figs. S1 to S22
Tables S1 to S7
Movies S1 and S2

16 January 2014; accepted 28 February 2014
Published online 13 March 2014;
10.1126/science.1250944

11.3 Assembly across scales: DNA-directed hydrogel assembly

nature COMMUNICATIONS

ARTICLE

Received 24 Dec 2012 | Accepted 9 Jul 2013 | Published 9 Sep 2013

DOI: 10.1038/ncomms3275

DNA-directed self-assembly of shape-controlled hydrogels

Hao Qi[1,2,3], Majid Ghodousi[1,2,3], Yanan Du[1,2,3,†], Casey Grun[1], Hojae Bae[1,2], Peng Yin[1,4] & Ali Khademhosseini[1,2,3]

Using DNA as programmable, sequence-specific 'glues', shape-controlled hydrogel units are self-assembled into prescribed structures. Here we report that aggregates are produced using hydrogel cubes with edge lengths ranging from 30 μm to 1 mm, demonstrating assembly across scales. In a simple one-pot agitation reaction, 25 dimers are constructed in parallel from 50 distinct hydrogel cube species, demonstrating highly multiplexed assembly. Using hydrogel cuboids displaying face-specific DNA glues, diverse structures are achieved in aqueous and in interfacial agitation systems. These include dimers, extended chains and open network structures in an aqueous system, and dimers, chains of fixed length, T-junctions and square shapes in the interfacial system, demonstrating the versatility of the assembly system.

[1] Wyss Institute for Biologically Inspired Engineering, Harvard University, Boston, Massachusetts 02115, USA. [2] Department of Medicine, Center for Biomedical Engineering, Brigham and Women's Hospital, Harvard Medical School, Boston, Massachusetts 02115, USA. [3] Harvard-MIT Division of Health Sciences and Technology, Massachusetts Institute of Technology, Cambridge, Massachusetts 02139, USA. [4] Department of Systems Biology, Harvard Medical School, Boston, Massachusetts 02115, USA. † Present address: Department of Biomedical Engineering, School of Medicine, Tsinghua University, Beijing 100084, China. Correspondence and requests for materials should be addressed to P.Y. (email: py@hms.harvard.edu) or to A.K. (email: alik@rics.bwh.harvard.edu).

Self-assembly is the process by which small components self-organize into larger structures. Initially developed as a concept for engineering molecular complexes[1], self-assembly has been used to fabricate structures across scales, using monomer units ranging from nanoscale to macroscale dimensions[2]. Diverse techniques have been developed for mesoscale (micrometer to millimeter scale) self-assembly using magnetic force[3], hydrophile–lipophile balance[4,5], capillary interaction[6] and synthetic chemical binding[7] to control the assembled architecture.

Increasing the complexity of mesoscale self-assembly faces a crucial challenge, namely the difficulty of engineering a large set of orthogonal-specific binding interactions between the monomer units. This challenge can be potentially addressed by using DNA, biology's information carrier, as a programmable 'glue' to direct the assembly of mesoscale units. DNA contains four different nucleotide bases, each of which forms a base pair with another complementary base according to a set of canonical rules: adenine with thymine and guanine with cytosine. By simply arranging the sequence of these four nucleotide bases in different DNA strands, a combinatorially large set of binding interactions can be designed as specific hybridizations between complementary DNA strands. DNA hybridization-based self-assembly principles have been utilized successfully in the field of DNA nanotechnology to generate diverse complex synthetic DNA/RNA nanostructures[8–11] with arbitrarily prescribed geometry[12–29] and dynamic functions[30–41]. Furthermore, DNA strands can be made into hydrogels through covalent[42–44] or non-covalent interactions[45]. DNA has also been used as templates or glues to mediate the self-assembly of fluorophores[46], proteins[47], inorganic nanoparticles[48–51], carbon nanotube[52], lipid vesicles[53] and even living cells[54]. Recently, it was reported that short single-stranded DNA probes attached to a glass surface can successfully catch 100 μm size hydrogel microspheres decorated with sequences complementary to the probes[55]. Building on these previous successes, we address the next challenge here: to fully utilize the versatile programmability of DNA to direct the self-assembly of mesoscale objects into complex higher order structures with precisely prescribed architecture and geometry.

As part of our work to increase the complexity of the architectural and geometrical control of DNA-directed mesoscale assembly, here, we report on combining DNA-directed assembly principles with microfabrication technology to assemble mesoscale objects using shaped-controlled hydrogel units. The central conceptual innovation here is the decoration of DNA glues onto the prescribed surfaces of a non-spherical hydrogel object to produce an asymmetric glue pattern. These new assembling units, by combining the molecular programmability of the DNA glue and the shape controllability of microfabrication, will provide a powerful platform to achieve programmable assembly of complex mesoscale structures. To implement this strategy, a crucial technical innovation was necessary: we invent a novel strategy to use *in situ* rolling circle amplification (RCA) to produce and attach 'giant' DNA glues to the surface of hydrogel cubes. On the basis of this technical innovation, we demonstrate that giant DNA glue strands, but not short DNA primers, induce the assembly of hydrogel gel cubes with edge lengths across scales (30 μm to 1 mm), and that they result in the self-assembly of cube dimers in a highly multiplexed manner (25 orthogonal dimer pairs from 50 distinct cube species in one pot mixing). We then develop a method to engineer hydrogel cuboids that display giant DNA only on designated faces. Using this technology, we demonstrate the assembly, in aqueous and in interfacial systems, of diverse structures: linear chains with extended or fixed length, open networks, T-junctions and 2 × 2 square structures. Thus, we establish DNA-directed assembly of shape-controlled mesoscale units as a promising route to produce complex structures with sophisticated geometrical and architectural control.

Results

Self-assembly of hydrogels with uniform surface DNA glues. In the first part of our study, we developed a strategy to use complementary DNA molecules as glue to direct the self-assembly of hydrogel cubes with an edge length of 250 μm. Our initial attempt to assemble such hydrogel cubes carrying short complementary DNA strands (36 nt poly-T linker followed by 20 nt complementary sequences) failed to induce hydrogel assembly (Fig. 2c). This failure may be attributed to the rugged surface morphology of the hydrogel, as revealed by scanning electron microscopy (SEM, Fig. 1d), and the relatively small size and weak binding interactions between short complementary DNA strands. To accommodate for this rugged hydrogel surface, we developed a strategy to decorate hydrogel surface with 'giant' single-stranded DNA (Fig. 1a). Specifically, in step 1, amine-bearing short DNA strands (brown, 56 nt) were conjugated to PEG–NHS monomers (blue, MW 3,500 Da) using a standard protocol[56]. In step 2, the DNA–PEG–acrylate was mixed with photocrosslinkable poly (ethylene glycol) diacrylate (PEGDA, 4,000 MW) and 0.5 wt% photoinitiator, and exposed to UV under a photomask with 250 × 250 μm square holes. The height of the cubes was controlled using No. 2 microscope cover glass slides (250 μm in thickness) as spacers. Upon UV exposure, 250 × 250 × 250 μm hydrogel cubes uniformly modified with short DNA primers were produced. In step 3, the DNA primers hybridized with complementary, circular DNA templates (produced by circularization of short linear DNA using CircLigase), through a published procedure known as RCA[57]; the primer was amplified to produce a long strand with repeated sequences complementary to the circular template. In this paper, we call this long single-strand DNA product 'giant DNA'.

We first verified the successful production of giant DNA via RCA reaction in free solution and on glass slides (Supplementary Fig. S2a, agarose gel showed the synthesis of high molecular-weight product; Supplementary Fig. S2b, fluorescent microscopy image showed the formation of large membrane-like giant DNA; Supplementary Fig. S2c, SEM image showed the fiber-like giant DNA on glass slides). We then fabricated hydrogel cubes carrying giant DNA as described above and characterized them using fluorescent DNA staining. In comparison with hydrogels carrying short 56-nt DNA primers (Fig. 1b, phase contrast imaging; Fig. 1c, fluorescent imaging, DNA was stained by SYBR Gold), 3 h of RCA amplification at 37 °C resulted in significant DNA staining by SYBR Gold (Fig. 1e, phase contrast imaging; Fig. 1f, fluorescent imaging). As the DNA primer was tethered to the gel precursor, it was anticipated that giant DNA was amplified both inside and on the surface of hydrogel cubes. This is consistent with our experimental observation that only after RCA amplification, the hydrogel cubes stained with fluorescent DNA dye appeared with expected fluorescence under microscope (Fig. 1c,f). We note that as the RCA process is diffusion dependent and it is anticipated that it would be diffusion limited in the regions inside the gels relative to the gel surface. It is important that SEM imaging of the gel surface before (Fig. 1d) and after (Fig. 1g) the RCA amplification provided direct evidence that giant DNA was amplified on the gel surface. After the amplification, the initially rugged surface of the gel was covered uniformly by fiber-like structures, with reduced surface roughness (SEM image, Fig. 1g). Collectively, the above experiments suggested that the surfaces of hydrogel cubes were decorated with giant DNA produced via RCA, as designed.

Next, we demonstrated the giant-DNA-directed assembly of hydrogel cubes. Using the procedure described above, we

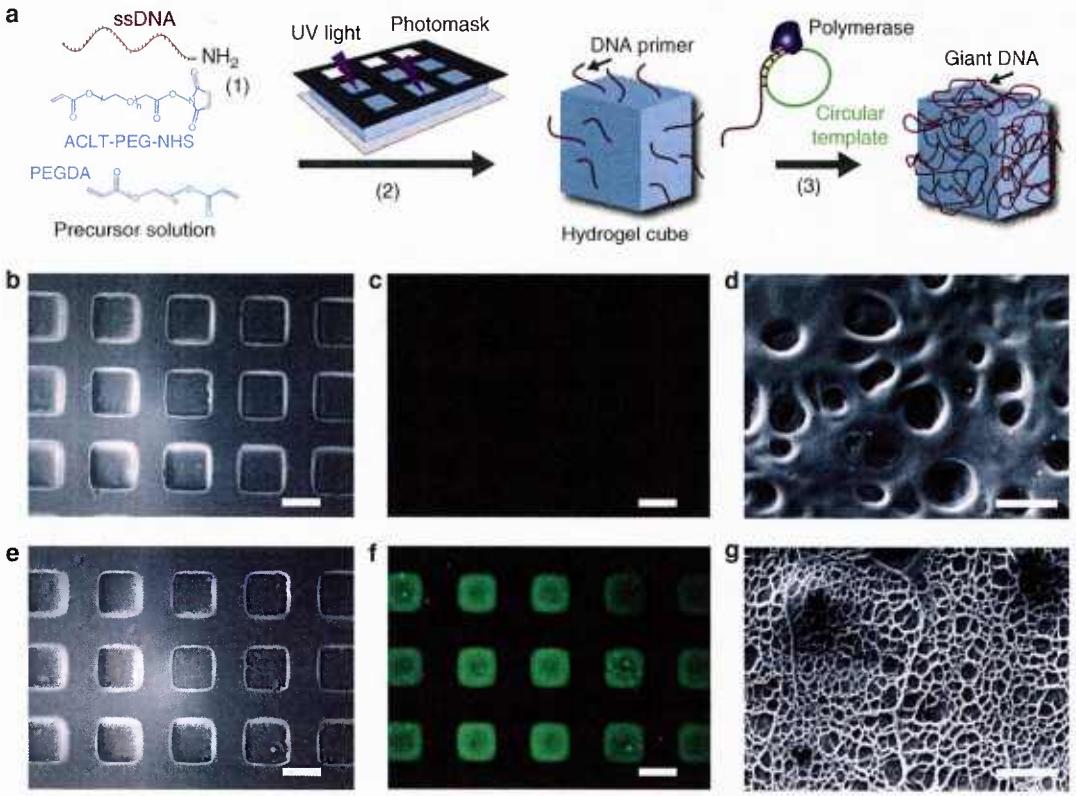

Figure 1 | Fabrication of hydrogel cubes with uniform giant DNA glue modification. (**a**) Schematic of the fabrication process of hydrogel cubes uniformly modified with giant DNA. Phase contrast (**b**,**e**), fluorescent (**c**,**f**) and SEM (**d**,**g**) images of hydrogels carrying short 56-nt single-stranded DNA primers (**b**–**d**) or amplified single-stranded giant DNA (**e**–**g**). The gels in **c** and **f** were stained with SYBR Gold before imaging. Scale bar, 200 μm in **b**, **c**, **e** and **f**; scale bar, 10 μm in **d** and **g**.

fabricated 250 × 250 × 250 μm hydrogel cubes carrying giant DNA encoding tandem repeated complementary sequence (Fig. 2a), and self-assembly was performed by mixing these hydrogel cubes in a 0.5 ml microtube filled with assembly buffer under mild rotation, using a tube rotator with a fixed speed of 18 r.p.m. (Fig. 2b, see details in Methods). To visualize the assembled structure, the two species of hydrogel cubes carrying complementary DNA sequences *a* and *a** were labelled with red (fluoresbrite microspheres with excitation at 512 nm and emission at 554 nm) or blue (fluoresbrite microspheres with excitation 360 nm and emission 407 nm) fluorescent microbeads, respectively. After the assembly reaction in the tube, the hydrogel cubes were transferred to a 1.6-cm diameter Petri dish for imaging (Fig. 2b). Large aggregates were observed for hydrogel cubes carrying complementary giant DNA (Fig. 2d, left, phase contrast imaging; right, fluorescent imaging). In contrast, hydrogel cubes carrying only 56-nt short DNA primers without RCA amplification failed to produce aggregates under the same assembly conditions (Fig. 2c, left, phase contrast imaging; right, fluorescent imaging). Including DNA-free yellow hydrogel cubes (that is, cubes that contain yellow microbeads) in the reaction system did not change the assembly outcome for either the hydrogel cubes carrying 56-nt short DNA primers (Fig. 2e, left) or hydrogel cubes carrying giant DNA (Fig. 2e, right). Moreover, no yellow hydrogel cubes were observed in the assembled structure, confirming that the assembly was directed by giant DNA on the hydrogel cube surface. This giant-DNA-dependent nature of the assembly was further verified in a DNA-degradation experiment (Fig. 2f): assembled hydrogel cubes carrying complementary giant DNA became dispersed after treatment with DNase, which was expected to degrade the giant DNA on the hydrogel cube surface. In previous work, using short DNA strand as glues, researchers were successful in catching small spherical particles (100 μm diameter) on a surface. However, in our system, relatively large cuboid-shaped particles (250 μm edge width) needed to assemble in a strong agitation (to disrupt non-specific interactions) solution-based system, and thus much stronger glue interactions were likely required to enable the assembly. Over 70% specific binding was observed by analyzing the binding event between two hydrogel cubes uniformly carrying same or complementary DNA glues. The giant-DNA-directed hydrogel cube binding was also quantified under different temperatures (4, 25 and 37 °C). We observed that the specific assembly yield increased as the temperature decreased (Supplementary Fig. S3). However, non-specific binding also increased significantly at 4 °C (data not shown). The assembly experiments in the remainder of the paper were performed under room temperature (Supplementary Fig. S3).

We next demonstrated that the interaction between complementary giant DNA was capable of directing the assembly of hydrogel cubes with a wide range of edge lengths. Cubes carrying complementary DNA *a* or *a** were labelled with red or blue colour microbeads, respectively. Assembly reaction was performed as described above. Aggregates were observed from hydrogel cubes with edge lengths of 30, 200, 500 and 1,000 μm (Fig. 2g–j). These experiments indicate that the hybridization

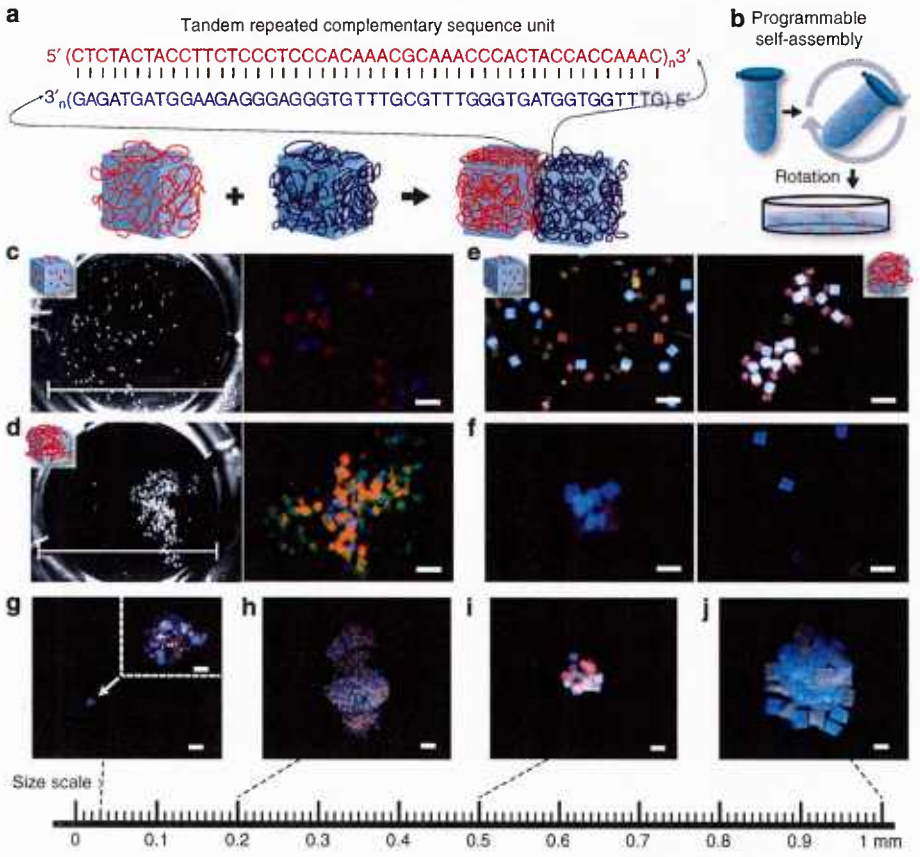

Figure 2 | Self-assembly of hydrogel cubes with uniform giant DNA glue modification. (**a**) Schematic of giant-DNA-directed hydrogel assembly. Giant DNA containing tandem repeats of complementary 48-nt sequences was uniformly amplified on the surface of red and blue hydrogel cubes. Hybridization between the complementary DNA sequences resulted in assembly of hydrogel cubes. (**b**) Hydrogel cubes were assembled in a 0.5 ml tube filled with assembly buffer under mild rotation, transferred to a Petri dish with 1.6 cm diameter and imaged under microscope. See Methods for details. (**c**,**d**) Phase contrast and fluorescent microscopy images of the post-assembly system, in which hydrogel cubes were modified with short 56-nt (**c**) or amplified giant (**d**) DNA strands. Hydrogel cubes carrying complementary DNA *a* or *a** were labelled with red or blue fluorescent microbeads, respectively, and stained with SYBR Gold. (**e**) Red and blue hydrogel cubes carrying complementary short (left) or giant (right) DNA strands failed (left) or succeeded (right) to assemble into aggregates, in the presence of competitive yellow hydrogel cubes that were not modified with DNA. (**f**) Aggregates assembled from red and blue hydrogel cubes carrying complementary giant DNA fell apart after 1 h Baseline-ZERO DNase treatment (left: before DNase treatment; right: after DNase treatment). Scale bar, 500 μm in **c**, **d**, **e** and **f**. (**g**–**j**) Aggregates were assembled from red and blue hydrogel cubes with various edge lengths: (**g**) 30 μm, (**h**) 200 μm, (**i**) 500 μm and (**j**) 1 mm. Giant DNA glue was uniformly amplified on the hydrogel surface. Scale bar, 1 mm in the main panels; 50 μm in the inset of **g**.

between complementary giant DNA was sufficiently strong to induce the assembly of hydrogel cubes across scales.

As complementary DNA molecules hybridize with each other in a sequence-dependent manner, it is possible to generate a large number of specific interactions using giant DNA glues with orthogonal sequences. To test whether such DNA sequence-dependent specificity can be applied in our hydrogel cube self-assembly system, fifty 24-nt DNA sequences were designed to produce 25 pairs of orthogonal-specific interactions (Fig. 3a; also see Methods and Supplementary Table S1 for DNA sequences). To visually differentiate distinct cube species under stereomicroscope, coloured microbeads were trapped in the core and periphery parts of the cubic hydrogel (Fig. 3c, top left corner), and pairwise combinations of 5 colours (red, blue, yellow, black and violet) generated 25 distinct signatures. Following fabrication, giant DNA containing tandem repeated sequence was amplified using RCA reaction on the hydrogel surface as described before. The 25 structures were self-assembled in aqueous assembly system. To avoid forming large aggregates that can trap microgels inside and hence hinder the quantification of specific assembly yields, only one copy for each of the 50 hydrogel species was included in one of five independent experiments (Fig. 3a). The assembly was performed using agitation of repeated mild rotation at a fixed speed of 18 r.p.m. and strong hand shaking every 30 min to disrupt non-specific binding. The assembled structures were then transferred to a Petri dish for imaging and quantification. Each of the 25 expected specific dimer structures were all identified (Fig. 3b,c). In total, 83 structures were analyzed in five independent experiments: of which about 66% dimerized specifically to their complementary sequence, whereas only 16% formed non-specific dimerized pairs (Fig. 3d). These experiments demonstrated that the interaction between giant DNA glue is sequence specific and that highly multiplexed assembly can be achieved using our system. To the best of our knowledge, this system includes more specific interactions than all reported mesoscale self-assembly work.

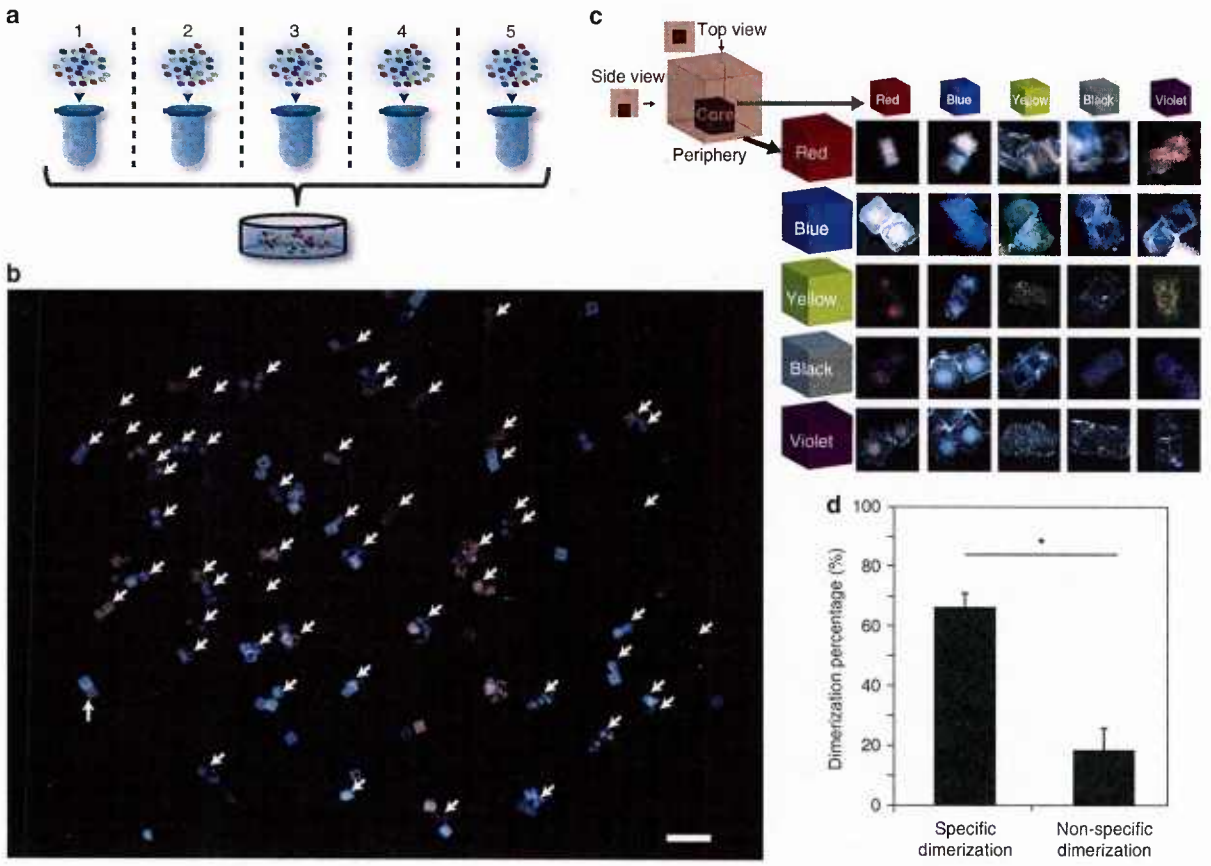

Figure 3 | Self-assembly of multiple hydrogel cubes dimers. (**a**) Schematic for multiplexed self-assembly of 25 orthogonal pairs of dimers in five independent experiments. (**b**) The final assembled structure from five independent experiments were pooled together into a single Petri dish for imaging, and the assembled specific structure was indicated by a white arrow. Scale bar, 1 mm. (**c**) Schematic (top left) describes the double layer structure of hydrogel cube used in the multiplexed self-assembly of 25 dimers. The core cube was 100 × 100 × 100 μm and the periphery cube was 300 × 300 × 300 μm. See Methods for fabrication details. The core and periphery hydrogel cubes were labelled with distinct coloured microbeads respectively, and pairwise combinations of five colours (red, blue, yellow, black and violet) generated 25 distinct signatures. Images of 25 corresponding dimers are shown. (**d**) Hydrogel cube dimers were identified under microscopy and quantified as the specific (66 ± 5%) and non-specific (18 ± 7%) binding events, $n = 5$, $^*P < 0.05$.

Self-assembly of hydrogels with face-specific DNA glues. To assemble structures with controlled architecture rather than aggregates, we fabricated hydrogel cuboid units with face-specific giant DNA modification. The procedure is illustrated in Fig. 4a. In steps 1–4, we describe the procedure to make a two-component cube composite structure where a lager 'body-cube' displays smaller DNA-modified 'pad-cubes' on its designated sides; in steps 5 and 6, we describe the agitation system for their assembly. (Step 1) The 150 × 150 × 150 μm hydrogel pad-cubes were made from a precursor solution that contains 20 wt% PEGDA (4 kDa) and PEG (3.5 kDa) acrylate-ssDNA primers using photolithography. A photomask with 150 × 150 μm square holes was used to control the cross-section shape of the pad-cube; No.1 microscope cover glass slides (150 μm in thickness) were used as spacers to control the height of the pad cube. (Step 2) The unpolymerized reagent was washed away and giant DNA was produced via RCA reaction as described before. We now have arrays of 150-μm pad-cubes (coloured green in Fig. 4a) with uniform giant DNA modification. (Step 3) To make the larger body-cube, we added a second solution that contained only 20 wt% PEGDA (4 kDa), and covered it with a second photomask with 250 × 250 μm square holes. This photomask was aligned carefully with the pad-cubes made in step 2 such that this photomask covered half of the cross-section area of each pad-cubes (to protect them from subsequent UV exposure). No. 2 microscope cover glass slides (250 μm in thickness) were used as spacers to control the height of the body-cubes. (Step 4) Subsequent UV treatment resulted in the polymerization of the second 250 × 250 × 250 μm body-cube. Unpolymerized reagent was washed away. At the end of step 4, we produced an array of cubes: the red 250 μm body-cube covered half of the green 150 μm pad-cubes; only the green 150 μm pad-cubes were modified with giant DNA. As a consequence, the cube composite only had giant DNA modification on designated faces that display the green pads. For exposition simplicity, we refer to this composite structure as a hydrogel cube with surface-specific DNA modifications. (Step 5) The hydrogel cubes were collected into a 0.5 ml microtube filled with the assembly buffer. (Step 6) Assembly was performed by rotating the tube. (Step 7) The solution was transferred to a Petri dish and imaged under microscope.

Using the above strategy, we demonstrated the multiplexed assembly of three hydrogel cube dimer species (Fig. 4b,c). In this

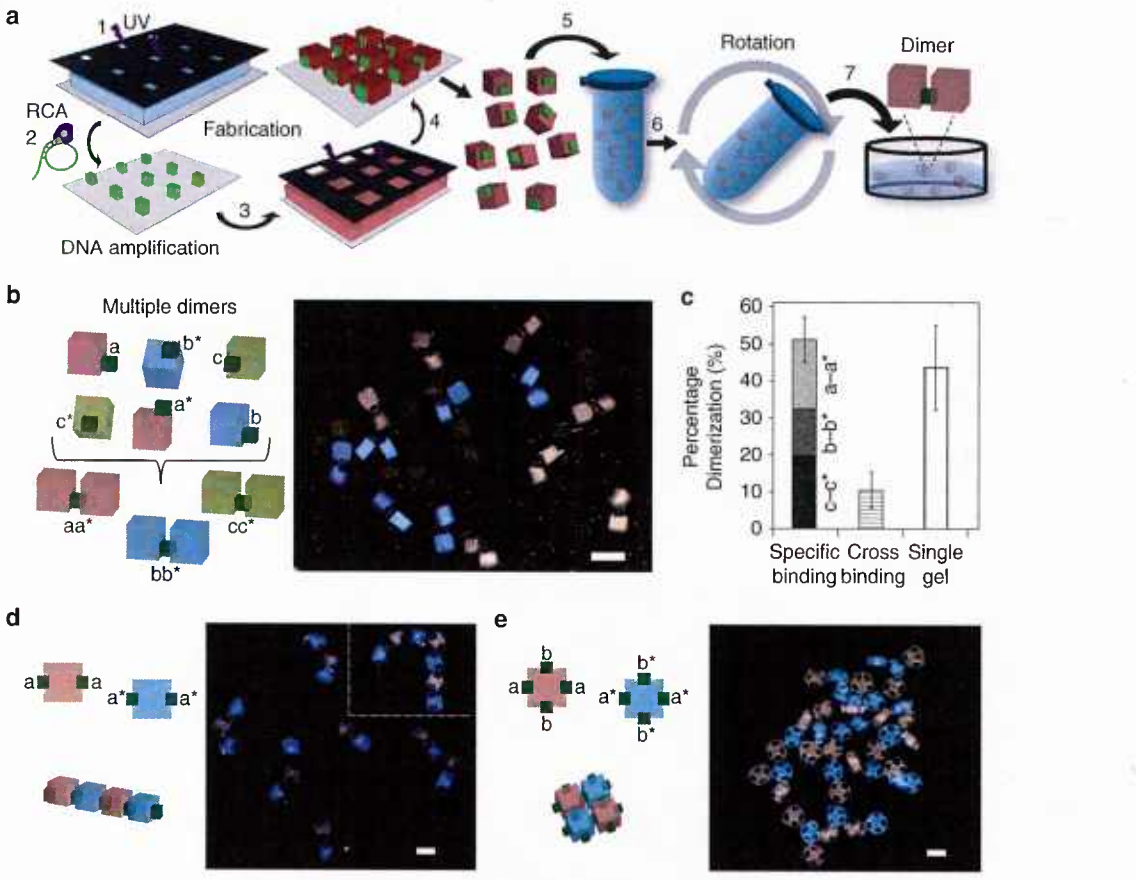

Figure 4 | Self-assembly of hydrogel cubes with face-specific DNA glue modifications. (**a**) Hydrogel cubes carrying giant DNA glue on designated faces were fabricated in steps 1-4, collected in a 0.5 ml microtube in step 5, mixed and agitated in step 6, and transferred to a Petri dish for imaging in step 7. (**b**) Hydrogel cubes displaying face-specific giant DNA with tandem repeats *a*/*a** (with the body cube labelled red), *b*/*b** (blue body cube) or *c*/*c** (yellow body cube). The pad cube carrying giant DNA glue is coloured green. Letters *x* and *x** denote complementary DNA sequences (see Supplementary Table S1 for sequence details). Scale bar, 500 μm. (**c**) Quantification of specific assembly, non-specific assembly and unassembled cubes. *$P<0.05$. (**d**) Linear chain structures were assembled from the red and blue gels. Left, schematic. Right, microscopy images. The inset shows a chain containing seven cubes. Scale bar, 200 μm. (**e**) Net-like structures were self-assembled from the red and blue cubes. Scale bar, 200 μm.

experiment, six hydrogel cube species were manufactured (Fig. 4b, left). The first species is a red hydrogel cube (that is, the body cube contained red microbeads) that displays giant DNA with tandem repeating sequence '*a*'. We call this cube the red cube *a*. The other five species are red cube *a** (where sequence *a** is complementary to sequence *a*), blue cube *b*, blue cube *b**, yellow cube *c* and yellow cube *c**. Multiple copies of each of the six cube species were made separately and then mixed at room temperature in the same tube for assembly (see Methods for details). After 6-h rotation, the solution was imaged (Fig. 4b, right). Three populations of the structures were observed and quantified (Fig. 4c). In total, 77 assembled structures were analyzed in six independent experiments: 46% were the expected, specific dimers that formed between two same-colour cubes that presumably carried complementary sequences; 10% were the dimers that formed between two different-colour cubes that carried non-complementary sequences; 44% were the unassembled single cubes. The specificity of dimer formation was quantified as 82% by dividing the number of specific dimers over the total number of dimers.

Using hydrogel cubes that display giant DNA on multiple designated faces, we next constructed linear chain structures and net-like structures. To make the chain structures, two cube species were made: a red cube that displays giant DNA *a* on two opposite faces, and a blue cube that displays giant DNA *a** on two opposite faces (Fig. 4d, left). The assembly of these two species produced chain structures that contained alternating red and blue cubes, as expected (Fig. 4d, right). The longest chain observed contained seven cubes (Fig. 4d, top-right corner). We then made a red cube species that displays giant DNA *a* on two opposite faces and giant DNA *b* on another two opposite faces, and a blue cube species that displays pairs of *a** and *b** on opposite faces (Fig. 4e, left). The assembly of these two species resulted in the formation of net-like structures with alternating red and blue cubes that were connected via DNA-modified sides (Fig. 4e, right). The linear and net-like structures were each assembled in three independent experiments, where each experiment used 40 red and 40 blue complementary cubes. In this experimental system, 39% of the gel cubes remained as unassembled, whereas 58% were assembled into a linear structure (due to their small size, 3% of cubes were lost during the assembly and quantification process). Among the 58% assembled cubes, 42% were only connected to a different colour cube and hence called specifically assembled cubes; the remaining 16% were connected non-

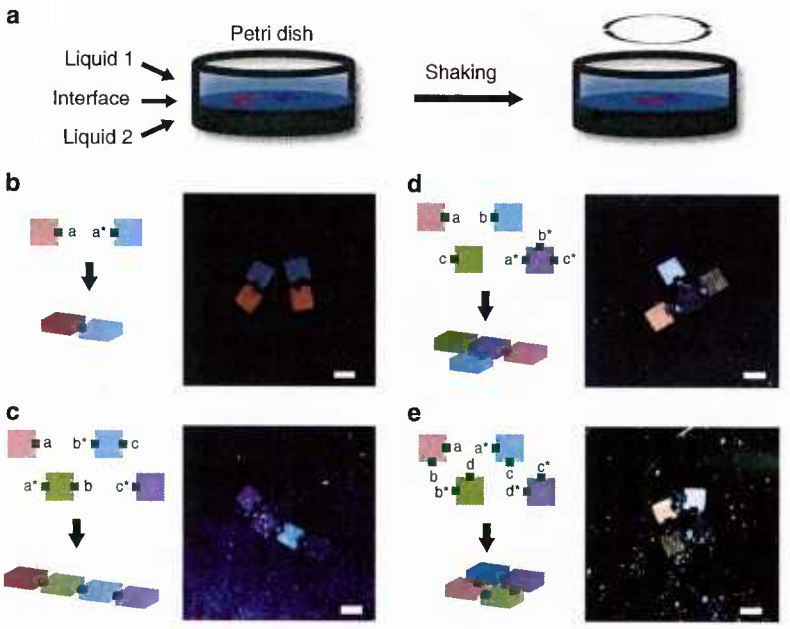

Figure 5 | Self-assembly of hydrogel cuboids at the liquid–liquid interface. (**a**) Schematic of hydrogel self-assembly at the liquid–liquid interface. Hydrogel cuboids were floated at the interface formed between upper aqueous PBS liquid and lower Fluorinert FC-40 liquid, and agitated with horizontal shaking. (**b**) Dimers were formed from the red and blue gels. See Supplementary Movie 1 for the assembly process. (**c**–**e**) Schematic and colour stereomicroscopy images of four hydrogel cuboids (labelled as red, blue, yellow and violet) self-assembled into chain (**c**) T-junction (**d**) or square shape (**e**) based on their surface DNA glue pattern. For the assembly process, see Supplementary Movies 2, 3 and 4, respectively. Scale bar, 1 mm.

specifically to at least one same colour cube, and were called non-specifically assembled cubes. For the net-like structures, the specifically assembled cubes, non-specifically assembled cubes and unassembled cube monomers were, respectively, 56%, 30% and 14%.

Interfacial self-assembly of hydrogel to complex structures. We next programmed the self-assembly of hydrogel units into prescribed finite structures. To avoid the rotation of the hydrogel cubes in the vertical direction during assembly, flat hydrogel cuboids were fabricated and floated on a liquid/liquid interface between aqueous PBS and Fluorinert FC-40 liquid; horizontal shaking was applied to facilitate assembly (Fig. 5a). The assembled structures were directly imaged in this interfacial system. We analyzed the binding between two hydrogel cubes carrying uniform DNA modification in the interfacial system. Over 70% stable specific binding was observed only between hydrogel cubes carrying complementary DNA, which is consistent with what we observed in the aqueous liquid. Using similar fabrication strategy as in Fig. 4a, we made a two-component gel composite: the body is a 1 (length) × 1 (width) × 0.3 mm (height) flat cuboid and the pads are DNA-modified 250 × 250 × 250 μm cubes. Note that the length ratio between the body and the pad cubes increased to 4:1 (as compared with the 1.7:1 in Fig. 4). Using the interfacial system and the flat cuboids that carry relatively smaller pads, we were able to assemble dimers (Fig. 5b), linear chains with finite length (Fig. 5c), a T-junction (Fig. 5d) and a square structure (Fig. 5e). Note that the linear chain, the T junction and the square are all composed of four distinct cuboid species; by simply changing the pad (and hence surface giant DNA) modification pattern, we were able to change the assembled structure from a chain to a T-junction, and to a square. The assembly process details are captured in time-lapse movies. Supplementary Movie 1 shows two copies of dimers self-assembly (Fig. 5b). Supplementary Movie 2 shows the chain structure self-assembly (Fig. 5c). Supplementary Movie 3 shows the T-junction self-assembly (Fig. 5d). Supplementary Movie 4 shows the self-assembly of the square structures (Fig. 5e).

For the dimer experiments (Fig. 5b), two copies of each component were included; for the linear (Fig. 5c), T-junction (Fig. 5d) and square (Fig. 5e) structures, only one copy of each component was included. We tested the assembly of each system for three times or more, and all together more than 20 experiments were performed for these structures. Out of these more than 20 experiments, the intended structure always formed as desired. However, it is important to note that such systems (involving only one copy of each component) are significantly simpler than systems that involve multiple copies of the same components. We have performed an experiment to form two copies of the T-junction. In this experiment (Supplementary Fig. S4), we started with 14 hydrogel cubes: two copies of centre hydrogel cube (purple) and four copies of each of the three side hydrogel cubes (red, blue and yellow). We attempted the experiments three times, and only successfully assembled two copies of T-junctions in one of the three experiments. It thus remains a challenge to assemble complex structures using multiple copies for each component in the interfacial systems.

Discussion

Although short DNA primer has been reported to assemble nano-particles and microscale hydrogels, we demonstrate, for the first time, the DNA-directed self-assembly of shape-controlled hydrogel modules to build complex structures in a programmable fashion. Acting like sequence-specific glue and tethered onto a microgel surface, giant single-stranded DNA exhibits a significant capability for binding objects across scales, with sizes ranging

from 30 micrometers to a millimeter. In addition, giant DNA glues offer significant diversity over current mesoscale self-assembly systems: 50 DNA sequences were designed to generate 25 orthogonal pairs of specific interactions. This is the largest of number of orthogonal-binding interactions that have been used simultaneously in the same reaction system for mesoscale assembly. The designable DNA glues thus provide much richer options for programming mesoscale self-assembly.

For self-assembling complex structures, the unit fabrication is crucial. As cube units uniformly carrying DNA glues assembled only into aggregates lack of architecture control, we developed a precisely controlled fabrication technique by which specific giant DNA glue is decorated on a prescribed face of a hydrogel cuboid. By changing the position of DNA glues, various structures including dimers, linear chains and open networks were assembled. In an interfacial system, we further demonstrated that hydrogel cuboids can be fabricated with four different DNA glues on four designated faces, and by simply changing the surface DNA decoration pattern, we assembled discrete structures including dimers, T-junctions, linear chains with fixed length and squares. We have successfully introduced programmability into self-assembling mesoscale structures.

We believe that there is still room for improvement in our self-assembly system. For example, it is possible to improve the assembly by tuning the strength of DNA glue through controlling the DNA density and length on the gel surface. In addition, better face-to-face alignment could be achieved by improving the gel fabrication method, for example, by minimizing the aspect ratio between the DNA carrying pads and the gel body (note that the assembly in Fig. 5 demonstrated improved face-to-face alignment over Fig. 4). Furthermore, advances in the mixing regimes that better regulate the hydrodynamic forces involved in the assembly process may be used to further enhance the assembly process.

By coupling novel *in situ* DNA amplification methods and microfabrication techniques, we successfully introduced the diversity and specificity of biomolecular interaction to mesoscale assembly. DNA-directed self-assembly of shape-controlled hydrogel modules proved to be highly programmable and controllable, and will open new doors to address the challenge of building complex self-assembled three-dimensional structures for diverse applications in materials science and especially in biomaterials. One particularly promising direction is to develop tissue engineering application, as recreating the highly defined complicate structure of tissue is a pressing challenge. For example, by encapsulating specific cells inside the hydrogel cubes, the self-assembled structures could be used to build the basic architectures of native tissues.

Methods

Materials. The pre-polymer solution of PEGDA with average molecular weight 4,000 Da was prepared by diluting PEG (Monomer-Polymer & Dajac Labs) in DPBS (Gibco) to a final concentration of 20 wt% with 0.5 wt% photo-initiator, 1-(4-(2-Hydroxyethoxy)-phenyl)-2-hydroxy-2-methyl-1-propane-1-one (IRGACURE 2959 Ciba) for hydrogel modules fabrication. A circular DNA template was produced by ligating 5′ and 3′ ends of DNA (Invitrogen) with 5′ end phosphate modification using a CircLigase ssDNA ligase (EPICENTRE Biotechnology). DNA sequence for DNA glue synthesis was designed using software NUPACK (www.nupack.org) to minimize mis-hybridization between orthogonal sequences. DNA was ordered from Invitrogen. The baseline-ZERO DNase was obtained from Epicentre Biotechnology and used with final concentration of 1 U ml^{-1}.

Sequence design. We designed 25 orthogonal sequence pairs using a modified version of the Domain Design software described by Zhang *et al.*[58] We first designed 25 domains of 24 bases each, and then concatenated these domains together into 25 domains of 48 bases each. Sequences were designed using a three-letter alphabet to reduce spurious hybridization. To reduce long regions of repeated bases (for example, poly-A, poly-G, and so on), we assign a higher reward to sequences with a higher Shannon entropy. Using NUPACK thermodynamic analysis package, unintended interactions between the concatenated products were calculated to be $\sim 10^8$ times less favourable than the intended interactions[59].

Fabrication of PEG hydrogels carrying DNA glues. We followed a standard protocol to synthesize acrylate–PEG–DNA by adopting NHS chemistry to conjugate a 5′ amine-modified DNA strand (containing a poly(T-36) linker segment followed by a primer segment) to acrylate–PEG–NHS (Jenkem Technology). Shape-controlled PEG hydrogel was fabricated by following a general photolithograph process as described in our previous work[60], in which the photomask was designed using AutoCAD software with 200,000 dpi resolution (CAD/Art Services; Bandon, OR). Before DNA amplification, hydrogel was washed with PBS and DNA amplification buffer thoroughly (40 mM Tris–HCl pH 7.5, 50 mM KCl, 10 mM $MgCl_2$, 5 mM $(NH_4)_2SO_4$, and 4 mM dithiothreitol). Giant DNA was amplified by soaking hydrogel in reaction solution containing 50 μM circular DNA template and 5 U μl^{-1} of Phi29 DNA polymerase (EPICENTRE Biotechnology) in 1 × DNA amplification buffer at 37 °C overnight according to the manufacturer's instructions. Hydrogel carrying patterned DNA glue was fabricated in a two-step fabrication process. In step 1, DNA glue was amplified on a small hydrogel cube with edge width of 150–300 μm, which was fabricated by photolithography as described above. In step 2, DNA gel was washed with 1 × assembly buffer (0.5 M NaCl, 0.5 mM EDTA and 0.05% Tween-20 in 1 × PBS) thoroughly. Then 20 wt% pre-polymer PEG solution containing 1 v/v% colour microbead was added. The final shape of hydrogel was controlled by a secondary photomask which was aligned under microscope with the hydrogel to produce the desired DNA pattern.

Self-assembly of hydrogels in aqueous solution. Hydrogels carrying specific DNA glue was collected in a 0.5 ml microtube filled with assembly buffer containing 0.5 M NaCl, 0.5 mM EDTA and 0.05% Tween-20 in 1 × PBS buffer. To prevent non-specific binding between hydrogel and microtube, the inside surface of microtube was treated with a corona treater (BD-20AC from Electro-Technic Products Inc.) and then coated with 10% PEGDA (MW 1,000) beforehand. To achieve DNA-directed hydrogel assembly, microtube was subjected to agitation of continuous 360° upright rotation on a VWR Multimix tube rotator with a fixed speed of 18 r.p.m. and intermittent soft vortex or hand shaking every 30–60 min to disrupt non-specific binding or aggregates at room temperature. After assembly, hydrogel was transferred to a Petri dish filled with a solution of 20 wt% PEG (MW 3,350) in 1 × assembly buffer and subjected to further horizontal shaking at a speed of about 60 r.p.m. on a VWR standard orbital shaker. Assembled structures were identified, quantified and imaged using a Stereo Microscope.

Liquid/liquid interface self-assembly. Liquid/liquid interface was generated between Fluorinert electronic liquid FC-40 (bottom liquid, 3M Chemicals) and aqueous assembly buffer (top liquid) in a Petri dish. Hydrogel units were floated on the interface and subjected to agitation of continuous horizontal shaking at a low speed of 60 r.p.m. on a VWR standard orbital shaker (Model 1000, VWR) and intermittent 120 r.p.m. shaking or strong hand shaking every 30–60 min to break undesired, spurious aggregates at room temperature. Assembly process was recorded using an image recording software, HyperCam Version 2, under a Stereo Microscope.

Quantification of DNA-directed hydrogel assembly. To quantify the specificity of dimer formation, hydrogel cubes with an edge width of 250 μm were fabricated. A gel is uniformly decorated with a particular giant DNA glue species. In total, three different complementary pairs of DNA (*a*/*a**, red; *b*/*b**, blue; *c*/*c**, yellow) were used to generate giant DNA glues. Ten copies of hydrogels of each pair were placed in an Eppendorf tube ($n = 6$) filled with assembly buffer and rotated for over 3 h. Rotating the hydrogels generated dimers with all different combinations of the three colours. Self-assembly was performed in aqueous liquid system as described above, and the total specific binding among the pairs was identified under a Stereo Microscope. Quantification analysis was performed using STDEV function and TDIST function for s.d. and *P*-value, respectively, in software Excel (Microsoft).

Giant DNA analysis. Giant DNA was amplified by RCA using Phi29 DNA polymerase (EPICENTRE Biotechnology), as described earlier and analyzed on a 1% agarose gel with SYBR Green staining. The morphology of giant DNA on surface of microgel or glass slide was analyzed using a SEM (Ziess EVO SEM). After amplification, microgel was rinsed with PBS (GIBCO, DPBS) thoroughly and the liquid around the gel was dried up using Kimwipes. Following washing, microgel was frozen in − 80 °C freezer for 3 h and transferred to a freeze drier for 2 days before SEM imaging.

Assembly of 25 orthogonal pairs of hydrogel dimmers. DNA strands, *D001*, *D001**, *D002*, *D002** …… *D025*, *D025** (Supplementary Table S1:DNA sequences), and poly(T-36) with a 5′ end amine modification were purchased from Integrated DNA Technology and dissolved in water upon arrival.

DNA oligo phosphorylation. One phosphate group was added to the 3′ end of DNA strands by T4 polynucleotide kinase (PNK, EPICENTRE Biotechnology) before ligation with poly(T-36) or circularization. Phosphorylation master reaction containing 33 mM Tris–HCl (pH 7.5), 66 mM potassium acetate, 10 mM magnesium acetate, 0.5 mM dithiothreitol, 5 mM ATP, 100 μM DNA oligo and 10 U μl^{-1} PNK enzyme was incubated at 37 °C for 3 h and then PNK enzyme was inactivated by incubation at 70 °C for 30 min.

Circular DNA template preparation. Circular DNA template was prepared by circulating phosphate-modified DNA strand using Cirligase II ssDNA ligase (EPICENTRE Biotechnology). Circularization reaction was performed by supplementing 2.5 mM manganese chloride, 1 M Betaine and 5 U μl^{-1} ligase to phosphate-modified DNA strand solution and then incubated at 60 °C for 6 h. Then the ligase was inactivated at 80 °C for 10 min. Then exonuclease I (EPICENTRE Biotechnology) was added to remove linear DNA at 37 °C for 1 h and was inactivated at 80 °C for 30 min.

Conjugation of acrylate-PEG-DNA primer. First, phosphorylated DNA oligo was ligated to amine-poly(T-36). Ligation reaction was performed with supplementing 20 U μl^{-1} T4 RNA ligase (New England Biolab) and 100 μM amine-poly(T-36) in phosphate-modified DNA oligo solution and incubated at room temperature (25 °C) overnight. Following ligation, amine-poly(T-36)-DNA oligo was conjugated with acrylate-PEG-NHS (Jenkem Technology) as described earlier. Cubic PEG microgel with size of 250 × 250 × 250 μm carrying DNA primer was fabricated, and giant DNA was amplified as described earlier. Pairwise combination of the core and periphery gels that contain one of the five colour microbeads (polybead Red Dyed 1.0-μm microspheres, polybead Blue Dyed 0.5-μm microspheres, Polybead Yellow Dyed 3.0-μm microspheres, polybead Violet Dyed 1.0-μm microsphere and polybead Black Dyed 10.0-μm microspheres; Polysciences) generated 25 distinct labelling. Fabrication process is similar to that of microgel for dimer assembly as previously described except for the following modification. During the secondary photolithography, the second microgel (periphery) was fabricated to completely wrap the first microgel (core) to form the final structure. To decrease assembly time and avoid aggregation, a single copy of each microgel uniformly carrying DNA *D001*, *D001**, *D002*, *D002** …… *D025*, *D025** was collected in 0.5 ml Eppendorf microtubes filled with 1 × assembly buffer. Subsequent self-assembly was performed in aqueous liquid as described earlier. The assembled structure was identified under a Stereo Microscope.

References

1. Whitesides, G. M. & Grzybowski, B. Self-assembly at all scales. *Science* **295,** 2418–2421 (2002).
2. Breen, T. L., Tien, J., Oliver, S. R., Hadzic, T. & Whitesides, G. M. Design and self-assembly of open, regular, 3D mesostructures. *Science* **284,** 948–951 (1999).
3. Boncheva, M. *et al.* Magnetic self-assembly of three-dimensional surfaces from planar sheets. *Proc. Natl Acad. Sci. USA* **102,** 3924–3929 (2005).
4. Clark, T. D., Ferrigno, R., Tien, J., Paul, K. E. & Whitesides, G. M. Template-directed self-assembly of 10-microm-sized hexagonal plates. *J. Am. Chem. Soc.* **124,** 5419–5426 (2002).
5. Du, Y., Lo, E., Ali, S. & Khademhosseini, A. Directed assembly of cell-laden microgels for fabrication of 3D tissue constructs. *Proc. Natl Acad. Sci. USA* **105,** 9522–9527 (2008).
6. Bowden, N., Terfort, A., Carbeck, J. & Whitesides, G. M. Self-Assembly of mesoscale objects into ordered two-dimensional arrays. *Science* **276,** 233–235 (1997).
7. Harada, A., Kobayashi, R., Takashima, Y., Hashidzume, A. & Yamaguchi, H. Macroscopic self-assembly through molecular recognition. *Nat. Chem.* **3,** 34–37 (2011).
8. Seeman, N. C. DNA in a material world. *Nature* **421,** 427–431 (2003).
9. Lin, C., Liu, Y., Rinker, S. & Yan, H. DNA tile based self-assembly: building complex nanoarchitectures. *Chem. Phys. Chem.* **7,** 1641–1647 (2006).
10. Aldaye, F. A., Palmer, A. L. & Sleiman, H. F. Assembling materials with DNA as the guide. *Science* **321,** 1795–1799 (2008).
11. Torring, T., Voigt, N. V., Nangreave, J., Yan, H. & Gothelf, K. V. DNA origami: a quantum leap for self-assembly of complex structures. *Chem. Soc. Rev.* **40,** 5636–5646 (2011).
12. Chen, J. H. & Seeman, N. C. Synthesis from DNA of a molecule with the connectivity of a cube. *Nature* **350,** 631–633 (1991).
13. Fu, T. J. & Seeman, N. C. DNA double-crossover molecules. *Biochemistry* **32,** 3211–3220 (1993).
14. Winfree, E., Liu, F., Wenzler, L. A. & Seeman, N. C. Design and self-assembly of two-dimensional DNA crystals. *Nature* **394,** 539–544 (1998).
15. Chworos, A. *et al.* Building programmable jigsaw puzzles with RNA. *Science* **306,** 2068–2072 (2004).
16. Rothemund, P. W., Papadakis, N. & Winfree, E. Algorithmic self-assembly of DNA Sierpinski triangles. *PLoS Biol.* **2,** e424 (2004).
17. Shih, W. M., Quispe, J. D. & Joyce, G. F. A 1.7-kilobase single-stranded DNA that folds into a nanoscale octahedron. *Nature* **427,** 618–621 (2004).
18. Rothemund, P. W. Folding DNA to create nanoscale shapes and patterns. *Nature* **440,** 297–302 (2006).
19. He, Y. *et al.* Hierarchical self-assembly of DNA into symmetric supramolecular polyhedra. *Nature* **452,** 198–201 (2008).
20. Yin, P. *et al.* Programming DNA tube circumferences. *Science* **321,** 824–826 (2008).
21. Andersen, E. S. *et al.* Self-assembly of a nanoscale DNA box with a controllable lid. *Nature* **459,** 73–76 (2009).
22. Dietz, H., Douglas, S. M. & Shih, W. M. Folding DNA into Twisted and Curved Nanoscale Shapes. *Science* **325,** 725–730 (2009).
23. Douglas, S. M. *et al.* Self-assembly of DNA into nanoscale three-dimensional shapes. *Nature* **459,** 414–418 (2009).
24. Zheng, J. *et al.* From molecular to macroscopic via the rational design of a self-assembled 3D DNA crystal. *Nature* **461,** 74–77 (2009).
25. Han, D. *et al.* DNA origami with complex curvatures in three-dimensional space. *Science* **332,** 342–346 (2011).
26. Delebecque, C. J., Lindner, A. B., Silver, P. A. & Aldaye, F. A. Organization of intracellular reactions with rationally designed RNA assemblies. *Science* **333,** 470–474 (2011).
27. Wei, B., Dai, M. & Yin, P. Complex shapes self-assembled from single-stranded DNA tiles. *Nature* **485,** 623–626 (2012).
28. Ke, Y., Ong, L. L., Shih, W. M. & Yin, P. Three-dimensional structures self-assembled from DNA bricks. *Science* **338,** 1177–1183 (2012).
29. Han, D. *et al.* DNA gridiron nanostructures based on four-arm junctions. *Science* **339,** 1412–1415 (2013).
30. Yurke, B., Turberfield, A. J., Mills, Jr A. P., Simmel, F. C. & Neumann, J. L. A DNA-fuelled molecular machine made of DNA. *Nature* **406,** 605–608 (2000).
31. Yan, H., Zhang, X., Shen, Z. & Seeman, N. C. A robust DNA mechanical device controlled by hybridization topology. *Nature* **415,** 62–65 (2002).
32. Ding, B. & Seeman, N. C. Operation of a DNA robot arm inserted into a 2D DNA crystalline substrate. *Science* **314,** 1583–1585 (2006).
33. Seelig, G., Soloveichik, D., Zhang, D. Y. & Winfree, E. Enzyme-free nucleic acid logic circuits. *Science* **314,** 1585–1588 (2006).
34. Zhang, D. Y., Turberfield, A. J., Yurke, B. & Winfree, E. Engineering entropy-driven reactions and networks catalyzed by DNA. *Science* **318,** 1121–1125 (2007).
35. Yin, P., Choi, H. M., Calvert, C. R. & Pierce, N. A. Programming biomolecular self-assembly pathways. *Nature* **451,** 318–322 (2008).
36. Omabegho, T., Sha, R. & Seeman, N. C. A bipedal DNA Brownian motor with coordinated legs. *Science* **324,** 67–71 (2009).
37. Lund, K. *et al.* Molecular robots guided by prescriptive landscapes. *Nature* **465,** 206–210 (2010).
38. Gu, H., Chao, J., Xiao, S. J. & Seeman, N. C. A proximity-based programmable DNA nanoscale assembly line. *Nature* **465,** 202–205 (2010).
39. Qian, L., Winfree, E. & Bruck, J. Neural network computation with DNA strand displacement cascades. *Nature* **475,** 368–372 (2011).
40. Qian, L. & Winfree, E. Scaling up digital circuit computation with DNA strand displacement cascades. *Science* **332,** 1196–1201 (2011).
41. Douglas, S. M., Bachelet, I. & Church, G. M. A logic-gated nanorobot for targeted transport of molecular payloads. *Science* **335,** 831–834 (2012).
42. Um, S. H. *et al.* Enzyme-catalysed assembly of DNA hydrogel. *Nat. Mater.* **5,** 797–801 (2006).
43. Park, N. *et al.* High-yield cell-free protein production from P-gel. *Nat. Protoc.* **4,** 1759–1770 (2009).
44. Park, N., Um, S. H., Funabashi, H., Xu, J. & Luo, D. A cell-free protein-producing gel. *Nat. Mater.* **8,** 432–437 (2009).
45. Lee, J. B. *et al.* A mechanical metamaterial made from a DNA hydrogel. *Nat. Nanotech.* **7,** 816–820 (2012).
46. Lin, C. *et al.* Submicrometre geometrically encoded fluorescent barcodes self-assembled from DNA. *Nat. Chem.* **4,** 832–839 (2012).
47. Yan, H., Park, S. H., Finkelstein, G., Reif, J. H. & LaBean, T. H. DNA-templated self-assembly of protein arrays and highly conductive nanowires. *Science* **301,** 1882–1884 (2003).
48. Nykypanchuk, D., Maye, M. M., van der Lelie, D. & Gang, O. DNA-guided crystallization of colloidal nanoparticles. *Nature* **451,** 549–552 (2008).
49. Sharma, J. *et al.* Control of self-assembly of DNA tubules through integration of gold nanoparticles. *Science* **323,** 112–116 (2009).
50. Hung, A. M. *et al.* Large-area spatially ordered arrays of gold nanoparticles directed by lithographically confined DNA origami. *Nat. Nanotech.* **5,** 121–126 (2010).
51. Macfarlane, R. J. *et al.* Nanoparticle superlattice engineering with DNA. *Science* **334,** 204–208 (2011).
52. Maune, H. T. *et al.* Self-assembly of carbon nanotubes into two-dimensional geometries using DNA origami templates. *Nat. Nanotech.* **5,** 61–66 (2010).

53. Beales, P. A., Nam, J. & Vanderlick, T. K. Specific adhesion between DNA-functionalized "Janus" vesicles: size-limited clusters. *Soft Matter* **7,** 1747–1755 (2011).
54. Gartner, Z. J. & Bertozzi, C. R. Programmed assembly of 3-dimensional microtissues with defined cellular connectivity. *Proc. Natl Acad. Sci. USA* **106,** 4606–4610 (2009).
55. Li, C. Y., Wood, D. K., Hsu, C. M. & Bhatia, S. N. DNA-templated assembly of droplet-derived PEG microtissues. *Lab. Chip.* **11,** 2967–2975 (2011).
56. Schlingman, D. J., Mack, A. H., Mochrie, S. G. & Regan, L. A new method for the covalent attachment of DNA to a surface for single-molecule studies. *Colloids Surf. B. Biointerfaces.* **83,** 91–95 (2011).
57. Schopf, E. & Chen, Y. Attomole DNA detection assay via rolling circle amplification and single molecule detection. *Anal. Biochem.* **397,** 115–117 (2010).
58. Zhang, D. Y. Towards domain-based sequence design for DNA strand displacement reactions. *Lect. Notes Comput. Sci.* **6518,** 162–175 (2011).
59. Dirks, R. M., Bios, J. S., Schaeffer, J. M., Winfree, E. & Pierce, N. A. Thermodynamic analysis of interacting nucleic acid strands. *SIAM Rev.* **49,** 65–88 (2007).
60. Qi, H. *et al.* Patterned differentiation of individual embryoid bodies in spatially organized 3D hybrid microgels. *Adv. Mater.* **22,** 5276–5281 (2010).

Acknowledgements

We thank Wei Sun and Tom Schaus for discussions. This work is funded by the NIH (EB008392; DE019024; HL099073; AR057837; HL092836), NSF CAREER Award DMR0847287 and ONR grants to A.K., and by ONR Young Investigator Program Award N000141110914, ONR Grant N000141010827, NSF CAREER Award CCF1054898, NSF grant 1162459, NIH Director's New Innovator Award 1DP2OD007292 and Wyss Institute Faculty Startup Fund to P.Y.

Author contributions

H.Q. designed and conducted the experiments, performed data analysis and wrote the paper; M.G. designed and performed experiments and data analysis. Y.D., H.B. and C.G. assisted in designing and performing experiments. P.Y. and A.K. conceived, designed and supervised the study, interpreted the data and prepared the manuscript.

Additional information

Supplementary Information accompanies this paper at http://www.nature.com/naturecommunications

Competing financial interests: The authors declare competing financial interests in the form of a pending provisional patent (U.S. Provisional Application No.: 61/727,344, filed on 11/16/12 Nucleic acid hydrogel self-assembly).

Reprints and permission information is available online at http://npg.nature.com/reprintsandpermissions/

How to cite this article: Qi, H. *et al.* DNA-directed self-assembly of shape-controlled hydrogels. *Nat. Commun.* 4:2275 doi: 10.1038/ncomms3275 (2013).

11.4 Structural DNA nanotechnology application

11.4.1 Structural DNA nanotechnology application: Geometrically encoded fluorescent barcodes

ARTICLES
PUBLISHED ONLINE: 24 SEPTEMBER 2012 | DOI: 10.1038/NCHEM.1451
nature chemistry

Submicrometre geometrically encoded fluorescent barcodes self-assembled from DNA

Chenxiang Lin[1,2,3], Ralf Jungmann[1,4], Andrew M. Leifer[5†], Chao Li[1,6], Daniel Levner[1,6], George M. Church[1,6], William M. Shih[1,2,3]* and Peng Yin[1,4]*

The identification and differentiation of a large number of distinct molecular species with high temporal and spatial resolution is a major challenge in biomedical science. Fluorescence microscopy is a powerful tool, but its multiplexing ability is limited by the number of spectrally distinguishable fluorophores. Here, we used (deoxy)ribonucleic acid (DNA)-origami technology to construct submicrometre nanorods that act as fluorescent barcodes. We demonstrate that spatial control over the positioning of fluorophores on the surface of a stiff DNA nanorod can produce 216 distinct barcodes that can be decoded unambiguously using epifluorescence or total internal reflection fluorescence microscopy. Barcodes with higher spatial information density were demonstrated via the construction of super-resolution barcodes with features spaced by ~40 nm. One species of the barcodes was used to tag yeast surface receptors, which suggests their potential applications as *in situ* imaging probes for diverse biomolecular and cellular entities in their native environments.

Fluorescence microscopy is a versatile tool used to visualize nanometre- to micrometre-sized entities. To study multiple species of interest, it is essential to develop multiplexed fluorescent tags (barcodes). Most existing fluorescent barcodes are constructed using either intensity encoding (for example, microbeads with anisotropically embedded fluorophores[1–5], cells with combinatorially expressed fluorescent proteins[6], nanoarrays that consist of different fluorescent (deoxy)ribonucleic acid (DNA) tiles[7] and messenger ribonucleic acid hybridized to fluorescent probes[8]) or geometrical encoding (for example, inorganic particles with optical features[9–14] and nucleic acid double helices with tandem fluorescent labels[15,16]). Intensity encoding relies on the combination of multiple spectrally differentiable fluorophores in a controlled molar ratio. Geometrical encoding, however, is obtained by separating optical features beyond the microscope's resolution limit (typically ~250 nm for diffraction-limited imaging and ~25–40 nm for current super-resolution imaging[17]) and arranging them in a specific geometric pattern. The multiplexing capability of geometrically encoded barcodes increases exponentially as additional spatially distinguishable fluorophores are incorporated. Thus, with a structurally stiff scaffold capable of defining the spatial arrangement of the fluorescent molecules, combinatorially large barcode libraries may be constructed.

Despite the remarkable success in synthesizing fluorescent barcodes for *in vitro* multiplexed detection[1–5,7,9–16], little effort has been made to create robust single-molecule barcodes suitable as *in situ* imaging probes. Additionally, most existing fluorescent barcodes are in the range 2–100 μm in size and the construction of barcodes with smaller dimensions remains challenging, with only a few reports[3,7,8,12] of submicrometre barcodes and no more than 11 distinct barcodes demonstrated experimentally[8]. Here, we report a group of geometrically encoded fluorescent barcodes self-assembled from DNA. These barcodes are 400–800 nm in length, structurally stiff, reprogrammable in a modular fashion and easy to decode using epifluorescence or total internal reflection fluorescence (TIRF) microscopy. As evidence of their multiplexing power, 216 distinct barcode species were constructed and resolved using diffraction-limited TIRF microscopy Unlike the NanoString nCounter[15], no stretching step is necessary. The separation between the fluorescent spots was created exclusively by the stiffness of the DNA nanorod. Furthermore, barcodes with fluorescent features spaced below the diffraction limit were resolved using super-resolution microscopy. Finally, one species of the barcodes was used to tag yeast surface receptors, which suggests their potential application as *in situ* imaging probes.

Structural DNA nanotechnology exploits the well-defined double-helical structure of DNA and the predictable Watson–Crick base-paring rules to self-assemble designer nano-objects and devices[18–23]. A particularly effective method is DNA origami[24–30]. By folding a long, single-stranded 'scaffold strand' using many short synthetic 'staple strands', this approach generates complex, shape-controlled, fully addressable nanostructures with sizes of up to hundreds of nanometres. By functionalizing selected staple strands, such nanostructures can be used to organize fluorescent guest molecules spatially, including small organic molecules[31–33], and metallic[34] and semiconductive nanoparticles[35]. These properties make DNA origami a promising platform on which to build robust fluorescent barcodes, as the control over the exact ratio of different fluorophores allows intensity encoding and the spatial positioning of the fluorophores facilitates geometrical encoding, which can help to minimize undesired interfluorophore quenching.

Fluorescent barcodes with single-labelled zones

We first designed a family of 27 barcodes based on six-helix bundle DNA nanorods[36] that were ~800 nm long (Fig. 1a). Three zones of

[1]Wyss Institute for Biologically Inspired Engineering, Harvard University, Boston, Massachusetts 02115, USA, [2]Department of Biological Chemistry and Molecular Pharmacology, Harvard Medical School, Boston, Massachusetts 02115, USA, [3]Department of Cancer Biology, Dana-Farber Cancer Institute, Boston, Massachusetts 02115, USA, [4]Department of Systems Biology, Harvard Medical School, Boston, Massachusetts 02115, USA, [5]Program in Biophysics, Harvard University, Cambridge, Massachusetts 02138, USA, [6]Department of Genetics, Harvard Medical School, Boston, Massachusetts 02115, USA; †Present address: Lewis Sigler Institute for Integrative Genomics, Princeton University, Princeton, New Jersey 08544, USA. *e-mail: py@hms.harvard.edu; william_shih@dfci.harvard.edu

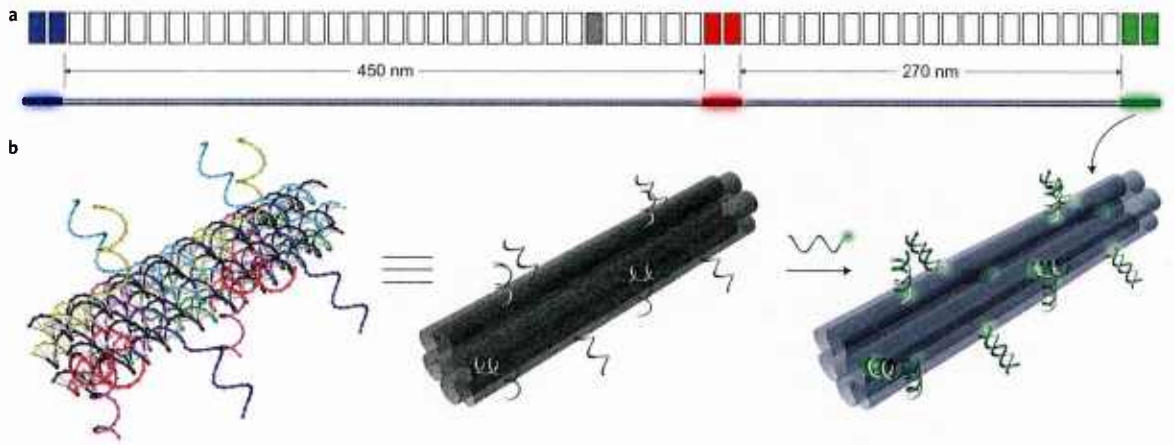

Figure 1 | Design of a barcode based on a DNA nanorod. a, Two schematics of the blue//red/green (BRG) barcode with a segment diagram on the top and a three-dimensional (3D) view at the bottom ('//' and '/' denote longer and shorter interzone distances in the barcode, respectively). The main body of the barcode is a DNA nanorod formed by dimerizing two origami monomers, each consisting of 28 segments of 42 bp (~14 nm in length). The grey segment in the middle represents the junction where the two monomers join together. Three zones of the nanorod of 84 bp were labelled fluorescently (shown as blue, red and green segments) to produce the BRG barcode. **b**, 3D illustrations to show the details of one fluorescently labelled zone. The left diagram shows a strand model of an 84 bp zone before labelling. Each of the twelve 63-base staples (rainbow colours) contains two parts: the 42-base region at the 5′-end to fold the scaffold (black) into a six-helix bundle nanorod and the 21-base extension at the 3′-end protrudes out for fluorescent labelling. The middle diagram shows a simplified model to emphasize the six-helix bundle structure (each helix is shown as a semitransparent grey cylinder) and the positioning of the 12 staple extensions (light-grey curls). The diagram on the right shows the zone with 'green' fluorescent labelling. The labelling is achieved by hybridizing the Cy3 (glowing green spheres)-modified strands to the staple extensions.

84 base pairs (bp; ~28 nm) on the nanorod were selected for fluorescent labelling, with interzone distances of 450 nm and 270 nm between the first and the last two zones, respectively. The fluorescently labelled zones were arranged spatially to generate an asymmetric fluorescent pattern that is decodable by diffraction-limited microscopy. For example, labelling the three zones (from left to right in Fig. 1a) with 'blue' (B, Alexa Fluor 488), 'red' (R, Alexa Fluor 647) and 'green' (G, Cy3) fluorophores (the pseudocolours reflect the excitation wavelength of the fluorophores) resulted in a BRG barcode that should be distinguishable from a GRB barcode. Therefore, $3^3 = 27$ different barcodes can be made from three spectrally distinguishable fluorophores. Within each zone (Fig. 1b), fluorescently modified oligonucleotides were hybridized to the twelve 21-base staple extensions (~6 nm between adjacent fluorophores) that protruded out from the main body of the nanorod. To facilitate imaging, ten additional staple strands were designed with 5′-biotinylated extensions to enable surface attachment (Supplementary Fig. S1, Tables S1–S4).

We assembled DNA-origami nanorods following the published protocol[36] with slight modifications (Supplementary Methods and Materials). To validate our system, we randomly chose five distinct barcodes for quality-control experiments. Two distinct features of these barcodes were clearly visible from the TIRF and epifluorescence images (Fig. 2a (top) and Supplementary Figs S2,S3): first, each fluorescent zone was resolved as a single-colour spot and each complete barcode consisted of three such spots; second, two of the neighbouring spots were separated by a small gap with the other two neighbours sat closely together. Therefore, we can recognize visually the geometrically encoded barcodes based on the colour identity of the spots and their relative spatial positions, even without the aid of any specialized decoding software. Computer-aided analysis of the BRG barcodes (Supplementary Fig. S4, Table S5) measured the average centre-to-centre distance between the neighbouring spots to be 433 ± 53 nm (mean $\pm$ standard deviation (s.d.), $N = 70$, longer distance) and 264 ± 52 nm ($N = 70$, shorter distance), which confirmed the correct formation of the barcodes. The small discrepancy between these experimentally measured distances and the designed values (478 nm and 295 nm, respectively) may be attributed to random thermal bending of the nanorods (persistence length of ~1–2 μm (ref. 29); see Supplementary Fig. S5). Also, the spot intensities were not perfectly uniform across the whole image, which may be the result of factors such as uneven illumination of the sample and differences in labelling efficiency. Nevertheless, the TIRF images showed that the barcodes assembled as designed and were resolved unambiguously.

We then manually investigated TIRF images with an area of $50 \times 50\ \mu m^2$ for five selected barcode species (Fig. 2a, bottom). The objects in the images were first sorted into qualified (that is, three single-colour spots arranged in a nearly linear (with bending angle $\geq 120°$, see Supplementary Fig. S4) and asymmetric fashion, as designed) and unqualified (that is, all other objects) barcodes. A qualified barcode was further categorized as correct or incorrect (false positive) based on whether the geometric pattern of its constituent fluorescent spots corresponded to the designed type. The unqualified barcodes were sorted further into (1) monomer nanorods (single spot or two touching spots), (2) barcodes with the 'wrong' geometry (that is, extreme bending) and (3) barcodes that contained at least one spot with multiple colours. On average, >80% of the visible objects were determined as qualified barcodes (that is, ≤20% false negative out of 188 observed objects) and these qualified barcodes were all correct (that is, 0% false positive out of 154 qualified barcodes (see the Supplementary Technical Notes)).

For many applications it is necessary for several different barcode species to coexist in one pool. Thus, it is important to examine the performance of our system when different barcode species are mixed. In an initial test, BRG and RGB barcodes were synthesized separately, mixed together at an equal molar ratio and co-purified via gel electrophoresis. The TIRF analysis (Supplementary Fig. S6) confirmed the 1:1 stoichiometry of the two barcodes and an overall assembly success rate (qualified barcode/all objects) of ~80%, which suggests that both barcodes maintained their integrity

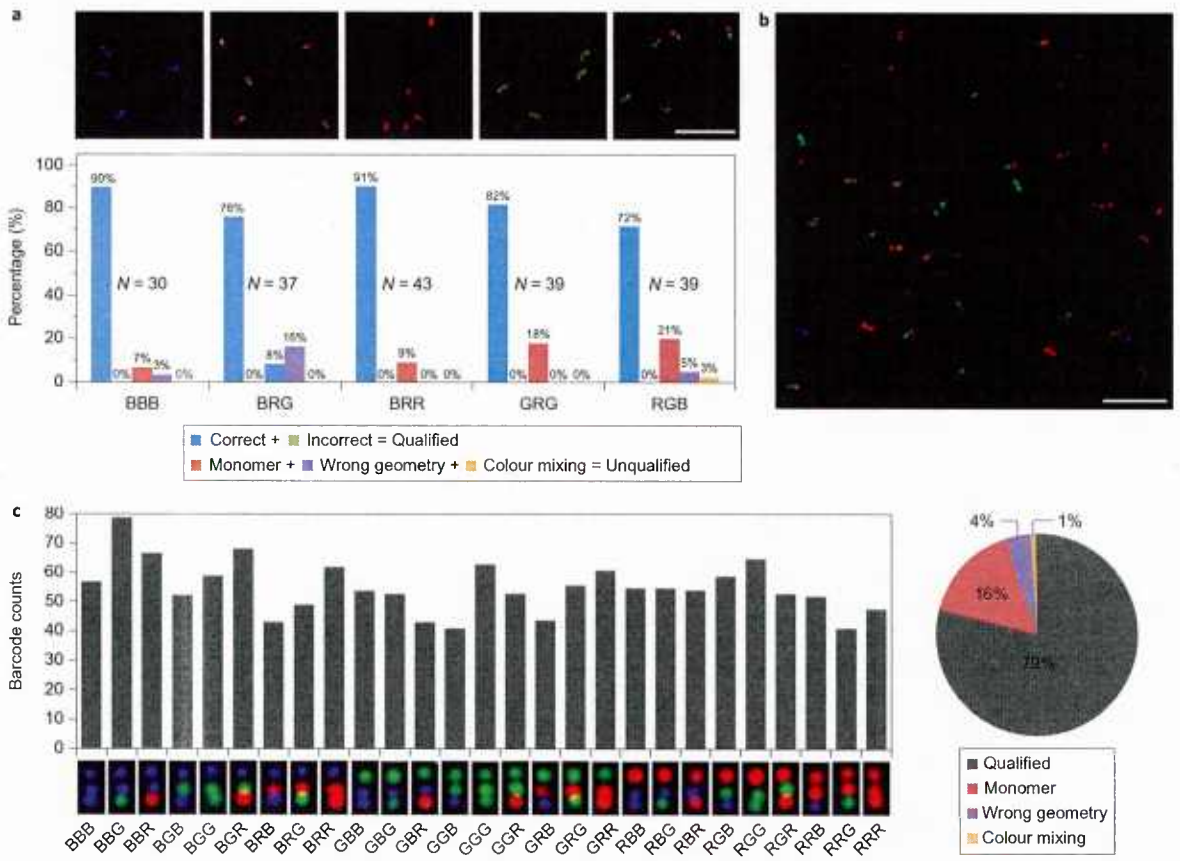

Figure 2 | Fluorescent barcodes with single-labelled zones. a, Superimposed TIRF microscopy images of five barcode species (top) and the statistics from manual counting (bottom). The barcode types are given below the horizontal axis of the diagram. Each bar graph was generated by manually counting the objects in a 50 × 50 μm^2 image (~40 barcodes; the exact sample size *N* is given next to the corresponding bar graph). **b**, A representative image of the equimolar mixture of 27 barcode species. **c**, Statistics obtained by analysing 27 images (50 × 50 μm^2) of the 27-barcode mixture (1,485 barcode molecules). The bar chart shows counts of the 27 species (55 ± 9, mean ± s.d.). A representative TIRF image (1.4 × 0.7 μm^2) of each barcode type is placed below the corresponding bar. The pie chart shows the object-sorting result. The colour scheme used for the bar graphs in (**a**) and the pie chart in (**c**) is: blue, correct barcodes (qualified barcode with expected identity); green, incorrect barcodes (qualified barcode with unexpected identity); red, monomer nanorods (one spot or two touching spots); purple, barcodes with the wrong geometry (bending angle <120°, see Supplementary Methods); orange, barcodes that contain at least one spot with two colours. In the 27-barcode pool, correct versus incorrect barcodes were not distinguishable because all barcode types were expected. As a result, the bars and pie slices that represent the qualified barcodes in (**c**) are shown in grey. Scale bars, 5 μm.

during the mixing and co-purification processes. In addition, over 98% of the qualified barcodes were either BRG or RGB barcodes. The 2% false-positive rate resulted from an unexpected barcode type, BGB (Supplementary Fig. S6), which could be attributed to the rare occasion on which the front monomer of the BRG barcode lay in close proximity to the rear monomer of the RGB barcode.

Next we imaged a pool of all 27 members of the barcode family in which all the species were mixed at an equimolar ratio. TIRF images (Fig. 2b and Supplementary Fig. S7) showed that all the types of barcodes were resolved. Statistical analyses of ~1,500 barcodes across 27 images (50 × 50 μm^2) revealed an average count of 55 barcodes per type with a s.d. of nine (Fig. 2c), in rough agreement with the expected stoichiometry, given pipetting and sampling errors. The distribution of observed objects over the four categories was consistent with the values measured from single-type barcode samples (here, correct versus incorrect barcodes were not distinguishable as all 27 types were included). The above observations suggest that the submicrometre-long DNA nanorod represents a reliable platform on which to construct geometrically encoded barcodes with built-in structural stiffness.

Fluorescent barcodes with dual-labelled zones

The multiplexing capability of the barcodes was enhanced by increasing the number of fluorophore species allowed per zone. We changed the sequence of six staple extensions per zone so that instead of using 12 identical fluorescent oligonucleotides for labelling, we used a combination of up to two fluorophore species, which allows more-distinct fluorescence signatures (pseudocolours) for each zone. This 'dual-labelling' strategy generates six pseudocolours (B, R, G, BG, BR and GR) from three spectrally differentiable fluorophores. Consequently, the total number of distinct barcodes was raised from $3^3 = 27$ to $6^3 = 216$. Five members from the barcode family with dual-labelled zones were chosen for quality-control testing (Fig. 3a). The barcodes can be decoded visually either solely from the superimposed TIRF image or by examining the three separate channels simultaneously. For example, as shown in the first column of Fig. 3a, the barcode 'BG//GR/BR' exhibited two spots each in the blue, green and red channels, but with descending gaps between them. In the superimposed image, the barcodes have the expected colour-mixing signature, cyan//yellow/pink. The correct formation of

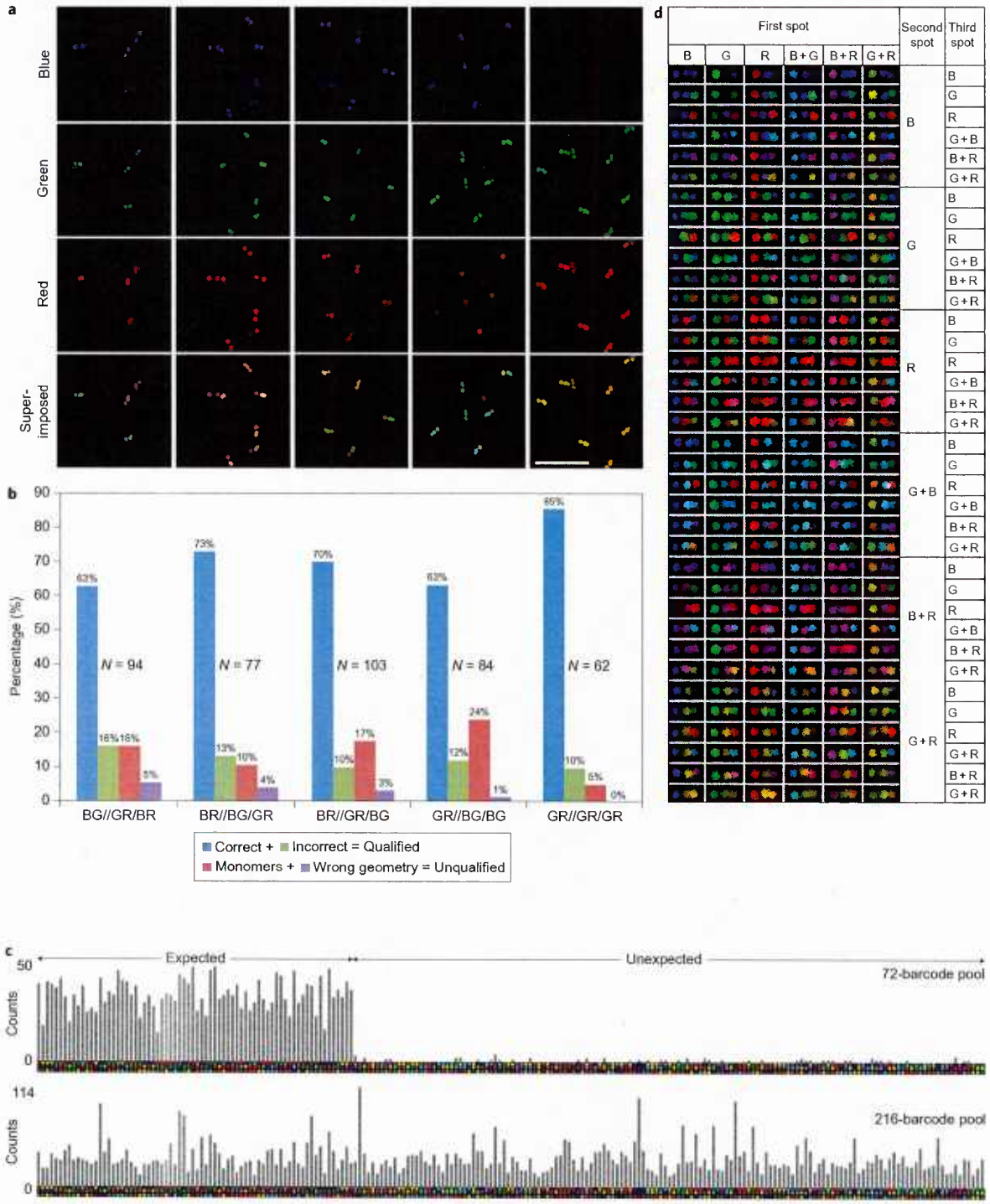

Figure 3 | Fluorescent barcodes with dual-labelled zones. **a**, Typical TIRF microscopy images of five selected barcode species, shown both in separate channels and as superimposed images. Scale bar, 5 μm. **b**, Statistics obtained by analysing two 50 × 50 μm^2 images of each barcode species (~85 barcodes, the exact sample size *N* is given beside the corresponding bar graph). The barcode types are given below the horizontal axis of the diagram. Colour scheme (unrelated to the pseudocolours of the fluorophores): blue, correct barcodes (correct geometry and colour identity); green, incorrect barcodes (correct geometry, but incorrect colour identity); red, monomer nanorods (one spot or two touching spots); purple, barcodes with the wrong geometry (bending angle <120°, see Supplementary Methods). **c**, Computer-aided barcode-counting results of the 72-barcode pool ($N = 2,617$) and the 216-barcode pool ($N = 7,243$), where the number of qualified barcodes are plotted as bar graphs (see Supplementary Tables S6,S7 for the numbers). A computer-generated reference barcode image is placed below the corresponding bar. The same horizontal axis is used for both bar-graph diagrams. **d**, One representative TIRF image (1.4 × 0.7 μm^2) for each of the 216 barcode species with dual-labelled zones.

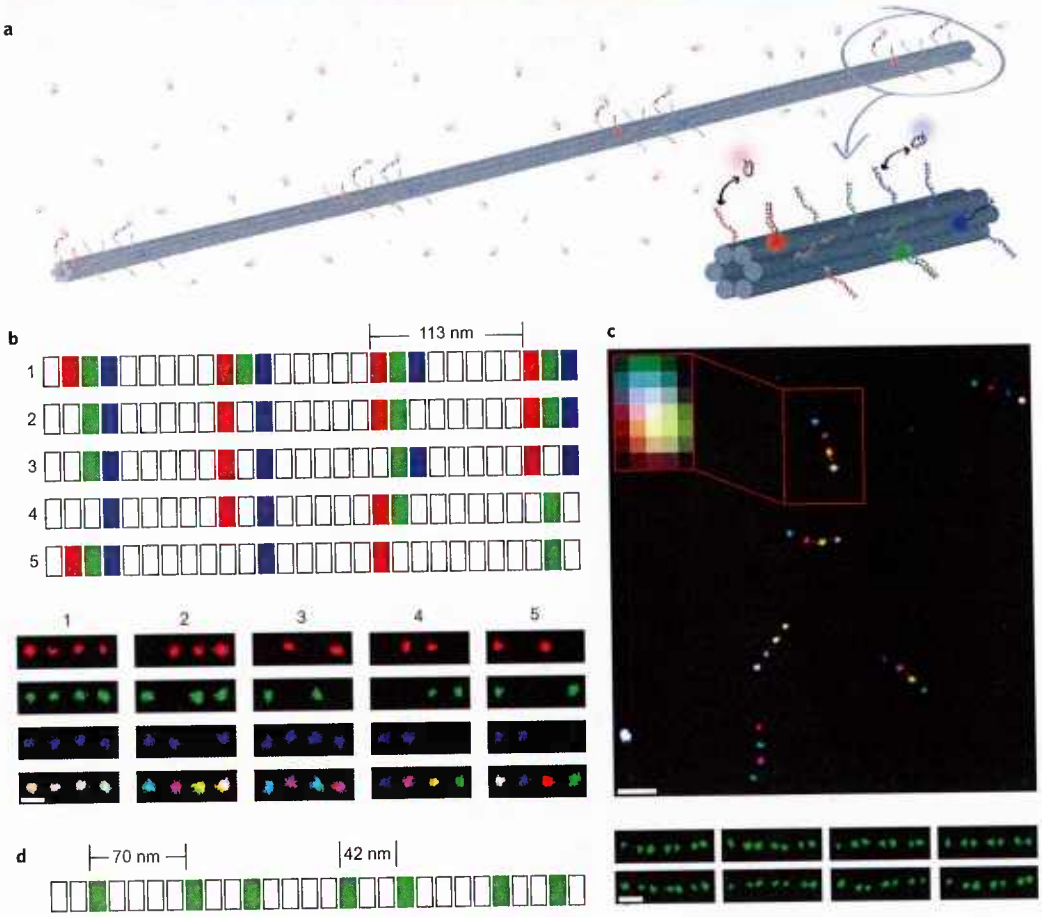

Figure 4 | Super-resolution fluorescent barcodes. a, Schematic of barcodes for DNA-PAINT super-resolution imaging. The 400 nm DNA nanorod consists of four binding zones evenly spaced by ~113 nm. Each zone can be decorated with the desired combination of 'docking' sequences for red, green or blue imager strands. The orthogonal imager strands bind transiently to their respective 'docking' sites on the nanorod, which creates the necessary 'blinking' for super-resolution reconstruction. **b**, The top panel is a segment diagram (similar to that in Fig. 1a) of the nanorod monomers used to create five barcodes. The lower panel comprises super-resolution images of the five barcodes shown in separate channels and as superimposed images. Scale bar = 100 nm. **c**, Super-resolution image showing all five barcodes from (**b**) in one mixture. The inset shows the diffraction-limited image of a barcode. Scale bar = 250 nm. **d**, An asymmetric barcode that consists of seven binding zones for green imager strands spaced at ~70 nm and ~42 nm for longer and shorter distances, respectively. Scale bar, 100 nm.

the other four barcode species was verified similarly (Fig. 3a and Supplementary Fig. S8). Although the pseudocolours of the dual-labelled zones were not always uniform (for example, some yellow spots were green tinted and others were red tinted) because of inconsistent labelling efficiency, the fluorescence signature of any given spot could be identified by checking the raw images acquired from the three imaging channels. Similar to barcodes with single-labelled zones, manual analysis of two $50 \times 50\ \mu m^2$ images of each of the five barcode species with dual-labelled zones revealed that 75–95% of the objects were qualified barcodes, of which 80–90% were of the correct type (Fig. 3b). Compared to barcodes in the single-labelled zone, the percentage of qualified barcodes remained the same, although the false-positive rate increased from zero (Fig. 2a) to 10–20%, which reflects the expected decrease in the robustness of the dual-labelling strategy (see Supplementary Technical Notes). All five barcodes examined here have each of their zones labelled with two distinct fluorophore species, which probably makes them among the most error-prone members of the barcode family with dual-labelled zones. Therefore, we would expect a lower average false-positive rate from the whole family.

We next imaged a mixture that contained 72 barcode species with dual-labelled zones that were individually assembled and co-purified (Supplementary Fig. S9). Custom MATLAB scripts were used to assist the decoding process (Supplementary Fig. S10) in either a fully automated unsupervised or in a supervised mode in which the software's best estimate of the barcode's identity was presented to the user for approval. Comparison between supervised and unsupervised decoding results showed >80% agreement between the computer software and the user (see Supplementary Methods and Fig. S11). The supervised analysis of 36 TIRF images ($64 \times 64\ \mu m^2$) registered 2,617 qualified barcodes that belonged to 116 different species (Fig. 3c, top panel, and Supplementary Table S6). The expected 72 species constituted ~98% of the total barcode population with an average barcode count of 36 per species and a s.d. of eight. In contrast, the unexpected species averaged only ~1.4 barcodes per species (maximum four counts). Finally, we analysed a mixture that contained all 216 members of the barcode family with dual-labelled zones (Supplementary Fig. S12). Unsupervised software analysis of 60 images ($64 \times 64\ \mu m^2$) registered an average count of 34 ± 17 (mean $\pm$ s.d., $N = 7{,}243$; see Fig. 3c, bottom panel, and

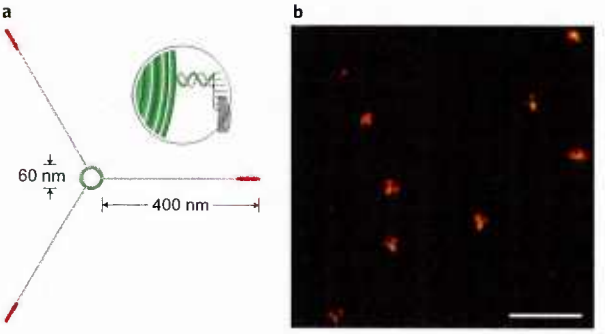

Figure 5 | Fluorescent barcode with nonlinear geometry. a, Schematic of three identical ~400 nm long DNA nanorods linked to the outer edge of a DNA ring (diameter ~60 nm) through the hybridization between staple extensions (inset). The ring and the end of the rod are labelled with Cy3 (green) and Cy5 (red), respectively. **b**, A representative TIRF microscopy image. Scale bar, 5 μm.

Supplementary Table S7) for each barcode species. This relatively large s.d. may be attributed to the increase in the number of distinct barcode species and to the decoding error in the fully automated data analysis. Although this system might be improved further to achieve better assembly and decoding accuracy, our study demonstrates that 216 barcode species were constructed and resolved successfully (Fig. 3d).

Subdiffraction fluorescent barcodes

The multiplexing capability of the barcodes can also be enhanced by increasing the number of fluorescent zones and resolving them using super-resolution techniques[37–40]. We here used DNA-PAINT[31] to obtain super-resolved images of barcodes with fluorescent zones spaced below the diffraction limit. In stochastic reconstruction microscopy[41,42] most molecules are switched to a fluorescent dark (OFF) state, and only a few emit fluorescence (ON state). Each molecule is localized with nanometre precision[43] by fitting its emission to a 2D Gaussian. DNA-PAINT exploits repetitive, transient binding of fluorescently labelled oligonucleotides ('imager' strands) to complementary 'docking' strands to obtain stochastic switching between fluorescence ON and OFF states (Fig. 4a). In the unbound state, only background fluorescence is observed. On binding of an imager strand, its fluorescence emission is detected using TIRF microscopy.

Previously published work demonstrated single-colour imaging with DNA-PAINT[31]. Here, we extended the technique to three-colour imaging by using orthogonal imager strand sequences coupled to three spectrally distinct dyes (Atto488, Cy3b and Atto655). To demonstrate the feasibility of the three-colour super-resolution barcode system, we designed a DNA nanorod monomer with four binding zones in a symmetric arrangement. The neighbouring zones were separated by ~113 nm, well below the diffraction limit. Each binding zone consisted of 18 staple strands, which can display three groups of orthogonal docking sequences (six per group) to which the blue, green or red imager strands can bind. As a proof-of-principle experiment, we designed five different barcodes (Fig. 4a and the top panel of Fig. 4b). The bottom panel of Fig. 4b shows the super-resolution reconstruction for each channel separately, as well as an overlay of all the channels. Figure 4c shows a larger area that contains all five barcodes. The unique pattern of the barcodes in all three channels can be resolved. The transient, repetitive binding of imager strands to docking sequences on the nanorod not only creates the necessary 'blinking' behaviour for localization, but also makes the imaging more robust, as DNA-PAINT is not prone to photobleaching (Supplementary Fig. S13). We also constructed an asymmetric barcode version that consisted of seven binding zones for green imager strands with longer and shorter spacings of ~70 nm and ~42 nm, respectively (Fig. 4d, overview given in Supplementary Fig. S14). If three colours in this arrangement are used, $(2^3 - 1)^7 = 823{,}543$ different barcodes can be constructed. In principle, we could also construct shorter barcodes and maintain the multiplexing capability of the diffraction-limited barcode system. For example, ~100 nm long barcodes with three asymmetric binding zones would allow for 343 different signatures. The inherent modularity of our design allows the interzone distances to be tailored to a wide range of microscopes and applications.

Nonlinear fluorescent barcodes

More sophisticated barcodes can be generated using DNA nanostructures with nonlinear geometry. Figure 5 shows an example in which three ~400 nm DNA rods were linked to the outer edge of a ~60 nm DNA ring through hybridization between staple extensions (Fig. 5a, inset). Fluorescently labelling the ring and the far end of the nanorods generated a pattern that resembled a three-point star and was clearly resolvable under fluorescence microscopy. TIRF microscopy and transmission electron microscopy (Fig. 5b and Supplementary Figs S15,S16) revealed that about 50% of successfully assembled barcodes featured three nanorods that surrounded the ring with a roughly 120° angle between each other, as designed, although many other barcodes had significantly biased angles between neighbouring nanorods because of the semi-flexible double-stranded DNA linker between the ring and the nanorods. It is conceivable that we could increase the system's accuracy and robustness using a similar design to connect three identical 'satellite' linear barcodes to a central hub (here the three satellite barcodes may share the hub as a common fluorescently labelled zone). Such a design would triplicate the encoding redundancy. In addition, stiffer linkers between the ring and the protrusions (for

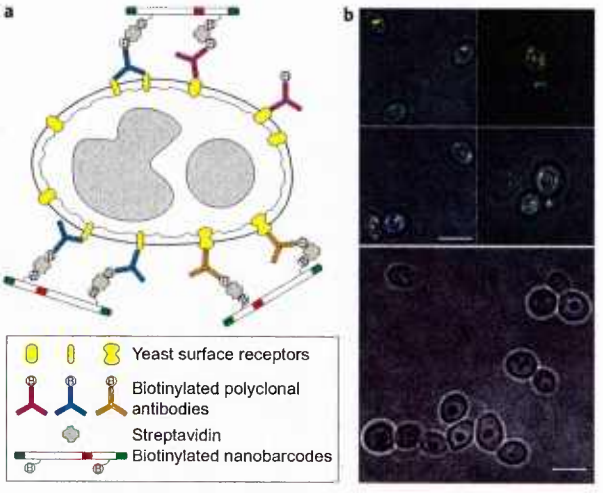

Figure 6 | Tagging yeast cells with the GRG barcodes as *in situ* imaging probes. a, In this illustration of the tagging mechanism, the biotinylated barcodes are anchored on the yeast cell through streptavidin molecules bound to biotinylated polyclonal antibodies coated on the yeast surface. For clarity, only two of the ten biotinylated staples on the barcode are shown. **b**, Superimposed microscopy images (acquired from bright-field and TIRF microscopy) of the yeast cells treated with the barcodes. The top four images show yeast cells treated as illustrated in (**a**). The bottom image is a negative control in which yeast cells were treated with non-biotinylated barcodes. Scale bars, 5 μm.

example, multihelix DNA with strand cross-overs) could be used to achieve better-defined barcode geometry.

Fluorescent barcodes as *in situ* imaging probes

Modifying the barcodes with functional ligands, such as antibodies and aptamers, would allow the barcodes to tag specific biological samples and serve as multiplexed *in situ* imaging probes. In a proof-of-principle experiment, the GRG barcode was used to tag wild-type *Candida albicans* yeast. The yeast cells were first mixed with a biotinylated polyclonal antibody specific to *C. albicans*, then coated with streptavidin and finally incubated with biotinylated GRG barcodes (Fig. 6a). TIRF microscopy revealed the barcodes attached to the bottom surface of the yeast cells (Fig. 6b, top panel, and Supplementary Fig. S17). Although some of the nanorods landed awkwardly on the uneven cell walls of the yeast cells, a number of GRG barcodes were resolved clearly. In contrast, no barcode tagging was observed when non-biotinylated antibodies or barcodes were used (Fig. 6b, bottom panel, and Supplementary Fig. S17), which suggests that no nonspecific interactions existed between the barcode and the cell surface. Here, only the bottom layer (~100 nm) of the 3D specimen was imaged to assure adequate lateral resolution and minimal background noise. With the development of 3D microscopy[44], protein conjugation chemistry[45–47] and DNA self-assembly techniques[21–23], we believe a quantitative and multiplexed *in situ* imaging system is within reach.

Discussion

In summary, we constructed a new kind of geometrically encoded fluorescent barcode using self-assembly based on DNA origami. Our approach differs from previous optically decodable barcoding systems[1–16] in three aspects.

First, our barcodes are 400−800 nm in length, substantially shorter than the existing geometrically encoded fluorescent barcodes. The submicrometre dimensions make them potentially useful as *in situ* single-molecule imaging probes. For example, we demonstrated the tagging of cell-surface proteins in yeast. The system also fulfils a technological challenge to build robust finite-size optical barcodes with the smallest feature approaching or even smaller than the diffraction limit of visible light.

Second, our barcodes are self-assembled from DNA. Unlike previous constructions, their synthesis and purification does not require enzymatic reaction[15], genomic engineering[6], photolithography[14], electrochemical etching[48] or microfluidic devices[1,14], and is easy to perform in a typical biochemistry laboratory (see Supplementary Technical Note for the barcode cost). The barcodes can be modified easily to display sequence-specific attachment sites simply through DNA-origami staple extensions.

Third, the robustness and programmability of the platform based on DNA origami enables a high multiplexing capability. Here, we constructed successfully 216 barcode species that were decoded in one pool (previous submicrometre-sized fluorescent barcodes contained no more than 11 distinct barcodes[3,7,8,12]). Even compared to a previous production of multicolour fluorescent barcodes up to 10 μm in size, our system is among the few examples[1,15] that demonstrate more than 100 distinct barcode species in practice. The NanoString nCounter demonstrated larger numbers of barcodes that coexisted in a homogenous solution[15]. However, the reporter probes of the NanoString (~7 kb or ~2 μm double-stranded RNA–DNA hybrid molecules) require stretching to make the barcodes resolvable, which makes them difficult to use as *in situ* probes. In contrast, the stiff barcodes based on DNA origami maintain their structural integrity when applied to cell surfaces, which suggests their potential use as *in situ* probes. Furthermore, combination of the DNA-PAINT imaging technique and the nanorods based on DNA origami allowed us to create nanoscopic 'super-resolution' barcodes, which suggests the potential to achieve >100,000 distinct barcodes. Such a large number of barcodes opens opportunities such as the measurement of human gene expression through *ex situ* imaging. In practice, it is probable that a small number of distinct codes could be sufficient to label the targets of interest in various application scenarios. For those applications, we could use selectively the best-performing subset of the barcode library and/or use barcodes of shorter sizes (for example, ~100 nm barcode with three fluorescent spots).

In the future, we expect our barcodes to interface with the rapidly growing protein/antibody library and tagging techniques[44–47] to yield a versatile imaging toolbox for single-molecule studies of biological events and biomedical diagnostics. For example, we can envision the utility of a library of barcodes modified with monoclonal antibodies against the clusters of differentiation molecules[49] (>300 known) for immunophenotyping applications[50]. However, moving from *in vitro* imaging on a glass surface to *in situ* imaging of a cell membrane may present substantial technical challenges. For example, crowding of multiple barcodes may render an individual barcode unresolvable. Although our current barcodes are potentially suitable for *in situ* labelling of multiple cell types (each carrying distinct surface markers), they are too bulky for a multiplexed detection of many subcellular identities in a single cell. This challenge could be addressed by using barcodes of a more compact size and stiffer structures (for example, DNA tetrahedrons with ~50 nm edges). Although such shorter barcodes may be used readily to tag the surface markers of fixed cells, imaging them in living cells will probably pose additional significant challenges. For example, to resolve barcodes on dynamic living cell membranes may require higher temporal resolution than that provided by current super-resolution microscopy techniques. The barcodes constructed here represent the first experimental demonstration of a large number of submicrometre geometrically encoded fluorescent barcodes that are structurally stiff and optically resolvable. The fast progress of nanotechnology's ability to engineer shape and microscopy's ability to resolve shape should enable the future construction of more versatile and powerful geometrically encoded barcodes for diverse biomedical applications.

Received 25 January 2012; accepted 8 August 2012; published online 24 September 2012

References

1. Fournier Bidoz, S. *et al.* Facile and rapid one-step mass preparation of quantum-dot barcodes. *Angew. Chem. Int. Ed.* **47,** 5577–5581 (2008).
2. Han, M., Gao, X., Su, J. Z. & Nie, S. Quantum-dot-tagged microbeads for multiplexed optical coding of biomolecules. *Nature Biotechnol.* **19,** 631–635 (2001).
3. Li, Y., Cu, Y. T. H. & Luo, D. Multiplexed detection of pathogen DNA with DNA-based fluorescence nanobarcodes. *Nature Biotechnol.* **23,** 885–889 (2005).
4. Marcon, L. *et al.* 'On-the-fly' optical encoding of combinatorial peptide libraries for profiling of protease specificity. *Mol. BioSyst.* **6,** 225–233 (2010).
5. Xu, H. *et al.* Multiplexed SNP genotyping using the Qbead system: a quantum dot-encoded microsphere-based assay. *Nucleic Acids Res.* **31,** e43 (2003).
6. Livet, J. *et al.* Transgenic strategies for combinatorial expression of fluorescent proteins in the nervous system. *Nature* **450,** 56–62 (2007).
7. Lin, C., Liu, Y. & Yan, H. Self-assembled combinatorial encoding nanoarrays for multiplexed biosensing. *Nano Lett.* **7,** 507–512 (2007).
8. Levsky, J. M., Shenoy, S. M., Pezo, R. C. & Singer, R. H. Single-cell gene expression profiling. *Science* **297,** 836–840 (2002).
9. Braeckmans, K. *et al.* Encoding microcarriers by spatial selective photobleaching. *Nature Mater.* **2,** 169–173 (2003).
10. Dejneka, M. J. *et al.* Rare earth-doped glass microbarcodes. *Proc. Natl Acad. Sci. USA* **100,** 389–393 (2003).
11. Gudiksen, M. S., Lauhon, L. J., Wang, J., Smith, D. C. & Lieber, C. M. Growth of nanowire superlattice structures for nanoscale photonics and electronics. *Nature* **415,** 617–620 (2002).
12. Li, X. *et al.* Controlled fabrication of fluorescent barcode nanorods. *ACS Nano* **4,** 4350–4360 (2010).
13. Nicewarner-Pena, S. R. Submicrometer metallic barcodes. *Science* **294,** 137–141 (2001).

14. Pregibon, D. C., Toner, M. & Doyle, P. S. Multifunctional encoded particles for high-throughput biomolecule analysis. *Science* **315,** 1393–1396 (2007).
15. Geiss, G. K. *et al.* Direct multiplexed measurement of gene expression with color-coded probe pairs. *Nature Biotechnol.* **26,** 317–325 (2008).
16. Xiao, M. *et al.* Direct determination of haplotypes from single DNA molecules. *Nature Methods* **6,** 199–201 (2009).
17. Toomre, D. & Bewersdorf, J. A new wave of cellular imaging. *Annu. Rev. Cell Dev. Biol.* **26,** 285–314 (2010).
18. Seeman, N. C. Nucleic acid junctions and lattices. *J. Theor. Biol.* **99,** 237–247 (1982).
19. Aldaye, F. A., Palmer, A. L. & Sleiman, H. F. Assembling materials with DNA as the guide. *Science* **321,** 1795–1799 (2008).
20. Lin, C., Liu, Y. & Yan, H. Designer DNA nanoarchitectures. *Biochemistry* **48,** 1663–1674 (2009).
21. Nangreave, J., Han, D., Liu, Y. & Yan, H. DNA origami: a history and current perspective. *Curr. Opin. Chem. Biol.* **14,** 608–615 (2010).
22. Shih, W. M. & Lin, C. Knitting complex weaves with DNA origami. *Curr. Opin. Struct. Biol.* **20,** 276–282 (2010).
23. Tørring, T., Voigt, N. V., Nangreave, J., Yan, H. & Gothelf, K. V. DNA origami: a quantum leap for self-assembly of complex structures. *Chem. Soc. Rev.* **40,** 5636–5646 (2011).
24. Rothemund, P. W. K. Folding DNA to create nanoscale shapes and patterns. *Nature* **440,** 297–302 (2006).
25. Douglas, S. M. *et al.* Self-assembly of DNA into nanoscale three-dimensional shapes. *Nature* **459,** 414–418 (2009).
26. Dietz, H., Douglas, S. M. & Shih, W. M. Folding DNA into twisted and curved nanoscale shapes. *Science* **325,** 725–730 (2009).
27. Andersen, E. S. *et al.* Self-assembly of a nanoscale DNA box with a controllable lid. *Nature* **459,** 73–76 (2009).
28. Han, D., Pal, S., Liu, Y. & Yan, H. Folding and cutting DNA into reconfigurable topological nanostructures. *Nature Nanotechnol.* **5,** 712–717 (2010).
29. Liedl, T., Högberg, B., Tytell, J., Ingber, D. E. & Shih, W. M. Self-assembly of three-dimensional prestressed tensegrity structures from DNA. *Nature Nanotechnol.* **5,** 520–524 (2010).
30. Han, D. *et al.* DNA origami with complex curvatures in three-dimensional space. *Science* **332,** 342–346 (2011).
31. Jungmann, R. *et al.* Single-molecule kinetics and super-resolution microscopy by fluorescence imaging of transient binding on DNA origami. *Nano Lett.* **10,** 4756–4761 (2010).
32. Steinhauer, C., Jungmann, R., Sobey, T. L., Simmel, F. C. & Tinnefeld, P. DNA origami as a nanoscopic ruler for super-resolution microscopy. *Angew. Chem. Int. Ed.* **48,** 8870–8873 (2009).
33. Lund, K. *et al.* Molecular robots guided by prescriptive landscapes. *Nature* **465,** 206–210 (2010).
34. Pal, S., Deng, Z., Ding, B., Yan, H. & Liu, Y. DNA-origami-directed self-assembly of discrete silver-nanoparticle architectures. *Angew. Chem. Int. Ed.* **49,** 2700–2704 (2010).
35. Bui, H. *et al.* Programmable periodicity of quantum dot arrays with DNA origami nanotubes. *Nano Lett.* **10,** 3367–3372 (2010).
36. Douglas, S. M., Chou, J. J. & Shih, W. M. DNA–nanotube-induced alignment of membrane proteins for NMR structure determination. *Proc. Natl Acad. Sci. USA* **104,** 6644–6648 (2007).
37. Hell, S. W. Far-field optical nanoscopy. *Science* **316,** 1153–1158 (2007).
38. Huang, B., Babcock, H. & Zhuang, X. Breaking the diffraction barrier: super-resolution imaging of cells. *Cell* **143,** 1047–1058 (2010).
39. Vogelsang, J. *et al.* Make them blink: probes for super-resolution microscopy. *ChemPhysChem.* **11,** 2475–2490 (2010).
40. Walter, N. G., Huang, C. Y., Manzo, A. J. & Sobhy, M. A. Do-it-yourself guide: how to use the modern single-molecule toolkit. *Nature Methods* **5,** 475–489 (2008).
41. Betzig, E. *et al.* Imaging intracellular fluorescent proteins at nanometer resolution. *Science* **313,** 1642–1645 (2006).
42. Rust, M. J., Bates, M. & Zhuang, X. Sub-diffraction-limit imaging by stochastic optical reconstruction microscopy (STORM). *Nature Methods* **3,** 793–795 (2006).
43. Yildiz, A. *et al.* Myosin V walks hand-over-hand: single fluorophore imaging with 1.5-nm localization. *Science* **300,** 2061–2065 (2003).
44. Jones, S. A., Shim, S. H., He, J. & Zhuang, X. Fast, three-dimensional super-resolution imaging of live cells. *Nature Methods* **8,** 499–508 (2011).
45. Gautier, A. *et al.* An engineered protein tag for multiprotein labeling in living cells. *Chem. Biol.* **15,** 128–136 (2008).
46. Keppler, A. *et al.* A general method for the covalent labeling of fusion proteins with small molecules in vivo. *Nature Biotechnol.* **21,** 86–89 (2003).
47. Klein, T. *et al.* Live-cell dSTORM with SNAP-tag fusion proteins. *Nature Methods* **8,** 7–9 (2011).
48. Cunin, F. *et al.* Biomolecular screening with encoded porous-silicon photonic crystals. *Nature Mater.* **1,** 39–41 (2002).
49. Matesanz-Isabel, J. *et al.* New B-cell CD molecules. *Immunol. Lett.* **134,** 104–112 (2011).
50. Maecker, H. T., McCoy, J. P. & Nussenblatt, R. Standardizing immunophenotyping for the Human Immunology Project. *Nature Rev. Immunol.* **12,** 191–200 (2012).

Acknowledgements

We thank C. Steinhauer and S. P. Laurien for help with super-resolution microscopy software development, the Harvard Center for Biological Imaging, as well as the Nikon Imaging Center at Harvard Medical School, for the use of their microscopes and S. M. Douglas for providing the transmission electron microscopy images used in Supplementary Fig. S5. This work is supported by a National Institutes of Health (NIH) Director's New Innovator Award (1DP2OD007292), a National Science Foundation Faculty Early Career Development Award (CCF1054898), an Office of Naval Research Young Investigator Program Award (N000141110914), an Office of Naval Research grant (N000141010827) and a Wyss Institute for Biologically Engineering Faculty Startup Fund to P.Y., and an NIH Director's New Innovator Award (1DP2OD004641) and a Wyss Institute for Biologically Inspired Engineering Faculty Award to W.M.S. C. Li, D.L. and G.M.C. acknowledge support from the National Human Genome Research Institute, Centers of Excellence in Genomic Science. R.J. acknowledges support from the Alexander von Humboldt-Foundation through a Feodor Lynen fellowship.

Author contributions

C. Lin conceived the project, designed and conducted the majority of the experiments, analysed the data and prepared the majority of the manuscript. R.J. conceived the super-resolution barcode study, designed and conducted experiments for this study, analysed the data and prepared the manuscript. A.M.L. wrote the MATLAB script for the automated barcode deciphering and prepared the manuscript. C. Li wrote the C script for the barcode geometry characterization. D.L. (with C. Lin) performed the yeast-tagging experiment. G.M.C. championed multiplexed *in situ*, supervised C. Li and D.L., and critiqued the data and the manuscript. W.M.S. conceived the project, discussed the results and prepared the manuscript. P.Y. conceived, designed and supervised the study, interpreted the data and prepared the manuscript. All authors reviewed and approved the manuscript.

Additional information

Supplementary information is available in the online version of the paper. Reprints and permission information is available online at http://www.nature.com/reprints. Correspondence and requests for materials should be addressed to P.Y. and W.M.S.

Competing financial interests

The authors declare competing financial interests: a provisional US patent application has been filed.

11.4.2 Structural DNA nanotechnology application: Metallized DNA as etching mask for graphene

nature COMMUNICATIONS

ARTICLE

Received 26 Nov 2012 | Accepted 4 Mar 2013 | Published 9 Apr 2013

DOI: 10.1038/ncomms2690

Metallized DNA nanolithography for encoding and transferring spatial information for graphene patterning

Zhong Jin[1], Wei Sun[2,3], Yonggang Ke[2], Chih-Jen Shih[1], Geraldine L.C. Paulus[1], Qing Hua Wang[1], Bin Mu[1], Peng Yin[2,3] & Michael S. Strano[1]

The vision for graphene and other two-dimensional electronics is the direct production of nanoelectronic circuits and barrier materials from a single precursor sheet. DNA origami and single-stranded tiles are powerful methods to encode complex shapes within a DNA sequence, but their translation to patterning other nanomaterials has been limited. Here we develop a metallized DNA nanolithography that allows transfer of spatial information to pattern two-dimensional nanomaterials capable of plasma etching. Width, orientation and curvature can be programmed by specific sequence design and transferred, as we demonstrate for graphene. Spatial resolution is limited by distortion of the DNA template upon Au metallization and subsequent etching. The metallized DNA mask allows for plasmonic enhanced Raman spectroscopy of the underlying graphene, providing information on defects, doping and lattice symmetry. This DNA nanolithography enables wafer-scale patterning of two-dimensional electronic materials to create diverse circuit elements, including nanorings, three- and four-membered nanojunctions, and extended nanoribbons.

[1] Department of Chemical Engineering, Massachusetts Institute of Technology, Cambridge, Massachusetts 02139, USA. [2] Wyss Institute for Biologically Inspired Engineering, Harvard University, Boston, Massachusetts 02115, USA. [3] Department of Systems Biology, Harvard Medical School, Harvard University, Boston, Massachusetts 02115, USA. Correspondence and requests for materials should be addressed to M.S.S. (email: strano@mit.edu) or to P.Y. (email: peng_yin@hms.harvard.edu).

Two-dimensional (2D) electronic materials such as graphene, a monolayer of sp^2-bonded carbon atoms, are emerging as promising candidates for next-generation nanoelectronics[1,2]. An important vision for these materials is to enable complex and diverse circuit designs directly patterned from an initial monolayer[3–5], thereby circumventing key challenges in the placement, orientation and electronic control of constituent nanocomponents, such as carbon nanotubes. In the case of graphene, nanopatterning can enable a diversity of electronic functions including quantum confined electronic band gaps in graphene nanoribbons[6,7], quantum interference effects and Aharonov–Bohm oscillations in graphene nanorings[8,9] and single-electron transport in graphene quantum dots[10,11]. Previously demonstrated methods for forming graphene nanostructures and nanoribbons in the literature can be grouped into three main categories: (a) top-down etching methods based on larger graphene sheets[12,13], (b) bottom-up synthesis methods from molecular building blocks[14] and (c) unzipping methods based on carbon nanotubes to form nanoribbons[15,16]. However, the preparative synthesis of arbitrarily shaped graphene nanostructures with specific spatial dimensions remains a significant challenge. For example, electron beam lithography (EBL) can be used for patterning graphene into specific shapes using a rastering approach, but cannot efficiently yield wafer-scale, pre-programmed graphene structures with sub-100 nm size.

DNA self-assembly[17–28], such as DNA origami[22–24] and single-stranded tile (SST) assembly[26–28], can create complex 2D[22,24,26,27] and 3D[18,20,23,28] structures by encoding structural information using oligonucleotide recognition. Both the SST strategy—assembling a structure from hundreds of synthetic SSTs (most are 42-bases long)—and the DNA origami strategy—assembling a structure by folding a long single-stranded DNA scaffold (7–8-kb long M13 viral genome) via its hybridization with hundreds of short synthetic 'staple strands'—permit the programming of complex 2D and 3D shapes with nanometre scale features. DNA nanostructures can be used to expand the morphological and functional diversity of other nanomaterials. For example, DNA nanostructures can template the positioning of nanoparticles and carbon nanotubes[29–33] and they can also be functionalized into metallic nanostructures[34–40]. However, the transfer of spatial information to other 2D materials remains unexplored. Metallization produces nanowires and particles composed of disconnected grains, which decrease the conductivity[34–40]. In this way, DNA metallization is limited in its ability to construct nanoelectronic devices[40]. DNA nanostructures have also been used as shadow masks for metal deposition[41] and SiO_2 etching[42–44]. However, unprotected DNA masks degrade under plasma exposure, hindering their use for nanolithography. For successful shape-specific lithography, the encoded information must be transferred to a more stable lithographic mask.

Results

Metallized DNA lithography. Herein we demonstrate an important advance towards complex nanopatterning of graphene by employing metallized DNA nanostructures as lithographic masks. Single-stranded DNA molecules are encoded with structural information (Fig. 1a) and hybridized with their complementary partners at specific locations which causes them to assemble into the prescribed 2D planar shape in solution (Fig. 1b). The DNA template is then adsorbed onto the graphene surface with the aid of a 1-pyrenemethylamine adhesion layer

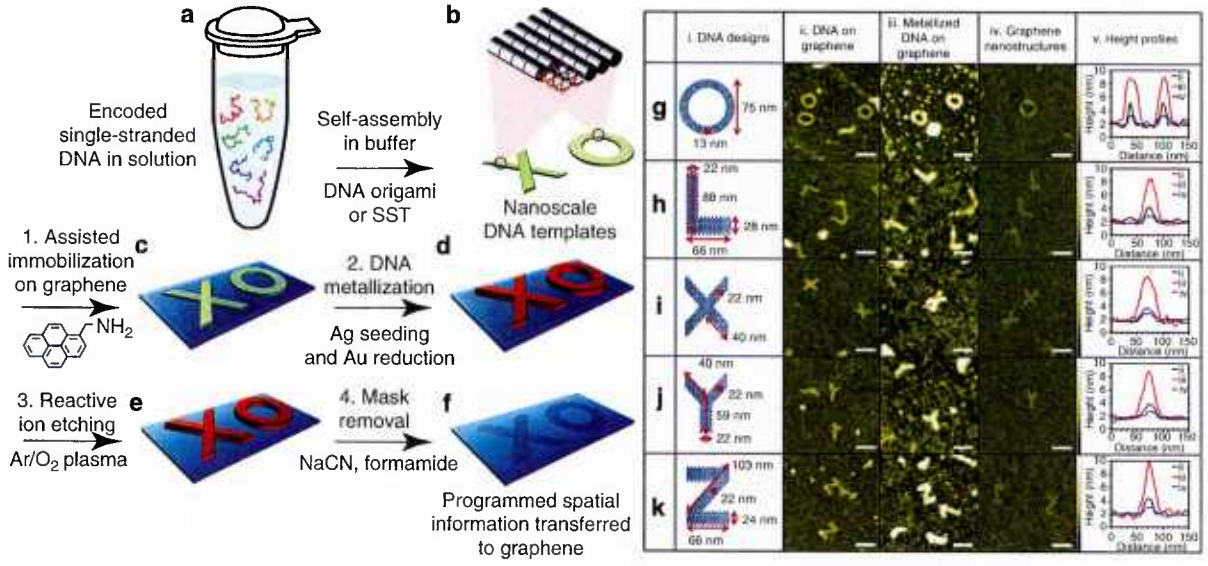

Figure 1 | Nanopatterning of graphene via metallized DNA structures that encode and transfer spatial information. (**a**) The encoded single-stranded DNA building blocks were programmed to fold into complex nanoscale DNA templates in solution. (**b**) Specific DNA templates, that is, X- and ring-shapes, were formed by DNA origami or SST. (**c**) Nano-sized DNA templates with specific shapes were deposited onto pre-synthesized graphene sheets (lithography step 1). (**d**) Metallization of the DNA templates generated custom-shaped gold masks on graphene (lithography step 2). (**e**) RIE removed unprotected graphene, leaving only gold mask-covered regions on wafer (lithography step 3). (**f**) Specifically shaped graphene nanostructures, that is, graphene X-shapes and nanorings, were obtained after mask removal (lithography step 4). (**g–k**) Graphene nanorings and letter-shapes derived from metallized DNA templates, from top to bottom, ring-, L-, X-, Y- and Z-shaped nanostructures, respectively. Columns (i–v), from left to right: (i) motif designs of DNA templates, (ii) AFM images of the DNA templates immobilized on graphene, (iii) the metallized templates on graphene, (iv) the final etched graphene shapes and (v) typical height profiles of the structures in column ii (black), iii (red) and iv (blue). Scale bars, 100 nm (AFM lateral); 10 nm (height scales).

(Fig. 1c). The DNA nanostructures are treated with glutaraldehyde to enable seeding with Ag[36], and are subsequently coated with Au (see the Methods section). This metallization of the DNA template renders it into a lithographic gold mask on the graphene that largely preserves its original spatial information (Fig. 1d). The metallization allows the DNA template to survive the subsequent etching process and to function as a positive relief mask. Ar/O_2 plasma reactive ion etching (RIE) removes the unprotected region of graphene (Fig. 1e) while allowing transfer of the spatial information from the metallized DNA templates to the final etched graphene products after metal dissolution (Fig. 1f).

We examined six types of DNA templates to test the transfer and preservation of spatial information (such angles and curvature) from the original DNA templates to eventual graphene nanostructures. A circular ring was designed using 3D DNA origami[24], whereas various 'letter-shaped' junctions and a nanoribbon were designed using 1D and 2D SST[26,27]. Crude products for DNA nanorings and letter-shapes were purified by 2% native agarose gel electrophoresis. Monolayer graphene sheets were grown on copper foils via chemical vapour deposition (CVD)[45] and subsequently transferred to SiO_2/Si wafers (300-nm thick SiO_2 layer) with the assistance of spin-coated poly (methyl methacrylate) (PMMA) films and a $CuCl_2$/HCl copper etchant. The hydrophobic nature of CVD graphene hinders an evenly distributed deposition of the DNA nanostructures onto the CVD-graphene sheet. We found that pre-adsorption of 1-pyrenemethylamine molecules onto the graphene significantly increased the surface adhesion and improved the dispersion of negatively charged hydrophilic DNA templates on graphene, without damaging either the DNA structures or the underlying graphene (as demonstrated below by Raman measurements). We also tested cationic surfactants, such as cetrimonium bromide (CTAB) and sodium dodecyl sulfate (SDS), to improve the surface wetting of graphene towards the negatively charged DNA templates. However, we found that DNA nanostructures did not survive in the presence of such ionic surfactants. In control experiments, mask removal of metallized DNA on graphene by sequential soaking in NaCN and formamide without subsequent etching recovered intact graphene without residue or observable defects. Further experimental details can be found in the Methods section.

The programming and transfer of DNA patterns is firstly demonstrated by the achievement of sub-100 nm graphene nanorings (Fig. 1g) that copied curvature from DNA templates. We also examined letter-shaped junctions, that is, L, X, Y and Z (Fig. 1h–k). The L-shaped DNA mask demonstrated the perpendicular alignment of two ribbons with different widths (Fig. 1h). The X-, Y-, and Z-shaped masks were used to demonstrate successful printing of junctions composed of two or three ribbons with distinct orientations (Fig. 1i–k). After each processing step, the morphological changes of deposited DNA templates, metallized DNA masks and final graphene nanostructures were investigated by atomic force microscopy (AFM) (Fig. 1 h–k, column ii–v; also see Supplementary Table S1 for statistical analysis). The graphene nanostructures were produced at preparative scale and depending on the concentration of initial DNA templates deposited on graphene, several letter-shaped graphene patterns can be observed in an area of 1 μm^2 (Fig. 1h–k, column iv). We note that the resolution of the lateral features under AFM scanning is limited by the sharpness of the AFM tip.

The designed width of the DNA nanorings is 13 nm with a 75-nm outer diameter. The measured height and width of glutaraldehyde-treated DNA nanorings deposited on graphene are 2.9 ± 0.3 and 16.1 ± 1.3 nm, respectively. The small increase in the width of the DNA templates compared with their design is likely due to the partial dehydration and flattening of the soft DNA structures on the dry surface. After metallization, the height and width of DNA nanorings were measured as 7.2 ± 1.4 and 29.4 ± 3.2 nm, respectively, confirming the success of the Au reduction. The metallized DNA masks are composed of fused gold nanoparticles that nucleated along the DNA skeletons and induced the size expansion. Upon subsequent RIE etching and mask-removal processing, the final graphene nanostructures were obtained, with a height and width of 1.2 ± 0.3 and 19.0 ± 4.3 nm, respectively. Plasma beam scattering at the edges of mask during the RIE process appears to shrink the resulting graphene edges, producing a narrower structure than that of the metallized DNA mask. However, the ring structure was preserved throughout all steps of the nanolithography. The competing effects of size expansion by metallization and shrinking by the etching process result in the fairly accurate preservation of spatial information. The average outer diameter of the initial DNA masks and the final graphene nanorings were 75.7 ± 5.6 and 81.7 ± 5.4 nm, respectively, indicating successful transfer of this spatial feature.

Similar fidelity was observed for the samples with letter-shaped DNA templates. The initial letter-shaped DNA templates deposited on graphene almost all have the same height, with an average value of 2.1 ± 0.3 nm. The metallized DNA masks of letter-shapes showed a height distribution of 6.7 ± 0.9 nm and an average arm-width increase from 20.9 ± 2.9 to 31.4 ± 5.0 nm. The final graphene nanostructures derived from all letter-shape templates has an average height of 1.1 ± 0.2 nm, and the distribution of arm-width has fallen back to a lower value, which is slightly wider but still close to the width of initial DNA templates. The features of letter-shaped junctions were also well preserved after DNA nanolithography. The right angle of L-shaped graphene was determined to be $94.4 \pm 4.2°$, in accordance with the right-angle value of $93.3° \pm 1.8°$ measured from deposited L-shaped DNA template on graphene. We also examined the feature change in X-shaped samples; the X-shaped DNA templates had an average acute arm-angle of $72.9 \pm 5.0°$ and an average arm-length of 37.4 ± 3.8 nm. After lithography steps, the resultant X-shaped graphene nanostructures showed an acute arm-angle of $75.0 \pm 6.4°$ and arm-length of 38.6 ± 6.9 nm, which suggests that the symmetry of X-shaped junctions has remained intact. Similarly, the obtuse arm-angle of Y-shaped patterns has been changed from $141.1 \pm 14.4°$ in initial Y-shaped DNA template to $139.9 \pm 16.2°$ in Y-shaped graphene nanostructures.

We found that the background deposition of metal nanoparticles on the substrate (Fig. 1g–k, column iii) did not disrupt the graphene patterning, although some tiny graphene quantum dots derived from the dispersed metal nanoparticles were found after plasma etching and mask removal (Fig. 1g–k, column iv). Generally, the shapes of the resulting graphene letter-shapes were well replicated from the original DNA templates, with the exception of a systematic increase in feature sizes and edge roughness inherited from the metallized DNA masks. The observed tolerances suggest that improvements in plasma beam scattering, and precision in the metallization step could allow for sub-10 nm widths.

Compared with traditional approaches, such as EBL, using DNA nanostructures as templates to achieve diverse shaped conductive materials has some key advantages: mass production of distinct structures and relatively high fabrication resolution. Especially, the ring-shaped graphene nanostructures produced by DNA-templated lithography, with $\sim$40 nm inner diameter and $\sim$20 nm width, cannot be easily reproduced using EBL. Moreover, because this is the first pattern transfer from a DNA nanostructure to a conductive 2D material that we are aware of,

we suggest this DNA nanolithography is an advance for the field and a promising application of the DNA self-assembly technology.

Modelling the transfer of spatial information. A central issue in this work is the transfer and partial degradation of spatial information from the DNA template to the final graphene structure after each step of the lithography (DNA template deposition, metallization, etching and mask removal). The boundary of the template surface $T(r)$ imprinted in final form on the graphene can be represented as a probability distribution function, $p[T]$, expressed as a convolution of T with transfer functions $\sigma(r)$ that represent the distortion of spatial information in the each step of the lithography:

$$p[T] = \int_{-\infty}^{\infty} T(r-r')\cdot\sigma(r)dr' \equiv T(r) * \sigma(r) \qquad (1)$$

Each lithography step preserves or distorts the emerging boundary through a series of transfer functions based on physical processes such that $\sigma(r) = \sigma_0(r) * \sigma_1(r) * \sigma_2(r) * \sigma_{3,4}(r)$, where $\sigma_0(r)$ is the original spatial information programmed in the DNA template. For example, the shape-distortion processes corresponding to dry transfer to the graphene surface (lithography step 1), metallization (lithography step 2), and etching and mask removal (lithography step 3 and 4) approximate a Gaussian process $\sigma_i(r) = \exp(-(r-R)^2/4D_{r,i}t_i)$ after time t. Here, the effective diffusivity of step i, $D_{r,i}$ can be estimated from the actual experimental variances, as detailed in the Supplementary Table S1.

As a programmable template, DNA is unique in the spatial precision that it affords in transferring desired coordinates to the physical structure, approximating a delta function: $\sigma_0(r) \sim \delta(r-R)$ for the boundary at R (Fig. 2a,e). Transfer to the dry substrate (Fig. 2b,f) distorts the template by compressing the height and altering the lateral dimensions through van der Waals contraction. However, the largest degradation of spatial information occurs during metallization, which involves two consecutive steps that reduce resolution: Ag seeding, which extends the surface boundary by the diameter of the nucleated particles, and Au deposition, which extends the already roughened boundary (Fig. 2c,g). Imperfections formed during the metallization step are clearly transmitted to the underlying graphene, and include irregularities in the mask width, and discontinuities in the mask edge at the junctions between Au nanoparticles. For example, C-shaped graphene or graphene arcs (see Supplementary Fig. S1), were occasionally observed besides graphene nanorings as byproducts, with breaks in the ring structure observed in addition to the average width distribution of 19.3 ± 4.2 nm. The final etching and mask-removal step (Fig. 2d,h) is relatively non-dispersive but does contract the boundary in the radial direction as the plasma beam scattering in the lateral dimensions. From the convolution model, for the first time we show that spatial information is lost in very specific ways with each patterning step according to the physics and chemistry of the lithography process. For example, the metallization step has the disadvantage that it currently causes the dispersion of the boundary. One consequence of the model is its prediction that non-dispersive transfer steps are essential to precision in spatial patterning using this approach. In theory, if all the lithography steps could be replaced with those possessing minimal dispersion, information transfer from templates to nanopatterns could be perfect. Future work will explore other different patterning strategies that utilize the high fidelity of the DNA templates directly, hence enabling higher resolution.

Raman spectra and surface-plasmon enhancement. We used Raman spectroscopy with an excitation wavelength of 633 nm to study the electronic and structural changes[46–49] that occur in the graphene during the different steps of the nanolithography. Typical Raman spectra (Fig. 3a–d) and deconvoluted G band structures (Fig. 3e–h) were collected after each lithography step over a ~1-μm spot size containing just one graphene

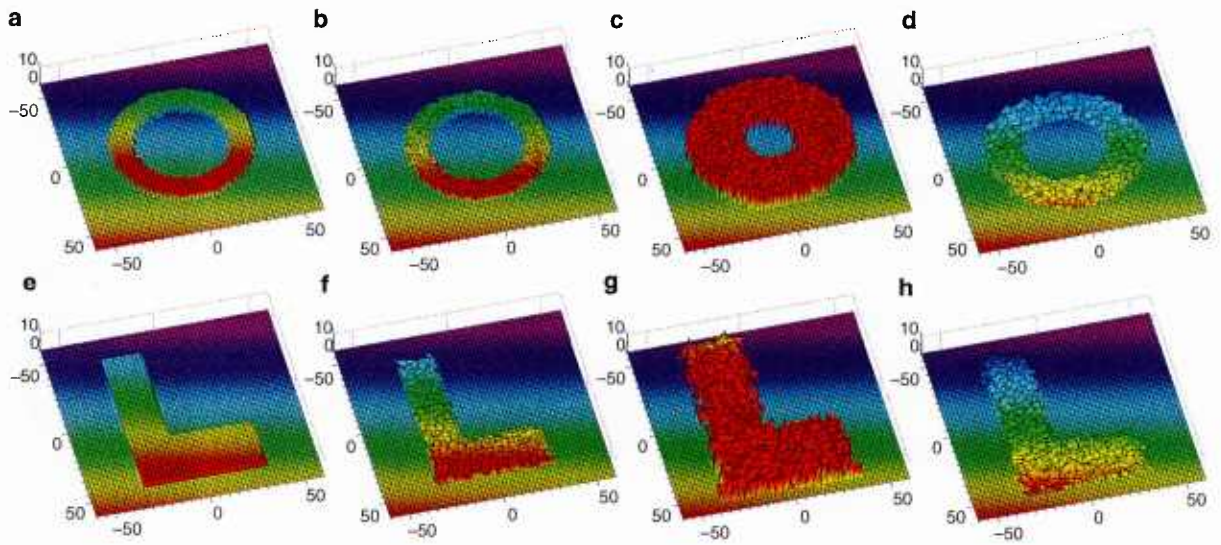

Figure 2 | Modelling the transfer of spatial information from the DNA templates to final graphene nanostructures. (**a**,**e**) The boundary of the original DNA templates programmed with specific shapes (ring- and L-shape). (**b**,**f**) The transfer of DNA templates to the dry substrate (lithography step 1) distorts the dimensions due to environmental interactions, such as the partial dehydration and flattening of soft DNA structures. (**c**,**g**) The metallization on DNA template (lithography step 2) expands its size and increased the roughness of boundary. (**d**,**h**) The RIE etching and mask removal (lithography step 3 and 4) shrinks the dimensions of final graphene nanostructures as the plasma beam scattering in the lateral edges. The unit of length scale in all images is nm, and the height and distance of the modelled nanostructures and substrate surface are indicated by the colour gradients.

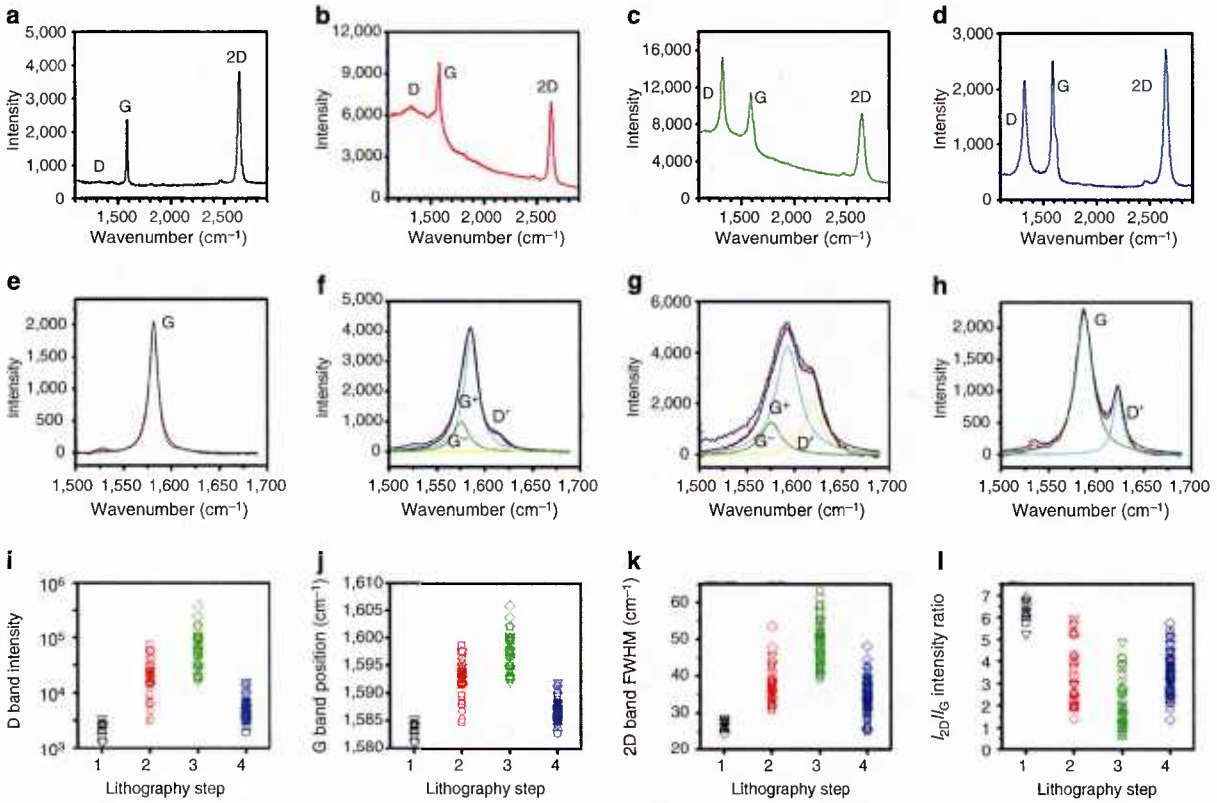

Figure 3 | Raman characterizations. Typical Raman spectra and the deconvolution of G bands of (**a**,**e**) graphene sheets with aforementioned DNA templates (lithography step 1), (**b**,**f**) graphene sheets with metallized DNA masks (lithography step 2), (**c**,**g**) after RIE etching (lithography step 3) and (**d**,**h**) graphene nanostructures after mask removal (lithography step 4). The overall statistical histograms of (**i**) integrated D band intensity, (**j**) G band position, (**k**) 2D band FWHM value and (**l**) I_{2D}/I_G value distribution of Raman spectra collected after each lithography step 1-4.

nanostructure. All the Raman peaks were fit to Lorentzians after background subtraction for further analysis. Statistical information was collected for the integrated D band intensity, G band position, full width at half maximum (FWHM) of the 2D band and the intensity ratio of 2D and G bands (I_{2D}/I_G), shown in Fig. 3i–l and additionally in Supplementary Table S2. We observed that the shape of the DNA letter template (O-, X-, Y-, Z- or L-shape) does not influence the resulting Raman spectra because of their similar sizes; there is minimal variation in the Raman signal of the graphene patterns derived from the five different DNA letter-shapes for each lithography step. Therefore, the following analysis of Raman spectroscopy is based on the statistical results of all letter-shapes combined and is thus representative for each shape.

After deposition of the DNA template, the Raman spectrum (Fig. 3a) showed a minuscule D band, a G band at $\sim$1,583 cm^{-1} and a sharp and single 2D band at $\sim$2,638 cm^{-1} with a FWHM of $<$30 cm^{-1}, similar to pristine, largely defect-free graphene[47]. After metallization, the Raman spectrum (Fig. 3b) showed significantly increased scattering intensity, consistent with surface-enhanced Raman scattering (SERS) generated from the light-excited surface plasmons on gold nanostructures attached to the DNA template[50]. The average intensity of D, G and 2D bands increased by a factor of 9.6, 4.0 and 2.0, respectively. We observe that compared with the 2D band, the G band has a larger enhancement of the scattering cross-section, which is reflected in the decrease of the I_{2D}/I_G value from 6.2 to 3.6. This is consistent with literature observations[50–52] and ascribed to a combination of doping-induced electron–phonon and electron–electron scattering[53] generated by the metal nanoparticles on metallized DNA masks as dopants[50–52]. A larger D band and a new D′ band at $\sim$1,620 cm^{-1} appeared in the SERS spectra (Fig. 3b,f). The height increase of D band is assigned to the SERS enhancement, because the metallization process itself is not symmetry breaking and does not greatly increase the concentration of lattice defect sites on graphene sheets[51]. The Au metal deposition also dopes the graphene, as evidenced by the increase of the G peak position, the G and 2D peak width and decrease of the I_{2D}/I_G value (lithography step 3 in Fig. 3i–l)[47]. The splitting of the G band (Fig. 3f) into components at 1,580 cm^{-1} (G$^-$) and 1,592 cm^{-1} (G$^+$) is indicative of strained graphene[54]. The increase in the FWHM of 2D band (from 20 cm^{-1} after lithography step 1 to 37 cm^{-1} after lithography step 2) is an inhomogeneous broadening due to increased charge fluctuations in the graphene caused by different types of charge carriers[55].

An advantage of the nanolithography is that after RIE etching of the graphene, the remaining metallized mask generates a persistent SERS enhancement, allowing a sensitive assessment of symmetry breaking defects after the harshest step. Figure 3c,g show that the SERS persists and that there is a further up-shift of the G band to 1,597 cm^{-1} and of 2D band to 2,658 cm^{-1}, with a 49 cm^{-1} FWHM of 2D band. The I_{2D}/I_G value further decreased to a value of 2.4. These changes are consistent with further doping. We also observed symmetry breaking by RIE etching as demonstrated by the strongly increased D and D′ band intensity with factors of 5.3 and 3.0, respectively. After the final mask

removal (Fig. 3d,h), the SERS effect was eliminated as expected, yet strong D and D′ bands remain, consistent with permanent symmetry breaking from the patterning itself. Overall, the intensity ratio of D and G bands (I_D/I_G) approaches ~1.0 after mask removal; the D band is caused both by rough edges and the residual defects on the graphene structures[56,57]. The FWHM of G and 2D bands were greatly decreased after mask removal, with a downshifting back to ~1,587 cm^{-1} and ~2,647 cm^{-1}. However, some residual p-doping remains after the etching process.

Patterning and electron transport of graphene nanoribbons. We applied the DNA nanolithography technique to generate graphene nanoribbons. This allows us to test the method's ability to generate extended structures with microns in length, commensurate in aspect ratio with a carbon nanotube. DNA ribbon templates with 60 nm width and several microns in length[26] were synthesized (Fig. 4a), and based on the same metallization-etching protocol, continuous graphene nanoribbons were fabricated all over the wafer surface. AFM (Fig. 4b) shows a graphene nanoribbon with an average height of 1.1 ± 0.2 nm and up to ~10 μm in length. The width of the graphene nanoribbons matches that of the original DNA templates before metallization within the resolution limit of the AFM image[26]. Distribution in the width is expected from the observed curvature and curl of the DNA nanoribbons on the graphene surface and nonuniformity associated with the metallization process.

Raman spectroscopy suggests an average I_D/I_G value of ~0.7 for graphene nanoribbons (Fig. 4c), which is lower than those for letter-shaped graphene nanostructures (I_D/I_G ~1.0) owing to the larger size. A high I_D/I_G value can be attributed to both bulk lattice defects[48] and atomically rough edges[53,57]. Because the perimeter-to-surface ratio is smaller for the wider graphene nanoribbons compared with the letter-shaped nanostructures, width confinement is diminished in the 60-nm wide ribbons, and we assign bulk defects to the graphene lattice accumulated throughout the different lithography steps, as the main contributors to the I_D/I_G value of the graphene nanoribbons.

Unlike the letter-shaped graphene nanostructures that are hard to image with scanning electron microscopy (SEM) due to their tiny size and semiconductive nature, it is possible to observe the much longer graphene nanoribbons. A characteristic SEM image (Fig. 4d) shows that the graphene nanoribbons were distributed all over the substrate, highlighting the effectiveness for batch production of graphene ribbons via the metallized DNA masks.

Field effect transistor (FET) devices based on the graphene nanoribbons were fabricated to characterize their electrical properties, as shown in Fig. 4e,f. Graphene nanoribbons were synthesized on a 300-nm thick SiO_2/p-doped Si substrate, followed by EBL and deposition of Cr/Au to form source/drain contact electrodes on a target nanoribbon (see the inset of Fig. 4f). The conductivity, G, of a 60-nm wide nanoribbon as a function of

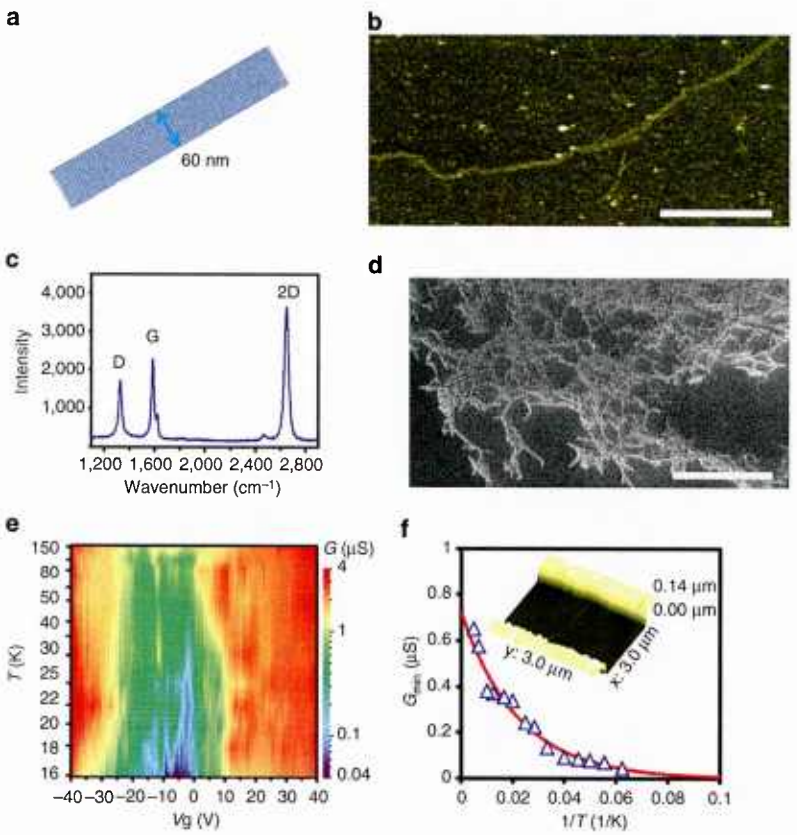

Figure 4 | Characterizations and electronic measurements of graphene nanoribbons. (**a**) Design of a SST DNA nanoribbon with 60 nm width, assembled by thousands of short-strand tiles. (**b**) AFM image of a graphene nanoribbon derived from metallized DNA nanolithography. Scale bar, 1 μm. (**c**) Raman spectrum of a single-layer graphene nanoribbon. (**d**) SEM image of graphene nanoribbons under an operation voltage of 1.0 kV. Scale bar, 10 μm. (**e**) The contour plot of the conductance G of a graphene nanoribbon FET under different gate voltages and low temperatures. The applied V_{ds} is 0.1 V. (**f**) Minimum conductance G_{min} of a graphene nanoribbon device at different temperatures. The inset shows a 3D-rendered AFM topography of the device with a channel length of 2 μm.

gate voltage, V_g, was characterized at different temperatures T (16–200 K), as shown in Fig. 4e. The conductivity corresponding to high carrier density, n, does not vary over the temperature range considered; however, the minimum conductivity corresponding to $n=0$, G_{min}, decreases significantly from 0.65 to 0.043 μS as the temperature decreases from 200 to 16 K. Therefore, the on/off current ratio increases approximately one order of magnitude from 200 to 16 K. The measured value of G_{min} as a function of $(1/T)$ is displayed in Fig. 4f. For the temperatures considered, we find that the conductivities are well described by the activation model with one activation energy, $G_{min} = G_1 \exp\left[-E_g/k_B T\right]$. The activation energy, E_g, is approximately the transport band gap, indicating successful quantum confinement from the patterning[58,59]. For the device shown in Fig. 4f, the transport gap equals 3.9 meV, which is comparable to values obtained using EBL[6] or unzipping of carbon nanotubes[16]. This suggests that the defects and disorders generated during the metallization and etching processes do not increase carrier scattering compared with other methods. We conclude that this method is able to produce large amounts of micron-long graphene nanoribbons at wafer scale (Fig. 4d), with subsequent FET device qualities commensurated with previously published results obtained via other methods. The metallized DNA lithography does not disrupt Raman or electronic properties in the resulting products more than other methods do. Because it is possible to open a wider band gap by reducing the ribbon width[60], the potential of programming ultra-narrow DNA templates is compelling and will be the subject of future efforts.

Discussion

In summary, we have demonstrated the first information transfer from encoded DNA nanostructures to another high-quality conductive material, such that metallized DNA templates can direct the formation of electronic devices. The cooperation between DNA self-assembly and 2D thin-film nanomaterials offers opportunities for both fields. Transferring structural information into graphene enables engineering of the electronic band diagram and quantum confinement of the resulting graphene nanostructures via the shape programmability of DNA nanostructures. Meanwhile self-assembled DNA structures expand the shape complexity of traditional lithographic processing for graphene, and this transfer allowed us to evaluate the imprinted fidelity for the first time using a convolution model. Prescribed 2D/3D DNA templates can be fabricated, enabling the production of not only linear, but also branched and ring-like graphene nanostructures. Scaling up the integration of graphene nanotransistors could be achieved through integrating circuit topology into larger size DNA masks that could be constructed using hierarchical or algorithmic self-assembly strategies. This would solve the difficulties of scaling up the fabrication of individual nanoscale graphene transistors with aligned orientation and location control. The DNA templates also make it possible to systematically alter the size of graphene nanostructures. A higher fabrication resolution will also be explored to enhance the quantum confinement and increase the transport gap of resulting FET devices. Another objective on this project is focusing on a unique, quantum interference transistor enabled by the patterned ring structures that we report in this paper. In addition to graphene, other atomic layered materials, such as MoS_2 and BN, may also be patterned with the current methodology for the design of diverse electronic devices.

Methods

Preparation and transfer of monolayer CVD graphene. Large-area monolayer graphene films were grown via CVD method on copper foils and then transferred to the surface of SiO_2/Si wafers (with 300-nm thick thermally grown SiO_2 layer)[45]. Typically, an ~4 cm^2 copper foil (Aldrich, 99.999%, 25-μm thick) was placed at the centre of a 1-inch diameter fused quartz tube in a tube furnace. The furnace tube was evacuated and heated to 1,000 °C under a 30 sccm H_2 gas flow with a pressure of ~600 mTorr. After annealing for 30 min under these conditions, a CH_4 gas flow of 3.0 sccm was introduced and the temperature in the furnace tube was maintained at 1000 °C for 30 min. The CH_4 gas flow was stopped after the growth period. The copper foil was cooled to room temperature under H_2 gas flow and taken out from the tube furnace. A PMMA film was spin-coated (3,000 r.p.m., 1 min) onto the copper foil covered with CVD-graphene film and heated up to 150 °C for 2 min to cure the PMMA film. Then the PMMA/CVD-graphene layer was separated from the copper foil by etching in a 1 M $CuCl_2$/6 M HCl aqueous solution and subsequently placed on the surface of Milli-Q water to remove any water-soluble residues. The PMMA/CVD-graphene film was then transferred to the designated substrate and dried with a nitrogen gun. The PMMA film was dissolved away by soaking the substrate in acetone for 6 h, thus leaving only the CVD-graphene sheet remaining on the substrate.

Preparation of DNA nanorings. DNA nanorings[24] were produced by mixing 100 nM of p7308 scaffold strand, 400 nM of each staple strand, purified by reverse-phase cartridge (Bioneer, Inc.), buffer and salts including 5 mM Tris (Fisher Scientific) + 1 mM EDTA (Sigma-Aldrich, pH 8.0 at 20 °C) and 12 mM $MgCl_2$ (Fisher Scientific). The mixture was subjected to a thermal annealing ramp according to the following schedule: 80–61 °C at 5 min $°C^{-1}$, 60–24 °C at 150 min $°C^{-1}$. Crude products for DNA nanorings were purified by 2% native agarose gel electrophoresis (SYBR safe purchased from Invitrogen, freeze 'N Squeeze DNA gel extraction spin columns purchased from Bio-Rad, pellet pestles purchased from Scientific America and agarose purchased from Lonza).

Preparation of letter-shaped DNA junctions. Each specific shaped DNA letter[27] was produced by mixing 200 nM SST strands in 5 mM Tris + 1 mM EDTA (pH 8.0 at 20 °C) and 12.5 mM $MgCl_2$. The mixture was subjected to a thermal annealing ramp from 90 to 25 °C over 17 h according to the following schedule: 80–61 °C at 10 min $°C^{-1}$, 60–24 °C at 20 min $°C^{-1}$. Crude products for DNA letter-shapes were purified by 2% native agarose gel electrophoresis.

Preparation of DNA nanoribbons. DNA nanoribbons[26] were prepared by stoichiometrically mixing each SST strand to a final concentration of ~1 μM in 5 mM Tris + 1 mM EDTA (pH 8.0 at 20 °C), and 12.5 mM $MgCl_2$. The mixture was subjected to a thermal annealing ramp from 90 to 25 °C over 17 h according to the following schedule: 80–61 °C at 10 min $°C^{-1}$, 60–24 °C at 20 min $°C^{-1}$.

Glutaraldehyde treatment of DNA nanostructures. Purified self-assembled DNA nanostructures were incubated with 0.2% glutaraldehyde (Sigma-Aldrich) diluted in 0.5 × TBE/10 mM $MgCl_2$ buffer on ice for 20 min and then at room temperature for another 20 min, after which the sample was loaded into a spin column with Molecular Weight Cut Off (MWCO) of 100 kDa (Millipore) and washed with 500 μl 0.5 × TBE/10 mM $MgCl_2$ for three times to remove the excess glutaraldehyde.

Deposition of DNA nanostructures on graphene. To get better affinity with negatively charged DNA structures, graphene samples were firstly dipped into 0.1 mg ml^{-1} 1-pyrenemethylamine methanol solution for 5 min, and then gently dried with a nitrogen gun. We also tried 1-pyrenebutylcarboxylic acid, 1-pyrenesulfonate and 4-(1-Pyrene) butyric acid N-hydroxysuccinimide ester as controls. We found that among these chemicals, 1-pyrenemethylamine provides the best dispersion of DNA on the surface of graphene. Subsequently, 5 μl of glutaraldehyde-treated DNA in 0.5 × TBE/10 mM $MgCl_2$ buffer was dropped onto graphene surface. Five minutes later, when the DNA drop had nearly completely dried in air, the graphene sample was rinsed in water twice for 15 s to remove excessive glutaraldehyde and residual buffer, and then dried with a nitrogen gun.

DNA metallization. The graphene sample covered with glutaraldehyde-treated DNA was incubated in the dark with a 0.1 M solution of $AgNO_3$ in ammonia buffer (pH = 10.5) at room temperature for 1 h to trigger the growth of silver seeds on DNA skeletons, after which the excessive reagents were rinsed off with deionized water. Final incubation with Gold Enhance EM Formulation (Nanoprobes) was processed according to the manufacturer's instructions. First, a unit of enhancer (A) was mixed with a unit of activator (B), and then a unit of initiator (C) and a unit of buffer (D) was added to the mixture. A volume of 10 μl of this mixture was freshly deposited onto a graphene substrate and incubated for 2 min to produce gold-covered DNA nanostructures. Excess reagent was rinsed off form the sample with deionized water.

Etching of graphene nanostructures. The graphene samples covered with metallized DNA masks were exposed to RIE conditions (10 mTorr Ar and

10 mTorr O_2 flow at 50 W for 8 s in a Nexx ECR RIE system) to remove the unprotected region of graphene.

Mask removal. The RIE-treated samples were soaked in 0.1 M $NaCN/H_2O$ solution for 10 min to remove metal masks, and then rinsed in water for 10 s. Subsequently, the samples were put into 99.5% deionized formamide for another 10 min and then rinsed in water for 10 s to remove any possible DNA residue.

Characterizations and electronic measurements. AFM was conducted on an Asylum Research MFP-3D system in AC mode (alternating current mode, also called noncontact or tapping mode) using silicon probes (Olympus OMCL-AC240TS). Raman spectroscopy was performed on a Horiba Jobin Yvon LabRAM HR800 system using a 633-nm excitation laser, $\times 100$ objective lens with $\sim 1\,\mu m$ diameter spot size and 600 lines per mm grating. All the Raman spectra were collected with exposure time of 5 s and accumulated two times. The Raman peaks are fit to Lorentzians after background subtraction. SEM was performed on a Zeiss FESEM Ultra Plus system under high vacuum and operation voltage of 1 kV. Back-gated graphene nanoribbon devices on 300 nm SiO_2/Si substrates were fabricated using conventional lithography and the source/drain electrodes were prepared by electron beam deposition of 25/75-nm thick Cr/Au layers sequentially under high vacuum. Electronic measurements of the graphene nanoribbon FET devices were collected with an ARS PSF-10-1-4 Cryogenic Probe Station and an Agilent E5270B analyzer at 15–200 K and pressure $< 10^{-6}$ Torr.

References

1. Novoselov, K. S. *et al.* Electric field effect in atomically thin carbon films. *Science* **306,** 666–669 (2004).
2. Novoselov, K. S. *et al.* Two-dimensional gas of massless Dirac fermions in graphene. *Nature* **438,** 197–200 (2005).
3. Avouris, P., Chen, Z. & Perebeinos, V. Carbon-based electronics. *Nat. Nanotechnol.* **2,** 605–615 (2007).
4. Dubois, S. M. M., Zanolli, Z., Declerck, X. & Charlier, J. C. Electronic properties and quantum transport in graphene-based nanostructures. *Eur. Phys. J. B* **72,** 1–24 (2009).
5. Dutta, S. & Pati, S. K. Novel properties of graphene nanoribbons: a review. *J. Mater. Chem.* **20,** 8207–8223 (2010).
6. Han, M. Y., Ozyilmaz, B., Zhang, Y. & Kim, P. Energy band-gap engineering of graphene nanoribbons. *Phys. Rev. Lett.* **98,** 206805 (2007).
7. Li, X. L., Wang, X. R., Zhang, L., Lee, S. W. & Dai, H. J. Chemically derived, ultrasmooth graphene nanoribbon semiconductors. *Science* **319,** 1229–1232 (2008).
8. Recher, P. *et al.* Aharonov-Bohm effect and broken valley degeneracy in graphene rings. *Phys. Rev. B* **76,** 235404 (2007).
9. Russo, S. *et al.* Observation of Aharonov-Bohm conductance oscillations in a graphene ring. *Phys. Rev. B* **77,** 085413 (2008).
10. Silvestrov, P. G. & Efetov, K. B. Quantum dots in graphene. *Phys. Rev. Lett.* **98,** 016802 (2007).
11. Stampfer, C. *et al.* Tunable graphene single electron transistor. *Nano Lett.* **8,** 2378–2383 (2008).
12. Bai, J., Duan, X. & Huang, Y. Rational fabrication of graphene nanoribbons using a nanowire etch mask. *Nano Lett.* **9,** 2083–2087 (2009).
13. Wang, X. & Dai, H. Etching and narrowing of graphene from the edges. *Nat. Chem.* **2,** 661–665 (2010).
14. Cai, J. *et al.* Atomically precise bottom-up fabrication of graphene nanoribbons. *Nature* **466,** 470–473 (2010).
15. Kosynkin, D. V. *et al.* Longitudinal unzipping of carbon nanotubes to form graphene nanoribbons. *Nature* **458,** 872–876 (2009).
16. Jiao, L., Zhang, L., Wang, X., Diankov, G. & Dai, H. Narrow graphene nanoribbons from carbon nanotubes. *Nature* **458,** 877–880 (2009).
17. Seeman, N. C. DNA in a material world. *Nature* **421,** 427–431 (2003).
18. Goodman, R. P. *et al.* Rapid chiral assembly of rigid DNA building blocks for molecular nanofabrication. *Science* **310,** 1661–1665 (2005).
19. Feldkamp, U. & Niemeyer, C. M. Rational design of DNA nanoarchitectures. *Angew. Chem. Int. Ed.* **45,** 1856–1876 (2006).
20. Simmel, F. C. Three-dimensional nanoconstruction with DNA. *Angew. Chem. Int. Ed.* **47,** 5884–5887 (2008).
21. Lin, C., Liu, Y. & Yan, H. Designer DNA nanoarchitectures. *Biochemistry* **48,** 1663–1674 (2009).
22. Rothemund, P. W. K. Folding DNA to create nanoscale shapes and patterns. *Nature* **440,** 297–302 (2006).
23. Douglas, S. M. *et al.* Self-assembly of DNA into nanoscale three-dimensional shapes. *Nature* **459,** 414–418 (2009).
24. Dietz, H., Douglas, S. M. & Shih, W. M. Folding DNA into twisted and curved nanoscale shapes. *Science* **325,** 725–730 (2009).
25. Shih, W. M. & Lin, C. Knitting complex weaves with DNA origami. *Curr. Opin. Struct. Biol.* **20,** 276–282 (2010).
26. Yin, P. *et al.* Programming DNA tube circumferences. *Science* **321,** 824–826 (2008).
27. Wei, B., Dai, M. & Yin, P. Complex shapes self-assembled from single-stranded DNA tiles. *Nature* **485,** 626 (2012).
28. Ke, Y., Ong, L. L., Shih, W. M. & Yin, P. Three-dimensional structures self-assembled from DNA bricks. *Science* **388,** 1177–1183 (2012).
29. Keren, K., Berman, R. S., Buchstab, E., Sivan, U. & Braun, E. DNA-templated carbon nanotube field-effect transistor. *Science* **302,** 1380–1382 (2003).
30. Berti, L. & Burley, G. A. Nucleic acid and nucleotide-mediated synthesis of inorganic nanoparticles. *Nat. Nanotechnol.* **3,** 81–87 (2008).
31. Sharma, J. *et al.* Control of self-assembly of DNA tubules through integration of gold nanoparticles. *Science* **323,** 112–116 (2009).
32. Tan, S. J., Campolongo, M. J., Luo, D. & Cheng, W. Building plasmonic nanostructures with DNA. *Nat. Nanotechnol.* **6,** 268–276 (2011).
33. Kuzyk, A. *et al.* DNA-based self-assembly of chiral plasmonic nanostructures with tailored optical response. *Nature* **483,** 311–314 (2012).
34. Keren, K. *et al.* Sequence-specific molecular lithography on single DNA molecules. *Science* **297,** 72–75 (2002).
35. Deng, Z. & Mao, C. DNA-templated fabrication of 1D parallel and 2D crossed metallic nanowire arrays. *Nano Lett.* **3,** 1545–1548 (2003).
36. Yan, H., Park, S. H., Finkelstein, G., Reif, J. H. & LaBean, T. H. DNA-templated self-assembly of protein arrays and highly conductive nanowires. *Science* **301,** 1882–1884 (2003).
37. Liu, J. *et al.* Metallization of branched DNA origami for nanoelectronic circuit fabrication. *ACS Nano* **5,** 2240–2247 (2011).
38. Pilo-Pais, M., Goldberg, S., Samano, E., LaBean, T. H. & Finkelstein, G. Connecting the nanodots: Programmable nanofabrication of fused metal shapes on DNA templates. *Nano Lett.* **11,** 3489–3492 (2011).
39. Schreiber, R. *et al.* DNA origami-templated growth of arbitrarily shaped metal nanoparticles. *Small* **7,** 1795–1799 (2011).
40. Pearson, A. C. *et al.* DNA origami metallized site specifically to form electrically conductive nanowires. *J. Phys. Chem. B* **116,** 10551–10560 (2012).
41. Deng, Z. & Mao, C. Molecular lithography with DNA nanostructures. *Angew. Chem. Int. Ed.* **43,** 4068–4070 (2004).
42. Becerril, H. A. & Woolley, A. T. DNA shadow nanolithography. *Small* **3,** 1534–1538 (2007).
43. Surwade, S. P., Zhao, S. & Liu, H. Molecular lithography through DNA-mediated etching and masking of SiO_2. *J. Am. Chem. Soc.* **133,** 11868–11871 (2011).
44. Zhang, G., Surwade, S. P., Zhou, F. & Liu, H. DNA nanostructure meets nanofabrication. *Chem. Soc. Rev.* **42,** 2488–2496 (2013).
45. Li, X. S. *et al.* Large-area synthesis of high-quality and uniform graphene films on copper foils. *Science* **324,** 1312–1314 (2009).
46. Ferrari, A. C. & Robertson, J. Interpretation of Raman spectra of disordered and amorphous carbon. *Phys. Rev. B* **61,** 14095–14107 (2000).
47. Ferrari, A. C. *et al.* Raman spectrum of graphene and graphene layers. *Phys. Rev. Lett.* **97,** 187401 (2006).
48. Ferrari, A. C. Raman spectroscopy of graphene and graphite: Disorder, electron-phonon coupling, doping and nonadiabatic effects. *Solid State Commun.* **143,** 47–57 (2007).
49. Rao, R., Tishler, D., Katoch, J. & Ishigami, M. Multiphonon Raman scattering in graphene. *Phys. Rev. B* **84,** 113406 (2011).
50. Schedin, F. *et al.* Surface-enhanced Raman spectroscopy of graphene. *ACS Nano* **4,** 5617–5626 (2011).
51. Lee, J., Shim, S., Kim, B. & Shin, H. S. Surface-enhanced Raman scattering of single- and few-layer graphene by the deposition of gold nanoparticles. *Chem. Eur. J.* **17,** 2381–2387 (2011).
52. Lee, J., Novoselov, K. S. & Shin, H. S. Interaction between metal and graphene: dependence on the layer number of graphene. *ACS Nano* **5,** 608–612 (2011).
53. Basko, D. M., Piscanec, S. & Ferrari, A. C. Electron-electron interactions and doping dependence of the two-phonon Raman intensity in graphene. *Phys. Rev. B* **80,** 165413 (2009).
54. Mohiuddin, T. M. G. *et al.* Uniaxial strain in graphene by Raman spectroscopy: G peak splitting, grüneisen parameters, and sample orientation. *Phys. Rev. B* **79,** 205433 (2009).
55. Wang, Q. H. *et al.* Understanding and controlling the substrate effect on graphene electron-transfer chemistry via reactivity imprint lithography. *Nat. Chem.* **4,** 724–732 (2012).
56. Basko, D. M. Boundary problems for Dirac electrons and edge-assisted Raman scattering in graphene. *Phys. Rev. B* **79,** 205428 (2009).
57. Casiraghi, C. *et al.* Raman spectroscopy of graphene edges. *Nano Lett.* **9,** 1433–1441 (2009).
58. Taychatanapat, T. & Jarillo-Herrero, P. Electronic transport in dual-gated bilayer graphene at large displacement fields. *Phys. Rev. Lett.* **105,** 166601 (2010).

59. Xia, F., Farmer, D. B., Lin, Y.-M. & Avouris, P. Graphene field-effect transistors with high on/off current ratio and large transport band gap at room temperature. *Nano Lett.* **10**, 715–718 (2010).
60. Barone, V., Hod, O. & Scuseria, G. E. Electronic structure and stability of semiconducting graphene nanoribbons. *Nano Lett.* **6**, 2748–2754 (2006).

Acknowledgements

This work was primarily funded by 2009 US Office of Naval Research Multi University Research Initiative (MURI) grant on Graphene Advanced Terahertz Engineering (GATE) at MIT, Harvard and Boston University. The work is also supported by a DARPA Young Faculty Award N66001-11-1-4136, an ARO Grant W911NF1210238, an ONR Young Investigator Program Award N000141110914, an ONR Grant N000141010827 and an NSF CAREER Award CCF1054898 to P.Y. M.S.S. appreciates characterization support from the Institute of Soldier Nanotechnologies at MIT funded by a grant from the US Army Research Office.

Author contributions

Z.J., W.S. and M.S.S. conceived the idea of DNA-templated lithography. Z.J. and W.S. designed the experiments. W.S. and Y.K. prepared the DNA templates. Z.J. and W.S. carried out DNA nanostructure metallization experiments. Z.J. carried out the metallized DNA lithography experiments. Z.J. performed the AFM, Raman, SEM characterizations, device fabrication and electrical characterizations. M.S.S. and Z.J. performed the modelling of spatial information transfer. C.-J.S., G.L.C.P., Q.H.W. and B.M. contributed to the data analysis. Z.J., W.S., M.S.S. and P.Y. wrote the manuscript while all authors discussed the results and provided the feedback on the manuscript. M.S.S. and P.Y. supervised the project.

Additional information

Supplementary Information accompanies this paper on http://www.nature.com/naturecommunications

Competing financial interests: The authors declare no competing financial interests.

Reprints and permission information is available online at http://npg.nature.com/reprintsandpermissions/

How to cite this article: Jin, Z. *et al.* Metallized DNA nanolithography for encoding and transferring spatial information for graphene patterning. *Nat. Commun.* 4:1663 doi: 10.1038/ncomms2690 (2013).

11.4.3 Structural DNA nanotechnology application: Patterning inorganic oxides using DNA templates

JACS
JOURNAL OF THE AMERICAN CHEMICAL SOCIETY

Communication

pubs.acs.org/JACS

Nanoscale Growth and Patterning of Inorganic Oxides Using DNA Nanostructure Templates

Sumedh P. Surwade,[†] Feng Zhou,[†] Bryan Wei,[‡,§] Wei Sun,[‡,§] Anna Powell,[†] Christina O'Donnell,[†] Peng Yin,*[,‡,§] and Haitao Liu*[,†]

[†]Department of Chemistry, University of Pittsburgh, Pittsburgh, Pennsylvania 15260, United States

[‡]Wyss Institute for Biologically Inspired Engineering, Harvard University, Boston, Massachusetts 02115, United States

[§]Department of Systems Biology, Harvard Medical School, Boston, Massachusetts 02115, United States

Supporting Information

ABSTRACT: We describe a method to form custom-shaped inorganic oxide nanostructures by using DNA nanostructure templates. We show that a DNA nanostructure can modulate the rate of chemical vapor deposition of SiO_2 and TiO_2 with nanometer-scale spatial resolution. The resulting oxide nanostructure inherits its shape from the DNA template. This method generates both positive-tone and negative-tone patterns on a wide range of substrates and is compatible with conventional silicon nanofabrication processes. Our result opens the door to the use of DNA nanostructures as general-purpose templates for high-resolution nanofabrication.

Recent advances in DNA nanotechnology make it possible to construct arbitrary-shaped DNA nanostructures at a theoretical precision down to 2 nm.[1−9] This level of shape control is unmatched by any other self-assembled material systems, such as block copolymers, self-assembled monolayers, and protein/peptide assemblies.[10−13] These DNA nanostructures can be deterministically deposited onto silicon wafers,[14−16] making them ideal templates for high-resolution nanofabrication.[4,12,14,15,17−28] Compared with competing top-down and bottom-up approaches for nanoscale patterning,[10−13] DNA-based nanofabrication could offer high throughput, high resolution, and potentially very low capital and operational costs: even with the current price of DNA synthesis, the cost of DNA template for patterning an area of 1 m^2 could be as low as $6.[17]

A major challenge in using a DNA nanostructure for nanoscale patterning involves transfer of its pattern to an inorganic substrate (e.g., a silicon wafer). Because of their limited chemical stability, DNA nanostructures are not compatible with the harsh chemical reaction conditions that are typically used to etch and deposit inorganic materials, such as KOH etching and plasma-assisted chemical vapor deposition (CVD). One approach to address this challenge is to deposit metal onto DNA via solution chemistry or vacuum evaporation.[18,22,23,26−29] However, existing approaches for DNA metallization typically produce nonconformal metal coatings, leading to a significant loss of resolution. DNA-mediated etching of SiO_2 was recently reported to transfer the pattern of a DNA origami to a SiO_2 substrate with ~25 nm resolution.[20] However, this approach could only produce features with limited vertical contrast, typically 2−3 nm. There is an urgent need to develop pattern-transfer reactions that can offer high resolution, high contrast, and compatibility with both DNA nanotechnology and existing semiconductor nanofabrication processes.

Herein we report a shape-conserving, room-temperature CVD process to convert a DNA nanostructure into an inorganic oxide nanostructure of the same shape. Our method has a number of advantages compared with the early developments of area-selective CVD and the closely related area-selective atomic layer deposition (ALD). First of all, the shape of a DNA nanostructure is configurable, and the feature size can be as small as 2 nm. If the DNA nanostructure could be overcoated with a 1 nm thick layer of CVD-grown inorganic oxide, it should be possible to produce custom-shaped features with sub-5 nm resolution. In contrast, previous studies on area-selective CVD and ALD have mostly relied on photolithography to define the area for selective material deposition;[30−34] consequently, the resolution of these CVD-grown patterns was limited by that of the photolithography. Although in some cases chemically synthesized inorganic nanostructures (e.g., nanoparticles) have been used as templates,[35] they cannot produce custom-shaped patterns. Second, our approach can be carried out at room temperature and is compatible with DNA nanostructures and potentially many other self-assembled supramolecular assemblies. Third, and most importantly, our CVD method is the first to achieve selective deposition of inorganic oxide onto a DNA nanostructure in the presence of a SiO_2 substrate, and vice versa. Both DNA and SiO_2 are active substrates in traditional high-temperature CVD and ALD processes.[36] However, through control of the adsorption of water at room temperature, our CVD process is able to differentiate these two substrates and achieve selective deposition with nanometer-scale resolution.

Our CVD produces a conformal oxide coating on the DNA template. Since oxide is one of the most commonly used etching masks, this method opens the door to integrating DNA nanotechnology with modern nanofabrication processes. As an example, we have demonstrated deep anisotropic etching of a silicon wafer by using the CVD-grown oxide as a hard mask.

Received: February 19, 2013
Published: April 10, 2013

dx.doi.org/10.1021/ja401785h | J. Am. Chem. Soc. 2013, 135, 6778−6781

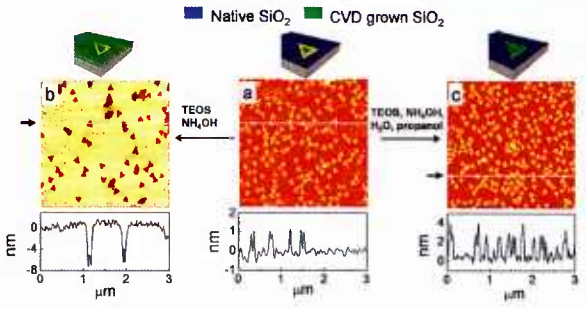

Figure 1. DNA-templated CVD growth of inorganic oxides. Cartoon representations (top), AFM images (middle), and AFM cross sections (bottom) are shown for (a) DNA origami triangles deposited on a Si substrate, (b) negative-tone triangular patterns obtained for CVD-grown SiO_2 (reaction time 12 h), and (c) positive-tone triangular patterns obtained for CVD-grown SiO_2 (reaction time 6 h).

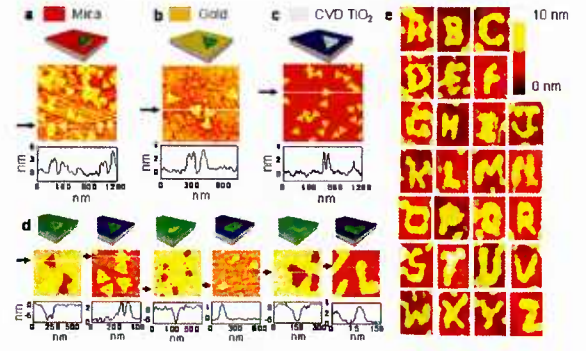

Figure 2. DNA-templated CVD growth of inorganic oxides of different shapes and substrates. (a–c) Cartoon representations (top), AFM images (middle), and AFM cross sections (bottom) of positive-tone triangular patterns of (a) CVD-grown SiO_2 on a mica substrate, (b) CVD-grown SiO_2 on a gold substrate, and (c) CVD-grown TiO_2 on a Si substrate. (d) Cartoons, high-resolution AFM images, and AFM cross sections of both positive-tone and negative-tone SiO_2 patterns on a silicon wafer templated by DNA nanostructures with three different shapes: triangle, rectangle, and L shape. (e) High-resolution AFM images (140 nm × 160 nm) of 26 positive-tone SiO_2 letters (A to Z) obtained using the corresponding DNA letters as templates. The arrows and white lines in (a–d) indicate the locations of the cross sections.

Figures 1 and 2 summarize our method for DNA-mediated CVD of oxide materials on various inorganic substrates. In a typical experiment, a DNA nanostructure is first deposited onto a substrate (e.g., Si wafer, mica, or gold). The CVD is carried out at room temperature in a closed glass chamber, inside which several liquid reservoirs deliver the CVD precursor and other required chemicals to the substrate through the gas phase. Both positive-tone and negative-tone patterns can be obtained. The detailed experimental procedure can be found in the Supporting Information (SI) (see Figures S1–S17).

Figure 1a shows an atomic force microscopy (AFM) image of triangular DNA templates deposited on a silicon wafer that has a thin layer (ca. 2 nm) of native oxide (also see Figure S1). The height and width of the edge of the DNA triangle were 1.2 ± 0.1 nm and 27 ± 1 nm, respectively (all reported width values are full widths at half-maximum; also see Table S1). When this sample was exposed to a mixed vapor of $Si(OEt)_4$ (TEOS), H_2O, and NH_3, deposition of SiO_2 occurred selectively on the SiO_2 surface that was not covered by the DNA template, resulting in a negative-tone pattern of SiO_2 (Figure 1b). The width of the trenches in Figure 1b was 42 ± 5 nm, while the depth was 7 ± 2 nm. The center void of the triangle template was retained in almost all of the structures, although with a reduced height contrast. To reverse the area selectivity of the CVD, we introduced propanol vapor and increased the relative humidity of the reaction chamber. In this case, the CVD reaction selectively deposited SiO_2 onto the DNA nanostructures to produce a positive-tone pattern (Figure 1c). After the CVD, the average height of the triangle structures increased from 1.2 ± 0.1 nm to 2.6 ± 0.5 nm while the width of the ridges increased from 27 ± 1 nm to 37 ± 3 nm. We note that the lateral dimension measured by AFM is likely limited by the tip–sample convolution effect and should be regarded as an upper limit. Nevertheless, faithful pattern transfer was clearly achieved for almost every DNA template under both positive-tone and negative-tone conditions. Our results contrast with those from previous work on metallization of DNA nanostructures, where the metal-plating process typically produced grainy and sometimes discontinuous metal nanostructures.[18,22,23,26–29]

This DNA-mediated CVD method is a versatile tool for general-purpose nanofabrication. First of all, the area-selective deposition of oxide materials is not limited to silicon wafer and can be extended to pattern other substrates. For example, Figure 2a,b shows the positive-tone CVD of SiO_2 onto DNA nanostructures deposited on mica and gold substrates, respectively (also see Figures S2, S3, S12, and S13). Second, oxide materials other than SiO_2 can also be deposited in a similar fashion by using suitable CVD precursors. For example, using titanium isopropoxide $[Ti(O^iPr)_4]$ as the precursor, we successfully produced positive-tone TiO_2 structures on a silicon wafer using the same triangular DNA templates (Figures 2c and S17). Finally, this CVD method is compatible with custom-shaped DNA templates. Figure 2d shows high-resolution AFM images of both positive-tone and negative-tone SiO_2 patterns templated by DNA nanostructures with three different shapes: triangle, rectangle, and L shape. Figure 2e shows high-resolution AFM images of positive-tone SiO_2 patterns templated by 26 letters constructed using the single-strand tiles (SST) approach.[1]

The chemical composition of the CVD-grown oxide nanostructures was confirmed by X-ray photoelectron spectroscopy (XPS) and energy-dispersive X-ray spectroscopy (EDX). For the XPS analysis, we used the SiO_2 triangle structures grown on a gold substrate because the other two substrates (silicon wafer and mica) contained silicon, which interfered with the data analysis. The XPS spectra (Figures S18 and S19) showed the presence of peaks for Si 2p (103.6 eV), Si 2s (154.8 eV), and O 1s (532.8 eV). The observed peak positions are consistent with the standard values for SiO_2.[37] XPS gave an Si:O ratio of 1:2.08 (or $SiO_{2.08}$), consistent with the deposition of SiO_2. EDX analysis of the CVD-grown SiO_2 triangles gave the expected Si and O peaks, while the TiO_2 structures gave the expected Ti and O peaks (Figure S20). Both the XPS and EDX spectra indicated the presence of carbon, which could arise from either the DNA or adsorption of CVD precursors and/or hydrocarbon contaminants in air. In addition to these spectroscopic characterizations, we also found that both the SiO_2 and TiO_2 structures could survive a 600 °C heating treatment in air, further confirming their inorganic nature (Figures S21 and S22).

dx.doi.org/10.1021/ja401785h | J. Am. Chem. Soc. 2013, 135, 6778–6781

a

$$Si(OC_2H_5)_4 + 2H_2O \xrightarrow{NH_3} SiO_2 + 4C_2H_5OH$$

b

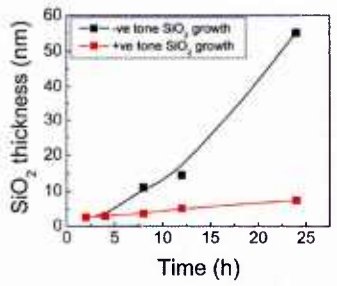

Figure 3. (a) Balanced chemical equation for the CVD of SiO_2 by hydrolysis of $Si(OEt)_4$ in the presence of NH_3 as a catalyst. (b) Temporal evolution of the average thickness (as measured by ellipsometry) of CVD-grown SiO_2 under positive-tone (red) and negative-tone (black) growth conditions. The lines are guide to the eye.

The key to achieving high-resolution area-selective CVD is to control the adsorption of water at the nanoscale. In our CVD process, the oxide precursors [$Si(OEt)_4$ and $Ti(OiPr)_4$] require water to hydrolyze (Figure 3a). In addition, NH_3 was used as a catalyst to enhance the reaction kinetics at room temperature.[38,39] Consequently, the rate of CVD should be closely related to the local concentration of adsorbed water and/or NH_3 catalyst. In the negative-tone CVD (Figure 1b), the Si/SiO_2 substrate was placed in the reaction chamber with two open vials, one containing CVD precursor and the other concentrated ammonia solution. Under these conditions, the SiO_2 CVD preferentially occurred on the existing SiO_2 surface, implying that SiO_2 is the preferred adsorption site for water and/or NH_3 under these conditions. In addition, one would also expect that the SiO_2 CVD should prefer to nucleate and grow onto an existing oxide surface. In this case, we used ellipsometry to track the average thickness of the oxide layer and observed a continuous increase in the oxide thickness from 2.6 nm (the thickness of the native oxide) to 14.5 nm after 12 h and 55.1 nm after 24 h (Figure 3b). Since the depth of the triangular trenches was 7 ± 2 nm after 12 h of reaction, we estimate that the deposition rate of CVD SiO_2 on the wafer surface was ca. 4 times faster than on the DNA nanostructures (see the SI for the detailed calculation).

To reverse the selectivity and achieve preferential oxide deposition onto the DNA nanostructure, it was necessary to decrease the activity of the SiO_2 surface and increase that of the DNA. We found that the former could be achieved by introducing *n*-propanol vapor into the CVD chamber. It has been shown that the coadsorption of *n*-propanol and water on a flat SiO_2 surface gives a binary adsorbate layer in which the adsorbed *n*-propanol molecules lie at the adsorbate–gas interface and water molecules are embedded underneath the *n*-propanol layer.[40] Although the detailed mechanism is still under investigation, we believe that under these conditions, the adsorbed water is not directly accessible to the CVD precursor, which should lead to significantly slower deposition of SiO_2 onto the flat SiO_2 surface. This prediction was indeed verified in our experiment: we saturated the CVD chamber with *n*-propanol vapor by introducing an open vial of *n*-propanol; in this case, we observed that the CVD still resulted in a negative-tone pattern transfer; however, the trenches were extremely shallow (<0.5 nm at 12 h; Figure S23), indicating a significant decrease (by a factor of at least 5) in the rate of SiO_2 deposition onto the flat SiO_2 surface. However, in this case, the DNA nanostructures still were not active toward SiO_2 CVD.

To increase the activity of the DNA nanostructures toward SiO_2 deposition, it was necessary to enhance their adsorption of water. This was achieved by introducing an additional open vial of water to increase the relative humidity inside the CVD chamber. Indeed, positive-tone pattern transfer was achieved when the above two efforts were combined. As shown in Figure 3b, in the presence of *n*-propanol vapor and increased relative humidity, the overall rate of SiO_2 deposition onto the wafer surface was still slow (ca. $^1/_{14}$ of that in the absence of *n*-propanol); however, in this case, AFM imaging showed a consistent increase in the height of the DNA nanostructures, which reached ~7 nm at 24 h (Figure S14). From both the AFM and ellipsometry data, we estimate that the rate of SiO_2 CVD onto DNA was at least 2.6 times faster than onto the wafer surface (see the SI for the detailed calculation).

The formation of both positive-tone and negative-tone patterns is kinetically controlled. Because CVD-grown oxide is deposited conformally, the quality of the pattern transfer deteriorates, and fine features are lost at long reaction times. For example, after 24 h of reaction, the negative-tone SiO_2 patterns disappeared completely (Figure S8) while the positive-tone patterns lost the central void feature and became solid triangles (Figure S14).

Water adsorption also explains the behavior of different substrates in our CVD process. For example, we found that only positive-tone growth could be achieved for DNA triangles deposited on a gold substrate, even under conditions that produced a negative-tone pattern on a Si wafer (Figures S7 and S10). This observation is consistent with the chemical inertness of gold, which does not allow water and ammonia to adsorb strongly on its surface.[41] For a mica substrate, the contrast of the negative-tone pattern was very small, presumably because of the very small difference in the adsorption isotherms of water on DNA and mica.[42,43]

The SiO_2 nanostructure produced by our CVD process can be used as a hard mask for etching the underlying silicon substrates. In fact, SiO_2 is one of the most often used masks in silicon nanofabrication. To demonstrate this feasibility, we carried out deep anisotropic etching of silicon using the CVD-grown SiO_2 as a hard mask (Figure 4). Briefly, we deposited DNA triangles onto a silicon [110] wafer and grew a negative-tone SiO_2 pattern. The wafer was then exposed to a SF_6/O_2 plasma that selectively etches Si but not SiO_2.[44] After the plasma etching, we removed the CVD-grown SiO_2 mask with hydrofluoric acid (HF) to expose the underlying silicon. AFM imaging of the wafer revealed triangular trenches on the surface, indicating successful pattern transfer to the silicon layer. As shown in Figure 4, the depth of the trenches was 25 ± 2 nm, while the width was 55 ± 3 nm. For comparison, the depth and width of the trenches of the CVD-grown SiO_2 mask were 7 ± 2 and 42 ± 5 nm, respectively. Almost all of the triangles showed the center void feature, although with a reduced vertical contrast. The silicon surface was rough, which we believe to be a result of the amorphous nature of the SiO_2 grown under our current CVD process.

In conclusion, we have developed a novel approach to pattern custom-shaped inorganic oxide nanostructures by using a DNA nanostructure template. Our area-selective CVD method converts a DNA nanostructure into an oxide one,

dx.doi.org/10.1021/ja401785h | J. Am. Chem. Soc. 2013, 135, 6778–6781

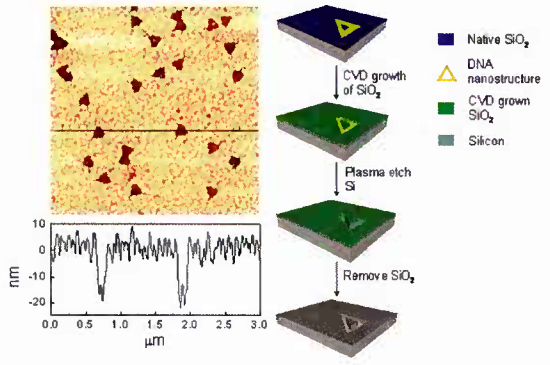

Figure 4. (left) AFM image and cross section of triangular trenches obtained by SF_6/O_2 plasma etching of a Si substrate using a negative-tone CVD-grown SiO_2 as a hard mask. The black line indicates the location of the cross section. (right) Schematic illustration of the use of a DNA nanostructure to pattern silicon.

which can be used as a hard mask for conventional semiconductor nanofabrication. Recently, two studies have demonstrated the deterministic deposition of DNA nanostructures on a silicon wafer.[14,15] This advance, together with our results described here, opens up the possibility to integrate DNA nanotechnology with conventional nanolithography to create high-resolution patterns. Although the resolution demonstrated here cannot yet compete with that of the best extreme UV lithography and electron-beam lithography, our approach is parallel, high-throughput and has the potential to drastically reduce the capital investment and operational cost of high-resolution (<20 nm) nanofabrication.[17]

■ ASSOCIATED CONTENT

Supporting Information

Experimental details, additional figures, and a table. This material is available free of charge via the Internet at http://pubs.acs.org.

■ AUTHOR INFORMATION

Corresponding Author

hliu@pitt.edu; peng_yin@hms.harvard.edu

Notes

The authors declare no competing financial interest.

■ ACKNOWLEDGMENTS

H.L. acknowledges financial support from AFOSR Young Investigator Program (FA9550-13-1-0083), the Mascaro Center for Sustainable Innovation, and the Central Research Development Fund of the University of Pittsburgh. The work is also supported by a DARPA Young Faculty Award N66001-11-1-4136, an ONR Young Investigator Program Award N000141110914, an ONR Grant N000141010827 and an NSF CAREER Award CCF1054898 to P.Y.

■ REFERENCES

(1) Wei, B.; Dai, M. J.; Yin, P. *Nature* **2012**, *485*, 623.
(2) Pinheiro, A. V.; Han, D.; Shih, W. M.; Yan, H. *Nat. Nanotechnol.* **2011**, *6*, 763.
(3) Han, D.; Pal, S.; Nangreave, J.; Deng, Z.; Liu, Y.; Yan, H. *Science* **2011**, *332*, 342.
(4) Sharma, J.; Chhabra, R.; Cheng, A.; Brownell, J.; Liu, Y.; Yan, H. *Science* **2009**, *323*, 112.
(5) Endo, M.; Sugiyama, H. *ChemBioChem* **2009**, *10*, 2420.
(6) Douglas, S. M.; Dietz, H.; Liedl, T.; Hogberg, B.; Graf, F.; Shih, W. M. *Nature* **2009**, *459*, 414.
(7) Dietz, H.; Douglas, S. M.; Shih, W. M. *Science* **2009**, *325*, 725.
(8) Rothemund, P. W. *Nature* **2006**, *440*, 297.
(9) Ke, Y.; Ong, L. L.; Shih, W. M.; Yin, P. *Science* **2012**, *338*, 1177.
(10) Gazit, E. *Chem. Soc. Rev.* **2007**, *36*, 1263.
(11) Hawker, C. J.; Russell, T. P. *MRS Bull.* **2005**, *30*, 952.
(12) Yan, H.; Park, S. H.; Finkelstein, G.; Reif, J. H.; LaBean, T. H. *Science* **2003**, *301*, 1882.
(13) Xia, Y.; Whitesides, G. M. *Angew. Chem., Int. Ed.* **1998**, *37*, 550.
(14) Hung, A. M.; Micheel, C. M.; Bozano, L. D.; Osterbur, L. W.; Wallraff, G. M.; Cha, J. N. *Nat. Nanotechnol.* **2010**, *5*, 121.
(15) Kershner, R. J.; Bozano, L. D.; Micheel, C. M.; Hung, A. M.; Fornof, A. R.; Cha, J. N.; Rettner, C. T.; Bersani, M.; Frommer, J.; Rothemund, P. W. K.; Wallraff, G. M. *Nat. Nanotechnol.* **2009**, *4*, 557.
(16) Gao, B.; Sarveswaran, K.; Bernstein, G. H.; Lieberman, M. *Langmuir* **2010**, *26*, 12680.
(17) Zhang, G.; Surwade, S. P.; Zhou, F.; Liu, H. *Chem. Soc. Rev.* **2013**, *42*, 2488.
(18) Pearson, A. C.; Liu, J.; Pound, E.; Uprety, B.; Woolley, A. T.; Davis, R. C.; Harb, J. N. *J. Phys. Chem. B* **2012**, *116*, 10551.
(19) Kuzyk, A.; Schreiber, R.; Fan, Z.; Pardatscher, G.; Roller, E. M.; Hogele, A.; Simmel, F. C.; Govorov, A. O.; Liedl, T. *Nature* **2012**, *483*, 311.
(20) Surwade, S. P.; Zhao, S.; Liu, H. *J. Am. Chem. Soc.* **2011**, *133*, 11868.
(21) Schreiber, R.; Kempter, S.; Holler, S.; Schuller, V.; Schiffels, D.; Simmel, S. S.; Nickels, P. C.; Liedl, T. *Small* **2011**, *7*, 1795.
(22) Puchkova, A. O.; Sokolov, P.; Petrov, Y. V.; Kasyanenko, N. A. *J. Nanopart. Res.* **2011**, *13*, 3633.
(23) Geng, Y.; Liu, J.; Pound, E.; Gyawali, S.; Harb, J. N.; Woolley, A. T. *J. Mater. Chem.* **2011**, *21*, 12126.
(24) Li, H.; Carter, J. D.; La Bean, T. H. *Mater. Today* **2009**, *12*, 24.
(25) Becerril, H. A.; Woolley, A. T. *Chem. Soc. Rev.* **2009**, *38*, 329.
(26) Becerril, H. A.; Woolley, A. T. *Small* **2007**, *3*, 1534.
(27) Hulme, J. P.; Gwak, J.; Miyahara, Y. *J. Am. Chem. Soc.* **2006**, *128*, 390.
(28) Deng, Z.; Mao, C. *Angew. Chem., Int. Ed.* **2004**, *43*, 4068.
(29) Kim, H. J.; Roh, Y.; Hong, B. *Langmuir* **2010**, *26*, 18315.
(30) Jiang, X.; Bent, S. F. *J. Phys. Chem. C* **2009**, *113*, 17613.
(31) Farm, E.; Kemell, M.; Ritala, M.; Leskela, M. *J. Phys. Chem. C* **2008**, *112*, 15791.
(32) Lee, J. P.; Sung, M. M. *J. Am. Chem. Soc.* **2004**, *126*, 28.
(33) Walker, A. V. *Langmuir* **2010**, *26*, 13778.
(34) Hampden-Smith, M. J.; Kodas, T. T. *Chem. Vap. Deposition* **1995**, *1*, 39.
(35) Weber, M. J.; Mackus, A. J. M.; Verheijen, M. A.; van der Marel, C.; Kessels, W. M. M. *Chem. Mater.* **2012**, *24*, 2973.
(36) Lu, Y.; Bangsaruntip, S.; Wang, X.; Zhang, L.; Nishi, Y.; Dai, H. *J. Am. Chem. Soc.* **2006**, *128*, 3518.
(37) Naumkin, A. V.; Kraut-Vass, A.; Powell, C. J. *NIST X-ray Photoelectron Spectroscopy Database*; NIST Standard Reference Database 20, version 3.5; http://srdata.nist.gov/xps/Default.aspx.
(38) Klaus, J. W.; George, S. M. *J. Electrochem. Soc.* **2000**, *147*, 2658.
(39) Deng, X.; Mammen, L.; Butt, H.-J.; Vollmer, D. *Science* **2012**, *335*, 67.
(40) Barnette, A. L.; Kim, S. H. *J. Phys. Chem. C* **2012**, *116*, 9909.
(41) Kay, B. D.; Lykke, K. R.; Creighton, J. R.; Ward, S. J. *J. Chem. Phys.* **1989**, *91*, 5120.
(42) Malani, A.; Ayappa, K. G. *J. Phys. Chem. B* **2009**, *113*, 1058.
(43) Balkose, D.; Alp, B.; Ulku, S. *J. Therm. Anal. Calorim.* **2008**, *94*, 695.
(44) Tzeng, Y.; Lin, T. H. *J. Electrochem. Soc.* **1987**, *134*, 2304.

11.4.4 Structural DNA nanotechnology application: DNA Foundries for Shape-controlled inorganic material synthesis

Sciencexpress Research Articles

Casting inorganic structures with DNA molds

Wei Sun,[1,2] Etienne Boulais,[3] Yera Hakobyan,[3] Wei Li Wang,[1,2] Amy Guan,[1] Mark Bathe,[3]* Peng Yin[1,2]*

[1]Wyss Institute for Biologically Inspired Engineering, Harvard University, Boston, MA 02115, USA. [2]Department of Systems Biology, Harvard Medical School, Boston, MA 02115, USA. [3]Department of Biological Engineering, Massachusetts Institute of Technology, Cambridge, MA 02139, USA.

*Corresponding author. E-mail: py@hms.harvard.edu (P.Y.); mark.bathe@mit.edu (M.B.)

We report a general strategy for designing and synthesizing inorganic nanostructures with arbitrarily prescribed three-dimensional shapes. Computationally designed DNA strands self-assemble into a stiff "nano-mold" that contains a user-specified three-dimensional cavity and encloses a nucleating gold "seed". Under mild conditions, this seed grows into a larger cast structure that fills and thus replicates the cavity. We synthesized a variety of nanoparticles with three nanometer resolution: three distinct silver cuboids with three independently tunable dimensions, silver and gold nanoparticles with diverse cross sections, and composite structures with homo-/heterogeneous components. The designer equilateral silver triangular and spherical nanoparticles exhibited plasmonic properties consistent with electromagnetism-based simulations. Our framework is generalizable to more complex geometries and diverse inorganic materials, offering a range of applications in biosensing, photonics, and nanoelectronics.

Synthesis of shape-controlled inorganic structures underlies diverse applications in biosensing (*1*), light harvesting (*2*), and nanophotonics (*3*). Although a wide variety of synthetic nanostructures have been reported, the formation of nanoparticles (NPs) with arbitrarily prescribed three-dimensional (3D) shape and positional surface modification of sub-5 nm resolution has not been demonstrated with inorganic materials. Top-down lithography (e.g., electron beam lithography) has limited resolution, particularly for 3D shapes (*1*, *4*). In addition, it is a slow serial process, and therefore unsuitable for large-scale production. Capping ligands can be used to tune the energy difference of selected crystallographic facets and hence NP growth dynamics to produce diverse symmetric shapes (*5–11*). However, reliable dynamic growth simulation models are typically limited to highly symmetric shapes of identical surface facets (*11–14*), and it is challenging to predict irregular shapes as well as control final NP dimensions.

Structural DNA nanotechnology (*15*) provides a promising route to overcoming the preceding limitations. Using DNA molecules as construction materials, researchers have rationally designed and synthesized diverse shape-controlled nanostructures (*16–28*). Building on this success, we have developed a general framework to program 3D inorganic shapes (fig. S1) (*29*). Our approach uses computationally designed, chemically stable, and mechanically stiff DNA nanostructures as molds to cast metallic NPs of user-specified 3D shape, which can be asymmetric. A "nanomold" is self-assembled from DNA strands, contains the user-designed 3D cavity, and encloses a small nucleating gold (Au) seed. Under mild conditions, the Au seed grows into a larger metal cast NP that fills the entire cavity of the mold, thereby replicating its 3D shape.

Using this nanocasting method, we constructed three distinct sub-25 nm 3D cuboid silver (Ag) NPs with three independently tunable dimensions. The shape versatility of DNA based nanocasting was further demonstrated via the synthesis of Ag NPs with equilateral triangular, right triangular, and circular cross sections. Material versatility was demonstrated via synthesis of a Au cuboid in addition to the Ag NPs. The DNA mold served as an addressable coating for the cast NP and thus enabled the construction of higher order composite structures, including a Y-shaped Ag NP composite and a quantum-dot (QD)-Ag-QD sandwiched structure. Finally, the designer equilateral Ag triangle and Ag sphere exhibited plasmonic properties that are consistent with electromagnetism-based simulations.

By serving both as an informational "genome" to carry the user-designed blueprint of the inorganic shape in a digitally precise fashion and as a physical "fabricator" for its faithful and accurate execution, DNA enables a new kind of shape-by-design framework for inorganic nanostructure fabrication and promises diverse transformative applications. For example, because the plasmonic properties of shape-controlled metal NPs can be predicted quantitatively *in silico*, the current shape-by-design framework can be further generalized to be a property-by-design framework for producing inorganic nanostructures with prescribed functional properties.

Casting a Ag cuboid

Figure 1A depicts the process of casting a cuboid shaped Ag NP. First, we construct a DNA mold for the casting (steps 1-3). In steps 1a and 1b, an open-ended DNA nanostructure barrel and two DNA lids are respectively designed and assembled based on computed stiffness design. In step 2, a 5 nm Au NP is anchored to the interior surface of the barrel. In step 3, the attachment of the two lids to the barrel results in a box-like DNA mold with a cuboid cavity. At the end of step 3, we have constructed a DNA mold with a cuboid cavity and a Au seed inside. With this mold, in step 4 (the casting step), under suitable chemical conditions, the Au seed grows into a Ag NP confined by the mold. Using this strategy and its variants, we fabricated diverse shape controlled NPs (Fig. 1B). We next describe the design and construction details for casting a Ag cuboid NP using the afore-mentioned strategy (Fig. 1A).

Computational design of the DNA mold

Specifically, to design mechanically stiff molds for geometrically constrained metal growth in solution, we used scaffolded DNA origami (*22*), which enables the precise nanometer-scale design of complex 3D cavities of prescribed mechanical properties. The DNA sequences for the DNA mold were designed using software caDNAno (*30*), and its mechanical ground-state 3D solution structure and mechanical properties were then predicted by CanDo (*31*, *32*). Briefly, CanDo computes 3D solution structure by modeling B-form DNA as a continuous elastic rod with effective geometric and material properties. Crossovers are assumed to rigidly constrain adjacent helices on a square or honeycomb lattice. Effective mechanical properties of the molds, including their ground-state solution structures and their mechanical deformations in response to loading forces, are computed using the finite element method (*29*).

We first designed a multilayer DNA mold with a cuboid cavity. The sidewalls of the DNA mold were designed to possess two or three layers of parallel DNA helices with 12 crossovers per helix on average (Fig. 1A). Two to three layer sidewall thickness was selected to balance the

competing needs to optimize structural stiffness and to increase the cavity dimensions: thicker sidewalls result in higher structural stiffness but smaller cavity size, owing to the length limit of the scaffold strand (8,064 nucleotides). The *x*-*y* cross section of the central cavity was designed to be eight helices by six helices, with a *z*-dimensional height of nine helical turns. This provides a designed cuboid cavity (after the lid attachment in step 3) measuring 21 nm by 16 nm by 31 nm, assuming a 2.6 nm hydrated helix width and a 3.4 nm helical turn length (*33*). Simulation by CanDo verified that the ground-state solution structure of the DNA mold adopted the cuboid shape cavity (Fig. 2A and fig. S4A). We additionally examined the structural integrity of the mold using normal mode analysis (*29*).

To effectively confine metal growth, it is important that the DNA mold be sufficiently stiff. We therefore studied its response to different loading forces along the *x*- and *y*-direction (Fig. 2, B and C). The ground-state structure of the cuboid mold was used as the initial configuration to which two types of loading were applied to model distinct types of mechanical inhibition from the mold onto a given growing NP, namely point-contact (fig. S2) or distributed-contact (fig. S3). In the point-contact model, a growing NP is assumed to contact a single pair of directly opposing points of the mold (Fig. 2B and table S1, top); equal and opposite point forces are applied to the mold and its deformation is computed. In the distributed-contact model, a growing NP is assumed to fully fill the mold cavity so that the NP applies a uniformly distributed force along opposing interior walls of the cavity (Fig. 2C and table S1, bottom). Under the point-contact scenario, the force response for the barrel was 17 pN/nm in the *x*-direction, normal to the three-layer wall, and 10 pN/nm in the *y*-direction, normal to the two-layer wall. In comparison, higher force-response values were found for the distributed-contact scenario, around 30 pN/nm in the *x*-direction, normal to the three-layer wall, and 19 pN/nm in the *y*-direction, normal to the two-layered wall. Importantly, the simulated mechanical properties of the DNA mold (i.e., threshold force and linear deformation range) were found comparable to that of viral capsids (*34*) which have been used to effectively confine inorganic nano-materials grown within (*35*) [see (*29*) for calculation and comparison details]. This result suggests that the DNA mold is also sufficiently stiff to confine metal NP growth within, although growth expansion forces can produce slightly increased [up to 20% according to simulation; (*29*)] mold dimensions through elastic deformation of dsDNAs. Notably, mold stiffness was significantly affected by the sidewall thickness. Mechanical simulation revealed that the force response value increased seven-fold from one to three layers under the point-contact loading scenario (see tables S1, S4, and S5).

Design details

The above computation suggests that (1) our designed DNA mold has the expected ground-state solution conformation and that (2) it has sufficient mechanical stiffness to confine metal NP growth. Thus we used this design for step 1a. In step 1b, a three-layered DNA lid was designed with 18 helices in the *y*-direction, three helices in the *z*-direction and 13-helical turns in the *x*-direction (Fig. 1A).

In step 2, to attach the Au "seed" to the DNA barrel (*36*), twenty-seven 21-nucleotide (nt) single-stranded (ss) DNA "handles" were immobilized in the interior surface of the barrel (Fig. 1A). A 21-nt "anti-handle" (an ssDNA with sequence complementary to the handle) was immobilized onto the Au seed surface. The stoichiometric ratio between the anti-handle and the Au seed was set at 1:1 to achieve approximately one anti-handle per seed based on a previous report (*37*). The hybridization between the handle and the anti-handle anchored the Au seed to the interior of the barrel. Au seed was favored over Ag seed due to the stability and nucleation versatility of Au (*38–41*).

To assemble the seed-decorated barrel and the lids in step 3, the barrel was designed to carry fourteen and sixteen 16-nt ssDNA "connectors" on both ends (fig. S28, left), and one side of the lid was designed to carry twenty complementary "anti-connectors". Connectors and anti-connectors were designed to be positioned in roughly matching patterns. Hybridization between them brought the barrel and the two lids together, completing the assembly of a box-like mold with a fully enclosed cuboid cavity. The ~0.5 nm gap between neighboring DNA helices (not depicted in the figure) that comprised the mold was expected to permit the diffusion of small ions or molecules, such as metal ions and ascorbic acid, into the enclosed box. In step 4, under suitable chemical conditions (see details in the following paragraph), the Au seed would grow into a Ag cuboid that fills the cavity.

Experimental implementation

In a typical experiment, DNA barrels and lids were folded separately by slowly annealing the staple/scaffold mixtures from 80°C to 24°C over 72 hours. Crude products were subjected to 1.5% agarose gel electrophoresis with 0.5× TBE/10 mM $Mg(NO_3)_2$ as running buffer. Purified structures were extracted and subsequently recovered via centrifugation. Seed decoration was executed by incubating DNA barrels with 5-nm Au NPs (at a seed-to-barrel stoichiometry ratio of 2:1) at 35°C for 16 hours, and then annealed to 24°C over 3 hours. Excess Au seeds were removed by using a size-exclusion spin column. DNA lids were mixed with the seed-decorated DNA barrels (at lid-to-barrel stoichiometry ratio of 3:1) at 35°C for 16 hours, and annealed to 24°C over 3 hours. Growth of Ag NPs in step 4 was triggered by the addition of silver nitrate (1.4 mM) and ascorbic acid (2 mM). After growth for 10 min at room temperature in dark conditions, Ag NPs grown within DNA boxes were imaged by transmission electron microscopy (TEM). See (*29*) for experimental details of mold assembly and purification, metal growth, and TEM sample preparations.

TEM characterization

TEM imaging confirmed successful formation of barrels in step 1a (see fig. S23 for large-field-of-view images), formation of the lids in step 1b (see fig. S30 for large-field-of-view images), attachment of Au seed to the barrel in step 2 (see fig. S39 for large-field-of-view image), assembly of lids with the seed-decorated barrel in step 3 (Fig. 3B, middle column; see fig. S47 for large-field-of-view images), and finally formation of Ag cuboids with expected dimensions in step 4 (Fig. 3A; Fig. 3B, right column; see fig. S52 for large-field-of-view images). In a supporting experiment, lids also assembled successfully with a seed-free barrel (Fig. 3B, left).

From three projectional views of the TEM images (Fig. 3B, left column), the *x*-*y*, *x*-*z*, and *y*-*z* dimensions of the barrel cavity were measured respectively as 19.3 ± 1.5 nm by 13.3 ± 0.4 nm, 19.3 ± 1.5 nm by 30.5 ± 1.0 nm, and 13.3 ± 0.4 nm by 30.5 ± 1.0 nm ($N = 20$ for each projectional view), each approximately consistent with the designed 21 nm by 16 nm by 30 nm cuboid cavity enclosed in the box. From the *x*-*y* projection TEM image (Fig. 3B, middle row), thickness of top and bottom sidewalls of the barrel were measured to be 5.6 ± 0.2 nm ($N = 20$) while the left and right sidewalls were measured to be 7.8 ± 0.1 nm ($N = 20$, similar measurements were also obtained from *x*-*z* and *y*-*z* projections), which were in approximate agreement with two- or three-layered designs. However, due to partial dehydration and structural deformation during TEM sample preparation, small deviations of 2–3 nm were occasionally observed in some structures. The DNA lid exhibited designed 39.5 ± 2.6 nm by 47.7 ± 0.7 nm ($N = 20$) dimensions under TEM (see fig. S30 for large-field-of-view images). Because the barrel was designed to carry 27 handles, multiple seeds could in principle be attached to the barrel; here, we experimentally observed one–five seeds present in

a single barrel (Fig. 3B, middle column; see fig. S39 for large-field-of-view images).

After growth, the seed turned into a Ag cuboid, as revealed by the TEM images of dark rectangular projections in the *x*-*z*, *x*-*y*, and *y*-*z* planes, with an expected length of 21.2 ± 0.7 nm by 16.0 ± 0.4 nm by 32.1 ± 1.4 nm in *x*-*y*-*z* dimensions (N = 20 for each projectional view; Fig. 3A, large-field-of-view image; the right column of B, zoomed-in images; see figs. S51 and S52 for additional large-field-of-view and zoomed-in images). Measured dimensions of the NP were slightly larger than the measured dimensions of the cavity, suggesting compression of the DNA mold sidewalls by the Ag NP growth. The presence of 4–8 nm thick sidewalls (light colored) around the NP (dark colored) in the TEM images suggests that the DNA mold remained surrounding the NP after growth. Notably, all the Ag cuboids grown within the DNA molds exhibited round rather than sharp corners, in the absence of surface capping ligands. Such rounded corners are likely a consequence of surface energy minimization of Ag NPs by decreasing the number of dangling bonds at NP corners. In a supporting experiment, we removed one or two lids from the DNA box, and observed some Ag NPs grew out of the DNA barrel (fig. S50). These unconfined Ag NPs exhibited much larger dimensions than those within the DNA barrels, further confirming the designed confinement effect of DNA molds. We only observed NP growth within the mold, but not on its exterior surface, confirming the effectiveness of seed-nucleated growth.

Casting yield

Casting yield (40%, Table 1) from step 4 was defined as the ratio between the number of NPs with designed projectional shapes and the total number of seed-decorated boxes (with both lids well attached) in the TEM image (*29*) (fig. S51). Additionally, the reaction yields for each step in constructing a DNA mold in Fig. 1A were defined in (*29*) and listed in table S6. Specifically, the barrel formation yield (20%) from step 1a (Fig. 1) was determined from agarose gel (fig. S22), and was measured as the ratio between the molar quantity of target structure (determined by comparing the SYBR Safe stained target band intensity and the intensity of a standard DNA marker with known molar quantity) and the molar quantity of the initial scaffold strand used in the experiment (*29*). Lid formation yield (12%) of step 1b was similarly defined and measured (fig. S29). Seed decoration yield (86%) from step 2 was determined as the ratio of the number of barrels with at least one seed attached to the interior surface and the total number of seed-decorated barrels in the TEM image (*29*). Box closure yield (31%) from step 3 was measured as the ratio of the number of seed-decorated barrels with both lids well attached and the total number of seed-decorated barrels in the TEM image (*29*).

Tuning the dimensions of the Ag cuboids

The dimensions of the Ag cuboid can be modified by changing the cavity size of the DNA mold. Using this strategy, we tested two additional barrels of different dimensions (see figs. S5 and S6 for solution conformation computation, tables S2 and S3 for loading force responses, and figs. S25 and S27 for large-field-of-view images), and assembled DNA boxes accordingly. First, we reduced the *z*-direction length of the DNA box mold from 30 nm (nine DNA helical turns) to 20 nm (six DNA helical turns), and thus obtained a box with a 19.0 ± 1.4 nm by 13.9 ± 0.3 nm by 22.0 ± 0.9 nm cuboid cavity (N = 20 for each projectional view; TEM image in Fig. 3C, left column). After successful seed decoration (see fig. S40), box closure (TEM image in Fig. 3C, middle column; see fig. S48 for large-field-of-view images) and growth, a cuboid with measured dimensions of 20.6 ± 0.7 nm by 16.8 ± 0.7 nm by 21.6 ± 0.9 nm was formed (N = 20 for each projectional view; Fig. 3C, right; see fig. S53 for large-field-of-view images).

We next further reduced the *x*-dimension from 21 nm (eight helices) to 16 nm (six helices), and obtained a box with a 13.6 ± 0.1 nm by 13.6 ± 0.1 nm by 22.2 ± 0.7 nm cuboid cavity (TEM image in Fig. 3D, left column). After seed decoration (fig. S41), box closure (Fig. 3D, middle; see fig. S49 for large-field-of-view images) and growth, the cuboid appeared under TEM with a 14.9 ± 1.5 nm by 14.9 ± 1.5 nm square in *x*-*y* projection (N = 20 for each projectional view; Fig. 3D, right, middle), and 14.9 ± 1.5 nm by 22.4 ± 0.7 nm rectangular shapes for *x*/*y*-*z* projections (N = 20 for each projectional view; Fig. 3D, right, top; see fig. S54 for large-field-of-view images). See Table 1 for casting yield (33-39%) and table S6 for yields of different steps in constructing the mold. For each DNA box design, the barrel formation yield (5-13%) (see figs. S24 and S26 for gel images), lid formation yield (12%), seed decoration yield (74-91%), box closure yield (13-21%), and the casting yield (33-39%) (table S6) (*29*) were determined following the same definition described above.

NPs with prescribed cross sections

Using a simplified design strategy, we cast Ag NPs with prescribed cross section shapes (without height control). Here, we used open-ended barrel molds containing tunnels with designed shapes. The barrels were designed to have four-layered sidewalls, and featured three distinct cross section cavities: an equilateral triangular channel (Fig. 4A; see fig. S32 for large-field-of-view images), a right triangular channel (Fig. 4B; see fig. S34 for large-field-of-view image), and a circular shape channel (Fig. 4C; see fig. S36 for large-field-of-view image). To capture the Au seed, each barrel was designed to display three 21-nt ssDNA handles on its interior surface.

In the equilateral triangular barrel, the cross section of a fully confined Ag NP exhibited an equilateral triangular shape under TEM, with an expected edge length of 25.2 ± 1.9 nm (N = 20) and three rounded corners (Fig. 4A, right; see fig. S56 for large-field-of-view images). The DNA mold remained intact after Ag growth, and wrapped around the Ag NP. No obvious bending or curvature of DNA sidewalls was observed. In the center of the Ag NP, a circular-shape shade with 5 nm diameter was observed and was assigned to the Au seed in the DNA mold. TEM imaging of a tilted conformation further confirmed the 3D nature of the NP (fig. S57A). High-resolution TEM plus electron diffraction characterization (fig. S57, B and C) also revealed the highly crystalline nature of the Ag NP, which was consistent with its smooth surface morphology (absence of grain boundaries) and single seed-mediated growth pathway. In the right triangular barrel with a measured 21.9 ± 1.1 nm by 30.2 ± 0.5 nm by 37.9 ± 0.5 nm cavity (N = 20), the fully grown Ag NP demonstrated a triangular cross section shape with 21.7 ± 0.6 nm by 24.2 ± 0.7 nm by 28.2 ± 0.7 nm dimension (N = 20; Fig. 4B, right; see fig. S58 for large-field-of-view images). Similar to the equilateral triangular NP, the right-triangular NP also exhibited rounded corners. In the circular-shaped channel, a Ag sphere NP was observed with a circular cross section diameter of 25.5 ± 1.6 nm (N = 20; Fig. 4C, right; see fig. S59 for large-field-of-view images; see fig. S60 for images of tilted conformations, an HRTEM image revealing the spherical nature of the cast NP, and the electron diffraction result), consistent with our design. In contrast to the capping ligand method, DNA-based nanocasting enabled one-pot parallel production of distinct prescribed shapes by mixing different molds in a single reaction solution (see three distinct Ag shapes in fig. S65).

In the open barrels, only NPs growing laterally rather than vertically were confined to form specific shapes. This resulted in NP casting yields of 10-18% (Table 1), which is significantly lower than that of the fully enclosed cavity. Most of the unconfined NPs exhibited spherical shapes, and did not fully occupy the channels (see figs. S55, S56, S58, and S59 for large-field-of-view images). See Table 1 for casting yield and table S6 for yields of different steps in constructing the mold. For each design

of open-ended DNA molds, the barrel formation yield (5-10%) (see gel images in figs. S31, S33, and S35), seed decoration yield (60-75%), and the casting yield (10-18%) (table S6) (*29*) were determined following the same definition described above.

Experimental characterization and simulation of plasmonic properties

Next we used electron energy loss spectroscopy (EELS) (*42*) and electromagnetism-based simulations (*29*) to characterize NP plasmonic behavior, both experimentally and theoretically, of the equilateral Ag triangle in Fig. 4A and Ag sphere in Fig. 4C.

For the equilateral Ag triangle, EELS measurement (Fig. 4E) showed an intense peak around 2.30 eV (corresponding to 540 nm) with a wide shoulder peak around 3.26 eV (corresponding to 380 nm). Simulation for the same equilateral Ag triangle (figs. S7 and S8) revealed, in the presence of the DNA mold and carbon film beneath, a strong dipolar mode around 1.95 eV from the plasmonic resonance near the corners (Fig. 4F), various resonance modes between 2.45 eV (corresponding to 506 nm) and 3.70 eV (corresponding to 336 nm) near the center and edges, and a bulk Ag plasmon mode at 3.80 eV (corresponding to 327 nm, fig. S9). The red-shifting of the simulated EELS spectra with respect to experiment may be due to variations in the carbon film thickness of the TEM grid, the dielectric function of the DNA mold, the NP thickness, as well as the radii of the rounded NP corners (figs. S10 and S11) (*29*). Simulation of optical properties of the NPs in aqueous environment indicated similar plasmonic properties to those in vacuum (figs. S16 to S21) (*29*), suggesting the potential utility of the NPs for biosensing applications. Comparison with a previously published EELS result for a triangular Ag NP of similar dimensions (*43*) indicates a relative offset of ~0.1 eV for the predicted NP dipolar mode resonance, which may be due to the distinct substrate (mica) and surface coating employed. In contrast, a larger energy offset of 0.4 eV is observed relative to a previously examined larger Ag triangle of 75 nm dimension (*43*), indicating the importance of NP size on the resonance energy.

A highly distinct EELS response was measured for the Ag sphere (Fig. 4E), indicating shape-specific plasmonic properties. A single resonance band was observed near 3.26 eV (corresponding to 380 nm) experimentally, which was ascribed to the simulated (fig. S12) dipolar mode near 2.85 eV (corresponding to 435 nm, Fig. 4F) at the edge of the NP. Simulations also suggested several minor resonance modes between the 3.30 eV (corresponding to 376 nm) and 3.65 eV (corresponding to 340 nm) regions near the center of the NP (fig. S13). Similar environmentally-sensitive resonance was also observed for the cast Ag sphere (figs. S14 and S15).

Further high-resolution EELS characterization or polarized light excitation using dark-field microscopy on the surface immobilized metal NPs should reveal the spatial distribution of excited surface plasmons (*43*, *44*), which could enrich our fundamental understanding of nano-optics.

Casting a Au cuboid

To test the material versatility of our strategy, we cast a Au NP in a DNA barrel containing a 16 nm by 21 nm rectangular open tunnel. Compared to the Ag NP, the growth kinetics of the Au NP in 0.5× TBE/10 mM $Mg(NO_3)_2$ buffer was much slower. After 30 min reaction time, no obvious size increase was observed for the NP, which was ascribed to the chelating effect of EDTA to gold precursors. Removing EDTA from the reaction buffer significantly promoted the growth kinetics, where a reaction time of 30 min generated a Au NP with a 13.5 ± 0.7 nm by 19.0 ± 1.8 nm (N = 20) rectangular cross section within the barrel (Fig. 4D, right; see fig. S61 for large-field-of-view images). The casting yield (6%, table S6) was determined following the same definition described above. See (*29*) for yields of each step.

Composite structures

In addition to structural confinement and protection against undesired NP aggregation, the DNA mold provides a uniquely addressable three-dimensional coating for the NP to be cast, which facilitates the composition of the DNA molds into higher order complex structures. Here, we experimentally constructed a Y-shape Ag NP branched structure and a QD-Ag-QD composite structure.

A Y-shape DNA mold was assembled from three DNA barrels carrying complementary connector strands (fig. S37). Each barrel carries ssDNA handles to capture Au seeds. After seed decoration, TEM images revealed formation of the desired trimer (Fig. 5A, center; see fig. S45 for large-field-of-view images), as well as unintended byproducts, such as incomplete assembled dimers and multimers (e.g., pentamers and hexamers). Ag growth within the Y-shape barrel complex generated individual NP within each barrel, which together formed a Y-shape NP cluster (Fig. 5A, right; see fig. S62 for large-field-of-view images). The measured widths of Ag NP within each barrel were 22.7 ± 1.8 nm, 24.3 ± 1.4 nm, and 25.5 ± 0.9 nm (N = 20), slightly larger than the designed 21 nm width of the barrel mold. At the center of the Y-shape barrel complex, where the growth fronts of the Ag NPs met, narrow (< 2 nm) inter-particle gaps were observed. The casting yield (10%, table S6) was determined following the same definition described above. See (*29*) for yields of each step.

To build a composite structure where a Ag NP was sandwiched between two QDs, 5 or 6 biotin groups were introduced at both ends of a DNA barrel with a 21-16-30 nm cuboid tunnel (see fig. S38 for design details). After attaching Au seed inside the barrel, streptavidin coated QDs were introduced and bound to both ends of the barrel. TEM imaging revealed the formation of the designed sandwiched structure between QDs and the seed-decorated barrels (Fig. 5B, middle; see fig. S46 for large-field-of-view images). After staining with uranium salt (*29*), the white sphere with 16-21 nm diameter at the ends of the barrel was attributed to the PEG and streptavidin coating layer around QD cores (CdSe@ZnS; see fig. S64 for control experiments with QD only). 88% seed-decorated barrels (table S6) were conjugated with QDs at both ends (N = 129). Note that no QDs were found attached to side surfaces of DNA barrels, confirming that QD attachment was specifically mediated by biotins as designed. After Ag growth, TEM imaging revealed the formation of QD-Ag-QD composite structures (31% casting yield in table S6 and Fig. 5B, right) [see fig. S63 for large-field-of-view images and (*29*) for yields of each step]. Ag NPs exhibited a 20.5 ± 0.5 nm by 28.4 ± 1.3 nm projection (N = 20), consistent with the designed size of DNA barrel mold. Thus, we demonstrated the assembly of QD at prescribed locations on selected faces of a nonspherical metal NP.

Optimization of the casting process

The stoichiometry between anti-handle and Au seed was set to 1:1 to minimize the undesirable effect of surface-immobilized ssDNA on NP growth. To increase the formation yield of box-like DNA molds, the number of connectors on the barrels was optimized. Increasing the connectors from six to fourteen at each end of the barrel increased the yield from less than 10% to 31%; whereas changing the lid-to-barrel ratio from 2:1 to 6:1 only slightly raised the yield from 28% to 33%.

The effectiveness of the stiffness-based design strategy is verified by the following failed mold designs: single-layered DNA mold did not produce pre-designed cross section shapes (see fig. S67 for TEM images and table S4 for simulations); when the number of crossovers decreased to one or two, such as in the cases of DNA triangles that displayed less than 16 nm sidewalls, destructed DNA molds were observed during metal growth (see figs. S69 and S71 for examples). We also note that although chemical inhibition between phosphate groups and the growing NP is also expected to occur (*45*, *46*), it was not optimized as a design parameter for programming the shape in the current study. Additionally,

structural integrity of DNA molds was affected by the buffer ionic condition. At 10 mM magnesium nitrate concentration, DNA mold remained intact for 1 day at 1-2 mM reactant concentration, but deteriorated when the reactant concentration was higher than 20 mM.

For more detailed discussions on the optimization of nanocasting, and various sub-optimal or failed DNA molds used in the optimization experiments, see (*29*) and figs. S66 to S75.

Discussion

Previous work on casting NPs at a scale below 25 nm only had limited success, largely because of the lack of shape-programmable molds with both mechanical rigidity and surface programmability to enable site-specific seed decoration followed by constrained growth. High-stiffness nanomolds such as viral capsids (*35*) and porous inorganic materials (*47*) are difficult to program into arbitrary geometric shapes, limiting their utility for nanoscale casting of diverse NP geometries and dimensions. Previous reports have shown the programming of 2D inorganic shapes with DNA templates. For example, the growth of metals mediated by randomly-distributed nanocluster seeds (*48–52*) or strategically-positioned NP seeds (*53, 54*) on a DNA nanostructure surface has produced diverse 2D shapes. However, rough surface morphologies (*55*), and inhomogeneous width distributions along the DNA skeletons (*56*) are often observed for these unconfined metalized products. Our work differs by providing a general way to construct inorganic nanostructures with arbitrarily user-specified 3D shapes and precise prescribed dimensions, by using DNA nanostructures to spatially confine the growth of the final shape (rather than seeding the initial shape) of the inorganic NP. Importantly, the cast NP retains the addressable coating. To fabricate such surface modified NPs, traditional chemical synthesis typically involves multiple-step low-yield conjugation and purification after NP formation.

Rapid progress in DNA self-assembly will help to further expand the complexity and diversity of the NP shapes. Recent advances in scaffold-free, 3D construction with DNA bricks has already demonstrated highly complex cavities (e.g., toroidal shape cavity) and tunnels (e.g., crossed and branched tunnels) encoded in sub-25 nm DNA cuboids (*26*). It is conceivable that such complex cavity and tunnel shapes may be transferred to inorganic substrates via DNA nanocasting. Further, because of the length limitation of the M13 viral scaffold strand, current mutli-layered mold designs using scaffolded DNA origami are restricted to produce sub-25 nm cavities. However, by using scaffold-free construction with DNA bricks (*25, 26*), DNA origami made from longer scaffolds (*57*), or hierarchical assembly of multiple origami (*28, 58*) and brick structures, nanomolds with much larger and more complex cavities may be achieved. In addition to increasing the shape complexity of the cast NPs, further research will also focus on expanding the material diversity of the NPs. Aside from Ag and Au, the Au seed can also mediate the growth of other diverse inorganic materials [e.g., metals (*38, 39*), oxides (*40*) and complex salt (*41*)] at mild conditions, for potential casting with DNA molds. Replacing Au seed with metal bind peptides may further expand the cast diversity (e.g., metals, metal oxides, and chalcogenides) (*59*).

The casting yield (step 4) may be further optimized by using computer-aided design of DNA molds with high mechanical integrity to minimize mold distortion during growth. The formation of 3D enclosed, seed-decorated mold may be improved by optimizing self-assembly conditions [e.g., using isothermal folding (*60*)] or exploring alternative construction strategies [e.g., using DNA bricks (*26*)]. Additionally, replacing Au seeds (which tend to aggregate at DNA origami mold folding conditions) with more stable metal-binding peptides could simplify the current multi-step assembly strategy and enable one-step, high-yield formation of DNA molds with enclosed peptide seeds.

The shape- and surface-controlled inorganic NPs fabricated herein may eventually enable novel applications in diverse fields ranging from biosensing, to photonics, and to nanoelectronics. Near term applications are likely those based on single-particle properties. For example, DNA nanocasting produces a prescribed metal shape with a uniquely addressable coating, which may display the binding site for target molecule at the near-field maximum position and hence enable highly sensitive detection. Because optical simulations of the cast NPs in water suggest geometry-specific dipolar resonances and near-field distributions (*29*), highly multiplexed sensing may be achieved using diverse programmed metal shapes.

DNA-based nanoscasting represents a general approach for synthesizing inorganic nano-structures with arbitrarily prescribed 3D shapes (*29*). Together with other strategies for transferring the geometric information of DNA nanostructures to diverse inorganic materials [e.g., coating DNA nanostructures with inorganic oxides (*61*) or etching graphene using metalized DNA nanostrucures as lithography masks (*52*)], it points to a new kind of manufacture framework: DNA-directed, digitally programmable fabrication of inorganic nanostructures and devices. Such DNA-based inorganic nano-fabrication may eventually enable future production of sophisticated devices such as nanoscale optical circuits, electronic computers, and perhaps even inorganic molecular robots, each with their blueprints (or "genomes") encoded in the DNA molecules that constitute their "nano-fabricators".

Materials and methods

DNA mold design

caDNAno (*30*) was used to design the sequences and routing of staple strands using the scaffold strand (mutated P8064) derived from M13 bacteriophage.

Simulation of DNA mold mechanical properties

The mechanical properties of DNA molds were predicted using the finite element method based on the ground-state 3D solution structure predicted by CanDo and standard geometric and mechanical properties of B-form DNA (*31, 32*). Mechanical deformations of the molds were computed in response to internal point- and distributed-loading using the commercial finite element software ADINA (ADINA RD, Inc., Watertown, MA). Normal Mode Analysis was performed to compute the lowest energy modes of deformation of the molds (*29, 62, 63*).

DNA mold folding

Assembly of DNA-origami molds was accomplished following previous reported protocol (*22, 23*). In a one-pot reaction, 50 nM scaffold was mixed with 250 nM of every staple strands (Bioneer Inc. or IDTDNA Inc.) in a buffer including 5 mM Tris, 1 mM EDTA, 16 mM $MgCl_2$, (pH 8) and subjected to a thermal-annealing ramp that cooled from 80°C to 65°C over 75 min and then cooled from 64°C to 24°C over 70 hours.

Gel purification

40 μL of folding products were mixed with 10 μL of glycerol, and loaded into 1.5% agarose gel pre-stained with Sybr Safe containing 0.5× TBE and 10 mM $Mg(NO_3)_2$. The electrophoresis was running at 75 V for three hours in a gel box incubated in an ice-water bath. Monomer band was excised and origami was recovered by pestle crushing, followed by centrifugation for 3 min at 6000 rpm at room temperature using "Freeze 'N Squeeze" DNA Gel Extraction spin columns (Bio-Rad). Recovered DNA molds were stored at 4°C for further use.

DNA-decoration onto 5-nm Au seeds

Conjugation of thiolated DNA onto 5-nm Au seeds was achieved following previous reported protocol (*64*). In a typical experiment, 20 μL 2.5 μM phosphine-coated 5-nm Au seed was mixed with 0.5 μL 2 M $NaNO_3$ and 0.65 μL 100 μM thiolated DNA in 0.25× TBE buffer. The reaction solution was incubated at room temperature for 36 hours in dark. After that, the reaction solution was loaded into 1% agarose gel containing 0.5× TBE buffer. The electrophoresis was running at 95 V for 1 hour in a gel box on an ice-water bath. The purple band was recovered by pestle crushing, followed by centrifugation for 3 min at 10,000 rpm at room temperature using "Freeze 'N Squeeze" DNA Gel Extraction spin columns (Bio-Rad). Recovered DNA molds were stored at 4°C in dark for further use. The sequence for the thiolated DNA was: TATGAGAAGTTAGGAATGTTATTTTT-Thiol. Note that thiol group was modified at the 3′ end of anti-handle sequence TATGAGAAGTTAGGAATGTTA via a TTTTT spacer.

Seed decoration of DNA mold

Purified DNA molds were mixed with 50 mM $NaNO_3$ and 10 nM purified 5-nm Au-DNA conjugates(at a seed-to-barrel stoichiometry ratio of 2:1), and incubating at 35°C for 16 hours, followed by slowly annealing to 24°C over 3 hours. The reaction buffer was then purified using S300 spin column (GE healthcare) by centrifugation for 2 min at 750 g at room temperature to remove excessive Au-DNA conjugates.

Lid attachment onto DNA mold

DNA lids were mixed with the seed-decorated DNA barrels (at lid-to-barrel stoichiometry ratio of 3:1) at 35°C for 16 hours, and annealed to 24°C over 3 hours.

Metal growth

For Ag growth, to 5 μL purified seed-decorated DNA molds, 0.5 μL 14 mM $AgNO_3$ and 0.5 μL 20 mM ascorbic acid were added at room temperature, and pipetted for 30 times for mixing. Then the reaction solution was kept in dark at room temperature for 4 min to 20 min. For Au growth, 0.5 μL 14 mM $HAuCl_4$ and 0.5 μL 20 mM ascorbic acid were added to 5-μL purified seed-decorated DNA molds in 0.5× TB buffer at room temperature, and pipetted for 30 times for mixing. Then the reaction solution was kept in dark at room temperature from 20 min to 2 hours.

TEM

3.5 μL NPs were adsorbed onto glow discharged carbon-coated TEM grids for 2 min and then wiped away, followed by staining using 3.5 μL 2% aqueous uranyl formate solution containing 25 mM NaOH for 45 s. Imaging was performed using an JEOL 1400 operated at 80 keV. High-resolution TEM and electron diffraction were acquired using a JEOL 2010 with FEG operated at 200 keV for unstained NP sample deposited onto amorphous carbon film.

Yield analysis

Seed decoration yield from step 2, box closure yield from step 3, and casting yield from step 4 (*29*) in Fig. 1A were acquired through direct counting of NP with prescribed shapes and dimensions from each of the three projection views. For each individual barrel and lid, the barrel and the lid formation yield from step 1a (Fig. 1A) were determined from agarose gel (*29*).

EELS experimental characterization

The low loss EELS data were collected with TEAM I at the Lawrence Berkeley National Lab, a Monochromated TEM operated at 80 keV. The EELS data were collected in the TEM mode under vacuum for the unstained NP sample deposited onto amorphous carbon film.

Simulation of NP plasmonic and optical properties

EELS results were simulated using MNPBEM (*65*, *66*) that is freely available as a MATLAB (The MathWorks, Inc., Natick, MA) toolbox (*29*). Optical property simulations were performed using the commercial finite element software COMSOL (COMSOL Inc., Burlington, MA) employing the full 3D continuum electromagnetic Helmholtz equation (*29*, *67*, *68*).

References and Notes

1. P. P. Pompa, L. Martiradonna, A. D. Torre, F. D. Sala, L. Manna, M. De Vittorio, F. Calabi, R. Cingolani, R. Rinaldi, Metal-enhanced fluorescence of colloidal nanocrystals with nanoscale control. *Nat. Nanotechnol.* **1**, 126–130 (2006). Medline doi:10.1038/nnano.2006.93
2. F. Wang, C. Li, H. Chen, R. Jiang, L. D. Sun, Q. Li, J. Wang, J. C. Yu, C. H. Yan, Plasmonic harvesting of light energy for Suzuki coupling reactions. *J. Am. Chem. Soc.* **135**, 5588–5601 (2013). Medline doi:10.1021/ja310501y
3. A. V. Kildishev, A. Boltasseva, V. M. Shalaev, Planar photonics with metasurfaces. *Science* **339**, 1232009 (2013). Medline doi:10.1126/science.1232009
4. A. L. Koh, A. I. Fernández-Domínguez, D. W. McComb, S. A. Maier, J. K. W. Yang, High-resolution mapping of electron-beam-excited plasmon modes in lithographically defined gold nanostructures. *Nano Lett.* **11**, 1323–1330 (2011). Medline doi:10.1021/nl104410t
5. Y. Sun, Y. Xia, Shape-controlled synthesis of gold and silver nanoparticles. *Science* **298**, 2176–2179 (2002). Medline doi:10.1126/science.1077229
6. Y. Xia, Y. Xiong, B. Lim, S. E. Skrabalak, Shape-controlled synthesis of metal nanocrystals: Simple chemistry meets complex physics? *Angew. Chem. Int. Ed.* **48**, 60–103 (2009). Medline doi:10.1002/anie.200802248
7. T. Ming, W. Feng, Q. Tang, F. Wang, L. Sun, J. Wang, C. Yan, Growth of tetrahexahedral gold nanocrystals with high-index facets. *J. Am. Chem. Soc.* **131**, 16350–16351 (2009). Medline doi:10.1021/ja907549n
8. N. Ma, E. H. Sargent, S. O. Kelley, One-step DNA-programmed growth of luminescent and biofunctionalized nanocrystals. *Nat. Nanotechnol.* **4**, 121–125 (2009). Medline doi:10.1038/nnano.2008.373
9. S. E. Lohse, C. J. Murphy, Applications of colloidal inorganic nanoparticles: From medicine to energy. *J. Am. Chem. Soc.* **134**, 15607–15620 (2012). Medline doi:10.1021/ja307589n
10. Z. Wang, L. Tang, L. H. Tan, J. Li, Y. Lu, Discovery of the DNA "genetic code" for abiological gold nanoparticle morphologies. *Angew. Chem. Int. Ed.* **51**, 9078–9082 (2012). Medline doi:10.1002/anie.201203716
11. L. Ruan, H. Ramezani-Dakhel, C. Y. Chiu, E. Zhu, Y. Li, H. Heinz, Y. Huang, Tailoring molecular specificity toward a crystal facet: A lesson from biorecognition toward Pt111. *Nano Lett.* **13**, 840–846 (2013). Medline doi:10.1021/nl400022g
12. A. Puzder, A. J. Williamson, N. Zaitseva, G. Galli, L. Manna, A. P. Alivisatos, The effect of organic ligand binding on the growth of CdSe nanoparticles probed by ab initio calculations. *Nano Lett.* **4**, 2361–2365 (2004). doi:10.1021/nl0485861
13. J. Yu, M. L. Becker, G. A. Carri, A molecular dynamics simulation of the stability-limited growth mechanism of peptide-mediated gold-nanoparticle synthesis. *Small* **6**, 2242–2245 (2010). Medline doi:10.1002/smll.201000889
14. C. R. Bealing, W. J. Baumgardner, J. J. Choi, T. Hanrath, R. G. Hennig, Predicting nanocrystal shape through consideration of surface-ligand interactions. *ACS Nano* **6**, 2118–2127 (2012). Medline doi:10.1021/nn3000466
15. N. C. Seeman, DNA in a material world. *Nature* **421**, 427–431 (2003). Medline doi:10.1038/nature01406
16. J. H. Chen, N. C. Seeman, Synthesis from DNA of a molecule with the connectivity of a cube. *Nature* **350**, 631–633 (1991). Medline doi:10.1038/350631a0
17. E. Winfree, F. Liu, L. A. Wenzler, N. C. Seeman, Design and self-assembly of

two-dimensional DNA crystals. *Nature* **394**, 539–544 (1998). Medline doi:10.1038/28998
18. W. M. Shih, J. D. Quispe, G. F. Joyce, A 1.7-kilobase single-stranded DNA that folds into a nanoscale octahedron. *Nature* **427**, 618–621 (2004). Medline doi:10.1038/nature02307
19. P. W. K. Rothemund, Folding DNA to create nanoscale shapes and patterns. *Nature* **440**, 297–302 (2006). Medline doi:10.1038/nature04586
20. P. Yin, R. F. Hariadi, S. Sahu, H. M. Choi, S. H. Park, T. H. Labean, J. H. Reif, Programming DNA tube circumferences. *Science* **321**, 824–826 (2008). Medline doi:10.1126/science.1157312
21. Y. He, T. Ye, M. Su, C. Zhang, A. E. Ribbe, W. Jiang, C. Mao, Hierarchical self-assembly of DNA into symmetric supramolecular polyhedra. *Nature* **452**, 198–201 (2008). Medline doi:10.1038/nature06597
22. S. M. Douglas, H. Dietz, T. Liedl, B. Högberg, F. Graf, W. M. Shih, Self-assembly of DNA into nanoscale three-dimensional shapes. *Nature* **459**, 414–418 (2009). Medline doi:10.1038/nature08016
23. H. Dietz, S. M. Douglas, W. M. Shih, Folding DNA into twisted and curved nanoscale shapes. *Science* **325**, 725–730 (2009). Medline doi:10.1126/science.1174251
24. D. Han, S. Pal, J. Nangreave, Z. Deng, Y. Liu, H. Yan, DNA origami with complex curvatures in three-dimensional space. *Science* **332**, 342–346 (2011). Medline doi:10.1126/science.1202998
25. B. Wei, M. Dai, P. Yin, Complex shapes self-assembled from single-stranded DNA tiles. *Nature* **485**, 623–626 (2012). Medline doi:10.1038/nature11075
26. Y. Ke, L. L. Ong, W. M. Shih, P. Yin, Three-dimensional structures self-assembled from DNA bricks. *Science* **338**, 1177–1183 (2012). Medline doi:10.1126/science.1227268
27. D. Han, S. Pal, Y. Yang, S. Jiang, J. Nangreave, Y. Liu, H. Yan, DNA gridiron nanostructures based on four-arm junctions. *Science* **339**, 1412–1415 (2013). Medline doi:10.1126/science.1232252
28. R. Iinuma, Y. Ke, R. Jungmann, T. Schlichthaerle, J. B. Woehrstein, P. Yin, Polyhedra self-assembled from DNA tripods and characterized with 3D DNA-PAINT. *Science* **344**, 65–69 (2014). Medline doi:10.1126/science.1250944
29. See supplementary materials on *Science* Online.
30. S. M. Douglas, A. H. Marblestone, S. Teerapittayanon, A. Vazquez, G. M. Church, W. M. Shih, Rapid prototyping of three-dimensional DNA-origami shapes with caDNAno. *Nucleic Acids Res.* **37**, 5001–5006 (2009). Medline doi:10.1093/nar/gkp436
31. C. E. Castro, F. Kilchherr, D. N. Kim, E. L. Shiao, T. Wauer, P. Wortmann, M. Bathe, H. Dietz, A primer to scaffolded DNA origami. *Nat. Methods* **8**, 221–229 (2011). Medline doi:10.1038/nmeth.1570
32. D. N. Kim, F. Kilchherr, H. Dietz, M. Bathe, Quantitative prediction of 3D solution shape and flexibility of nucleic acid nanostructures. *Nucleic Acids Res.* **40**, 2862–2868 (2012). Medline doi:10.1093/nar/gkr1173
33. Y. Ke, S. M. Douglas, M. Liu, J. Sharma, A. Cheng, A. Leung, Y. Liu, W. M. Shih, H. Yan, Multilayer DNA origami packed on a square lattice. *J. Am. Chem. Soc.* **131**, 15903–15908 (2009). Medline doi:10.1021/ja906381y
34. J. P. Michel, I. L. Ivanovska, M. M. Gibbons, W. S. Klug, C. M. Knobler, G. J. Wuite, C. F. Schmidt, Nanoindentation studies of full and empty viral capsids and the effects of capsid protein mutations on elasticity and strength. *Proc. Natl. Acad. Sci. U.S.A.* **103**, 6184–6189 (2006). Medline doi:10.1073/pnas.0601744103
35. M. B. Dickerson, K. H. Sandhage, R. R. Naik, Protein- and peptide-directed syntheses of inorganic materials. *Chem. Rev.* **108**, 4935–4978 (2008). Medline doi:10.1021/cr8002328
36. Z. Zhao, E. L. Jacovetty, Y. Liu, H. Yan, Encapsulation of gold nanoparticles in a DNA origami cage. *Angew. Chem. Int. Ed.* **50**, 2041–2044 (2011). Medline doi:10.1002/anie.201006818
37. D. Zanchet, C. M. Micheel, W. J. Parak, D. Gerion, A. P. Alivisatos, Electrophoretic isolation of discrete Au nanocrystal/DNA conjugates. *Nano Lett.* **1**, 32–35 (2001). doi:10.1021/nl005508e
38. F. R. Fan, D. Y. Liu, Y. F. Wu, S. Duan, Z. X. Xie, Z. Y. Jiang, Z. Q. Tian, Epitaxial growth of heterogeneous metal nanocrystals: From gold nano-octahedra to palladium and silver nanocubes. *J. Am. Chem. Soc.* **130**, 6949–6951 (2008). Medline doi:10.1021/ja801566d
39. F. Wang, C. Li, L. D. Sun, H. Wu, T. Ming, J. Wang, J. C. Yu, C. H. Yan, Heteroepitaxial growth of high-index-faceted palladium nanoshells and their catalytic performance. *J. Am. Chem. Soc.* **133**, 1106–1111 (2011). Medline doi:10.1021/ja1095733
40. R. Ghosh Chaudhuri, S. Paria, Core/shell nanoparticles: Classes, properties, synthesis mechanisms, characterization, and applications. *Chem. Rev.* **112**, 2373–2433 (2012). Medline doi:10.1021/cr100449n
41. G. Maurin-Pasturel, J. Long, Y. Guari, F. Godiard, M. G. Willinger, C. Guerin, J. Larionova, Nanosized heterostructures of Au@Prussian blue analogues: Towards multifunctionality at the nanoscale. *Angew. Chem. Int. Ed.* **53**, 3872–3876 (2014). Medline doi:10.1002/anie.201310443
42. J. A. Scholl, A. L. Koh, J. A. Dionne, Quantum plasmon resonances of individual metallic nanoparticles. *Nature* **483**, 421–427 (2012). Medline doi:10.1038/nature10904
43. J. Nelayah, M. Kociak, O. Stéphan, F. J. García de Abajo, M. Tencé, L. Henrard, D. Taverna, I. Pastoriza-Santos, L. M. Liz-Marzán, C. Colliex, Mapping surface plasmons on a single metallic nanoparticle. *Nat. Phys.* **3**, 348–353 (2007). doi:10.1038/nphys575
44. V. Myroshnychenko, J. Nelayah, G. Adamo, N. Geuquet, J. Rodríguez-Fernández, I. Pastoriza-Santos, K. F. MacDonald, L. Henrard, L. M. Liz-Marzán, N. I. Zheludev, M. Kociak, F. J. García de Abajo, Plasmon spectroscopy and imaging of individual gold nanodecahedra: A combined optical microscopy, cathodoluminescence, and electron energy-loss spectroscopy study. *Nano Lett.* **12**, 4172–4180 (2012). Medline doi:10.1021/nl301742h
45. L. Berti, G. A. Burley, Nucleic acid and nucleotide-mediated synthesis of inorganic nanoparticles. *Nat. Nanotechnol.* **3**, 81–87 (2008). Medline doi:10.1038/nnano.2007.460
46. S. J. Tan, M. J. Campolongo, D. Luo, W. Cheng, Building plasmonic nanostructures with DNA. *Nat. Nanotechnol.* **6**, 268–276 (2011). Medline doi:10.1038/nnano.2011.49
47. C. Gao, Q. Zhang, Z. Lu, Y. Yin, Templated synthesis of metal nanorods in silica nanotubes. *J. Am. Chem. Soc.* **133**, 19706–19709 (2011). Medline doi:10.1021/ja209647d
48. E. Braun, Y. Eichen, U. Sivan, G. Ben-Yoseph, DNA-templated assembly and electrode attachment of a conducting silver wire. *Nature* **391**, 775–778 (1998). Medline doi:10.1038/35826
49. H. Yan, S. H. Park, G. Finkelstein, J. H. Reif, T. H. LaBean, DNA-templated self-assembly of protein arrays and highly conductive nanowires. *Science* **301**, 1882–1884 (2003). Medline doi:10.1126/science.1089389
50. J. Liu, Y. Geng, E. Pound, S. Gyawali, J. R. Ashton, J. Hickey, A. T. Woolley, J. N. Harb, Metallization of branched DNA origami for nanoelectronic circuit fabrication. *ACS Nano* **5**, 2240–2247 (2011). Medline doi:10.1021/nn1035075
51. R. Schreiber, S. Kempter, S. Holler, V. Schüller, D. Schiffels, S. S. Simmel, P. C. Nickels, T. Liedl, DNA origami-templated growth of arbitrarily shaped metal nanoparticles. *Small* **7**, 1795–1799 (2011). Medline doi:10.1002/smll.201100465
52. Z. Jin, W. Sun, Y. Ke, C. J. Shih, G. L. Paulus, Q. Hua Wang, B. Mu, P. Yin, M. S. Strano, Metallized DNA nanolithography for encoding and transferring spatial information for graphene patterning. *Nat. Commun.* **4**, 1663 (2013). Medline doi:10.1038/ncomms2690
53. M. Pilo-Pais, S. Goldberg, E. Samano, T. H. Labean, G. Finkelstein, Connecting the nanodots: Programmable nanofabrication of fused metal shapes on DNA templates. *Nano Lett.* **11**, 3489–3492 (2011). Medline doi:10.1021/nl202066c
54. A. Kuzyk, R. Schreiber, Z. Fan, G. Pardatscher, E. M. Roller, A. Högele, F. C. Simmel, A. O. Govorov, T. Liedl, DNA-based self-assembly of chiral plasmonic nanostructures with tailored optical response. *Nature* **483**, 311–314 (2012). Medline doi:10.1038/nature10889
55. E. C. Samano, M. Pilo-Pais, S. Goldberg, B. N. Vogen, G. Finkelstein, T. H. LaBean, Self-assembling DNA templates for programmed artificial biomineralization. *Soft Matter* **7**, 3240–3245 (2011). doi:10.1039/c0sm01318h
56. M. Fischler, U. Simon, H. Nir, Y. Eichen, G. A. Burley, J. Gierlich, P. M. Gramlich, T. Carell, Formation of bimetallic Ag-Au nanowires by metallization of artificial DNA duplexes. *Small* **3**, 1049–1055 (2007). Medline doi:10.1002/smll.200600534
57. H. Zhang, J. Chao, D. Pan, H. Liu, Q. Huang, C. Fan, Folding super-sized DNA origami with scaffold strands from long-range PCR. *Chem. Commun.* **48**, 6405–6407 (2012). Medline doi:10.1039/c2cc32204h
58. S. Woo, P. W. K. Rothemund, Programmable molecular recognition based on the geometry of DNA nanostructures. *Nat. Chem.* **3**, 620–627 (2011). Medline doi:10.1038/nchem.1070

59. M. Sarikaya, C. Tamerler, A. K. Y. Jen, K. Schulten, F. Baneyx, Molecular biomimetics: Nanotechnology through biology. *Nat. Mater.* **2**, 577–585 (2003). Medline doi:10.1038/nmat964
60. J.-P. J. Sobczak, T. G. Martin, T. Gerling, H. Dietz, Rapid folding of DNA into nanoscale shapes at constant temperature. *Science* **338**, 1458–1461 (2012). Medline doi:10.1126/science.1229919
61. S. P. Surwade, F. Zhou, B. Wei, W. Sun, A. Powell, C. O'Donnell, P. Yin, H. Liu, Nanoscale growth and patterning of inorganic oxides using DNA nanostructure templates. *J. Am. Chem. Soc.* **135**, 6778–6781 (2013). Medline doi:10.1021/ja401785h
62. M. Bathe, A finite element framework for computation of protein normal modes and mechanical response. *Proteins* **70**, 1595–1609 (2008). Medline doi:10.1002/prot.21708
63. B. Brooks, D. Janežič, M. Karplus, Harmonic analysis of large systems. I. methodology. *J. Comput. Chem.* **16**, 1522–1542 (1995). doi:10.1002/jcc.540161209
64. J. Sharma, R. Chhabra, C. S. Andersen, K. V. Gothelf, H. Yan, Y. Liu, Toward reliable gold nanoparticle patterning on self-assembled DNA nanoscaffold. *J. Am. Chem. Soc.* **130**, 7820–7821 (2008). Medline doi:10.1021/ja802853r
65. U. Hohenester, A. Trügler, MNPBEM a matlab toolbox for the simulation of plasmonic nanoparticles. *Comput. Phys. Commun.* **183**, 370–381 (2012). doi:10.1016/j.cpc.2011.09.009
66. U. Hohenester, Simulating electron energy loss spectroscopy with the MNPBEM toolbox. *Comput. Phys. Commun.* **185**, 1177–1187 (2014). doi:10.1016/j.cpc.2013.12.010
67. E. Boulais, R. Lachaine, M. Meunier, Plasma mediated off-resonance plasmonic enhanced ultrafast laser-induced nanocavitation. *Nano Lett.* **12**, 4763–4769 (2012). Medline doi:10.1021/nl302200w
68. E. Boulais, R. Lachaine, M. Meunier, Plasma-mediated nanocavitation and photothermal effects in ultrafast laser irradiation of gold nanorods in water. *J. Phys. Chem. C* **117**, 9386–9396 (2013). doi:10.1021/jp312475h
69. C. Desgranges, J. Delhommelle, Molecular dynamics simulation of the nucleation and growth of gold nanoparticles. *J. Phys. Chem. C* **113**, 3607–3611 (2009). doi:10.1021/jp8101546
70. M. Mariscal, J. Velázquez-Salazar, M. Yacaman, Growth mechanism of nanoparticles: Theoretical calculations and experimental results. *CrystEngComm* **14**, 544–549 (2012). doi:10.1039/c1ce05602f
71. L. Chuntonov, G. Haran, Maximal Raman optical activity in hybrid single molecule-plasmonic nanostructures with multiple dipolar resonances. *Nano Lett.* **13**, 1285–1290 (2013). Medline doi:10.1021/nl400046z
72. H. Liang, D. Rossouw, H. Zhao, S. K. Cushing, H. Shi, A. Korinek, H. Xu, F. Rosei, W. Wang, N. Wu, G. A. Botton, D. Ma, Asymmetric silver "nanocarrot" structures: Solution synthesis and their asymmetric plasmonic resonances. *J. Am. Chem. Soc.* **135**, 9616–9619 (2013). Medline doi:10.1021/ja404345s
73. O. D. Miller, C. W. Hsu, M. T. Reid, W. Qiu, B. G. DeLacy, J. D. Joannopoulos, M. Soljačić, S. G. Johnson, Fundamental limits to extinction by metallic nanoparticles. *Phys. Rev. Lett.* **112**, 123903 (2014). Medline doi:10.1103/PhysRevLett.112.123903
74. V. V. Thacker, L. O. Herrmann, D. O. Sigle, T. Zhang, T. Liedl, J. J. Baumberg, U. F. Keyser, DNA origami based assembly of gold nanoparticle dimers for surface-enhanced Raman scattering. *Nat. Commun.* **5**, 3448 (2014). Medline doi:10.1038/ncomms4448
75. E. D. Palik, *Handbook of Optical Constants of Solids III* (Academic Press, New York, 1998).
76. G. Mie, Beiträge zur Optik trüber Medien, speziell kolloidaler Metallösungen. *Ann. Physik* **330**, 377–445 (1908). doi:10.1002/andp.19083300302
77. M. A. Yurkin, A. G. Hoekstra, The discrete dipole approximation: An overview and recent developments. *J. Quant. Spectrosc. Radiat.Transf.* **106**, 558–589 (2007).
78. J. D. Jackson, *Classical Electrodynamics* (Wiley, New York, ed. 3, 1999).
79. P. B. Johnson, R. W. Christy, Optical constants of the noble metals. *Phys. Rev. B* **6**, 4370–4379 (1972). doi:10.1103/PhysRevB.6.4370
80. M. I. Stockman, Nanoplasmonics: Past, present, and glimpse into future. *Opt. Express* **19**, 22029–22106 (2011). Medline doi:10.1364/OE.19.022029
81. B. J. Wiley, S. H. Im, Z. Y. Li, J. McLellan, A. Siekkinen, Y. Xia, Maneuvering the surface plasmon resonance of silver nanostructures through shape-controlled synthesis. *J. Phys. Chem. B* **110**, 15666–15675 (2006). Medline doi:10.1021/jp0608628
82. D. K. Lim, K. S. Jeon, J. H. Hwang, H. Kim, S. Kwon, Y. D. Suh, J. M. Nam, Highly uniform and reproducible surface-enhanced Raman scattering from DNA-tailorable nanoparticles with 1-nm interior gap. *Nat. Nanotechnol.* **6**, 452–460 (2011). Medline doi:10.1038/nnano.2011.79
83. J. H. Lee, G. H. Kim, J. M. Nam, Directional synthesis and assembly of bimetallic nanosnowmen with DNA. *J. Am. Chem. Soc.* **134**, 5456–5459 (2012). Medline doi:10.1021/ja2121525
84. G. M. Church, Y. Gao, S. Kosuri, Next-generation digital information storage in DNA. *Science* **337**, 1628–1628 (2012). Medline doi:10.1126/science.1226355

Acknowledgments: The authors thank Y. Ke, J. Shen, and B. Wei for discussion, and E. Haney, D. Pastuszak and E. Chen for assistance in draft preparation. This work is supported by a DARPA Young Faculty Award (N660011114136), an Office of Naval Research (ONR) Young Investigator Program Award (N000141110914), ONR grants (N000141010827, N000141310593, and N000141410610), an Army Research Office grant (W911NF1210238), a National Institutes of Health (NIH) Director's New Innovator Award (1DP2OD007292), a National Science Foundation (NSF) Faculty Early Career Development Award (CCF1054898), an NSF Expedition in Computing Award (CCF1317291), NSF grants (CCF1162459, CMMI1333215, CMMI1334109, and CMMI1344915) and Wyss Institute funds to P.Y., and ONR grants (DURIP N000141310664 and N000141210621) and NSF-DMREF grant (CMMI1334109) to M.B., E.B., and Y.H. E.B. additionally acknowledges NSERC for funding. This work was performed in part at the Center for Nanoscale Systems (CNS), a member of the National Nanotechnology Infrastructure Network (NNIN), which is supported by the National Science Foundation under NSF award no. ECS-0335765. CNS is part of Harvard University. The EELS of the silver NPs was measured at NCEM, which is supported by the Office of Science, Office of Basic Energy Sciences of the U.S. Department of Energy under Contract No. DE-AC0205CH11231. W.S. designed the system, conducted the experiments, and analyzed the data E.B. designed and performed optical and EELS simulation, and analyzed the data. Y.H. designed and performed mechanical simulation, and analyzed the data. W.L.W. performed EELS experiments and analyzed the data. A.G. performed experiments and analyzed the data. M.B. designed and supervised the simulation study and interpreted the data. P.Y. conceived, designed, and supervised the study and interpreted the data. All authors wrote the manuscript. All data described in this Article are presented in the supplementary materials.

Supplementary Materials

www.sciencemag.org/cgi/content/full/science.1258361/DC1
Materials and Methods
Supplementary Text
Figs. S1 to S75
Tables S1 to S6
References (*69–84*)

7 July 2014; accepted 30 September 2014

Published online 9 October 2014
10.1126/science.1258361

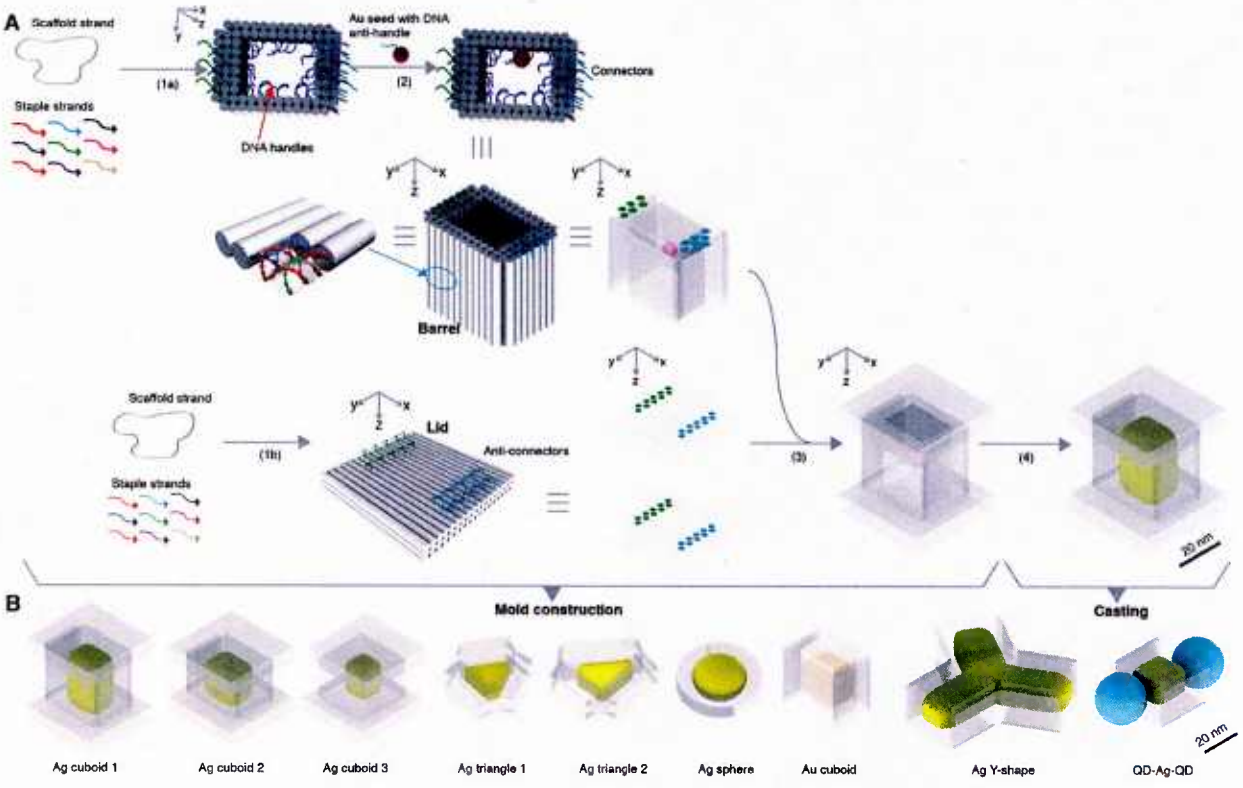

Fig. 1. Casting metal NPs with prescribed shapes using DNA nanostructure molds. (**A**) Design schematic for casting a Ag cuboid. Cyan and green dots denote (anti-)connectors. (**B**) Silver (yellow color) and gold (orange color) NPs cast within DNA molds (transparent layer). Ag, silver; Au, gold; QD, quantum dot (depicted as a cyan ball).

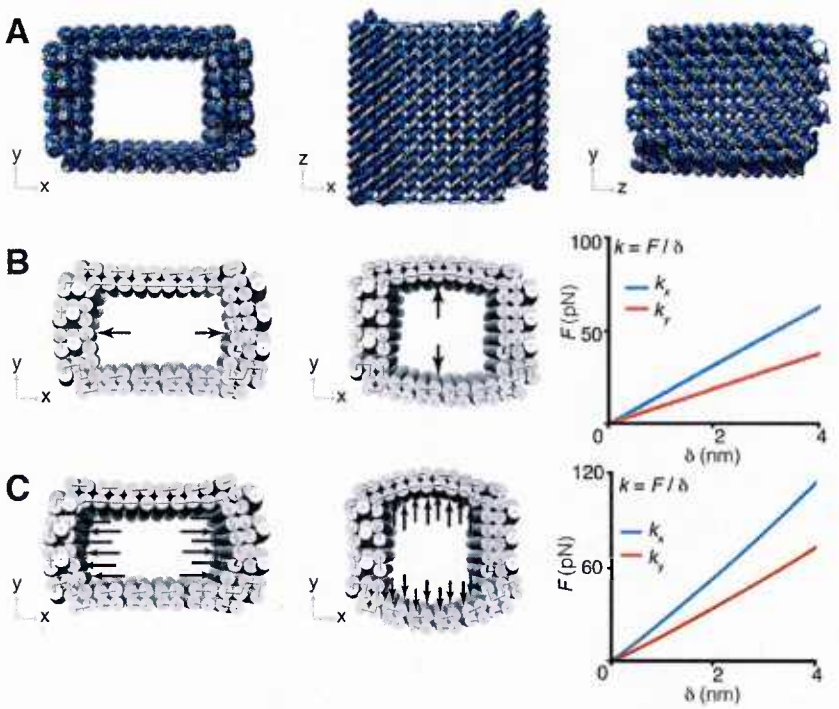

Fig. 2. Mechanical simulations of the rectangular DNA mold. (**A**) Ground-state solution conformation predicted for DNA mold with a 21 nm by 16 nm by 30 nm cuboid cavity. (**B** and **C**) Under point-contact loading (B) and distributed-contact loading (C), the force-deformation *F*-δ response in *x* and *y* directions for the DNA mold in (A). *k* is the simulated stiffness value along the specific direction.

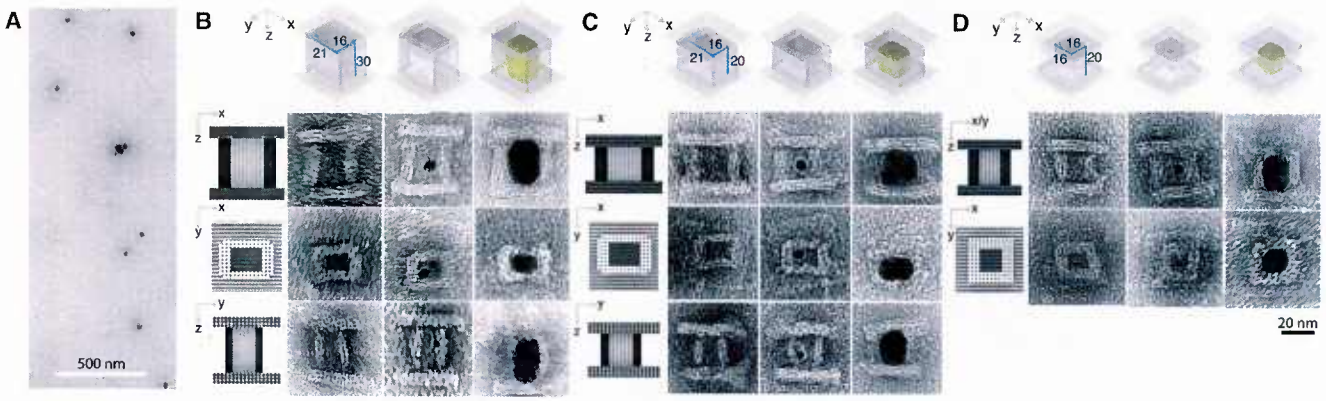

Fig. 3. Casting Ag cuboids with prescribed dimensions. (**A**) A large view TEM image for the Ag NP grown within the DNA mold with a 21 by 16 by 30 nm (or 21-16-30 nm) cuboid cavity [as shown in (B)]. (**B** to **D**) Design (top row) and TEM images (rows 2-4) of the Ag NPs grown in the DNA molds with dimensions of 21-16-30 nm (B), 21-16-20 nm (C), and 16-16-20 nm (D). In row 1 of each panel, a small purple dot represents a Au seed. Cast Ag NP is shown in yellow. In rows 2-4 of each panel, a projection model is presented to the left of the TEM images. The TEM images shows from left to right: the empty DNA box, the DNA box decorated with the Au seed (small dark dots; see figs. S47 to S49 for large-field-of-view images), the DNA box containing the fully grown Ag NP (dark rectangles with rounded corners; see figs. S52 to S54 for large-field-of-view images).

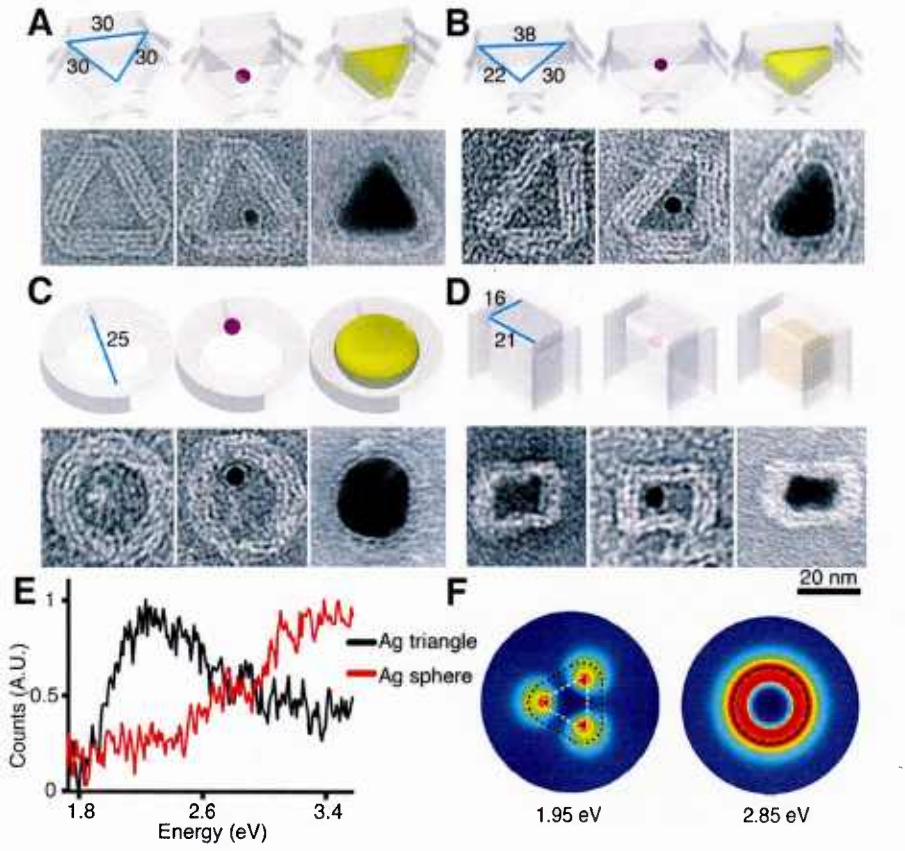

Fig. 4. Casting Ag and Au NPs with prescribed cross section shapes. In (A) to (D), the top row shows the design and the bottom row shows the TEM images of the empty barrel (left), the seed-decorated barrel (middle), and the fully grown NP (right). In the top row of each panel, a small purple dot represents a Au seed. Cast Ag NP is shown in yellow and Au NP is shown in orange. (**A**) A Ag NP with a 25 nm equilateral triangular cross section. See figs. S32, S42, and S56 for large-field-of-view images. (**B**) A Ag NP with a 22 nm - 24 nm - 28 nm right-angled triangular cross section. See figs. S34, S43, and S58 for large-field-of-view images. (**C**) A Ag NP with a 25 nm circular shape cross section. See figs. S36, S44, and S59 for large-field-of-view images. (**D**) A Au NP with 19 nm by 14 nm rectangle cross section. See figs. S23, S39, and S61 for large-field-of-view images. (**E**) EELS measurement for a Ag NP with a 25 nm equilateral triangular cross section [black, as in (A)] and a Ag sphere with 25 nm diameter circular cross section [red, as in (C)]. (**F**) The simulated EELS amplitude map for the dipolar resonant modes for a Ag NP with a 25 nm equilateral triangular cross section [as in (A), left] and a Ag NP with 25 nm diameter circular cross section [as in (C), right]. Colors represent simulated amplitude. The white and black dashed lines show the contour of the NP and the DNA mold, respectively.

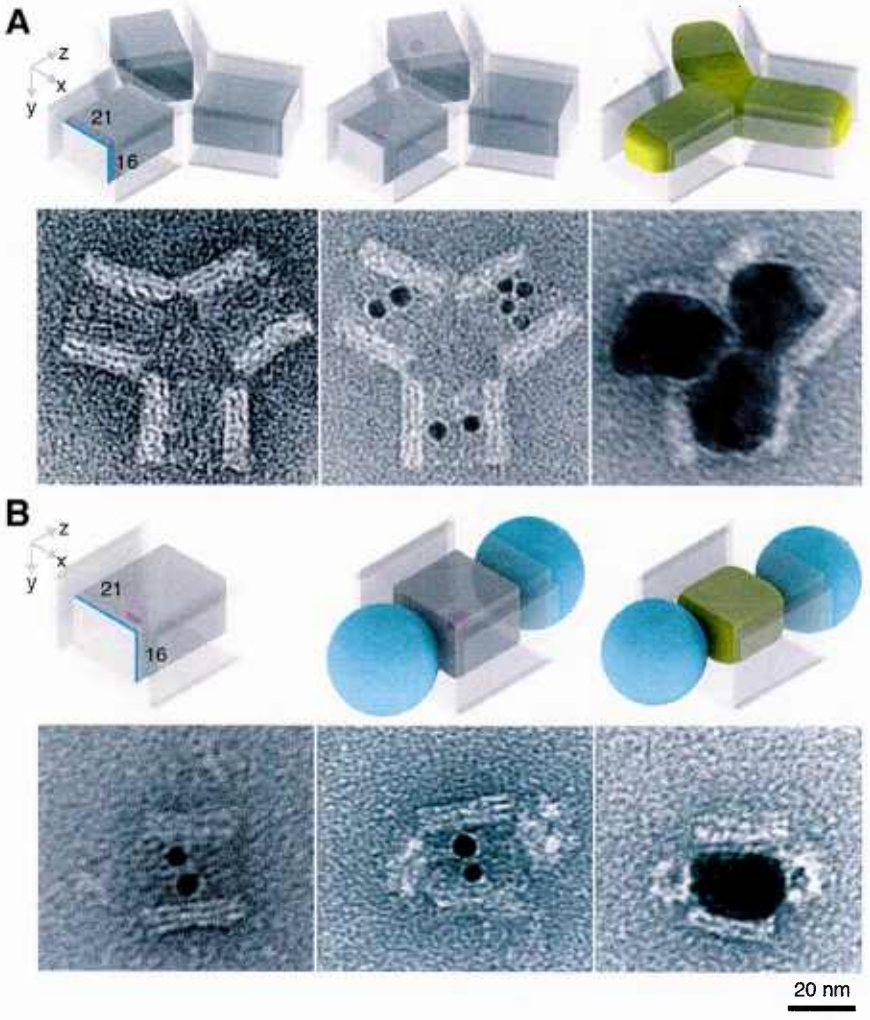

Fig. 5. Casting composite structures. (**A**) A Y-shaped Ag NP junction. Top, schematics; bottom, TEM images of a Y-shaped DNA barrel trimer (left), with seed-decoration (middle), and Ag NP grown within (right). See figs. S45 and S62 for large-field-of-view images. (**B**) A QD-Ag-QD composite structure. Top, schematics; bottom, TEM images of a DNA barrel with seed decoration (left), with QD attached (middle), and with Ag NP grown within (right). A small purple dot represents a Au seed. Cast Ag NP is shown in yellow. The streptavidin/PEG layer of QD is a depicted as a cyan ball. See figs. S46 and S63 for large-field-of-view images.

Table 1. Casting yield for different shaped NPs. The casting yield refers to the NP growth yield in step 4 in Fig. 1, and was calculated as the ratio between the number of DNA boxes with metal NPs of designed shapes and dimensions and the total number of seed-decorated DNA boxes. See main text and (*29*) for details. See table S6 for the yields of each step in constructing the seed-decorated molds, which are not accounted for in calculating the casting yield.

Shape	Casting yield (step 4)
Ag cuboid 1	40%
Ag cuboid 2	33%
Ag cuboid 3	39%
Ag triangle 1	10%
Ag triangle 2	14%
Ag sphere	18%
Au cuboid 1	6%
Ag Y-shape	10%
QD-Ag-QD	31%